EERL 2005-01
Earthquake Engineering
Research Laboratory

Performance of 18-Story Steel Moment-Frame Buildings During a Large San Andreas Earthquake – A Southern California-Wide End-to-End Simulation

by
Swaminathan Krishnan, Chen Ji, Dimitri Komatitsch, and Jeroen Tromp

This study was conducted at the
Seismological Laboratory

California Institute of Technology
Pasadena, California

2005

Acknowledgements

We wish to gratefully acknowledge the funding provided by the Seismological Laboratory at the California Institute of Technology. We also wish to thank Professors John F. Hall, Thomas Heaton, and Hiroo Kanamori of the California Institute of Technology for their insights and advice during the course of this study. The numerical simulations were performed on the Division of Geological & Planetary Sciences Dell cluster at the California Institute of Technology, USA, and the Seawulf cluster at the University of Toronto, Canada.

Summary

The mitigation of seismic risk in urban areas in the United States and abroad is of major concern for all governments. Unfortunately no comprehensive studies have attempted to address this issue in a rigorous, quantitative manner. This study tackles this problem head-on for two 18-story steel moment-frame buildings in southern California. The approach adopted here can be used as a template to study earthquake risk in other seismically sensitive regions of the world, such as Taiwan, Japan, Indonesia, China, South American countries (Chile, Bolivia, etc.), and the west coast of the United States (in particular, Seattle).

In 1857 a large earthquake of magnitude 7.9 [1] occurred on the San Andreas fault with rupture initiating at Parkfield in Central California and propagating in a southeasterly direction over a distance of more than 360 km. Such a unilateral rupture produces significant directivity toward the San Fernando and Los Angeles basins. Indeed, newspaper reports (Los Angeles Star [2, 3]) of sloshing observed in the Los Angeles river point to long-duration (1–2 min) and long-period (2–8 s) shaking which could have a severe impact on present-day tall buildings, especially in the mid-height range. To assess the risk posing the two steel moment-frame buildings from an 1857-like earthquake on the San Andreas fault, a finite source model of the magnitude 7.9 November 3, 2002 Denali fault earthquake is mapped on to the San Andreas fault with rupture initiating at Parkfield in Central California and propagating a distance of about 290 km in a south-easterly direction. As the rupture proceeds down south from Parkfield and hits the big bend on the San Andreas fault it sheds off a significant amount of energy into the San Fernando valley, generating large amplitude ground motion there. A good portion of this energy spills over into the Los Angeles basin with many cities along the coast such as Santa Monica and Seal Beach and more inland areas going east from Seal beach towards Anaheim experiencing long-duration shaking. In addition, the tail-end of the rupture sheds energy from SH/Love waves into the San Gabriel valley (Baldwin Park-La Puente region). These seismic waves get trapped and amplified in the basin. The peak velocity is of the order of 1 m.s^{-1} in the Los Angeles basin, including downtown Los Angeles, and 2 m.s^{-1} in the San Fernando valley. Significant displacements occur in the basins but not in the mountains. The peak displacements are in the neighborhood of 1 m in the Los Angeles basin and 2 m in the San Fernando valley. The ground motion simulation is performed using the spectral element method based seismic wave propagation program, SPECFEM3D.

To study the effects of the ground motion simulated at 636 sites (spread across southern California, spaced at about 3.5 km each way), computer models of an existing 18-story steel moment-frame building and a redesigned building with the same configuration (redesigned to current standards using the 1997 Uniform Building Code) are analyzed using the nonlinear structural analysis program, FRAME3D. For these analyses, the building Y direction is aligned with the geographical north direction. As expected, the existing building model fares much worse than the redesigned building model. Fracture occurs in at least 25% of the connections in this building when located in the San Fernando valley. About 10% of connections fracture in the building when located in downtown Los Angeles and the mid-Wilshire district (Beverly Hills), while the numbers are about 20% when it is located in Santa Monica, west Los Angeles, Inglewood , Alhambra, Baldwin Park, La Puente, Downey, Norwalk, Brea, Fullerton, Anaheim and Seal Beach. The peak interstory drifts in the middle-third and bottom-third of the existing building are far greater than the top-third pointing to damage being localized to the lower floors. The localization of damage in the lower floors rather than the upper floors could potentially be worse because of the risk of more floors pancaking on top of each other if a single story gives way. Consistent with the extent of fracture observed, the peak drifts in the existing building exceed 0.10 when located in the San Fernando valley, Baldwin Park and neighboring cities, Santa Monica, west Los Angeles and neighboring cities, Norwalk and neighboring cities, and Seal Beach and neighboring cities, which is well into the postulated collapse regime. When located in downtown Los Angeles and the mid-Wilshire district, the building would

barely satisfy the collapse prevention criteria set by FEMA [4] with peak drifts of about 0.05.

The performance of the newly designed 18-story steel building is significantly better than the existing building for the entire region. However, the new building still has significant drifts indicative of serious damage when located in the San Fernando valley or the Baldwin Park area. When located in coastal cities (such as Santa Monica, Seal Beach etc.), the Wilshire-corridor (west Los Angeles, Beverly Hills, etc.), Norwalk and neighboring cities, or the booming Orange County cities of Anaheim and Santa Ana, it has peak drifts of about 0.05 once again barely satisfying the FEMA collapse prevention criteria [5]. In downtown Los Angeles it does not undergo much damage in this scenario. Thus, even though this building has been designed according to the latest code it suffers damage that would necessitate closure for some time following the earthquake in most areas, but this should be expected since this is a large earthquake and building codes are written to limit the loss of life and ensure "collapse prevention" for such large earthquakes and not necessarily limit damage.

A second scenario considered in the study involves the same Denali earthquake source mapped to the San Andreas fault but with rupture initiating in the south and propagating to the north (with the largest amount of slip occurring to the north in Central California) instead of the other way around. The results of such a scenario indicate that ground shaking would be far less severe demonstrating the effects of directivity and slip distribution in dictating the level of ground shaking and the associated damage in buildings. The peak drifts in existing and redesigned building models are in the range of 0.02–0.04 indicating that there is no significant danger of collapse. However, damage would still be significant enough to warrant building closures and compromise life safety in some instances.

The ground motion simulation and the structural damage modeling procedures are validated using data from the January 17, 1994, Northridge earthquake while the band-limited nature of the ground motion simulation (limited to a shortest period of 2 s by the current state of knowledge of the 3-D Earth structure) is shown to have no significant effect on the response of the two tall buildings considered here with the use of observed records from the 1999 Chi Chi earthquake in Taiwan and the 2001 Tokachi-Oki earthquake in Japan.

Contents

List of Figures

List of Tables

Chapter 1 Introduction

The risk of earthquakes in southern California arises from two sources – well mapped out faults such as the San Andreas, Newport-Inglewood, and Santa Monica-Hollywood-Raymond faults that have some form of surface expression, and the network of blind-thrust faults hidden deep inside the Earth that includes the Northridge fault and the Puente Hills fault underneath downtown Los Angeles. While the San Andreas strike-slip fault system has the potential for large earthquakes (moment magnitude $\sim$8, roughly every 200 years [7, 8]), the blind-thrust faults have the potential for more moderate moment magnitude $\sim$7 earthquakes [9]. Fortunately, the urban areas of southern California have thus far been spared from the strongest shaking generated by large strike-slip earthquakes. However, the magnitude 6.7 earthquake of 1994 on the Northridge blind-thrust fault caused 57 deaths and economic losses in excess of $ 40 billion [10, 11]. This earthquake exposed the vulnerability of steel moment-resisting frame buildings to fracture [12, 13, 14]. These buildings resist lateral forces from an earthquake through bending in rigidly-connected (welded) beams and columns. Due to certain construction practices and the use of non-ductile weld material, a significant number of connections fractured in some of these buildings. Many of the moment-frame buildings in southern California were constructed before 1976 [15] when there was inadequate understanding of the nature and power of earthquake forces, and their effects on buildings. So the question arises as to what would happen to the many tall steel buildings in the mid-height range [1] in the Los Angeles and San Fernando basins if a large earthquake were to occur on the San Andreas fault. Can we estimate damage and consequent losses in these buildings? There have been many improvements in building codes and construction practices since 1994, and buildings designed according to the latest code (1997 Uniform Building Code, UBC97 [6]) are expected to perform far better than existing buildings [2] in large earthquakes. Will they in fact, and if so, is this performance adequate? Before these questions can be answered, more fundamental questions need to be addressed, e.g.: What kind of shaking would be experienced in this region during such an earthquake? What would the frequency content of the shaking be? What about the amplitude and duration of significant shaking?

In this study state-of-the-art computational tools in seismology and structural engineering are combined to perform an end-to-end three-dimensional (3-D) simulation of the rupture of a 290 km section of the San Andreas fault, the generation and propagation of the resulting seismic waves, the subsequent ground shaking in the Los Angeles and San Fernando basins, and the resulting damage to two 18-story steel moment-frame buildings in the region. A decade ago, Heaton et al. [16, 17, 18] simulated the near-source ground motions of a magnitude 7.0 thrust earthquake on a spatial grid of 60 km by 60 km using a vertically stratified crustal model that approximates the rock properties in the Los Angeles basin, and then modeled the response of a 20-story steel-frame building and a 3-story base-isolated building. Olsen et al. [19] and Graves [20] simulated seismic wave propagation generated by a magnitude 7.75 earthquake on a different section of the San Andreas fault. Here many aspects of the earthquake-structure problem are integrated into a comprehensive end-to-end simulation by including the finite-source model of a real earthquake [21, 22], 3-D

[1] There are many reasons to look at the performance of this particular class of buildings. The dominant modes of these buildings have natural periods in the range corresponding to that of the large-amplitude seismic waves expected from a large earthquake on the San Andreas fault. There are more steel buildings in this class than reinforced concrete ones (e.g., in 1993, there were 190 steel buildings above 8 stories as compared to 121 concrete buildings [15] in the Los Angeles and Ventura Counties. For buildings in the mid-height range this ratio is likely to be more skewed towards steel). However, this is not to say that concrete buildings will not perform poorly. Similarly, it is generally assumed that highrise buildings 40 stories and larger, with dual structural systems offering greater redundancy, and super-highrise buildings (60 stories and greater), with structural systems that resemble tubes to counter wind forces (which usually govern the design at these heights), will be able to resist shaking from a distant earthquake fairly well. However, no detailed damage analyses studies have been performed to confirm their safety during either large distant earthquakes or even moderate near-source earthquakes that could generate large displacement pulses at great velocities.

[2] For the purposes of this report, existing buildings are buildings designed using codes preceding the Uniform Building Code of 1997 [6] and new buildings are those that have been or will be designed using this code.

Earth structure [23, 24], 3-D seismic wave propagation [25], and 3-D nonlinear damage analyses of buildings using three-component ground motion [26, 27], validating these procedures using real data from recent earthquakes.

1.1 Scope of the Simulation

The seismological domain of our analysis includes all of southern California and extends north into the central valley beyond Parkfield. However, we restricted the engineering analysis to the main sedimentary basins of San Fernando, Los Angeles, and San Gabriel (Figure 1.1). For the scenarios considered in this study, ground motions south of Irvine going towards San Diego are unlikely to be strong enough to warrant a detailed engineering analysis. While the population of tall buildings in southern California is quite widespread, a major fraction is located in and around downtown Los Angeles, the mid-Wilshire district, west Los Angeles, and Santa Monica. There are quite a few tall buildings spread across the San Fernando valley as well, e.g., in Woodland Hills, Canoga Park, and Camarillo. There are about 30-40 tall buildings in Orange County (comprising the cities of Orange, Irvine, Costa Mesa, Newport Beach, Anaheim, Santa Ana, Garden Grove, etc.). A host of new tall buildings are being planned in Orange County with thirteen proposed high-rises in the cities of Anaheim and Santa Ana. Unfortunately, an inventory of steel buildings of different heights with geographical distribution is not readily available. The best available data in this regard comes from the EQE report [15] that states that in 1993 there were 190 steel buildings taller than 8 stories in Los Angeles and Ventura counties but had little information regarding their location and breakup in terms of height (beyond 8 stories). Given this lack of information on existing buildings, it was decided to divide the entire southern California region into a uniformly spaced grid (with a spacing of 1/32 of a degree or approximately 3.5 km each way) consisting of 636 sites shown by solid triangles in Figure 1.1. The strategy was to place structural models of the buildings considered in this study at each of these sites on the grid and analyze them for ground motion from the scenario earthquake considered. The results are presented in the form of damage/drift performance maps.

1.1.1 Scenarios Considered

Two scenarios involving the rupture of a 290 km segment of the San Andreas fault are considered in this study. The first scenario consists of the rupture initiating at Parkfield in central California and propagating in a south-easterly direction with the slip increasing gradually from Parkfield to a maximum value just north-west of the region of interest and dropping off abruptly to zero (Figure 1.1, inset). This slip distribution is derived from a finite-source inversion of the November 3, 2002, Denali earthquake. The second scenario consists of the same source but flipped in direction with the rupture initiating just north of the region of interest and terminating at Parkfield with the peak slip occurring close to Parkfield. These two scenarios were specifically chosen to illustrate the effects of directivity and slip distribution on the computed ground motion.

1.1.2 Buildings Considered

Two buildings have been considered in this study. The base building is an existing 18-story steel moment-frame building located on Canoga Avenue in Woodland Hills that had significant damage (moment-frame connection fractures) during the 1994 Northridge earthquake. This building has been the subject of detailed study by many research groups following the Northridge earthquake [13]. The second building is similar to the base building, but the structural system (lateral force-resisting system) has been redesigned according to the current building code, the 1997 Uniform Building Code (UBC97 [6]). The two fundamental differences between these two buildings is that the new building has been designed for larger earthquake forces (accounting for near-source effects) and for stringent redundancy requirements in the lateral force-resisting system. This leads to significantly different dynamic properties for the buildings. In gen-

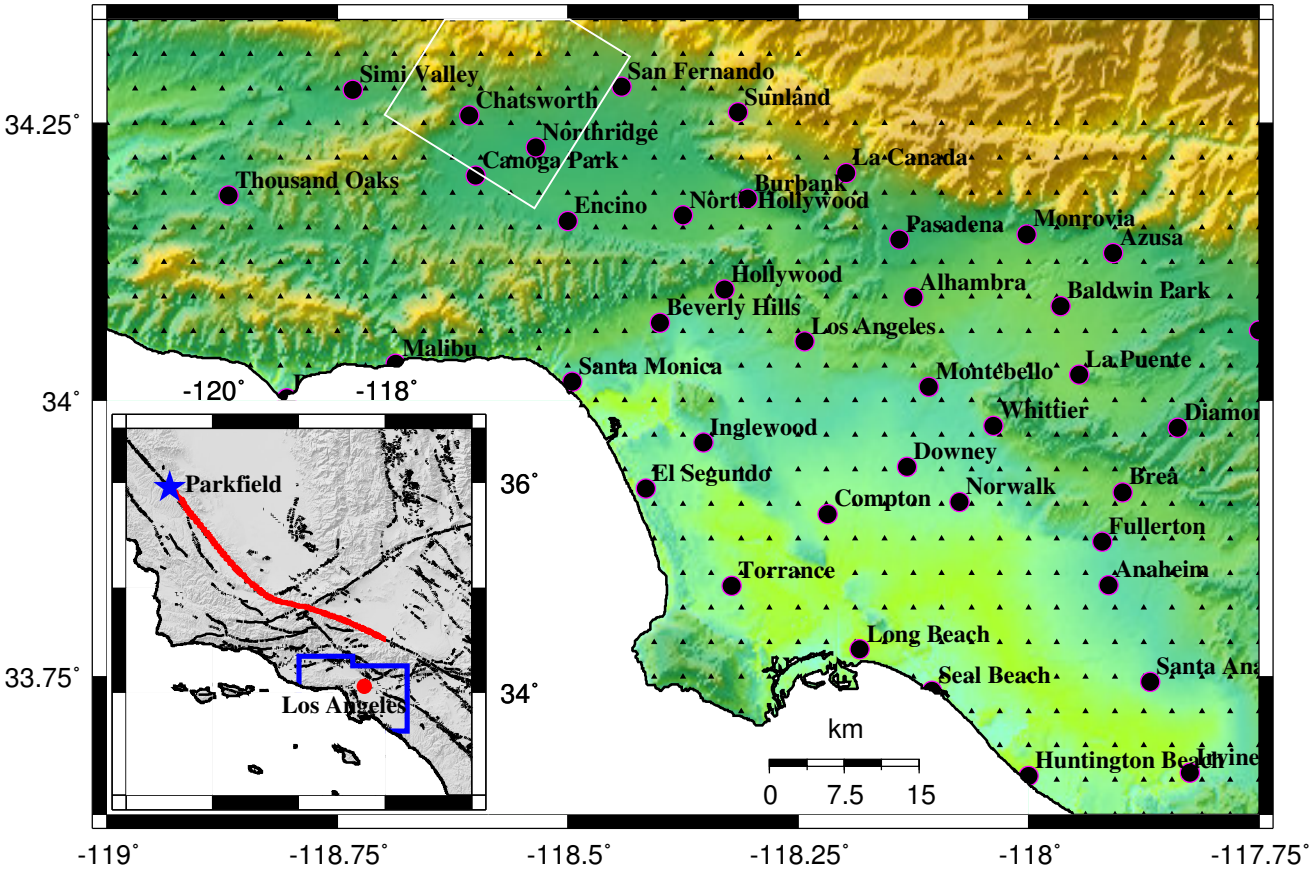

Figure 1.1: Geographical scope of the simulation (The color scheme reflects topography, with green denoting low elevation and yellow denoting mountains): The solid black triangles denote the 636 sites at which seismograms are computed and buildings are analyzed. The white box is the surface projection of the Northridge fault. The red line in the inset is the surface trace of the 290 km rupture of the San Andreas fault that is the primary focus of this study. The area enclosed by the blue polygon denotes the region covered by the 636 sites.

eral the redesigned building can be expected to perform better than the existing building in the event of an earthquake. The description of the two buildings, the design methodology for the new building, and the detailed comparison of the two buildings in terms of dynamic properties, static strength, and ductility, are presented in Chapter 2.

1.1.3 End-to-End Simulations

An end-to-end simulation is one that includes the simulation of fault rupture, seismic wave propagation, ground motion computation, and structural damage analyses. Chapter 3 details the state-of-the-art seismological and structural computational tools used for the end-to-end simulations in this study. The rest of the report is devoted to the validation of the simulation procedure using data from the Northridge eathquake (Chapter 5), the validity of utilizing the band-limited simulated ground motion for the analysis of the two buildings (Chapter 6), the historical activity on the San Andreas fault with emphasis on the 1857 earthquake (Chapter 7), description of the source model used in the simulations (Chapter 8), and the results of the two scenario earthquake simulations (Chapters 9 and 10). The last two chapters (11 and 12) summarize the main findings of the study and outline the future direction for research in this critical area of seismic research.

Chapter 2 Building Details

2.1 Existing Building

The existing building considered in this study is a modern 18-story welded steel moment-frame building located within five miles of the epicenter of the 1994 Northridge earthquake. The building was designed in 1984 for the lateral force requirements of the 1982 Uniform Building Code [28] and construction was completed in 1986-87. It has 17 office stories above ground and a mechanical penthouse above that. There is a single basement. The height of the building above ground is 248'-4" with a typical story height of 13'-0" and taller first, seventeenth, and penthouse stories. The plan configuration of the building is fairly uniform over its height. The lateral force resisting system consists of 2-bay welded steel moment-frames, two apiece in either principal direction of the building. There are a few setbacks that do not affect the lateral force-resisting system significantly. The east, west, and south moment-frames lie on the perimeter of the building, while the north frame is located one bay inside of the perimeter. This gives rise to some torsional eccentricity. Many moment-frame beam-to-column connections in the building fractured during the Northridge earthquake and the building has been extensively investigated since then by various engineering research groups [27, 13]. Their findings are outlined in Chapter 5. Figure 2.1A shows the isometric view of a structural model of the building. The floor plans are given in Figure 2.2 while the frame elevations with beam and column sizes are given in Appendix B. A36 steel with nominal yield strength of 36 ksi is used for all beams, while A572 Grade 50 steel with nominal yield strength of 50 ksi is used for all columns. The floor is made of lightweight concrete slab on metal deck supported by steel beams and girders framing into gravity and moment-frame columns.

2.2 Redesigned (New) Building

There have been many improvements in building codes and construction practices since 1994, and buildings designed according to the 1997 Uniform Building Code [6] are required to resist larger earthquake forces if located in regions close to major faults. Their lateral force-resisting systems are also required to be more redundant which, in the case of moment-frames, translates to a greater number of bays. They are expected to perform far better than existing buildings in large earthquakes and it is of interest to study the performance of such buildings under the scenario earthquakes considered here. To this end, the existing building has been redesigned for UBC97 requirements. The gravity and wind loading criteria from the existing building were retained for the design of the new building (these are given in the next few sections). The stricter lateral force and redundancy requirements led to a reconfiguration of the lateral system resulting in a greater number of bays of moment-frame in each direction (4 bays on each face of the building). The floor plans with the location of moment-frames are given in Figure 2.3. The frame elevations with beam and column sizes are presented in Appendix C. Note that the moment-frame that was located in the interior of the existing building on grid D has been moved to the perimeter to grid E. The 2-story space required at the lobby of the building precludes moment-frame beams on grid E at the second floor between grids 1 & 2, 3 & 4, and 4 & 5. This probably prompted the structural engineers of the existing building to move the frame to the interior of the building to grid D. But since the stiffness demand at the lower levels is not as high, it was concluded here that the frame would be stiff enough with a single beam at the second floor on grid E. Box-sections are used for the columns left unsupported laterally for two stories at E-1, E-4, E-5, and E-6, to keep the slenderness ratio governing the design within reasonable limits. ASTM A572 Grade 50 steel with nominal yield strength of 50 ksi is used for both beam and column sections, as well as for

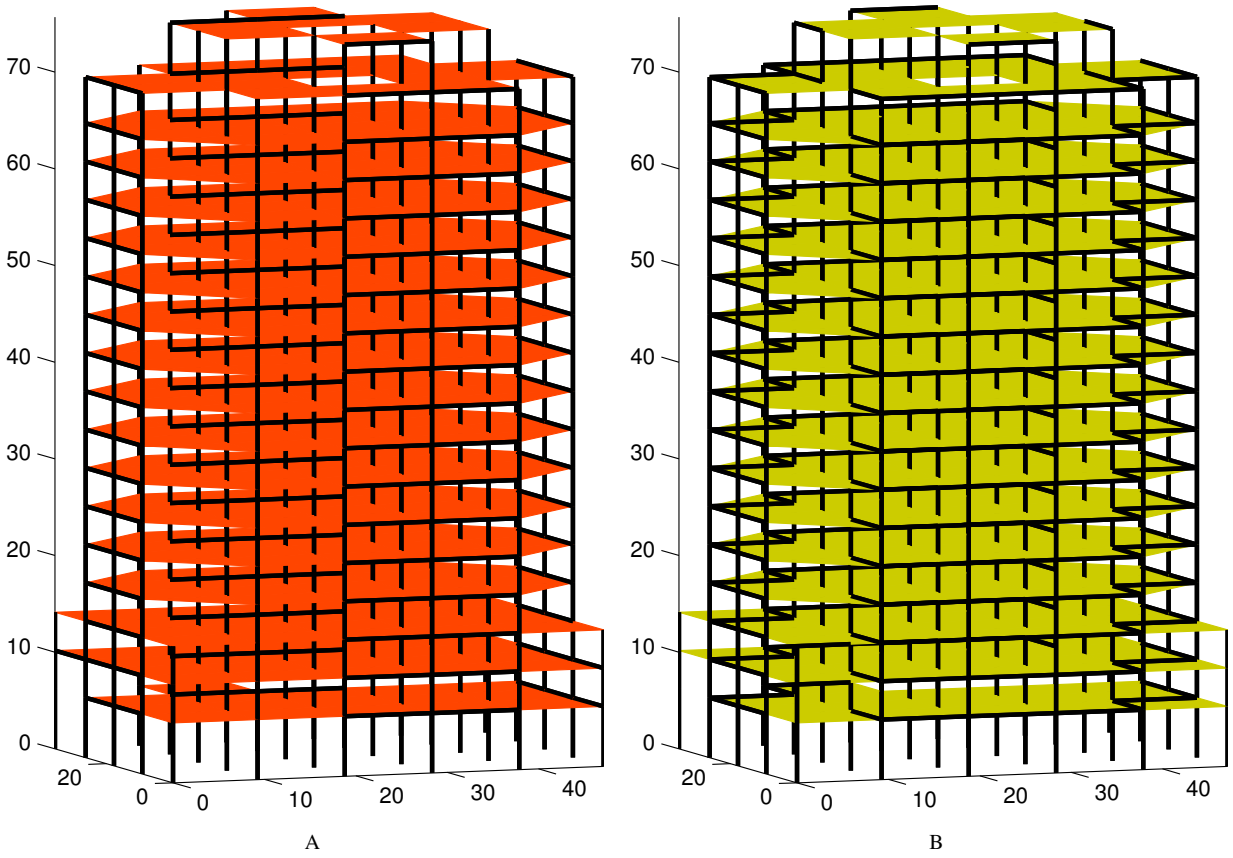

Figure 2.1: Structural models of buildings studied: [A] Perspective view of existing building (designed using codes prior to the 1997 Uniform Building Code). [B] Perspective view of redesigned (new) building (redesigned using the 1997 Uniform Building Code).

doubler plates that are provided to strengthen panel zones.

2.3 Gravity Loading Criteria for the Two Buildings

The gravity loading criteria for both buildings are given in Table 2.1. The loads are based on the occupancy particular to each floor. Thus, the loads on the typical floor of the two buildings correspond to the "office" occupancy category in this table while the loads on the mechanical/penthouse floor and the roof correspond to those listed in the "mechanical" and "roof" occupancy categories, respectively. Other loads not listed in the table include the self-weight of the lateral force-resisting system (moment-frame beams and columns) and the gravity columns.

2.4 Seismic Criteria for the Design of the New Building

All of southern California (the domain of interest in this study) falls under Seismic Zone 4 [6]. Hence, the new building is designed for Zone 4 requirements. It is assumed that the building is located at a distance of 5 km from a Type A fault [1]. The soil at the site is assumed to be of Type S_b which corresponds to a rock site with shear wave velocity in

[1]Seismic source types are classified based on the maximum magnitude, M, and the slip rate, SR, on the fault. Type A sources are faults that have a moment magnitude potential of $M \geq 7.0$ and a slip rate $SR \geq 5$mm/yr. These types of faults are considered to be active and capable of

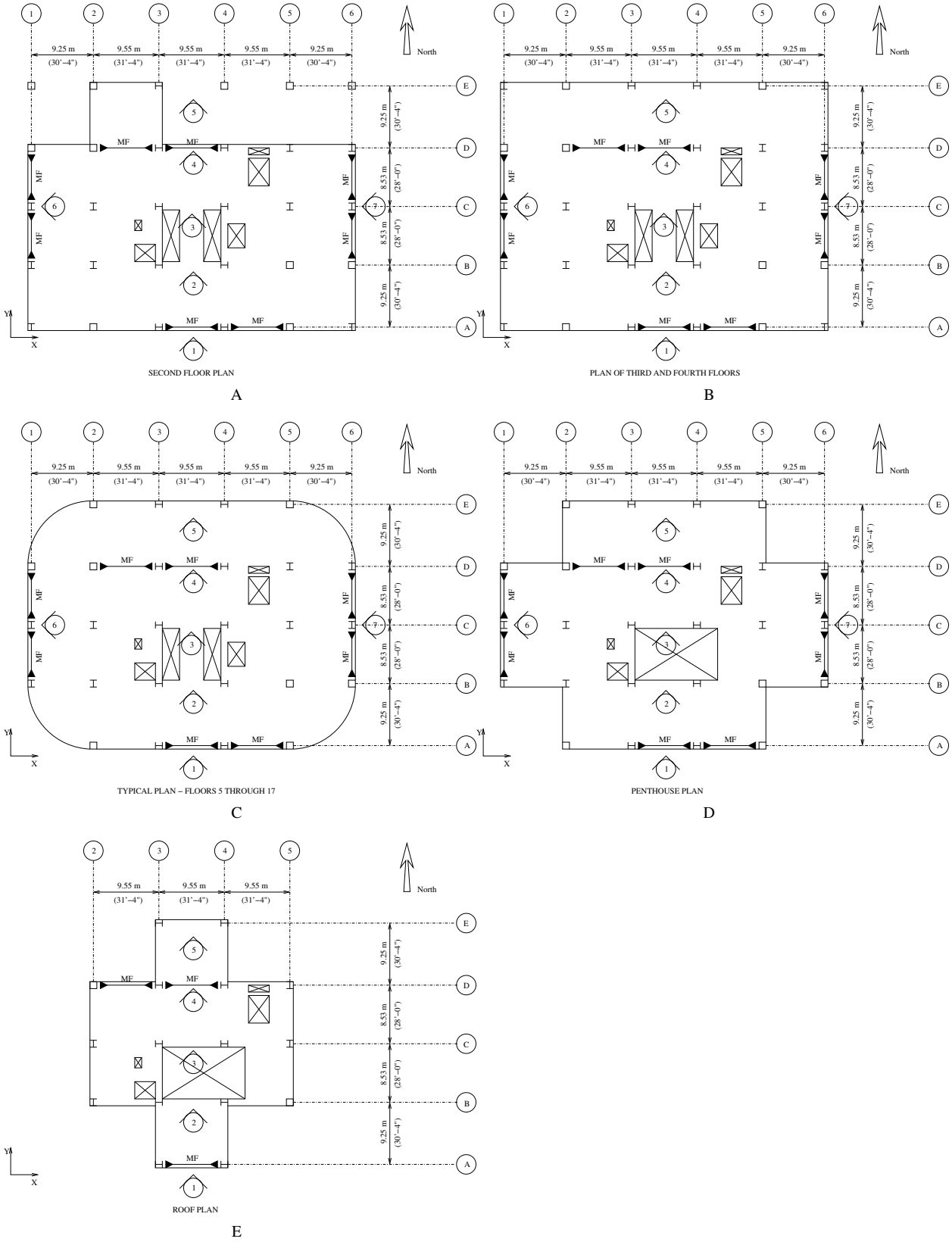

Figure 2.2: Plans of the existing building showing the location of columns and moment-frame (MF) beams (the frame elevations with beam and column sizes are given in Appendix B).

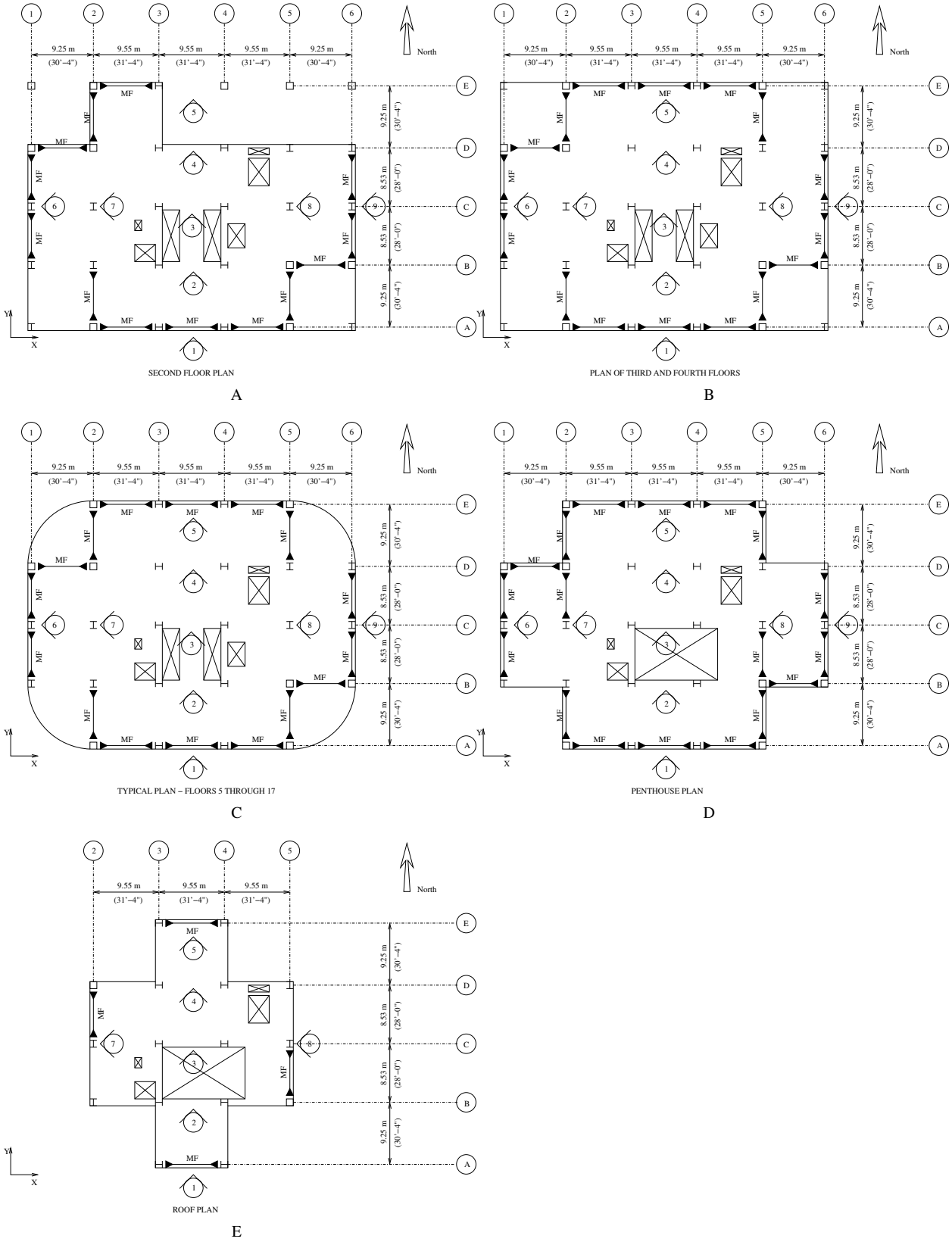

Figure 2.3: Plans of the redesigned building showing the location of columns and moment-frame (MF) beams (the frame elevations with beam and column sizes are given in Appendix C). Note the greater number of moment-frame bays in the redesigned building.

Occupancy	**Item**	**Load ($\frac{kg}{m^2}$)**
Office	Concrete Slab on Metal Deck Floor Fill (Carpet) Partitions (Metal Stud & Dry Wall) Mechanical Floor Framing Live Load	255.00 10.00 100.00 50.00 15.00 250.00
Mechanical	Concrete Slab on Metal Deck Floor Fill Mechanical Floor Framing Live Load	255.00 120.00 35.00 40.00 1200.00
Roof	Concrete Slab on Metal Deck Waterproofing Mechanical Floor Framing Live Load	255.00 10.00 35.00 15.00 250.00
Cladding	Glass Cladding	40.00

Table 2.1: Gravity loading criteria (UBC97 [6]).

Seismic Zone Factor (Z)	0.400
Seismic Source Type	A
Closest Distance to Source	5.000 km
Soil Type	Sb
Importance Factor (I)	1.000
Structural System Factor (R)	8.500
Structural Over-strength Factor (Ω_0)	2.800
Near-Source Factor (N_a)	1.200
Near-Source Factor (N_v)	1.600
Seismic Coefficient (C_a)	0.480
Seismic Coefficient (C_v)	0.640
Lateral System Type Factor (C_t)	0.085

Table 2.2: Seismic design criteria (UBC97 [6]).

Exposure	B
Basic Wind Speed (v)	70.00 mph
Importance Factor (I_w)	1.00
Windward Coefficient (C_q)	0.80
Leeward Coefficient (C_q)	0.50

Table 2.3: Wind design criteria (UBC97 [6]).

the range of 760–1500 m.s^{-1}. It should be recognized that these criteria may vary from one analysis site to the next in southern California but would be applicable to a large proportion of the considered analysis sites. The seismic design criteria for the new building are given in Table 2.2. Based on these criteria, the UBC97 design spectrum is computed and is shown in Figure 2.4.

2.5 Wind Criteria for the Design of the New Building

The new building is assumed to be located in an area that is categorized as Exposure B [2]. The wind design criteria for the new building are given in Table 2.3. Like the seismic criteria, the wind criteria assumed here would not be applicable to all the analysis sites but is fairly representative of southern Californian conditions.

producing large magnitude events. Most segments of the San Andreas fault fall under this category. See reference [26] for a summary of the design of buildings using UBC97.

[2]The code classifies terrains into three exposure categories, B, C, and D. Exposure B has terrain with buildings, forest, or surface irregularities, covering at least 20% of the ground level area extending 1 mile or more from the site. Exposures C and D correspond to progressively flatter terrain. Using the basic wind speed, defined as the fastest-mile wind speed associated with an annual probability of 0.02 measured at a point 10 m above the ground for an area having exposure category C, the wind stagnation pressure on the building is computed which is then corrected for height, exposure, gust conditions, and structure type to arrive at the incident wind forces on the windward and leeward faces of the building.

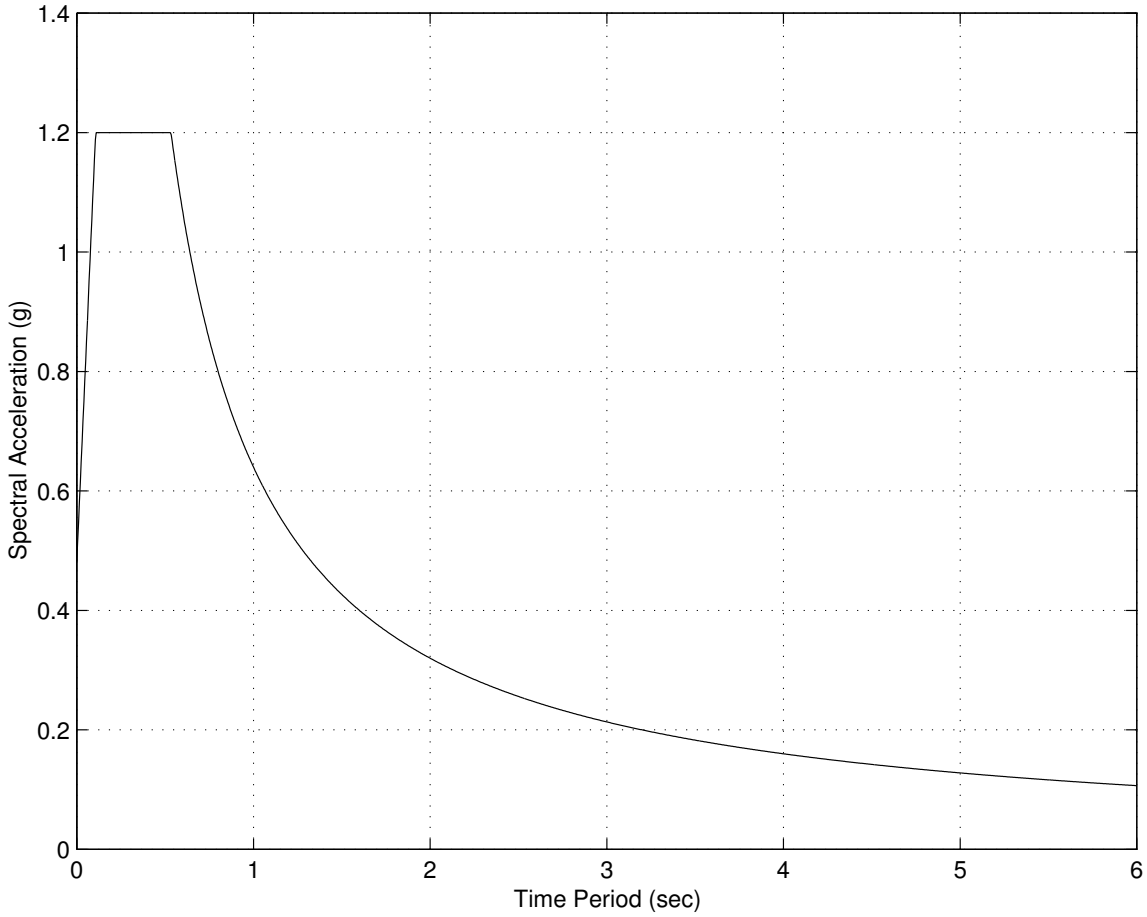

Figure 2.4: The 1997 Uniform Building Code response spectrum used in the design of the new building ($C_a = 0.48$ and $C_v = 0.64$).

2.6 Design of the New Building per UBC97 Using the Commercial Program ETABS

A three-dimensional linear elastic model of the building is built using the commercial program ETABS. In addition to the design of beams and columns, the program is capable of checking for the strong column-weak beam criterion in the code. $P-\Delta$ effects [3] are included in the analysis. The program accounts for $P-\Delta$ effects from the seismic weight (Dead Load) alone. However, there is a provision to specify a scaling factor for these effects. This factor can be used to include the $P-\Delta$ effects from Live Load. Assuming that during an earthquake, the building is loaded with 30% of the design Live Load (which on the average works out to about 15% of the design Dead Load), a value of 1.15 is used for this scale factor. The design procedure is outlined below. A rigid foundation is assumed.

1. After the structural model (with preliminary member sizes) including masses and loads is built, a linear dynamic response spectrum analysis is performed. For this purpose, the UBC97 [6] response spectrum (Figure 2.4) corresponding to the seismic parameters of the site given in Table 2.2 is used.

2. The program computes the frame-element weights and these are added on to the dead weight of the structure to arrive at the total seismic weight. The code static base shear is then computed based on this total seismic weight.

3. The program computes the dynamic spectral base shear. As per the code, this base shear can be scaled down to 100% of the static base shear for the design of irregular buildings and 90% of the static base shear for the design of regular buildings.

4. The program also computes the center of mass for each floor. As per the code accidental eccentricity criterion, the center of mass is shifted by 5% of the building dimension in each of the two principal directions. An eccentricity in the location of the center of mass would generate a torsional component in the response and the intent of the code is to ensure some torsional resistance in the design to account for modeling errors that may result in an incorrect center of mass location, e.g., not including floor slab openings for elevators and stairs in the model.

5. The analysis is repeated with the new center of mass and the spectral scaling factor. The member forces from this analysis are scaled up by the frame redundancy factors, ρ_x and ρ_y, in the two horizontal directions. The code requires that there be a minimum number of bays of moment-frames in each of the two principal directions and it penalizes those buildings that have insufficient redundancy by scaling up the member forces by ρ_x and ρ_y ([6], Section 1630.1.1).

6. The scaled member forces are used to check the stresses in the beams and columns. If the members are inadequate, the sizes are increased and the process is repeated. This iterative process is carried out until the design is satisfactory. Similarly, interstory drifts are checked against allowable limits and the stiffness of the structure is adjusted to satisfy the drift limits.

7. ETABS also computes the required doubler plates at joints as per UBC97 ([6], Section 2213.7.2). The thicknesses of these doubler plates are rounded to the nearest eighth of an inch.

8. The building design is then checked for wind forces. The wind pressure is computed per UBC97 [6] in conjunction with the wind design criteria specified in Table 2.3. The interstory drifts due to wind forces are restricted to the limit specified therein.

[3] When the forces from an earthquake displace a building laterally, the gravity loads acting vertically downward cause an overturning moment on the structure about its base, in addition to the overturning moment caused by the lateral forces themselves. This second-order effect that can lead to global instability of the building is termed the $P-\Delta$ effect.

Height of Building (H_n in meters)	75.690
Code Fundamental Period (sec)	2.181
Base Shear (V^*)	6.024%$^+$
Static Base Shear (metric Tonnes)	773.20$^+$
Base Shear for X-Drift Computation*	2.074%
Base Shear for Y-Drift Computation*	2.074%
System Redundancy Factor (ρ_x)	1.244
System Redundancy Factor (ρ_y)	1.249
Irregular Building?	No
Seismic Inelastic Drift Ratio Limit, Δ_M^{max}	0.02

** % of Seismic Weight*

+ Only 90% of this is used for design

Table 2.4: Seismic design parameters for the new building.

X-Direction Base Shear (metric Tonnes)	282.17
Y-Direction Base Shear (metric Tonnes)	374.06
Drift Ratio Limit	0.0025

Table 2.5: Wind design parameters for the new building.

The seismic design parameters and the wind design parameters for the new building are given in Tables 2.4 and 2.5, respectively.

The redesign of the existing building resulted in an average steel weight of 65.7 kg/m^2 compared to an average steel weight of 60.1 kg/m^2 for the existing building (these are based on a combined floor area of the second and upper floors including the roof amounting to 26338 m^2). These numbers include the allowance for floor framing given in Table 2.1.

The computed natural periods and modal directions for both buildings are given in Table 2.6. These are based on the assumption that Live Load does not contribute to the seismic mass (UBC97 guideline). The modal direction factors identify the predominant direction of excitation associated with each of the modes. The factors are percentages associated with the X- and Y-translational and Z-rotational directions. The sum of the three values add up to 100. The

Building ID	Mode Number	Period (sec)	Modal Direction Factors		
			X-Trans	Y-Trans	Z-Rotn
EB1	1	4.43	97.86	0.10	2.04
	2	4.22	0.10	99.89	0.01
	3	2.47	2.06	0.03	97.91
EB1R	1	3.72	47.24	52.72	0.04
	2	3.51	52.71	47.27	0.02
	3	2.24	0.08	0.01	99.91

Table 2.6: Building natural periods and modal directions (first 3 modes).

factors of a particular mode are given by:

$$\%X = 100 \sum_i M_i \phi_{X,i}^2 \tag{2.1}$$

$$\%Y = 100 \sum_i M_i \phi_{Y,i}^2 \tag{2.2}$$

$$\%Z = 100 \sum_i M_{\theta,i} \phi_{\theta Z,i}^2 \tag{2.3}$$

where the summations are over all the stories, M_i and $M_{\theta,i}$ represent the translational mass and the mass moment of inertia of the i^{th} story, respectively, $\phi_{X,i}$ and $\phi_{Y,i}$ represent the X and Y-translational mode shape components at the i^{th} story, respectively, and $\phi_{\theta Z,i}$ represents the corresponding Z-rotational mode shape component.

The computed interstory drift ratios from the response spectral analyses of the redesigned building are given in Table 2.7. The X and Y drifts corresponding to two cases – spectral direction corresponding to building X and Y directions – are listed. The elastic drift, Δ_s, is computed for each case by taking the square root of the sum of the squares (SRSS) of these drifts.

As per the Uniform Building Code [6], the Maximum Inelastic Response Drift, Δ_M, of the structure is extrapolated from the elastic drift ratio, Δ_s, as follows:

$$\Delta_M = 0.7R\Delta_s \tag{2.4}$$

where R is the Structural System Factor given in Table 2.2.

The code requires that the calculated interstory story drift, Δ_M, not exceed $\Delta_M^{max} = 0.025$ for structures having a fundamental period of less than 0.7 $seconds$ and $\Delta_M^{max} = 0.02$ for structures with greater periods.

The computed drift ratios from the wind analysis of the redesigned building are given in Table 2.8. The limit of 0.0025, although not set by the code, is enforced in the design of tall buildings so that non-structural components such as facades and partitions can be designed to accommodate this movement during design wind-storms. In the case of the new building this requirement governs the design of the beams. When compared to columns, beams usually play a greater role in controlling the stiffness of moment-frames.

Building ID	Spectral Direction	X-Drift	Y-Drift	SRSS Δ_s	SRSS Δ_M	Δ_M^{max}
EB1R	X	0.0015	0.0007	0.0017	0.0098	0.0200
	Y	0.0007	0.0015	0.0017	0.0098	0.0200

Table 2.7: Building seismic drift ratios.

Building ID	Wind Direction	X-Drift	Y-Drift	SRSS Δ_w	Δ_w^{max}
EB1R	X	0.00180	0.00011	0.00180	0.00250
	Y	0.00015	0.00240	0.00240	0.00250

Table 2.8: Building wind drift ratios.

2.7 Nonlinear Analysis of Buildings

3-D structural models of both the existing and the redesigned buildings are built using elastofiber elements for moment-frame beams and columns, panel-zone elements (with linear-quadratic shear stress-strain behavior) for joints, and elastic plane-stress elements for floor diaphragms. Gravity columns are modeled using plastic-hinge elements. Loads on these columns contribute to the $P-\Delta$ effect (see footnote 2 in Section 2.6) that plays a significant role in tall building response. Gravity beams that are used for supporting the floor slab and are pin-connected (simply supported at their ends with no moment transfer) are not included in the model as they do not contribute stiffness or strength to the lateral force-resisting system. The SAC report [13], from which the structural details of the existing building are extracted, does not clearly indicate whether the joints in the existing building were reinforced with doubler plates or not. For this study, it is assumed that doubler plates are not provided in the existing building. The new building designed for UBC97 regulations does have doubler plates reinforcing the panel zones in some of the beam-column connections. These are included in the computer model of the new building. In order to compute reactions at the base of the buildings, translational springs with large stiffness are placed in the two principal directions of the building at the base of all the columns. Pushover analyses are performed on the two building models in either direction to assess and compare their static lateral strengths and ductility. All the nonlinear analyses are carried out using the program, FRAME3D, details of which are given in the next chapter.

2.7.1 Analysis Assumptions

The following are the assumptions made in the analyses:

1. A rigid foundation is assumed with the base of all columns assumed fixed. Soil-structure interaction (SSI) is not included.

2. Strength degradation in the various elements due to weld fracture is included for the existing building but not for the new building (since weld defects have been corrected following the lessons learnt from the Northridge earthquake of 1994 and this mode of failure is not expected to occur in buildings built today). Thus, for the new building model collapse can occur only through $P-\Delta$ effects, whereas, for the existing building model element failures due to weld fractures in combination with $P-\Delta$ effects could result in global instability, especially if

the element happens to be a column in a lower story. While many probabilistic distributions of fiber fracture strains for elastofiber beam and column elements are investigated for the pushover analyses (described in the next section) and the validation of the numerical procedure using data from the Northridge earthquake (Chapter 5), the more realistic FRAC-S distribution described in the next section is used for the San Andreas simulations (Chapters 9 and 10).

3. Composite action arising out of the shear connection between the concrete slab on metal deck and the moment-frame beams is not included.

4. At each level, the story mass is lumped at column locations based on plan tributary area.

5. 30% of the Live Load is included along with the Dead Load in the lumped masses.

6. An average of 30% of the Live Load is included in the gravity loads for ground motion analyses.

7. Gravity columns are modeled using plastic hinge elements and their contribution to the $P-\Delta$ effects is automatically included. They are assumed continuous over the height of the building.

8. Trusses and horizontal braces are modeled using plastic hinge elements with pinned-end conditions.

9. Detailed material properties used in the analysis of the existing and redesigned building models are given in Tables 2.9 and 2.10, respectively.

10. An effective thickness of 10.16 cm (4 inches) is assumed for the plane-stress elements representing the concrete slab on metal deck.

11. The concrete elastic modulus is taken to be 2.53x10^9 kg/m^2 (3605 ksi) corresponding to a compressive strength f'_c of 2.81x10^6 kg/m^2 (4 ksi).

12. Poisson's ratio for the plane-stress elements is taken to be 0.3.

2.7.2 Pushover Analyses of the Two Buildings

To quantify the actual strength and ductility (deformation potential) of the two buildings in the two principal directions, pushover analyses are performed in either direction. In these analyses the building is subjected to a slow, ramped, horizontal ground acceleration that increases at the constant rate of 0.3 g/minute, and its response is computed dynamically. The structural model is identical to that used in the earthquake analyses except that masses for the horizontal degrees of freedom are recalculated to total the seismic design mass, W/g, with a distribution that is proportional to the UBC97 [6] seismic static design loads. Thus, in this analysis technique the lateral loads are essentially the horizontal seismic design forces proportionally increasing with time at a slow rate. The results of this analysis can also be used to quantify the ductility of the building in terms of its post-yield displacement capacity.

The results of the pushover analyses of both buildings are presented in Figure 2.5. The base shear in the direction of pushing is shown plotted as a percentage of the seismic weight of the building against the displacement at the 18^{th} floor (penthouse level) for the two models of the existing building that include fracture, denoted by "EB1-FRAC-S" & "EB1-FRAC-W", and fracture-excluded models of the existing and redesigned buildings, denoted by "EB1-UNFRAC" and "EB1R-UNFRAC", respectively. The seismic weights computed according to UBC97 for the existing and new buildings are 12689 metric tonnes (27974 K) and 12835 metric tonnes (28297 K), respectively. The ultimate strength of the existing building model in the X direction varies between 7.5% and 7.85% of its seismic weight for the three cases – FRAC-S, FRAC-W, & UNFRAC, while the ultimate strength of the redesigned building model in the X direction is 9.5% of its seismic weight. Plotted on Figure 2.5B are the base shear as a percentage of the seismic weight (solid

Usage	**Property**	$kgf - m$ **Units**	$Kip - in$ **Units**
Beams & Columns	Elastic modulus, E	20388731162.41 $\frac{kg}{m^2}$	29000.00 ksi
	Shear modulus, G	8155492464.96 $\frac{kg}{m^2}$	11600.00 ksi
	Strain-hardening slope, α^s_{ph}, for plastic hinge elements used to model gravity columns	0.02	0.02
	Yield stress, σ_y, for beam sections		
	W36x300–W36x230	32059522.10 $\frac{kg}{m^2}$	45.60 ksi
	W36x194–W36x135	33254723.59 $\frac{kg}{m^2}$	47.30 ksi
	Yield stress, σ_y, for column sections		
	W14x730	38457365.33 $\frac{kg}{m^2}$	54.70 ksi
	W14x500–W14x311	40285320.54 $\frac{kg}{m^2}$	57.30 ksi
	Yield strain, ϵ_y	0.0017	0.0017
	Slope at initiation of strain hardening, E_s, for Elastofiber Elements	407774623.25 $\frac{kg}{m^2}$	580.00 ksi
	Ultimate stress, σ_u, for elastofiber elements used to model beams	39652566.81 $\frac{kg}{m^2}$	56.40 ksi
	Ultimate stress, σ_u, for elastofiber elements used to model columns	48089283.16 $\frac{kg}{m^2}$	68.40 ksi
	Strain at initiation of strain hardening, ϵ_y, for elastofiber elements	0.0120	0.0120
	Ultimate strain, ϵ_u, for elastofiber elements	0.1600	0.1600
Panel Zones	Shear modulus, G	8155492464.96 $\frac{kg}{m^2}$	11600.00 ksi
	Shear yield stress, τ_y	19077524.83 $\frac{kg}{m^2}$	27.14 ksi

Table 2.9: Steel material properties used in the analysis of the existing building model.

Usage	**Property**	$kgf - m$ **Units**	$Kip - in$ **Units**
Beams & Columns	Elastic modulus, E	20388731162.41 $\frac{kg}{m^2}$	29000.00 ksi
	Shear modulus, G	8155492464.96 $\frac{kg}{m^2}$	11600.00 ksi
	Strain-hardening slope, α_{ph}^{s}, for plastic hinge elements used to model gravity columns	0.02	0.02
	Yield stress, σ_y, for beams	35152984.76 $\frac{kg}{m^2}$	50.00 ksi
	Yield stress, σ_y, for columns	35152984.76 $\frac{kg}{m^2}$	50.00 ksi
	Yield strain, ϵ_y	0.0017	0.0017
	Slope at initiation of strain hardening, E_s, for Elastofiber Elements	407774623.25 $\frac{kg}{m^2}$	580.00 ksi
	Ultimate stress, σ_u, for elastofiber elements used to model beams	45698880.19 $\frac{kg}{m^2}$	65.00 ksi
	Ultimate stress, σ_u, for elastofiber elements used to model columns	45698880.19 $\frac{kg}{m^2}$	65.00 ksi
	Strain at initiation of strain hardening, ϵ_y, for elastofiber elements	0.0120	0.0120
	Ultimate strain, ϵ_u, for elastofiber elements	0.1600	0.1600
Panel Zones	Shear modulus, G	8155492464.96 $\frac{kg}{m^2}$	11600.00 ksi
	Shear yield stress, τ_y	20295585.22 $\frac{kg}{m^2}$	28.87 ksi

Table 2.10: Steel material properties used in the analysis of the redesigned building model.

lines) and the penthouse displacement (dashed lines) as a function of time for the X-pushover of each model. The penthouse lateral displacement in the X direction at which ultimate strength is reached is about 68 inches (1.73 m) for both building models which corresponds to an average inclination of 2.3% over the height. Both building models are stronger in the Y direction with ultimate strengths of about 8%W for the existing building and close to 10%W for thr redesigned building. Plotted on Figure 2.5D are the base shear as a percentage of the seismic weight (solid lines) and the penthouse displacement (dashed lines) as a function of time for the Y-pushover for each case. The penthouse lateral displacement in the Y direction at which ultimate strength is reached is about 60 inches (1.52 m or 2.0% average inclination) for the three existing building models and 75 inches (1.91 m or 2.5% average inclination) for the new building model.

The FRAC-W model assumes a constant fracture strain of $0.9\epsilon_y$ (where ϵ_y is the yield strain) for all the bottom fibers of the moment-frame beams. For fracture strain of the beam top-flange and web fibers, the following probability distribution is assumed: 30% probability that the fracture strain is $10\epsilon_y$; 30% probability that it is $20\epsilon_y$; 20% probability that it is $40\epsilon_y$; and 20% probability that it is $80\epsilon_y$. For each fiber a random number is generated and using this number a fracture strain consistent with the assumed probability distribution is assigned to that fiber. For column flange and web fibers it is assumed that the fracture strains are far greater than the rupture strain, thus, precluding the occurrence of fractures.

The FRAC-S model makes the same assumptions with regard to the fracture strain as the FRAC-W model except that the fracture strains for the bottom-flange fibers of the moment-frame beams are determined based on the following probability distribution: 20% probability that the fracture strain is $0.9\epsilon_y$; 20% probability that it is $2\epsilon_y$; 20% probability that it is $5\epsilon_y$; 20% probability that it is $15\epsilon_y$; and 20% probability that it is $40\epsilon_y$.

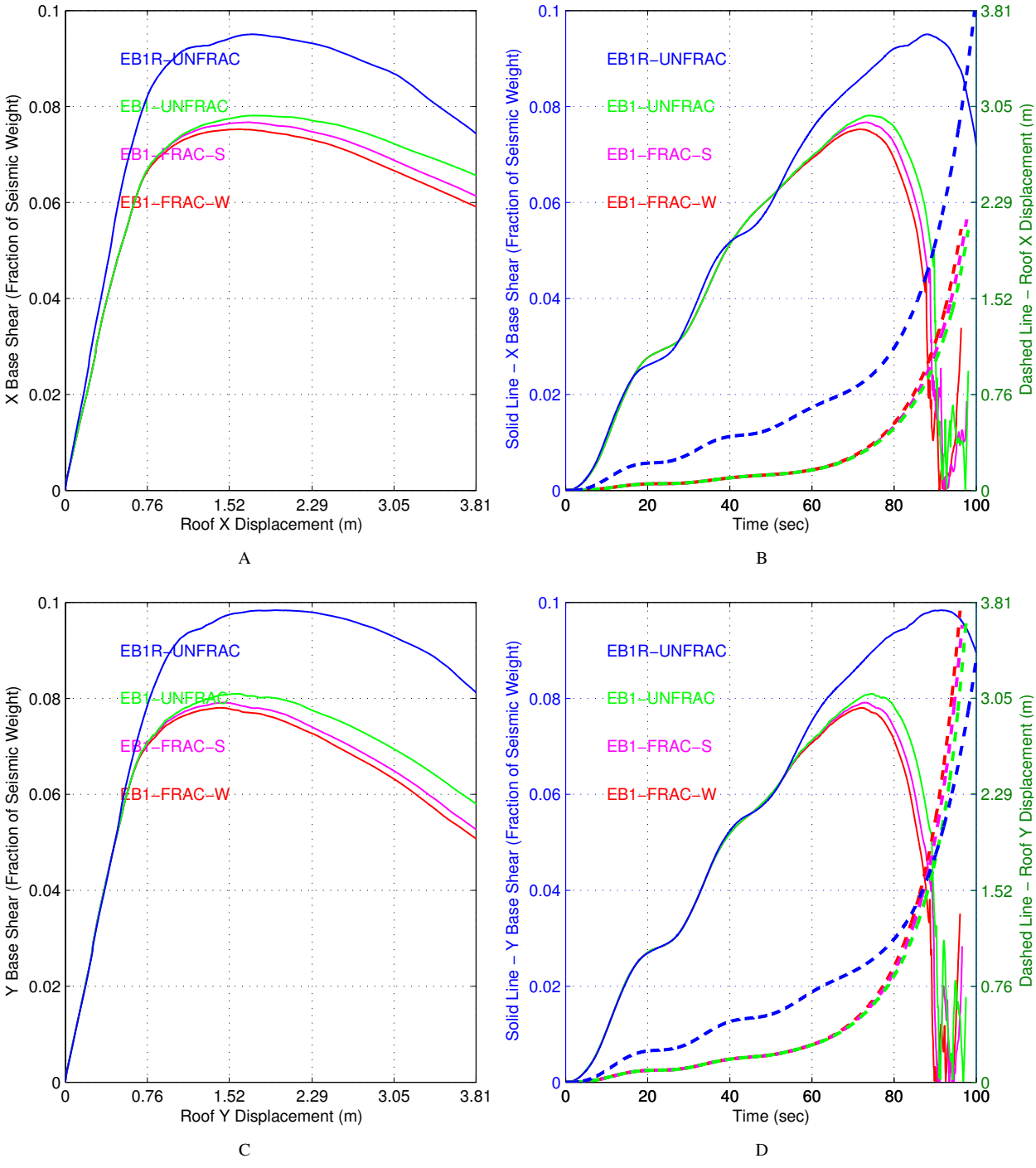

Figure 2.5: Pushover analysis of the existing and the redesigned buildings: (A) X direction pushover – roof displacement versus base shear. (B) X direction pushover – base shear (solid lines) and roof displacements (dashed lines) as functions of time. (C) Y direction pushover – roof displacement versus base shear. (D) Y direction pushover – base shear (solid lines) and roof displacements (dashed lines) as functions of time.

Chapter 3 Software Used for the End-to-End Simulations

3.1 SPECFEM3D

SPECFEM3D (http://www.geodynamics.org) is a 3-D seismic wave propagation software that uses the spectral element method [25] which is based upon a weak formulation of the equations of motion and combines the flexibility of a finite-element method with the accuracy of a global pseudospectral method. The finite-element mesh honors all first- and second-order discontinuities in the Earth model. To maintain a relatively constant resolution throughout the model in terms of the number of grid points per wavelength, the size of the elements is increased with depth in a conforming fashion, thus retaining a diagonal mass matrix. In the Earth's mantle and inner core we solve the wave equation in terms of displacement, whereas in the liquid outer core we use a formulation based upon a scalar potential. The three domains are matched at the inner core-outer core and core-mantle boundaries, honoring the continuity of traction and the normal component of velocity. The mesher accommodates lateral variations in compressional wave speed, shear-wave speed, and density, a 3-D crustal model, ellipticity, as well as topography and bathymetry. The solver can handle fully anisotropic 3-D Earth models as well as attenuation, and incorporates the effects of the oceans, rotation, and self-gravitation in the context of the Cowling approximation.

To simulate ground motion in the Los Angeles basin from regional earthquakes, a special version of SPECFEM3D, SPECFEM3D_BASIN, tailored to simulate seismic wave propagation in sedimentary basins is used. The mesh generator is specifically written for the simulation of wave propagation in southern California, but can be modified for use in other geographical areas. The solver is completely general and can be used to simulate seismic wave propagation on regional and local scales. The sedimentary basin model (Harvard-LA velocity model [29]) is constrained by hundreds of petroleum industry well logs and more than 20000 km of seismic reflection profiles. The numerical simulations account for three-dimensional variations of seismic wave speeds and density, topography and bathymetry, and attenuation. This method has been shown to reliably model ground motion down to a period of approximately 2 s [23, 24]. Thus the simulated ground motions can only be used to study the behavior of building structures whose dominant modes of vibration have natural periods greater than 2 s, which implies tall buildings of 15 stories or more. The top soil layer is not included in the Earth model due to lack of sufficient data and the numerical complexity associated with low shear wave velocities in the layer (the minimum S-wave speed in the basin for the Harvard-LA velocity model is 687 m.s^{-1}) which would require a very dense numerical grid to be correctly sampled. This typically softer layer may have the effect of amplifying the ground motion.

3.2 FRAME3D

Nonlinear damage analyses of the building models subjected to the simulated ground motion in this study are carried out using the program FRAME3D (http://www.frame3d.caltech.edu) that is based on the finite-element method and is capable of performing time-history analysis. A three-dimensional structural model of a framed building using this program consists of grids of beams and columns. The setup of the model is comprised of three element classes: panel zone elements for joints, beam elements for beams and columns, and diaphragm elements for floor and roof slabs. The arrangement of these elements in a typical structural model is illustrated in Figure 3.1. The two beam element types can be used for either beams or columns. The plastic hinge beam element consists of two nodes at which biaxial flexural yielding is permitted, leading to the formation of plastic hinges. Elastic rotational springs are connected across

the plastic hinge locations to model strain-hardening. Axial yielding is also permitted. The elastofiber beam element is divided into three segments – two end nonlinear segments and an interior elastic segment. The cross-sections of the end segments are subdivided into fibers. Associated with each fiber is a nonlinear hysteretic stress-strain law for axial stress and strain. This accounts for coupling of nonlinear material behavior between bending about the major and minor axes of the cross-section and axial deformation. The panel zone element models nonlinear shear deformation in the region of the joint where the beams and columns intersect. The joint region consists of a length of column within the depth of the connecting beams. Shear deformation is due, primarily, to opposing moments from the beams and columns at the joint caused by the frame being subjected to lateral loads. The joint is modeled by two planar orthogonal panels forming a cruciform section. Edges of these panels contain attachment points a, b, c, and d where beams attach, and e and f on the top and bottom,respectively, where columns attach (Figure 3.1). Each panel may yield and strain harden in shear. The diaphragm element is used to model the in-plane stiffness of floor slabs. It is essentially a 4-noded plane-stress element that remains elastic at all times. Refer to [26] for the detailed theory of each of these element types.

A key feature of FRAME3D is that full geometric updating is included in both static and dynamic analyses to accommodate large nodal translations and rotations. This automatically accounts for the $P - \Delta$ effects and allows the analysis to follow a building's response well into collapse. It involves updating the locations of the joint nodes, attachment points, and the local beam nodes, as well as the orientations of the local element coordinate systems [30, 31, 32]. The program utilizes an iteration strategy applied to an implicit time-integration scheme to solve the nonlinear equations of motion at each time-step.

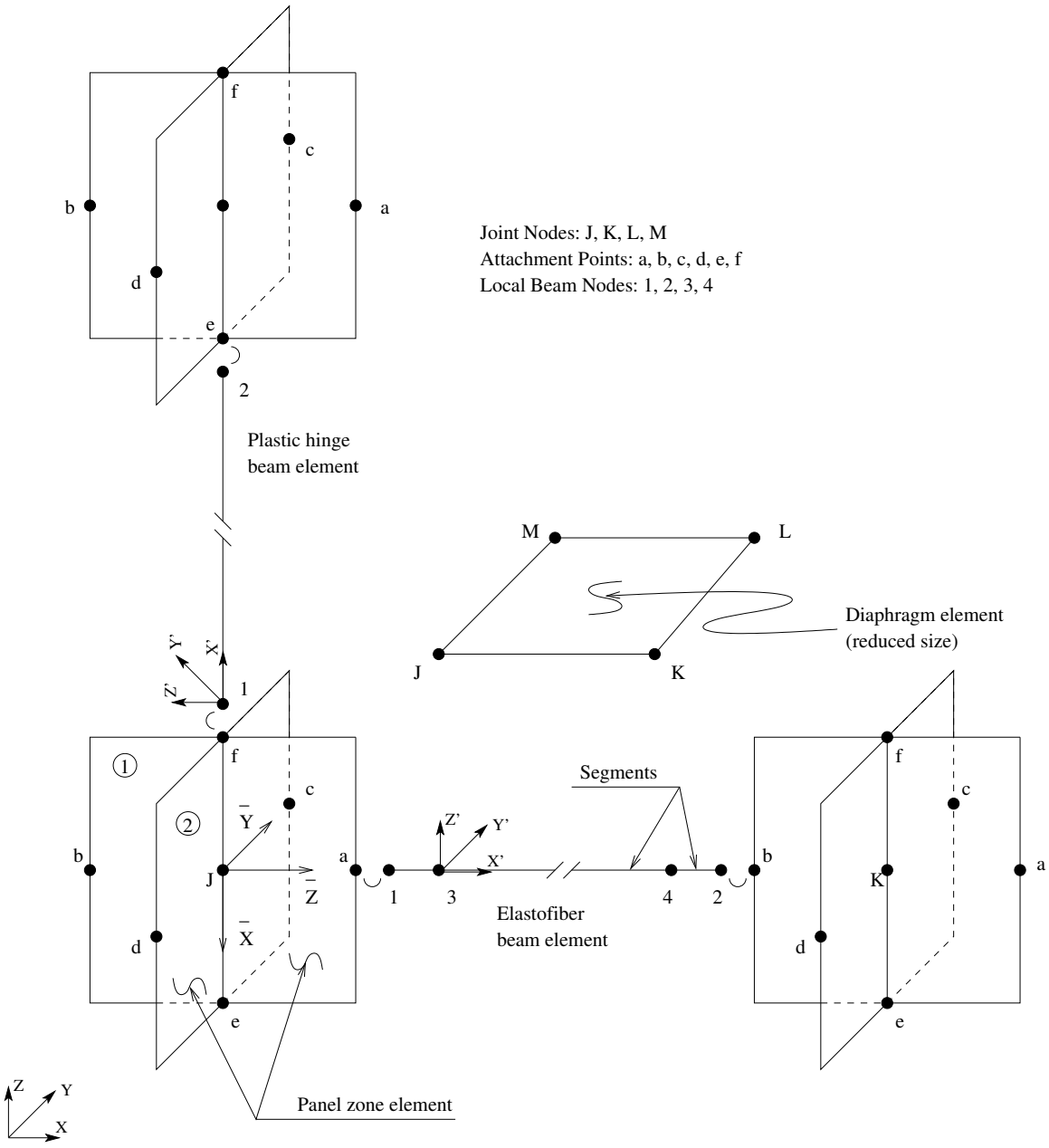

Figure 3.1: Element arrangement in frame model showing joint nodes, attachment points, local beam nodes and coordinate systems.

Chapter 4 Limitations of the Study

For a study such as this, that is of interest to various stake-holders that do not necessarily have a seismological or structural or technical background, it is crucial to list the limitations clearly to put the results in the right perspective. It is in this spirit that the following key limitations should be recognized while considering the results:

1. Validation of the numerical procedures adopted here is based on the magnitude 6.7 Northridge earthquake of January 17, 1994, while the scenario earthquakes simulated here are of magnitude 7.9 (with about two orders of magnitude greater energy release). Similarly, the source mechanism of the Northridge earthquake was a thrust mechanism that did not break the surface while the San Andreas simulation is one of strike-slip source mechanism with surface break. Furthermore, the amount of data collected during the Northridge earthquake, especially from building response, is fairly limited, and this restricts the extent to which the numerical procedures can be convincingly validated.

2. For the San Andreas simulation, only a single source model (from the finite-source inversion of the Nov. 3, 2002, Denali, Alaska earthquake) has been considered. Other sources could give noticeably different results. Having said this, the potential for large earthquakes with comparable amounts of slip does exist as evidenced by the San Andreas earthquake in 1857 (see Chapter 7), and it is critical to estimate accurately the implications through detailed modeling of at least one scenario at the expense of loss of generality.

3. The top soil layer (of about 30 m) close to the free surface is not included in the Earth model due to lack of sufficient data and the numerical complexity associated with low shear wave velocities in the layer. This typically softer layer may have the effect of amplifying the ground motion [33, 34]. Theoretically, the peak amplification occurs at periods $T_m = 4d_1/m\beta_1, m = 1, 3, 5, etc.$ where d_1 is the depth and β_1 is the shear-wave velocity in the overburden soft layer, and is given by $\rho_2\beta_2/\rho_1\beta_1$ where ρ_2 and ρ_1 are the densities of the basement and the overburden, respectively, and β_2 is the shear-wave velocity in the basement. This amplification could be quite different from place to place based on the depth of the top-soil layer, the density contrast, and the shear-wave speed contrast between the underlying basement and the overburden layer, and there is insufficient data to determine the amplification in the entire region. Having said this, the buildings that we analyze are long-period structures most affected by long-period waves with wavelengths far greater than the depth of the unmodeled soil layer; these waves simply do not see the layer and as a result the effect of the top soil layer on the simulated ground motion (with periods longer than 2 s) is likely to be insignificant. Furthermore, maps of the geotechnical layer do not currently exist for southern California. A final limitation is that 3-D seismic wave propagation codes that can handle a geotechnical layer are currently not available. Including the geotechnical layer, when a model becomes available, will require the consideration of very high frequencies and much higher resolution, and therefore the numerical cost would be high.

4. Ground motion, simulated using SPECFEM3D_BASIN, in the Los Angeles basin has been shown to be accurate down to a period of only 2 s [24]. Hence computed ground motions have been lowpass-filtered to this period using a Butterworth filter (actually bandpass-filtered between 2 and 1000 s). The effect of filtering ground motions on the response of tall buildings (especially of the type considered here) has been shown not to be significant in Chapter 6. Nevertheless, this could vary from case to case and the results should be viewed upon as being in the ballpark of (and not exactly) what to expect from such an earthquake.

5. The structure foundations have not been included in the structural models. Soil-structure interaction (SSI, e.g., [35, 36]) is not included in the analyses. Dynamic nonlinear SSI is not a well understood phenomenon because of the lack of recorded data and the difficulty to design accurate numerical tools to study it. One of the few real-world examples of extensive SSI research is a 14-story reinforced concrete storage building in Hollywood constructed in 1925 [37, 38, 39]. These studies indicate that the change in various structural response parameters in this building during the October 1, 1987, magnitude 5.9 Whittier Narrows earthquake due to SSI could have been up to 20%. SSI is an active area of research and should be incorporated into future studies of this kind.

6. Stiffness of partitions, and stair & elevator enclosures is not included.

7. Some critical failure modes such as local flange buckling of I-sections are not included in the structural modeling. Not including these failure modes could result in under-predicting the damage in these models.

8. Column splices have not been modeled. Column splices are typically located three feet above the floor slab with the intention of locating them away from the high-moment (high flexural stress) regions near beam-column joints. In the absence of axial load, the theoretical point of contraflexure (zero moment) is at mid-height of the column. In the case of columns, axial load does exist and buckling failure could occur at mid-height (first mode buckling). So the splice location of three feet above the floor slab is chosen to avoid the most vulnerable locations of the column. These splices are weak points and could fail especially if the column goes into tension during the earthquake. Once again, not including column splices could result in under-predicting the structural damage.

9. Composite action of moment-frame beams has not been included. Moment-frame beams are connected to the concrete slab on metal deck through shear connectors (studs). This leads to some part of the slab in the vicinity of the beam to act as being part of the beam, leading to increased stiffness and strength. The effect of this is two-fold. Firstly, it could make the moment-frames stiffer attracting greater seismic forces, but this could be partly offset by the increased strength from composite action. In addition since this would make the beams stronger in relation to the columns, it could have the effect of pushing the location of plastic yielding into the columns, which could result in greater overall building damage. Having said this, more analysis needs to be done to investigate the effect of composite action of moment-frame beams on overall building response.

10. It is not clear from the SAC report [13] whether doubler plates were provided to strengthen the panel zones in the columns of the existing building in Woodland Hills. If these were provided, then this data is missing in the SAC report. Hence no doubler plates are included in the existing building model in this study. With doubler plates, the performance of the model would be enhanced. The redesigned building has been provided with doubler plates per the UBC97 [6] provisions.

Chapter 5 Validation Using the Northridge Earthquake Data

The first step in a study such as this is the validation of the numerical procedure using data from a regional earthquake. The only major regional earthquake for which extensive data has been recorded in southern California is the magnitude 6.7, January 17, 1994, Northridge earthquake. Two independent data sets are required for validation. Using the first data set, a finite source model of the earthquake is created which is then used to simulate ground motion in the region. The computed seismograms are then compared against the second data set for validation.

While many research groups have determined kinematic fault models by fitting seismic waveform data [40, 41], a wavelet transform approach [21] that can extract more information about slip heterogeneity by simultaneously considering both the time and frequency characteristics of the waveforms is used. The resulting finite-source model is shown in Figure 5.1. Using the spectral-element method [25], ground motion generated by this finite-source model of the Northridge earthquake is then simulated. In addition to the 636 sites under consideration, seismograms are computed at southern Californian seismic stations that recorded the shaking during the earthquake. The synthetic seismograms (red) are compared against the recorded data (black) at nearby stations north of the fault and at distant stations in Figure 5.2. All the waveforms are lowpass-filtered with a corner period of 2 s (in practice, they are bandpass-filtered between 2–1000s). The synthetic seismograms are able to capture the large pulses in the nearby stations while there is a very good match in most waveforms corresponding to distant stations.

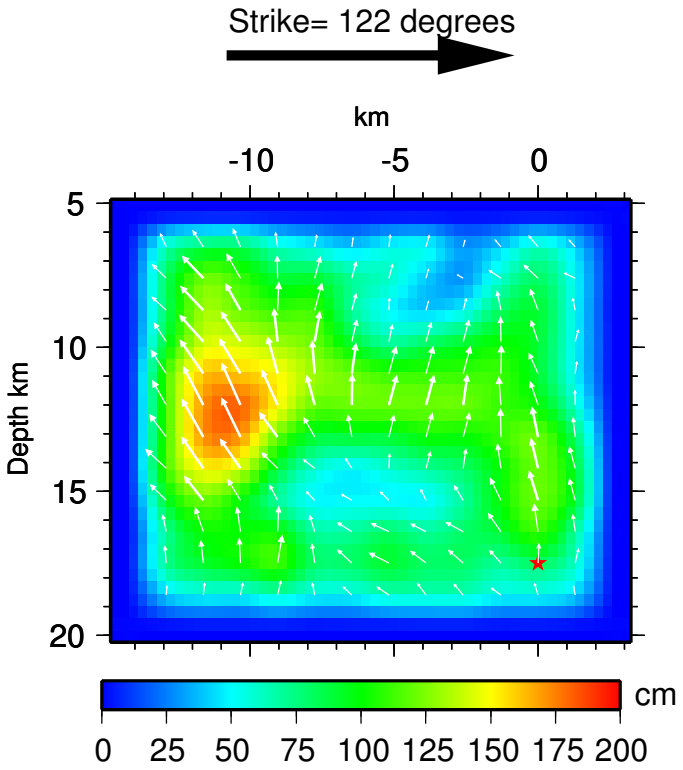

Figure 5.1: Slip model for the January 17, 1994, magnitude 6.7 Northridge earthquake determined using a wavelet transform approach. The red star denotes the hypocenter and the white arrows denote the slip vector. The dip angle of the fault is 40 degrees (see Figure 1.1 for the surface projection of the fault)

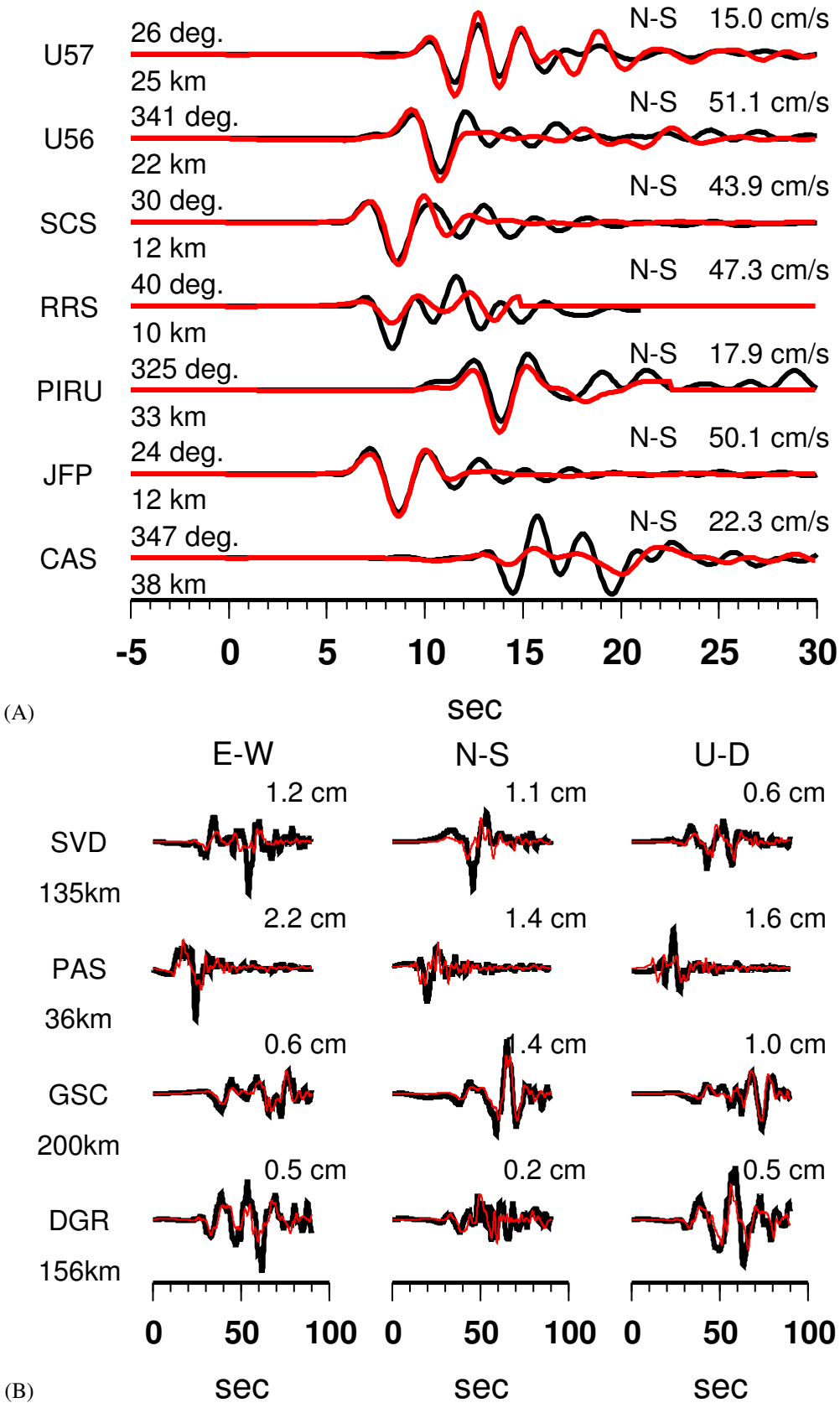

Figure 5.2: Northridge simulation – Data versus synthetic seismograms: (A) nearby stations north of the rupture; (B) distant stations.

While there is a sufficient amount of ground motion data to validate the seismological component of the numerical procedure, the same is not true of tall building performance. Not many tall buildings in the region were instrumented at the time, especially of the type considered here (18-story steel moment-frame buildings). One building that was instrumented was the 18-story steel moment-frame building described in Chapter 2. This building, located in Woodland Hills, was designed in 1984 using the 1982 Uniform Building Code and constructed in 1986-87. A computer model of this building is illustrated in Figure 2.1A. Following the Northridge earthquake, problems associated with the alignment of elevators prompted a survey which evaluated the plumbness of the building. The survey indicated that the building was leaning 6 inches to the north at roof level. A damage investigation of the building revealed fracture in 29 out of the 154 beam bottom flange-to-column welds in the east and west moment-resisting frames [13]. The investigation included visual inspection of all moment-frame beam bottom flange-to-column welds, and the ultrasonic testing of 39 top flange-to-column welds and some bottom flange-to-column welds. The west moment-frame had 23 weld fractures while the east moment-frame had 6 fractures. No weld fractures were observed in the north and south moment-frames. No top flange weld-fractures were observed in any of the moment-frames. All fractures that were observed were visible from the top of the bottom flange. The fractures included cracks through the weld, cracks at the back of the weld adjacent to the column flange, and cracks that went into the column flange and exited the column flange above the weld. All weld fractures seemed to have initiated from the root of the full penetration welds.

There was a three-component SMA-1 accelerograph on the 18^{th} floor of the building that recorded the floor acceleration [42]. Unfortunately, the closest free-field seismometer was at the Oxnard Boulevard seismic station (WHOX) located in Woodland Hills, about half a mile away from the building. Nevertheless, the building model was analyzed for shaking from the recorded WHOX data. This nonlinear damage analysis of the structure was performed using the finite-element-method-based program, FRAME3D, described in Chapter 3.

The computed displacements at the 18^{th} floor in the north-south and east-west directions are compared against the corresponding measured displacements in Figure 5.3. The computed peak displacement in the north-south direction is within 5% of the measured displacement. However, the peak displacement in the east-west direction is off by a factor of 2. There is a minor lengthening of the period in the measured displacement that is not captured by the computed displacements. Also, the measured displacement attenuates faster than the computed displacement. These differences could be due to any or all of the following reasons: the ground motion used in the analysis was not recorded at the base of the building but half-a-mile away; the instrument at the roof was maintained by the owner of the building and its reliability is uncertain; rocking of the building about its base (due to the finite stiffness of the soil), which is not included in the fixed-base structural model, could contaminate the displacement record measured at the roof and the observed period may actually be a combination of purely translational and rocking modes; as damage accumulates in a building during an earthquake, (non-hysteretic) damping increases significantly. However, in the structural model while hysteretic damping is modeled accurately in a non-linear fashion, non-hysteretic supplemental damping is considered to be viscous and linear, and as damage accumulates it does not increase correspondingly.

The location of the fractures in the four moment-frames in the building from the analyses is compared against the location of observed fractures in the building in Figure 5.4. Since all the fractures were observed in the bottom flange weld [13], for the purposes of this analysis, the fracture strain in all the welds in the building model, except the beam bottom-flange welds, was taken to be far greater than the steel fiber rupture strain. The fracture strain for the beam bottom-flange welds was varied and the structural analysis was carried out repeatedly until the total number of weld fractures in the model matched the observed number of fractures in the building following the Northridge earthquake. A beam bottom-flange weld fracture strain of 1.05 times the yield strain, ϵ_y, results in a total of 29 weld fractures in the analysis which is the same as what was observed in the field. The fracture distribution in the various moment-frames of the model is now compared against that observed in the building in Figure 5.4. In both cases the fractures are confined to the north-south moment-frames. Majority of the fractures occur in the top-third of the moment-frames in both cases. However, while most fractures (23) in the building occurred in the west moment-frame with fewer

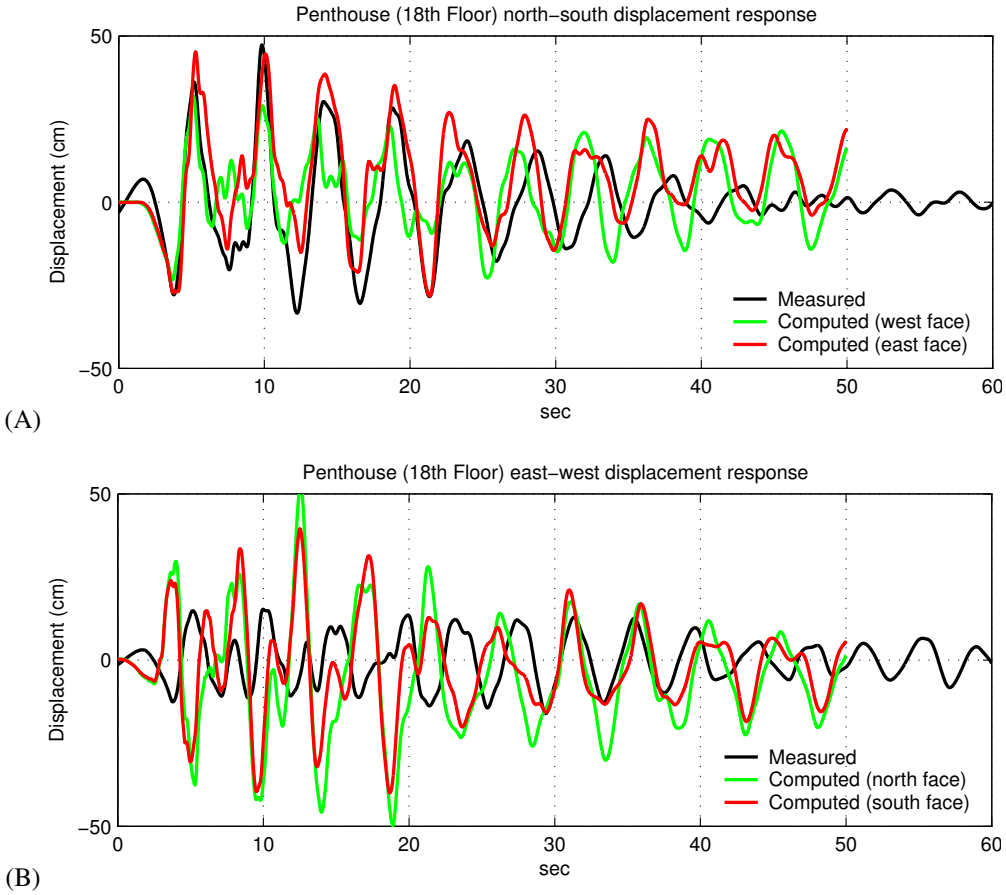

Figure 5.3: Northridge validation – analysis of existing building in Woodland Hills subjected to Oxnard Blvd. record (WHOX): Measured 18th floor (A) N-S and (B) E-W displacements versus corresponding computed displacements.

fractures (6) in the east moment-frame, the reverse is true for the model with 6 fractures in the west moment-frame and 20 fractures in the east moment-frame. If the sign of the east component of the ground motion is reversed, then the damage pattern in the model is similar to the observed pattern. However, based on personal communications with the California Geological Survey (CGS), it was determined that the recording instrument was a three-component SMA-1 strong motion accelerograph for which the orientation reversal of one of the two horizontal components is possible only in conjunction with the orientation reversal of the other horizontal component. The direction of the first arrival of the Oxnard Boulevard, Woodland Hills (WHOX, latitude 34.18, longitude -118.59) record (velocity) north component, agrees well with the north components of two nearby records, Canoga Park (CNPK, latitude 34.212, longitude -118.607) and Saticoy Street (SATI, latitude 34.209, longitude -118.517) as shown in Figure 5.5. This indicates that the orientation of the north component of the WHOX instrument is correct implying that the orientation of the east component must be correct as well since the instrument is of the SMA-1 type. But the orientation of the first arrival of the east component of the WHOX instrument seems to be out-of-phase with that of the CNPK instrument (also of the SMA-1 type) which cannot be explained. Adding to the mystery is the fact that a twin building with the same configuration, design, and orientation had a very different damage pattern compared to the building considered here (based on personal communication with Mr. Terrence Paret, Wiss, Janney, Elstner Associates, Inc.). The details of this building were not included in the SAC report [13].

To summarize, the seismological component of the numerical procedure was validated adequately using the mea-

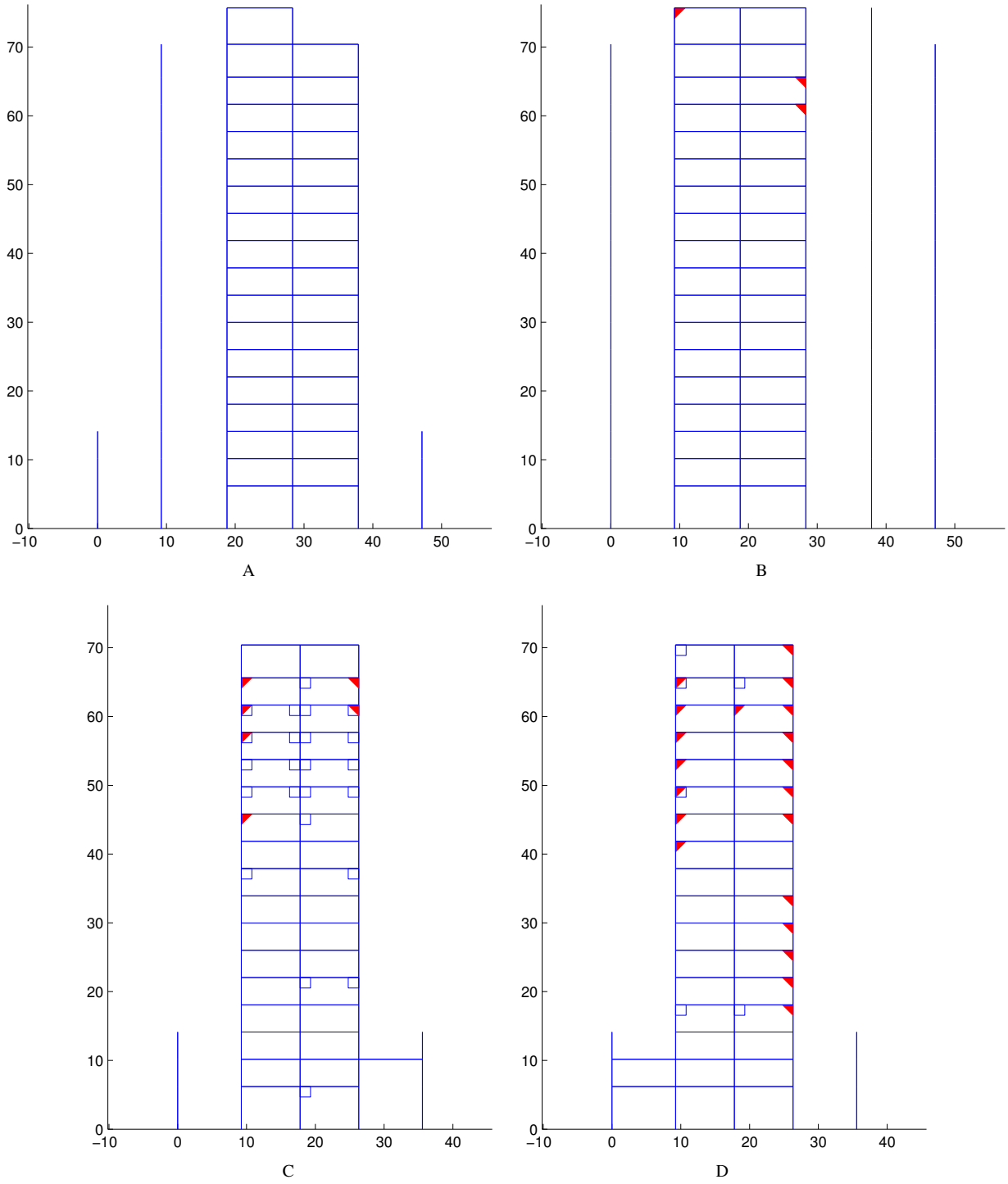

Figure 5.4: Analysis of the existing building subjected to the Oxnard Boulevard, Woodland Hills (WHOX) record from Northridge earthquake (station located 0.5 mile from the building): Observed connection fractures (squares) versus simulated fractures (solid triangles) – (A) South moment-frame (along grid A, east-west direction) of the building (Frame 1); (B) North moment-frame (along grid D, east-west direction) of the building (Frame 4); (C) West moment-frame (along grid 1, north-south direction) of the building (Frame 6); (D) East moment-frame (along grid 6, north-south direction) of the building (Frame 7).

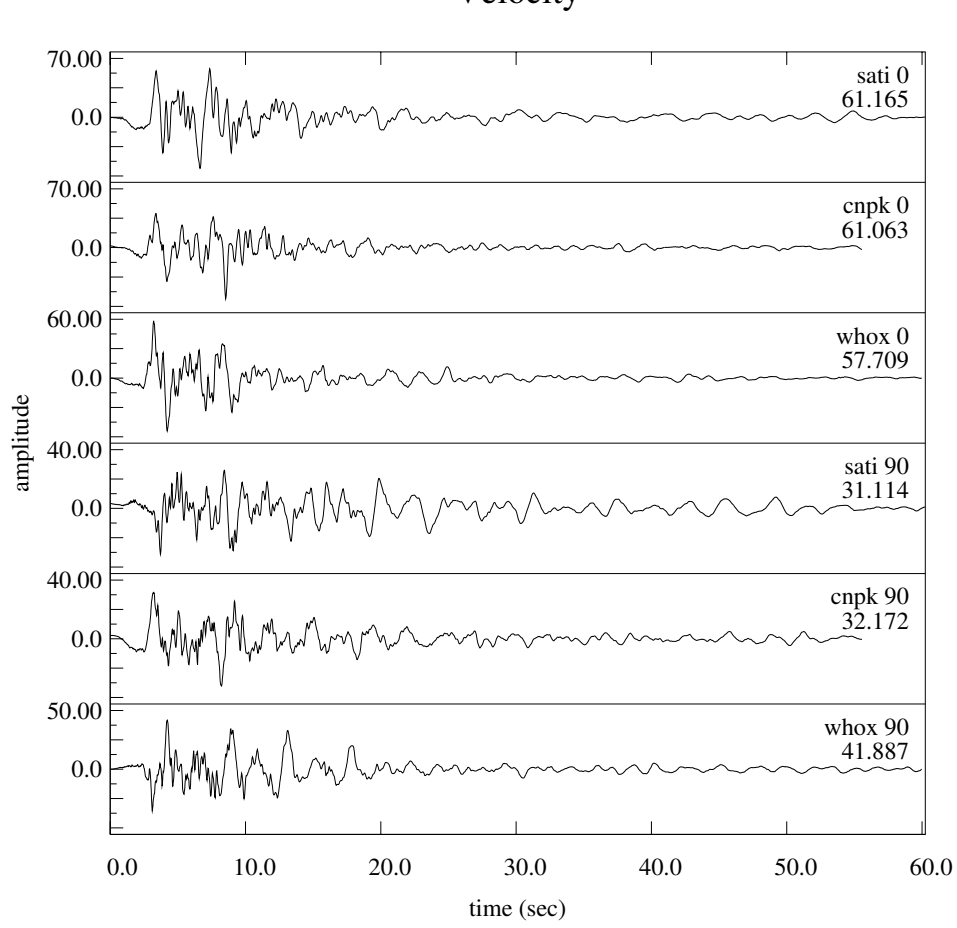

Figure 5.5: Comparison of the horizontal components of velocity of three records from the 1994 Northridge earthquake, SATI, CNPK, and WHOX (Source: URS Corporation).

sured records from the 1994 Northridge earthquake. However, the structural component of the procedure could be validated only to a limited extent due to unavailability of suitable data and variability in the quality of construction resulting in uncertainty in the modeling environment. While the various elements used for modeling buildings in the program FRAME3D have been tested individually [31, 32], validation of an assembled building has been a challenge. The pre-Northridge weld defects in steel moment-frames were due to many reasons, some of them human. Here is an extract from the Federal Emergency Management Agency document, FEMA-353 [43]: 'The joint between the bottom beam flange and column flange is typically made as a downhand field weld, often by a welder sitting on top of the beam flange, in a so-called "wildcat" position. To make the weld from this position each pass must be interrupted at the beam web, with either a start or stop of the weld at this location. This welding technique often results in poor quality welding at this critical location, with slag inclusions, lack of fusion and other defects. These defects can serve as crack initiators, when the connection is subjected to severe stress and strain demands.' From this description, it is clear that the presence or absence of defects in welds can and is often dictated by the skill and ability of the welder.

Finally, a note on the permanent tilt of the building at the penthouse level. Surveys conducted after the Northridge earthquake to check how far the building was tilted out-of-plumb indicated that the building was leaning six inches to the north [13]. The permanent tilt [1] on the four faces of the computational model are shown in Figure 5.6. Twisting of

[1] Permanent tilt at a given location in the building model is computed by taking the displacement time-history at that location and lowpass-

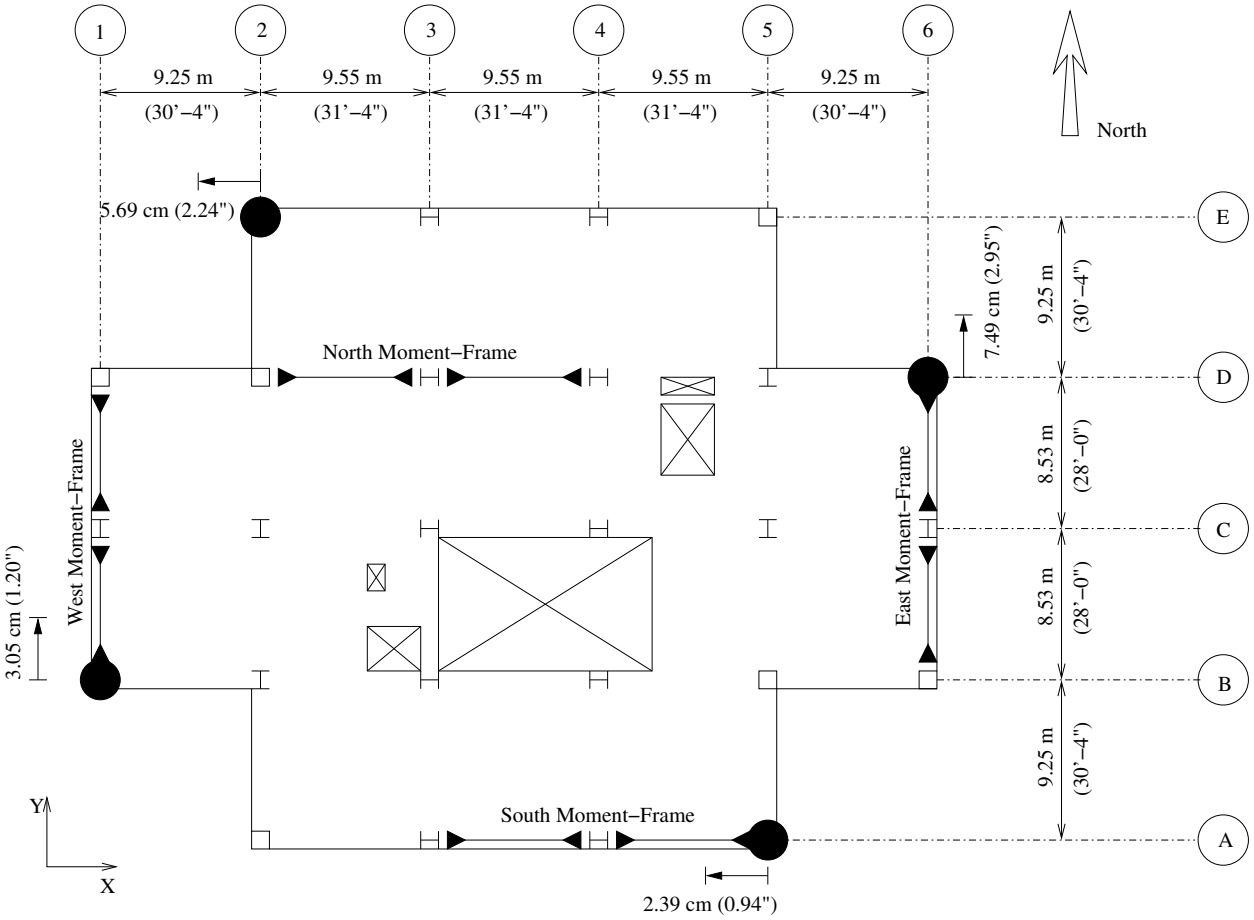

Figure 5.6: Permanent offsets on the four faces of the existing building model (penthouse plan shown here) computed using the WHOX record from the Northridge earthquake.

the model has resulted in a non-uniform pattern of permanent tilting on the four faces. The north-east corner has a net permanent tilt of 3.7 inches in a north-westerly direction.

filtering it using a Butterworth filter with the filter corner period at 10 s and taking the average over a time-window that has the minimum variance. The length of the time window was taken to be 5 s. Note that this is the tilt in the building that is relative to the ground and building tilt resulting from ground tilt or structure foundation differential settlement following the earthquake would not be captured by the structural model.

Chapter 6 Effect of Filtering Records on Building Analyses

As described in Chapter 4, ground motion simulated using SPECFEM3D_BASIN in the Los Angeles basin has been shown to be accurate down to a period of only 2 s. Due to this limitation, all the broadband time-histories computed using SPECFEM3D_BASIN are lowpass-filtered using a Butterworth filter with the corner period at 2 s (in practice bandpass-filtered between 2 s and 1000 s). The filtered ground motion records are used as input to building analyses. However, building response is a function of the entire frequency band of the ground motion with the building higher modes corresponding to shorter periods getting excited by high-frequency ground motion. So the question arises as to what the effect of excluding the high-frequency ground motion is on the response of the buildings considered in this study. Since dominant modes of the two 18-story buildings considered here have periods greater than 2 s, it is theorized that the effect of the higher-frequencies in the ground motion may not have a significant impact on their response. To confirm this hypothesis, the following study has been performed:

1. A total of 13 three-component records from the magnitude 7.5, September 21, 1999, Chi-Chi earthquake in Taiwan, and the magnitude 8.3, September 26, 2001, Tokachi-Oki earthquake in Japan, are considered. Response spectra of the north and east components of these records are shown in Figures 6.1 and 6.2, respectively. Also shown on these plots are the fundamental periods of the existing and redesigned buildings, and the corner period of the lowpass-filter for comparison. From the spectra, it is clear that the chosen records span a wide range of intensities of ground motion.

2. These records are bandpass-filtered between 2 s and 1000 s.

3. Nonlinear analyses of the existing and redesigned building models subjected to the filtered and unfiltered records are carried out using FRAME3D. Shown in Figures 6.3 and 6.4 are the peak interstory drift ratios computed in either building model using the filtered records plotted against those computed using the corresponding unfiltered records. If the high-frequency ground motion had no effect whatsoever on the response of the buildings, then all the points would fall on the diagonal. The fact that most of the points are aligned quite closely with the diagonal indicates that the effect of high-frequency ground motion (the range of frequencies not included in this study) on the building response (for the two buildings considered in this study) is not significant and can be safely ignored. In essence the initial S wave damages the building leading to its softening, thus shifting its natural frequency spectrum farther into the long-period regime and further reducing the effect of the high-frequency content in the ground motion. Note that the pen colors used to plot the points on these figures correspond to those used in plotting the response spectra in Figures 6.1 and 6.2. Thus, each point can be identified with the corresponding ground motion record.

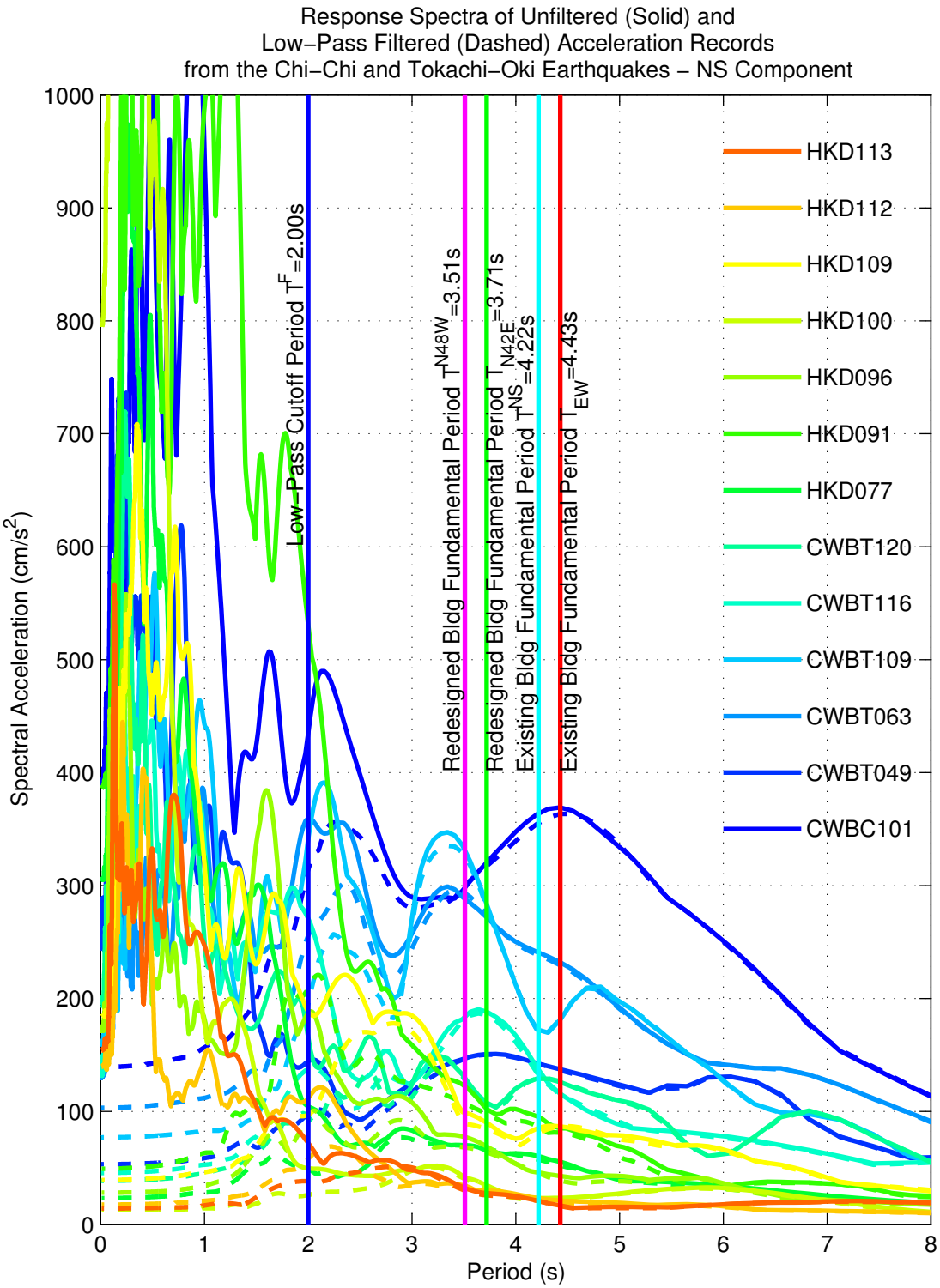

Figure 6.1: Pseudo-acceleration response spectra of records (north component) from the Chi-Chi and Tokachi-Oki earthquakes: Comparison of spectra of unfiltered (solid) and filtered (dashed) records.

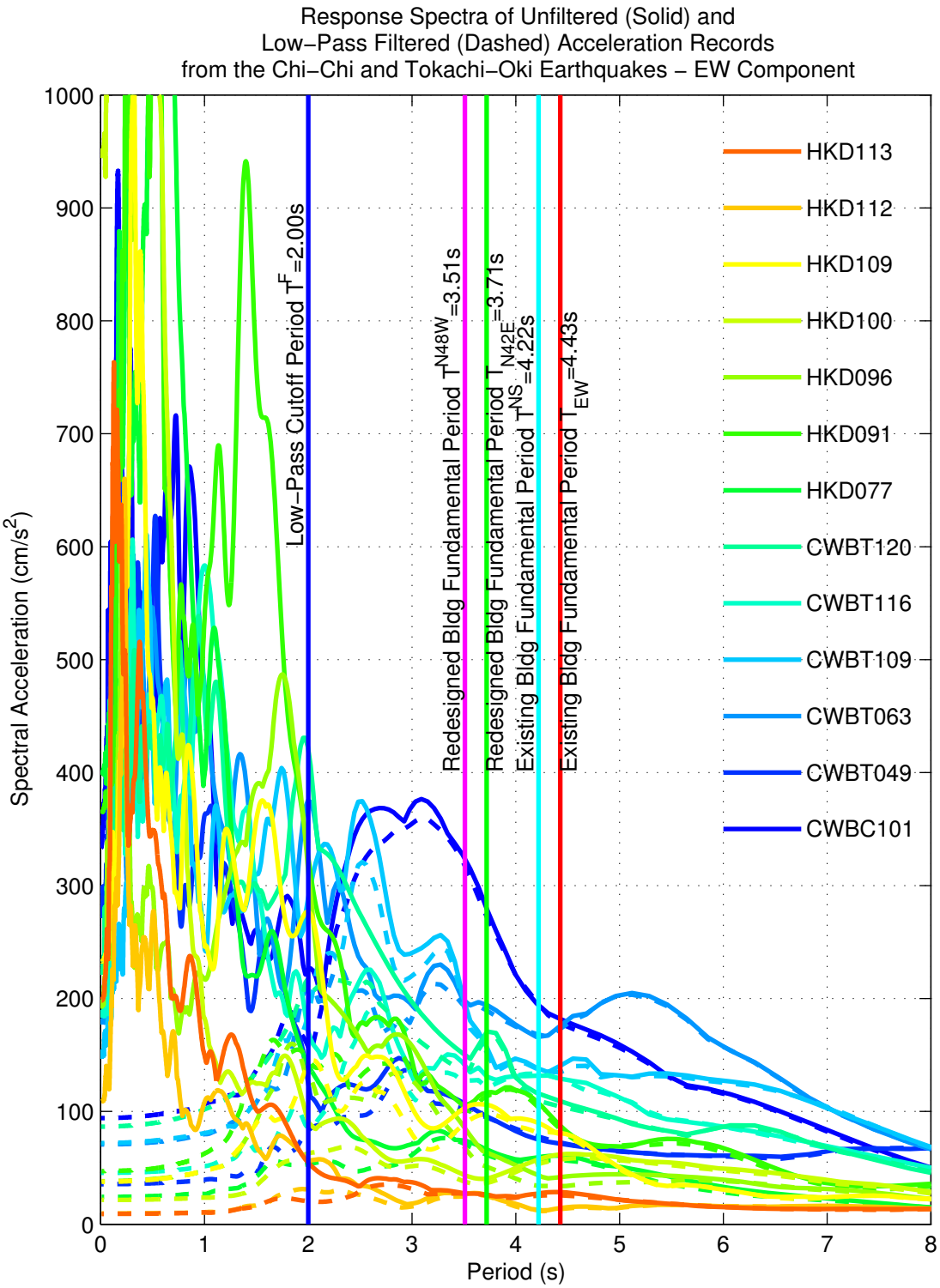

Figure 6.2: Pseudo-acceleration response spectra of records (east component) from the Chi-Chi and Tokachi-Oki earthquakes: Comparison of spectra of unfiltered (solid) and filtered (dashed) records.

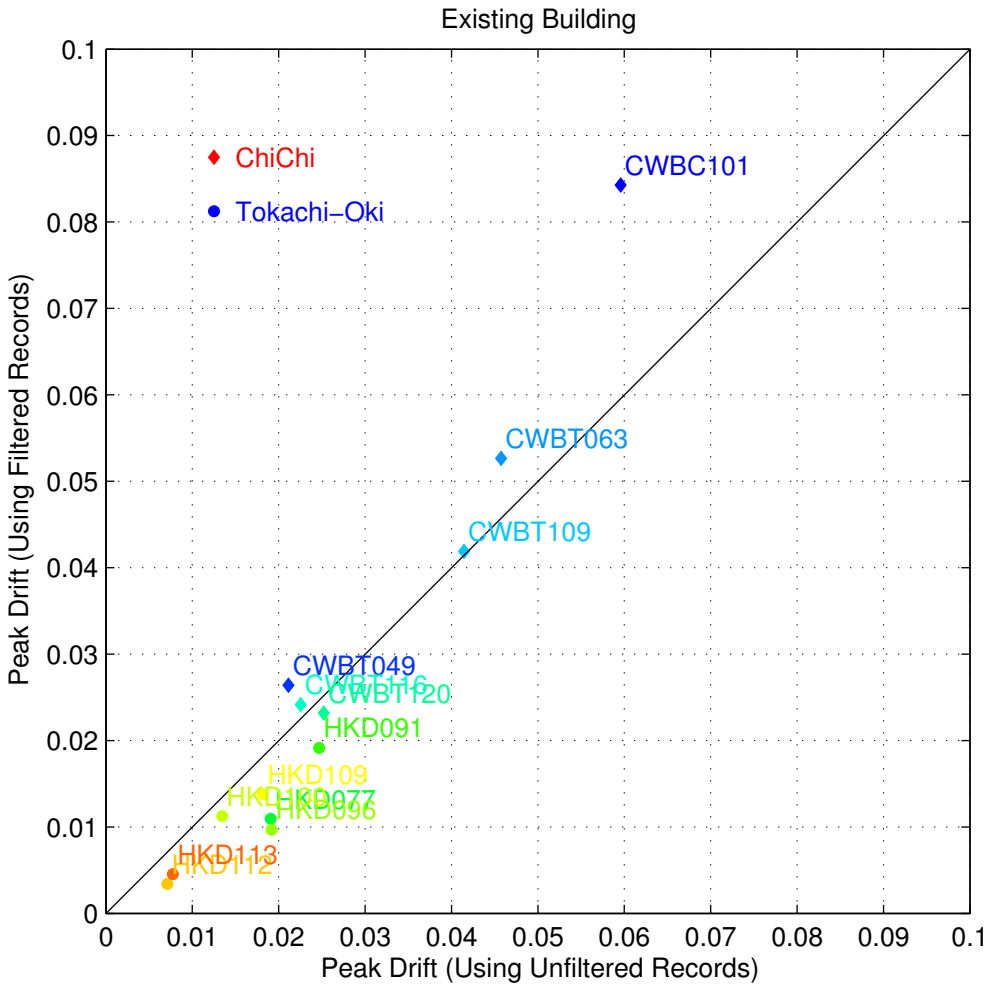

Figure 6.3: Peak drifts observed in the existing building – analyses using filtered and unfiltered records. Pen colors used to plot the points match those used in Figures 6.1 and 6.2.

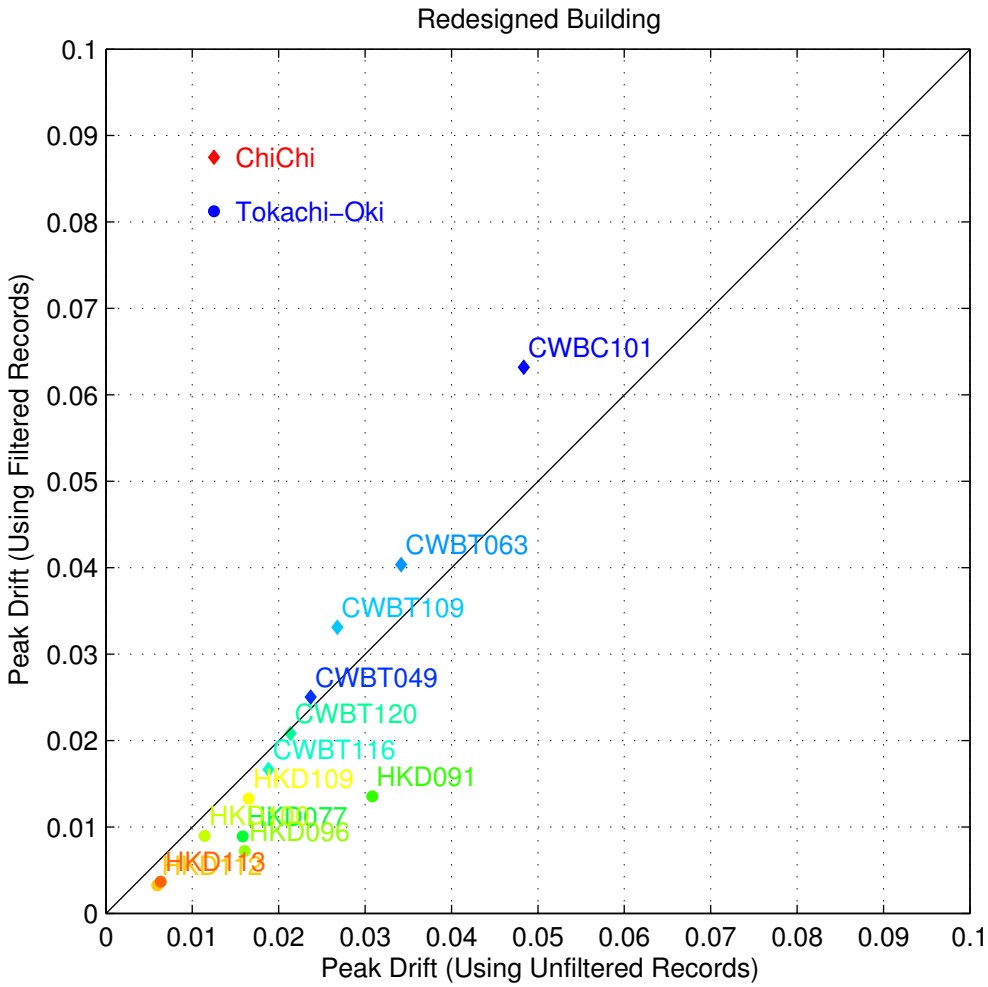

Figure 6.4: Peak drifts observed in the redesigned building – analyses using filtered and unfiltered records. Pen colors used to plot the points match those used in Figures 6.1 and 6.2.

Chapter 7 Past Earthquakes on the San Andreas Fault

Paleoseismology, the recognition and characterization of past earthquakes from evidence in the geological record, has contributed fundamentally to understanding earthquakes by extending the known record of earthquakes into past centuries and millennia. This extension of the historic and instrumental record has revealed the size, location, and timing of past earthquakes, as well as some clues about the length and regularity of earthquake cycles, and the variability of rupture magnitude and extent from event to event on a particular fault [44]. Extensive radiocarbon dating of earthquakes has been carried out at Pallett Creek, a paleoseismic site astride the San Andreas fault 55 km northeast of Los Angeles. This site contains a record of twelve large earthquakes preserved in interbedded marsh and stream deposits [7]. The dating of the ten most recent of these episodes leads to an estimate of the average interval between these episodes of about 132 years [44]. Five of the nine intervals are shorter than a century; three of the remaining four intervals are about two to three centuries long. These ten episodes occurred in four clusters, each of which consists of two or three events. Earthquakes within the clusters are separated by periods of several decades, but the clusters are separated by dormant periods of two to three centuries.

The last major earthquake on the southern half of the San Andreas fault was the Fort Tejon earthquake (magnitude originally estimated to be 7.9 by Sieh [1], but subsequently upgraded to approximately 8.25 by the US Geological Survey) that occurred on January 9, 1857, which was preceded by two estimated-magnitude 7.0 earthquakes on December 8 and 21, 1812. The 1857 event was produced by several meters of sudden lateral slip along the south-central reach of the fault and was felt over at least 350,000 km^2 [1]. Most reports indicate that the duration of the earthquake was between 1 and 3 min. Based on paleoseismological evidence, Kerry Sieh [1] reconstructed the slip distribution along the fault for this event. The rupture initiated at Cholame about 25 km south of Parkfield in Central California, grew to a peak slip of about 9.5 m at Wallace Creek (about 67 km from Cholame), and propagated south past Wrightwood in southern California for a total distance of about 330 km.

The next day, the following account appeared in the Los Angeles Star newspaper [2]: “Doors were slammed to and fro, water was turned out of bowls and pitchers, and in the river the water rushed violently to one bank and then back again, the motion being repeated several times”. William Wallace of Los Angeles wrote in his journal [3]: “This morning at 8.5 o’clock, I was walking to Wolfskill’s and was near his brick house. Suddenly I felt a sort of vertigo. My legs refused to support me. I swayed to and fro like a drunken man. The ground rose up before me, and I reached out my hand to sustain myself against the wall. The wall cracked and rocked. The water which usually runs downhill had doubled upon itself and was rushing with fury towards me. When I saw this, the idea of an earthquake occurred to me. The ground swayed vertically back and forth, without violence, but with considerable force continuing about 1.5 minutes.”

Both of these accounts are indicative of long-period, large-amplitude, long-duration ground motion. Since tall buildings have long natural periods, this could impose a severe demand on the tall building stock in southern California.

According to Weldon et al. [45], even though the current 148-year hiatus in activity on the San Andreas fault is not exceptional, since no lull in the past 1600 years appears to have lasted more than about 200 years when the current hiatus ends, a substantial portion of the fault is likely to rupture either as a single long rupture or a series of overlapping ruptures in a short time interval.

To conclude, the potential for a big earthquake with a large amount of slip on the San Andreas fault exists. In order to prepare for this, it is critical to quantify the effects of such a scenario and this study is an effort in that direction.

Chapter 8 Source Model Used in the Simulation of the Magnitude 7.9 Earthquakes on the San Andreas Fault

Large earthquakes occur as a result of a finite length of fault rupturing. When simulating ground motion from such earthquakes, it is critical to have a realistic source model (slip distribution in time along the fault). Assuming a point-source could lead to erroneous results. The prime objective of this study is to simulate an 1857-like earthquake on the San Andreas fault. Instead of empirically constructing an earthquake source which could add another dimension to the uncertainty inherent in a study of this nature, a finite-source model of the November 3, 2002, magnitude 7.9 earthquake on the Denali fault system in Alaska that is geometrically similar to the San Andreas fault is used in this study. The Denali earthquake initiated as a magnitude 7.1 thrust event on the Susitna Glacier fault, quickly changed to a strike-slip mode of rupture and propagated southeastward along the Denali fault for 218 km, before jumping to the Totschunda fault and continuing further for about 76 km [46]. The slip distribution of this earthquake has been estimated (Figure 8.1) using teleseismic body waves and strong motion waveforms as well as GPS vectors [22]. Here, the slip on the Denali and Totschunda faults (290 km long), amounting to a moment magnitude of 7.9, has been mapped on to the San Andreas fault with rupture initiating at Parkfield and progressing southeastward a distance of about 290 km (Figure 1.1 inset). The maximum depth of rupture is about 20 km. The surface slip (Figure 8.2) grows slowly to 7.4 m and then drops off drastically towards the end of the rupture [1]. The peak slip at depth is about 12 m. The peak particle velocity is 4.3 m.s^{-1} [2].

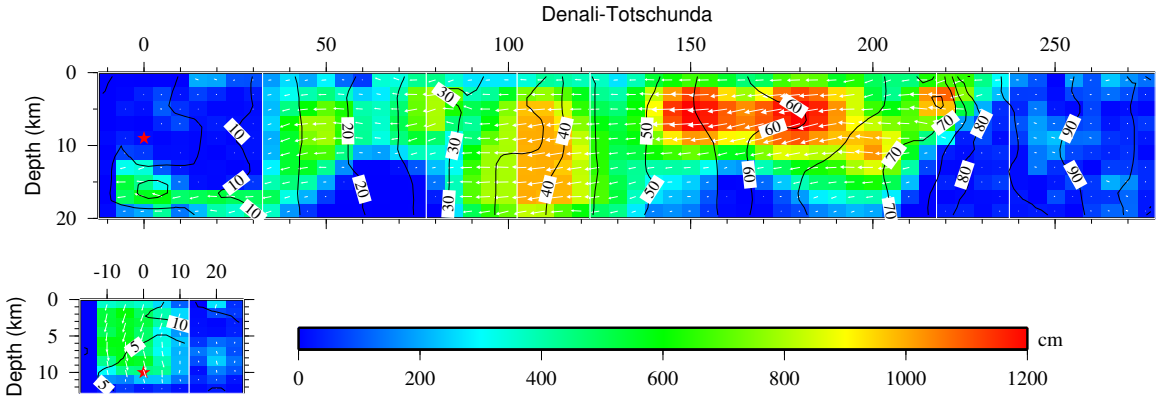

Figure 8.1: Slip distribution of the 2002 Denali earthquake constrained by teleseismic body and strong motion waveforms as well as GPS vectors. The color scheme reflects the slip amplitude and contours reflect the rupture initiation time. The hypocenter is indicated by the red star. White arrows denote the slip direction and magnitude

It should be noted that the prediction capability of the finite source used in this study is band limited. It is dependent on the shortest period of seismic signals used to construct the model, which in most cases is about 2 sec, but could be as short as 1 sec when the stations are close to the fault where the source signature is the strongest with little contamination from 3-D propagation effects, e.g., the 1994 Northridge earthquake.

[1] This is contrary to what happened in the 1857 San Andreas earthquake, where the slip along the fault is deduced to have grown quickly to a peak value of about 9.5 m and then dropped off gradually [1].

[2] Since particle velocity is not constrained as well as the slip in the inversion, a scenario in which the particle velocity is artificially capped at 1 m.s^{-1} is considered (Figure 8.3). The resulting ground motions in the region of interest (far away) are not significantly different from the uncapped particle velocity scenario in the context of the present study.

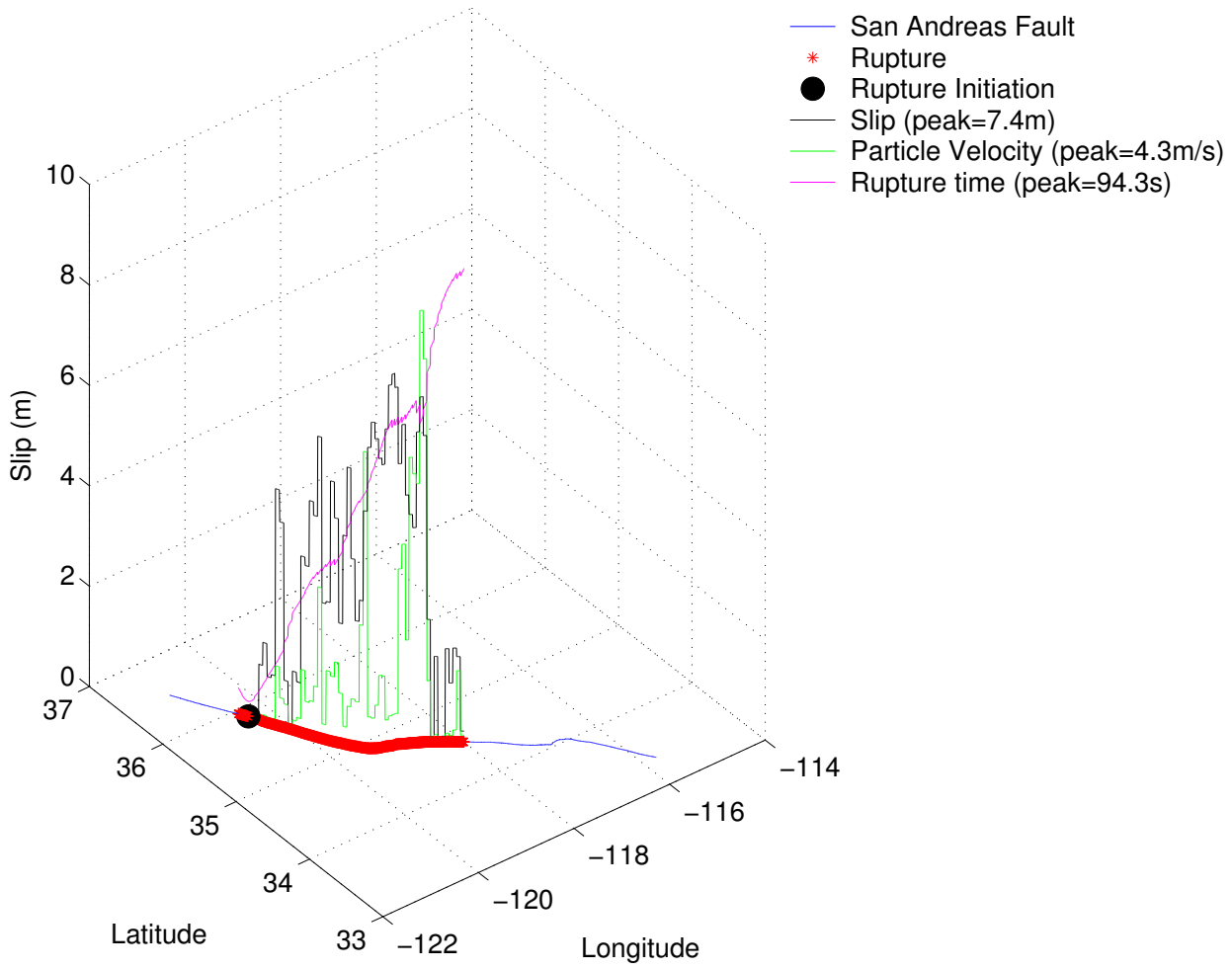

Figure 8.2: Surface slip, particle velocity, and rupture time, for the simulated magnitude 7.9 earthquake on the San Andreas fault – north-to-south rupture.

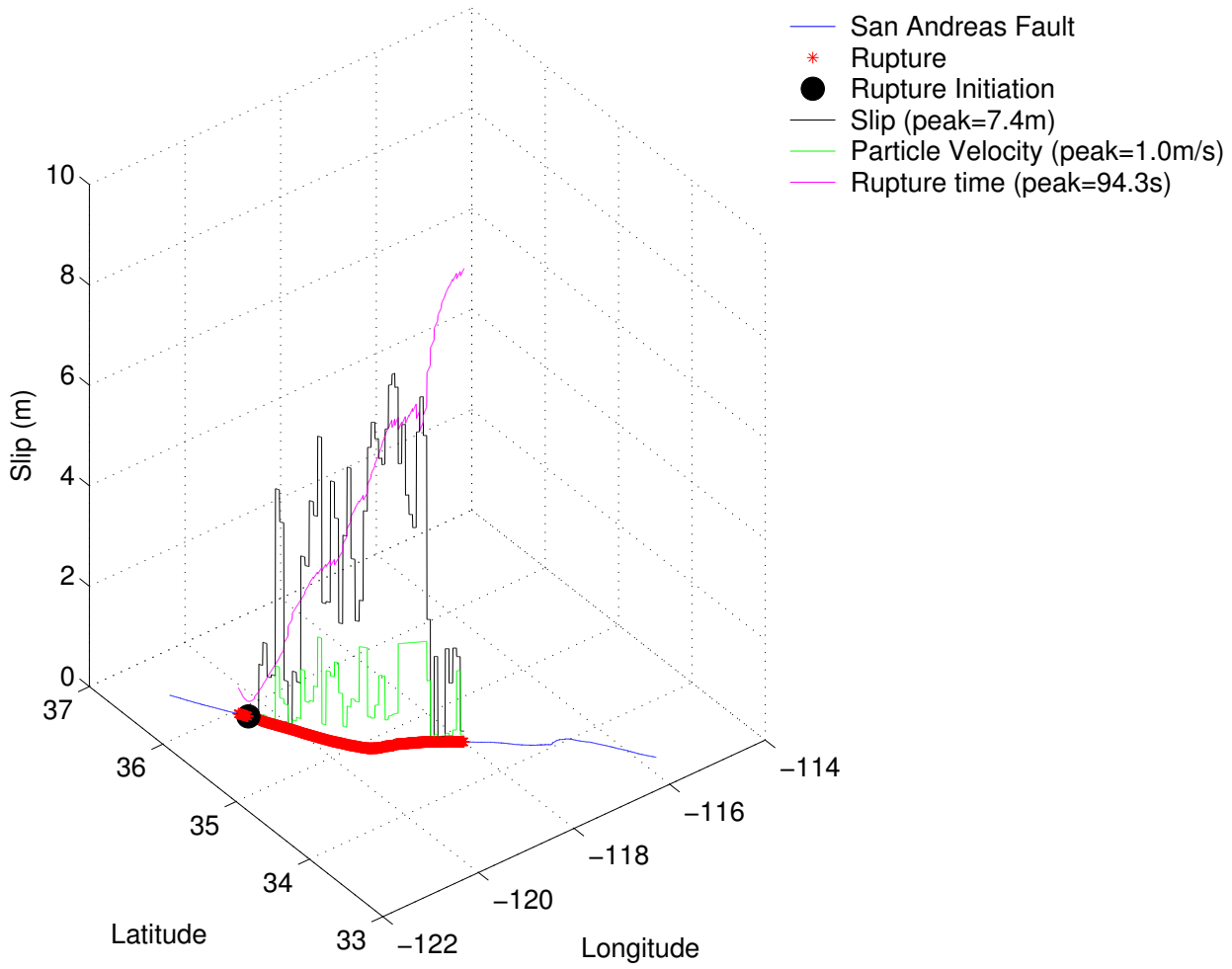

Figure 8.3: Surface slip, particle velocity, and rupture time, for the simulated magnitude 7.9 earthquake on the San Andreas fault – north-to-south rupture, capped particle velocity case.

Strong motion data in tandem with teleseismic and GPS data is used to constrain the Denali earthquake finite-source model. To demonstrate that finite-source models can be significantly improved by combining different types of data, a numerical experiment is conducted using the extensive strong motion dataset of the 1999 ChiChi earthquake. In addition to the data from many strong motion and GPS stations, twenty-one teleseismic P-waveforms downloaded from the Incorporated Research Institutions for Seismology (IRIS) data center have been included.

Three finite-source models (Figure 8.4) are constructed:

1. In the first case, teleseismic data alone is used to construct a single-plane fault model. The fault plane has a strike of 18° and a dip angle of 30° to the east. The location of the fault is defined using the hypocenter location obtained by the local network managed by Central Weather Bureau (CWB), Taiwan. The rupture plane is allowed to extend generously from surface to Moho and is divided into subfaults with dimensions of 5 km by 5 km. The inverted results are referred to as "Teleseismic".

2. In the second case, teleseismic data is combined with GPS data for the inversion of the rupture history, this time on a more realistic 3-plane fault geometry constructed using static data only [47]. In this case, the vertical extension of fault plane is limited to 18 km based on the previous GPS inversion. The inverted results in this case are referred to as "Tele+GPS".

3. In the third case, selected strong motion data is combined with GPS data and a more complex rise time function representation [22] is used to constrain the slip model. Given the abundant data involved and the care taken in its analysis, this model can be considered to be the most accurate representation of the actual rupture. It is labeled as "Strong+GPS".

Of the three models, the "Teleseismic" model explains the teleseismic data set the best. Adding the static data and using a realistic fault geometry only slightly decreases the waveform fits. This is consistent with the fact that the co-seismic field dominates the GPS measurements [48]. In addition, it suggests that fault bending could not be resolved using teleseismic P waves alone. Adding other teleseismic phases, such as SH, may be able to resolve this. The slip distributions of "Tele+GPS" and "Strong+GPS" models are quite similar to each other but there are substantial discrepancies between these and the slip distribution of the "Teleseismic" model, particularly at the northern end. This is primarily due to the difference in the assumed fault geometry. However, the big asperities of the "Teleseismic" are still very similar to the preferred model, "Strong+GPS", and not all events of this size have such radial geometrical complexity.

For the Denali earthquake source inversion, all the above mentioned datasets have been used and fault geometry has been constructed based on the surface break. Taking into consideration the limited number of strong motion and GPS stations, the accuracy of the Denali earthquake source model can be considered to be similar to the "Tele+GPS" case discussed above. While it is possible that the ground shaking could be underestimated to some extent, the simulations resulting from the use of this source model would be sufficiently reliable for the purposes of this study.

Finally, for the case of the Denali earthquake source inversion, synthetic seismograms have been computed at Pump Station 10 which is the only near-fault station and they match very well with the data in both velocity and displacement (Figure 8.5). Note that the shortest period used in the inversion is 2 sec.

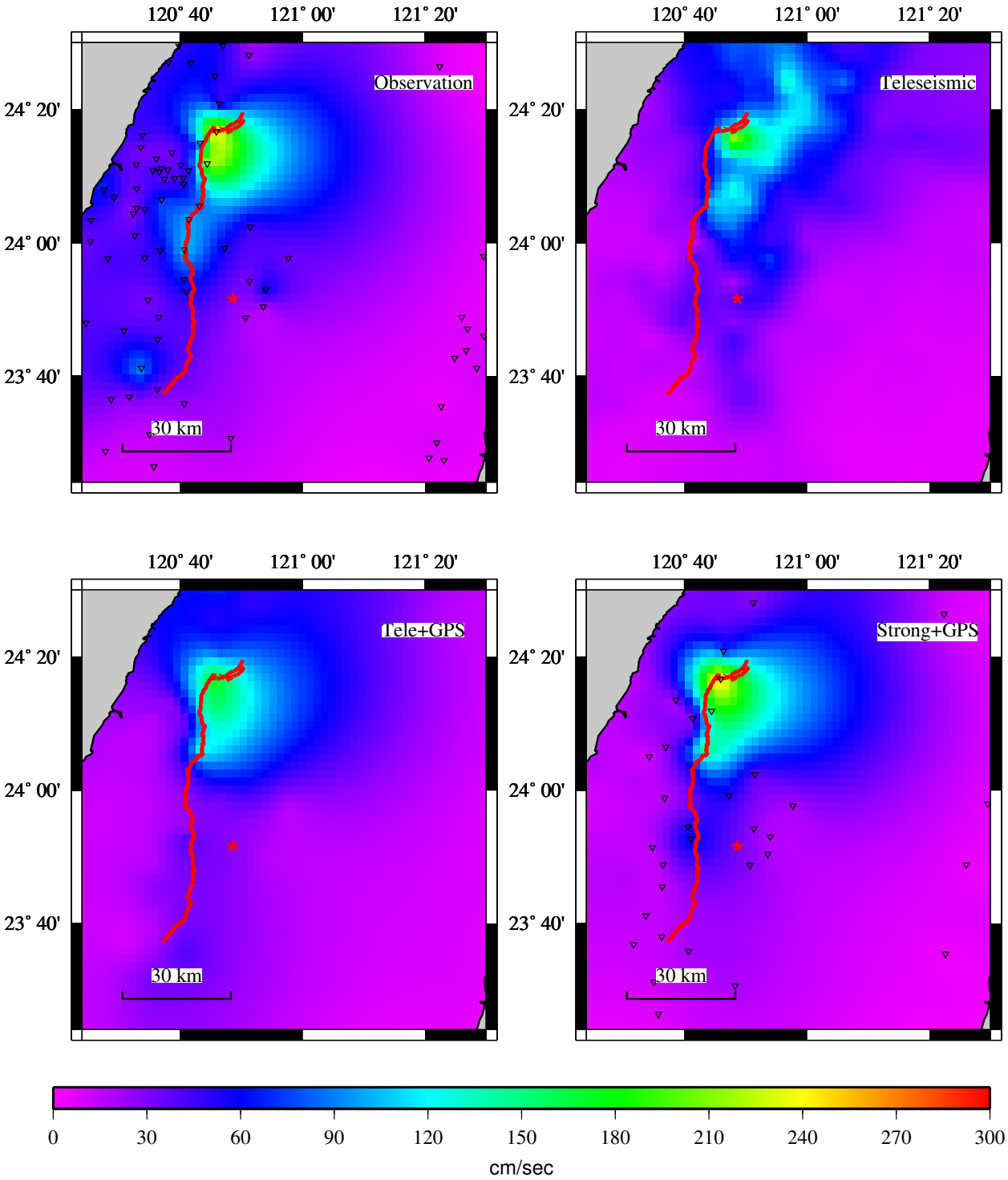

Figure 8.4: 1999 ChiChi earthquake: Peak ground velocities.

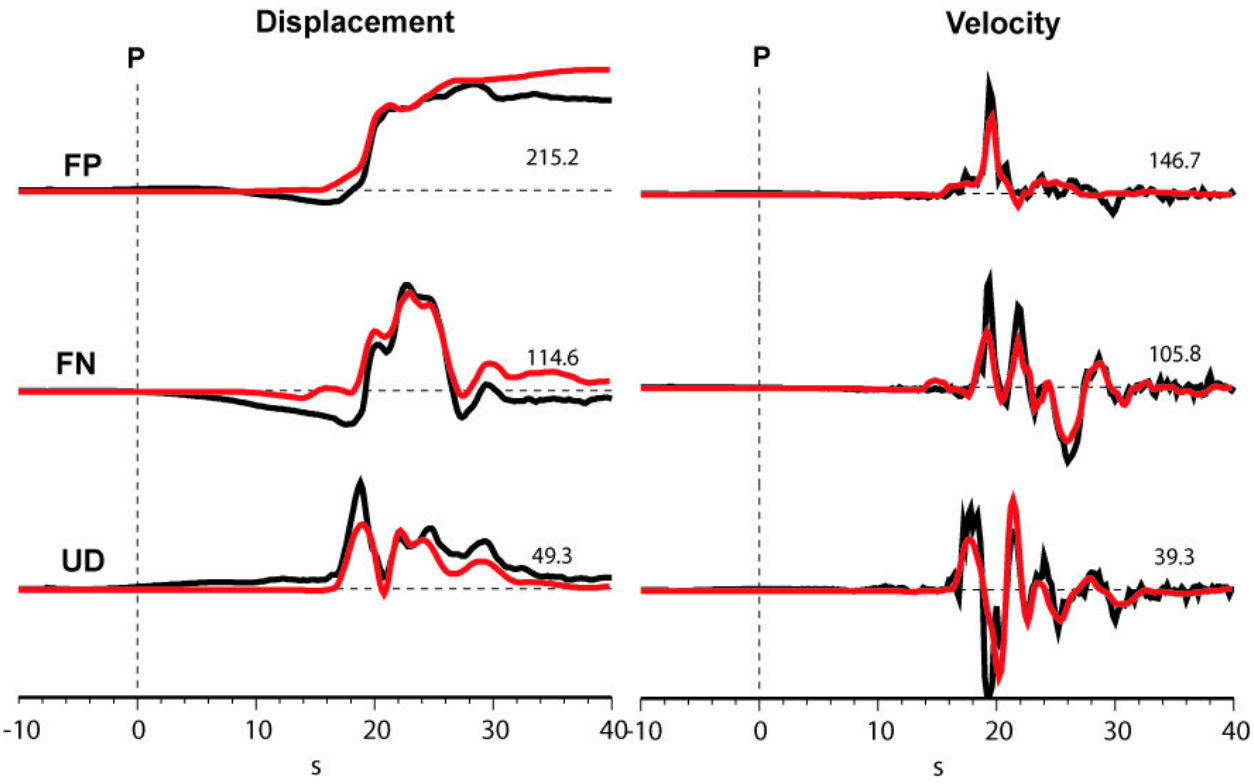

Figure 8.5: Denali source inversion: Data (black) versus synthetic seismograms (red) for Pump Station 10 (3 km from the fault trace).

Chapter 9 Scenario 1: North-to-South Rupture of the San Andreas Fault

The two techniques adopted by seismologists to simulate ground motion consist of either a deterministic or an empirical approach. In the deterministic approach, the elastic wave equation is solved numerically in a realistic 3-D Earth model and the ground motion is directly computed without any additional assumptions. In the case of the Los Angeles basin, the accuracy and frequency limitations depend on the quality of the 3-D Los Angeles basin model, which has improved steadily over the last decade, and on the numerical resolution of the 3-D seismic wave propagation simulation. For this study, one of the two well-accepted 3-D southern California Earth models, the Harvard-LA model [29], has been used (the other being the SCEC Community Velocity Model [49, 50, 51]). Both velocity models allow for the simulation of the basin response down to a shortest period of approximately 2 s [23]. The deterministic approach is considered the more reliable approach in the seismological society given the current state of knowledge.

The second commonly used seismological approach consists of generating broadband ground motion through empirical methods that combine a stochastic approach at high frequencies with a deterministic approach at low frequencies [52, 53]. These methods are still nascent in their development. They are tailored for a given earthquake and have to be re-tuned on a case-by-case basis. Being empirical, they cannot be proved or validated consistently for various types of earthquakes, and hence they are not reliable enough at this stage.

Given that the results of the study will not be affected significantly by excluding high-frequency content (Chapter 6), the robust, deterministic (read reproducible) approach to simulating the ground-motions has been adopted for this prototype study.

Using the spectral-element method, seismograms are computed at each of the 636 hypothetical tall-building sites (Figure 1.1). The minimum S wave velocity in the Harvard-LA basin model is 687 m.s^{-1}. The horizontal size of the mesh cells at the surface is approximately 270 m in each direction. The resulting number of grid points per S wavelength is about 5. The time step used for the computations is 9 ms, with a total number of 30000 steps, i.e., a total duration of 270 s. Shown in Figures 9.1–9.3 and 9.4–9.6 are maps of the three components of peak velocity and displacement, respectively, lowpass-filtered using a Butterworth filter with a corner period at 2 s. Gaussian smoothing over a nearest neighborhood interpolation scheme is used for all the maps. The solid circles in these maps correspond to the cities shown in Figure 1.1. The San Fernando valley experiences severe shaking. As the rupture proceeds down south from Parkfield and hits the bend in the San Andreas fault, it sheds off a significant amount of energy into the region that is directly in front of it, which happens to be the San Fernando valley (see http://www.ce.caltech.edu/krishnan for a movie of the rupture and seismic wave propagation). A good portion of this energy spills over into the Los Angeles basin, with many cities along the coast such as Santa Monica and Seal Beach and more inland areas going East from Seal beach towards Anaheim experiencing long-duration shaking. In addition, the tail-end of the rupture sheds energy from SH/Love waves into the San Gabriel valley (Baldwin Park-La Puente region), which is bounded by a line of mountains that creates a mini-basin, further amplifying the ground motion. The peak velocity is of the order of 1 m.s^{-1} in the Los Angeles basin, including downtown Los Angeles, and 2 m.s^{-1} in the San Fernando valley. The map of peak displacements has characteristics quite similar to that of the peak velocities, with significant displacements in the basins but not in the mountains. The peak displacements are in the neighborhood of 1 m in the Los Angeles basin and 2 m in the San Fernando valley.

To study the effects of the simulated ground motion on the two 18-story steel moment-frame buildings (Chapter 2) located at each of the 636 sites shown in Figure 1.1, computer models of the Woodland Hills existing and redesigned

buildings described in Chapter 2 are analyzed. As before, the analyses are performed using the FRAME3D program [30]. The peak interstory drift is the most reliable performance measure to evaluate structural performance. The Federal Emergency Management Agency (FEMA) proposes limits on the peak drift ratio for classifying building performance [1]. Another damage measure that can be used to rate structure performance is plastic rotation in beams, columns and panel zones. Plastic rotation at the ends of beams and columns is defined as the permanent rotation after unloading the element that has yielded in flexure and is measured in radians or % of a radian. Panel-zone plastic rotation is defined as the unrecoverable permanent shear strain in the joint and is also measured in radians or % of a radians. Excessive plastic rotations in the panel zones, beams and columns indicate damage and structural degradation, important factors in collapse potential. These plastic rotations can be compared against the structural performance levels set by the FEMA [4]. Even though this FEMA document is meant for the seismic rehabilitation of existing buildings, in this study the same performance standards are utilized for the redesigned building model as well for comparison with the existing building model. The three structural performance levels specified in FEMA-356 are Collapse Prevention, Life Safety, and Immediate Occupancy in decreasing order of structural damage. The plastic rotations at the ends of beams and columns, and in the panel zones can be compared to the acceptable limits prescribed in FEMA-356 [4] for each of the performance levels, and based on this, the performance of each of these components can be classified into one of IO, LS, CP performance levels or, alternately, a collapsed state.

In the modeling of the existing building beam-to-column connections, the fracture mode of failure that was widely observed during the Northridge earthquake is included. In the presence of weld-fracture, it is not clear how the performance levels can be assigned to beam-column components based on plastic rotations. For example, upon fracture of all fibers at the end of a beam, its stiffness drops to zero under tension and the beam would not be able to carry additional moment and hence the beam-end rotation does not grow any further. For small fracture strains the connection may fracture, but since the rotation is small, the connection could receive a "good" performance rating. Thus, while technically a fractured connection should receive a "CO" rating, it may end up with an "LS" rating. Hence, for the existing building model it may be better to classify connection performance using the fracture index which represents the percentage of connections in the building that fractured. Since the Northridge earthquake, this defect has been corrected and this mode of failure is not expected in buildings built today. So for the redesigned building, the performance indices based on the plastic rotations may be reasonable. Despite the complications arising out of fracture, the performance indices based on plastic rotation are provided for the existing building as well for comparison with the redesigned building. The results corresponding to the performance of the building models based on the plastic rotations are presented in Appendices D and E. Nevertheless, it is better to judge the performance of the existing and redesigned building models based on the interstory drift measure as it is devoid of the subjectivity associated with the empirical limits proposed for plastic rotations.

To put the results on existing buildings in perspective, note that while the population of tall buildings in southern California is quite widespread, a major fraction is located in downtown Los Angeles, the mid-Wilshire district (Beverly Hills), west Los Angeles, and Santa Monica. There are quite a few tall buildings spread across the San Fernando valley as well, e.g., in Woodland Hills and Canoga Park, and 30-40 tall buildings in Orange County (comprising the cities of Orange, Irvine, Costa Mesa, Newport Beach, Anaheim, Santa Ana, Garden Grove, etc.). A host of new tall buildings are being planned in Orange County with thirteen proposed high-rises in the cities of Anaheim and Santa Ana.

[1] Since there is very little usable data to assess the performance of tall buildings based on calculated interstory drifts, in this study an empirical approach proposed by the Federal Emergency Management Agency (FEMA) is taken. For rehabilitation of existing buildings, FEMA 356 [4] defines three performance levels: Immediate Occupancy (IO) refers to a post-earthquake damage state in which very limited structural damage has occurred. The risk of life-threatening injury as a result of structural damage is very low, and although some minor structural repairs may be appropriate, these would generally not be required prior to reoccupancy. Life Safety (LS) is a post-earthquake damage state that includes damage to structural components but retains a margin against onset of partial or total collapse. Collapse Prevention (CP) refers to a post-earthquake damage state that includes damage to structural components such that the structure continues to support gravity loads but retains no margin against collapse. For existing buildings, the interstory drift limits for the IO, LS, and CP performance levels specified by FEMA are 0.007, 0.025, and 0.05, respectively. For the design of new steel moment-frame buildings, FEMA 350 [5] defines only two performance levels, the IO and CP levels. For buildings taller than 12 stories, the specified interstory drift limits for these levels are 0.01 and 0.06, respectively.

The results of the building analyses (see http://www.ce.caltech.edu/krishnan for movies of buildings swaying under the earthquake resulting in permanent tilt or collapse) corresponding to a north-to-south rupture of the San Andreas fault are summarized in Figures 9.7 through 9.12 for the existing 18-story steel building and Figures 9.13 through 9.17 for the new 18-story steel building. Gaussian smoothing over a nearest neighborhood interpolation scheme is used for all the maps. Figure 9.12 shows the percentage of connections where fracture occurs in the existing building. Fracture occurs in at least 25% of the connections in this building when located in the San Fernando valley. Note that the scale saturates at 25% and that this number is exceeded at many locations. About 10% of the connections fracture in the building when it is located in downtown Los Angeles and the mid-Wilshire district (Beverly Hills), while the numbers are about 20% when it is located in Santa Monica, west Los Angeles, Inglewood, Alhambra, Baldwin Park, La Puente, Downey, Norwalk, Brea, Fullerton, Anaheim, and Seal beach. Figures 9.7 through 9.9 show the peak interstory drift that occurs in the top-third, middle-third, and bottom-third of the existing building, respectively. Figure 9.10 collates these into a single map showing the peak drift occurring in the building. The fact that the peak interstory drifts in the middle-third and bottom-third of the existing building model are far greater than the top-third indicates that the damage is localized in the lower floors. The localization of damage in the lower floors rather than the upper floors could potentially be worse because of the risk of more floors pancaking on top of each other if a single story gives way. Peak interstory drifts beyond 0.10 are indicative of probable collapse, drifts beyond 0.06 are indicative of severe damage, while drifts below 0.01 are indicative of minimal damage not requiring any repairs. Consistent with the extent of fracture observed, the peak drifts in the existing building model exceed 0.10 when it is located in the San Fernando valley, Baldwin Park and neighboring cities, Santa Monica, west Los Angeles and neighboring cities, Norwalk and neighboring cities, and Seal Beach and neighboring cities, which is well into the postulated collapse regime (see footnote 1). Note that the scale saturates at 0.10, and in fact the drifts exceed this number in many locations in these regions. When located in downtown Los Angeles and the mid-Wilshire district, the building would barely satisfy the collapse prevention criteria set by FEMA [4] with peak drifts of about 0.05. Plotted on Figure 9.11 are the magnitude and direction of the permanent offset of the building at the penthouse level following the earthquake [2]. The length of the arrow is proportional to the magnitude. The scale is saturated at 1.5 m which corresponds roughly to an average inclination of 2% over the height of the building.

The performance of the newly designed 18-story steel building is significantly better than the existing building for the entire region. However, note that the new building has significant drifts indicative of serious damage when located in the San Fernando valley or the Baldwin Park area. Figures 9.13 through 9.15 show the peak interstory drift that occurs in the top-third, middle-third, and bottom-third of the redesigned building, respectively. Figure 9.16 collates these into a single map showing the peak drift occurring in the building. When located in coastal cities (such as Santa Monica, Seal Beach etc.), the Wilshire corridor (west Los Angeles, Beverly Hills, etc.), the mid-city region (Downey, Norwalk, etc.) or the booming Orange County cities of Anaheim and Santa Ana, it has peak drifts of about 0.05, once again barely satisfying the FEMA collapse prevention criteria [5]. In downtown Los Angeles it does not undergo much damage in this scenario. Thus, even though this building has been designed according to the latest code, it suffers damage that would necessitate closure for some time following the earthquake in most areas, but this should be expected since this is a large earthquake and building codes are written to limit the loss of life and ensure "collapse prevention" for such large earthquakes, but not necessarily limit damage.

Plotted on Figure 9.17 are the magnitude and direction of the permanent offset of the building at the penthouse level following the earthquake. The redesigned building too has large permanent offsets at many locations.

For eight representative sites out of the 636 analysis sites, detailed results of building performance are given in Appendix F. These sites are located in Thousand Oaks, Northridge, West Los Angeles, Baldwin Park, Anaheim, Long

[2]This permanent offset is a result of the irrecoverable plastic deformation in the structural components – beams, columns, and joints. The building leaning in such a fashion would lead to scores of problems starting with misalignment of elevators. As an example, the 6 inch tilt in the Woodland Hills building following the Northridge earthquake led to misalignment in the elevators. Bringing the building back to plumb would inevitably result in building closure and significant direct and indirect costs.

Beach, and Santa Ana. Of these, the existing building model is seen collapsing in Thousand Oaks and Northridge. Included in this appendix are snapshots of building deformation immediately following the earthquake, time histories of the three components of ground velocity and displacement (bandpass-filtered between 2 s and 1000 s), time histories of the east and north components of the penthouse displacements of the existing and redesigned building models, tables detailing the performance of the structural components (plastic rotation in beams, columns, and panel zones), bar diagrams illustrating the peak interstory drifts over the height of the two building models, maps of plastic rotation in beams, columns, and panel zones, and, finally, maps of fracture locations in the moment-frames of the existing building.

It should be mentioned that for the north-to-south rupture of the San Andreas fault considered here, if the slip distribution along the fault were like the 1857 earthquake, i.e., rising quickly to the peak value and then gradually dropping off [1], instead of the other way around, results could be quite different. Also, directivity can have a significant impact on ground shaking and the resulting building damage. For example, for a south-to-north rupture of the same earthquake described in the next chapter, building damage is far less severe.

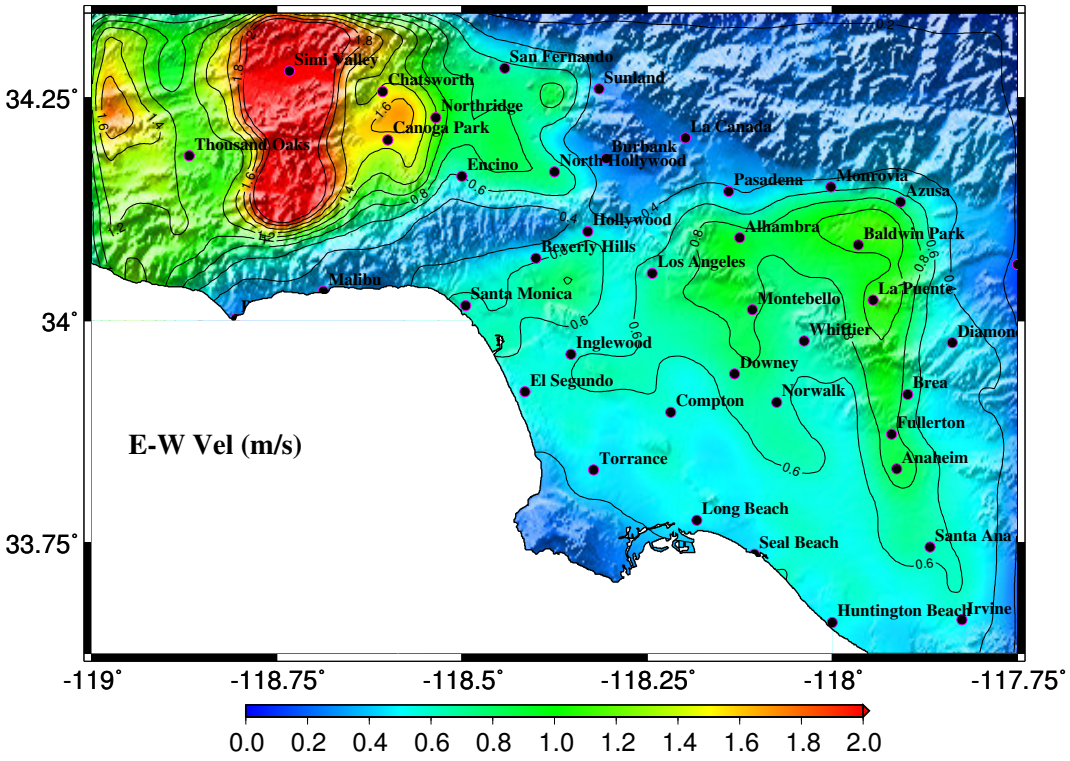

Figure 9.1: M_w7.9 earthquake (north-to-south rupture) on the San Andreas Fault – ground shaking: Map of peak velocities (east component).

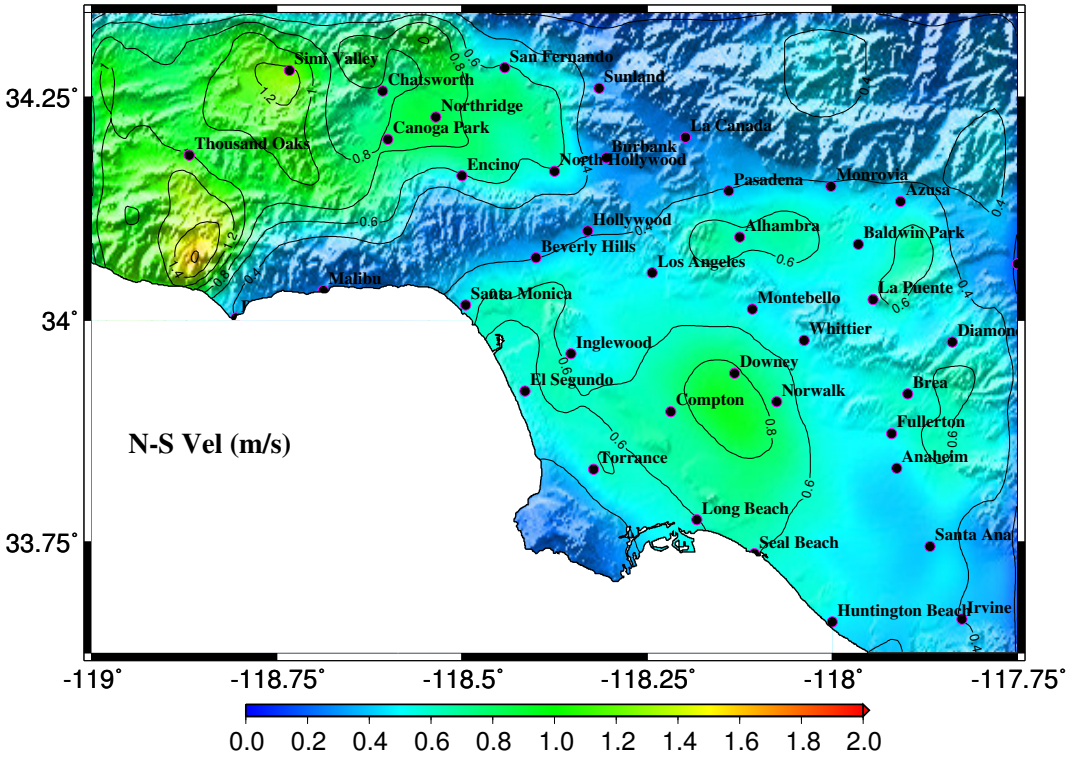

Figure 9.2: M_w7.9 earthquake (north-to-south rupture) on the San Andreas fault – ground shaking: Map of peak velocities (north component).

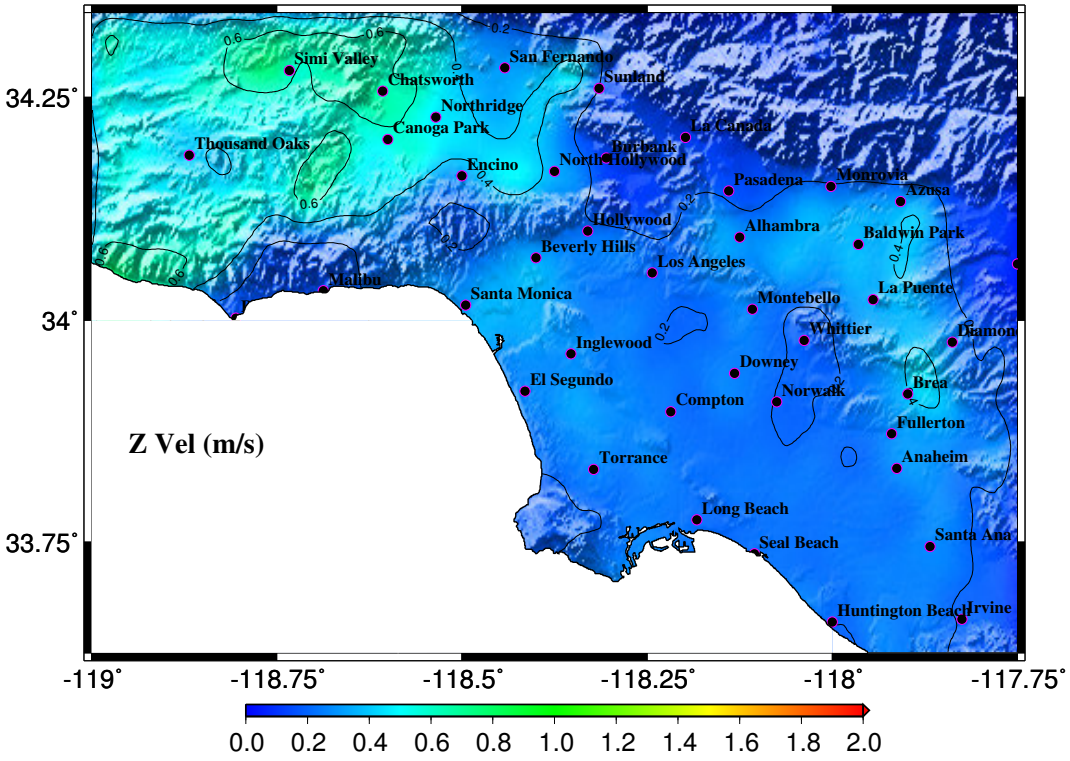

Figure 9.3: M_w7.9 earthquake (north-to-south rupture) on the San Andreas fault – ground shaking: Map of peak velocities (vertical component).

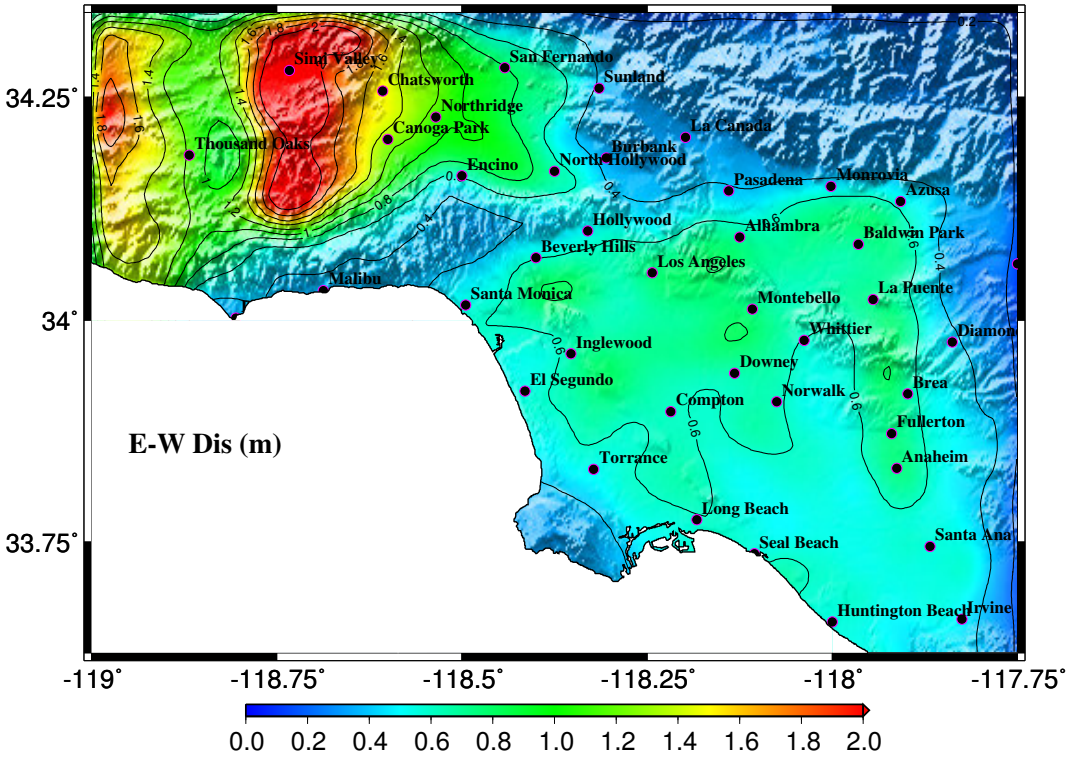

Figure 9.4: M_w7.9 earthquake (north-to-south rupture) on the San Andreas fault – ground shaking: Map of peak displacements (east component).

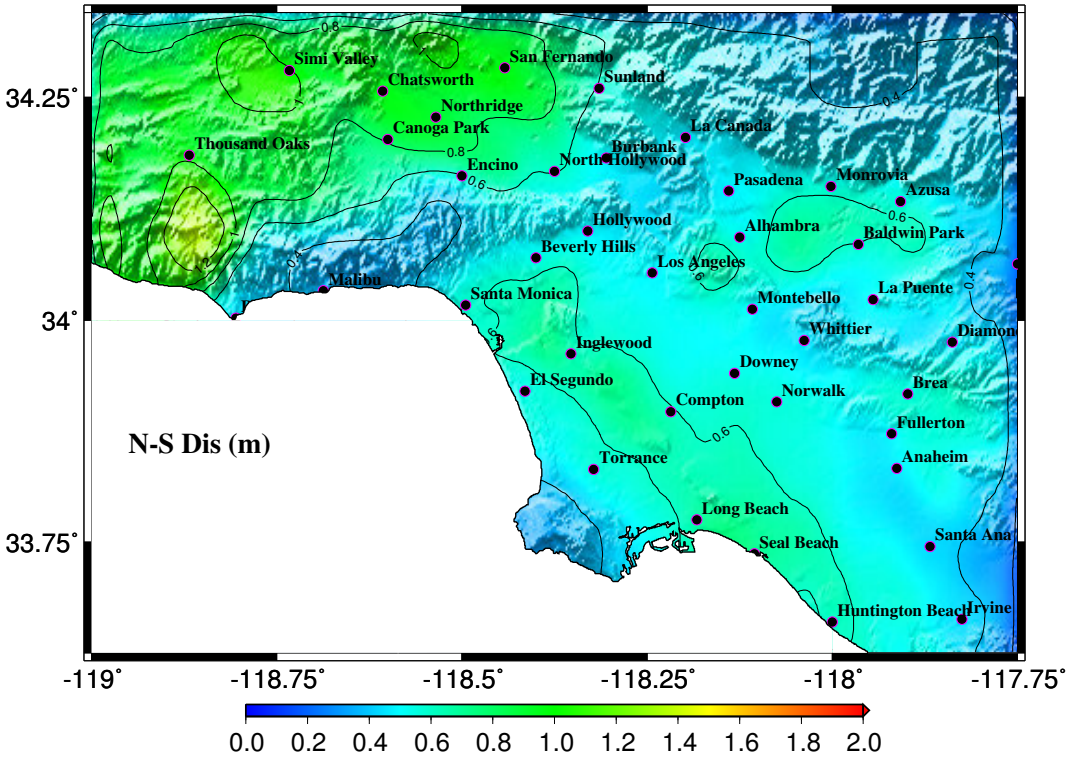

Figure 9.5: M_w7.9 earthquake (north-to-south rupture) on the San Andreas fault – ground shaking: Map of peak displacements (north component).

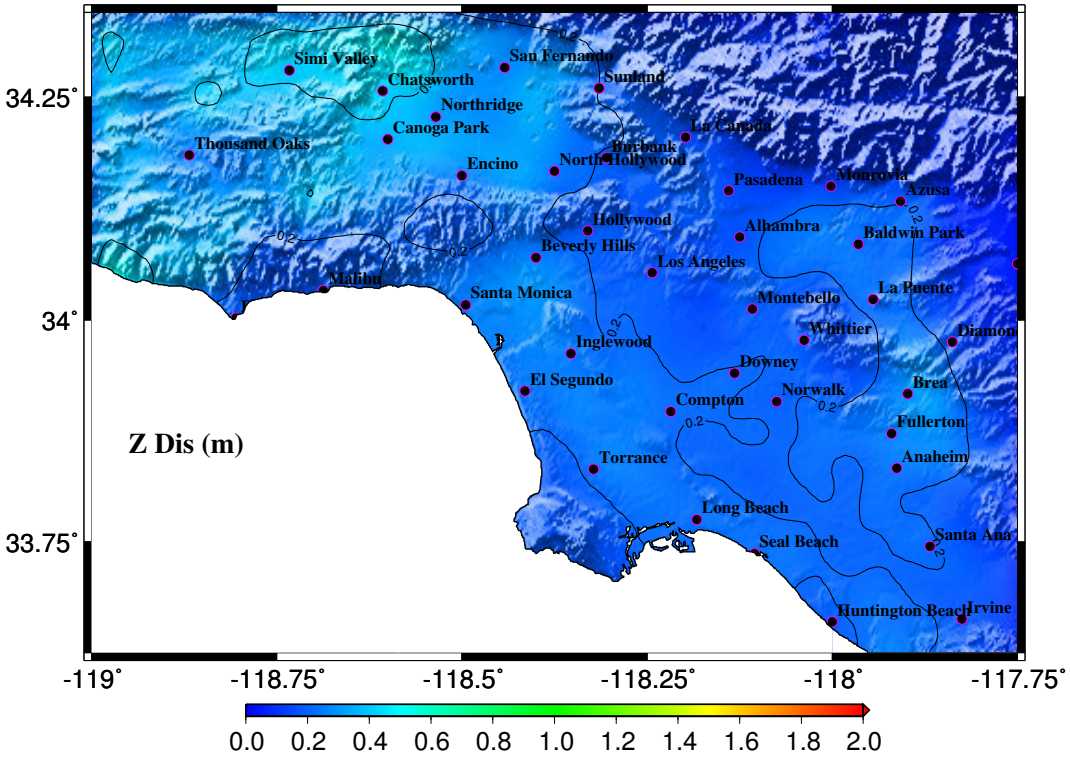

Figure 9.6: $M_w 7.9$ earthquake (north-to-south rupture) on the San Andreas fault – ground shaking: Map of peak displacements (vertical component).

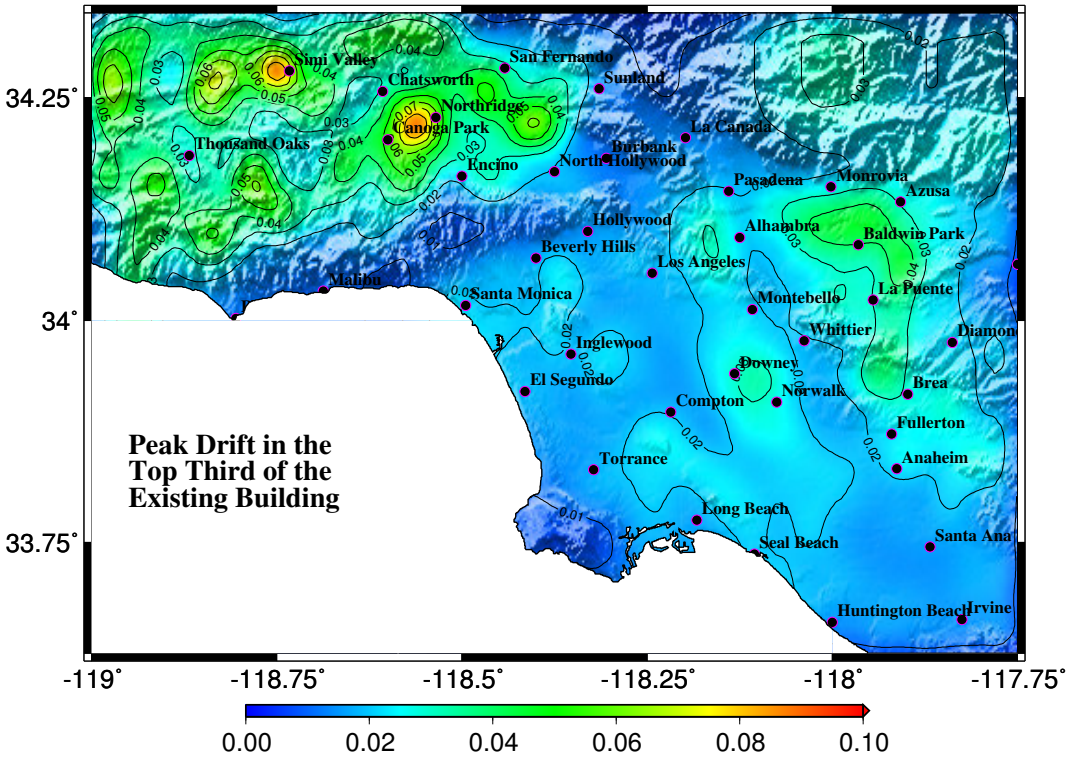

Figure 9.7: M_w7.9 earthquake (north-to-south rupture) on the San Andreas fault – existing building performance: Peak drift ratios in the top-third of the building.

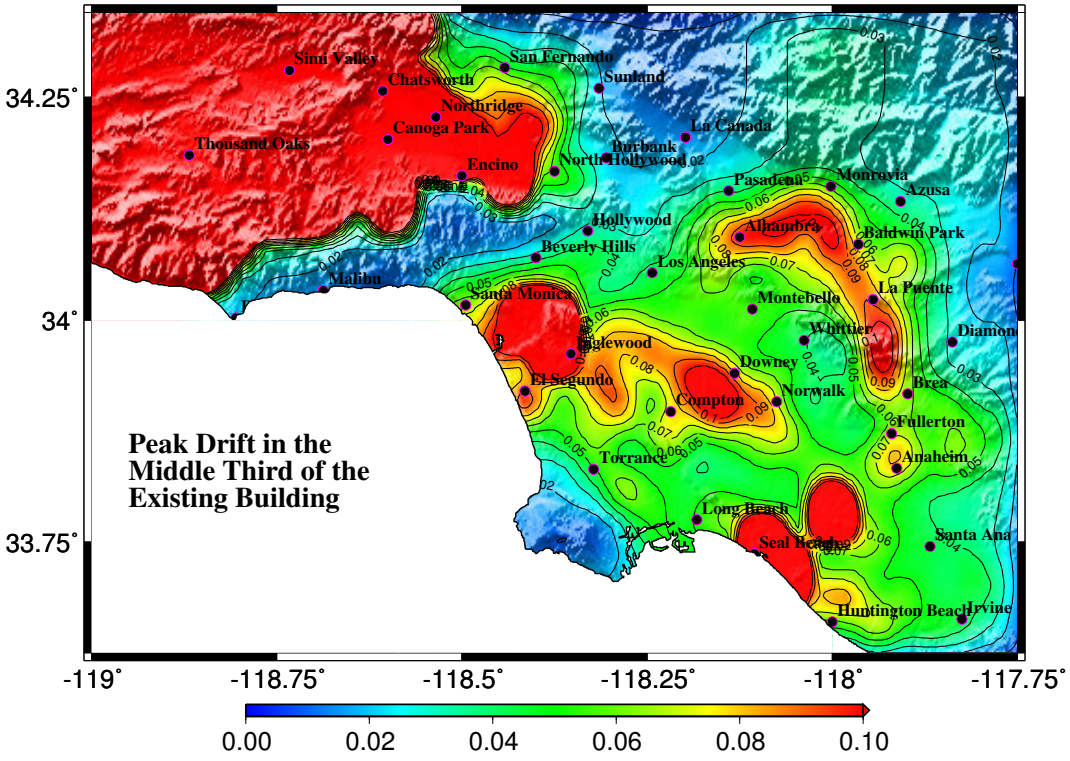

Figure 9.8: M_w7.9 earthquake (north-to-south rupture) on the San Andreas fault – existing building performance: Peak drift ratios in the middle-third of the building.

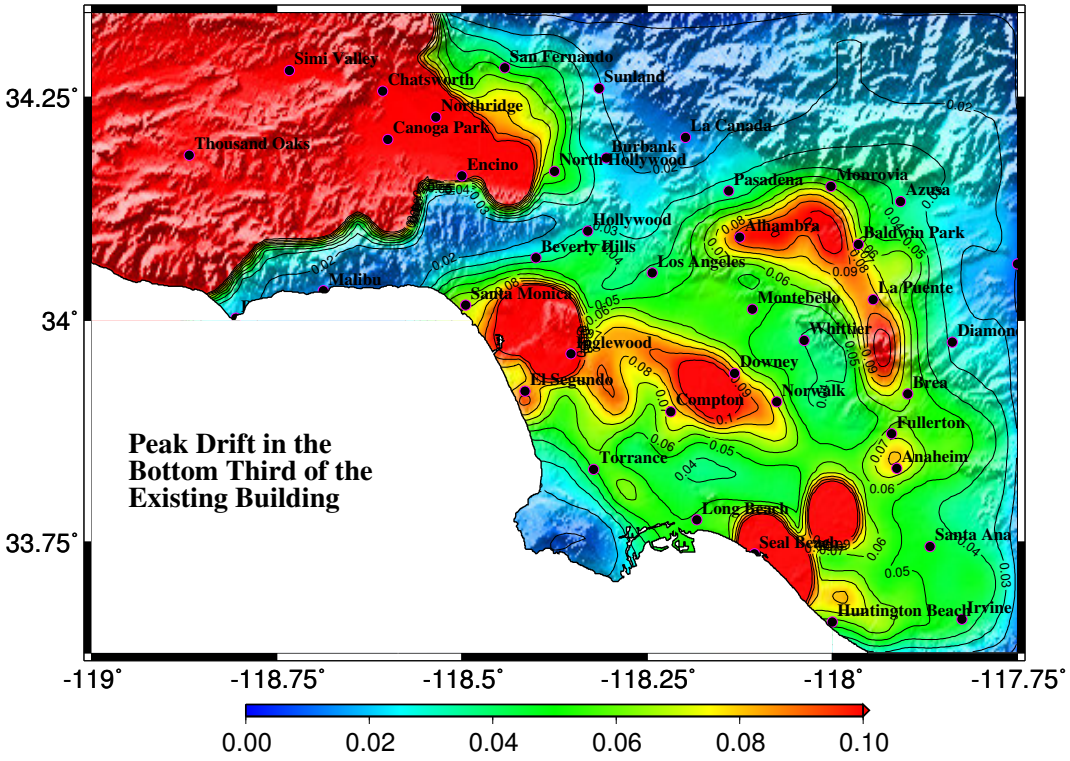

Figure 9.9: M_w7.9 earthquake (north-to-south rupture) on the San Andreas fault – existing building performance: Peak drift ratios in the bottom-third of the building.

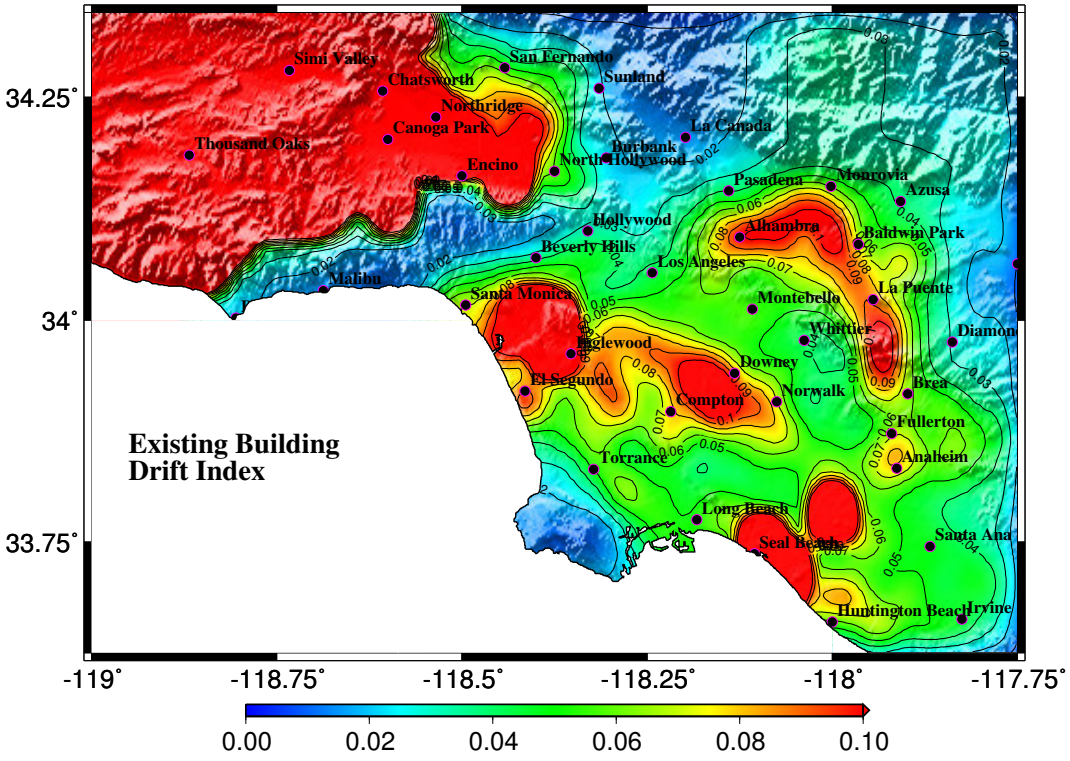

Figure 9.10: M_w7.9 earthquake (north-to-south rupture) on the San Andreas fault – existing building performance: Peak drift ratios anywhere in the building.

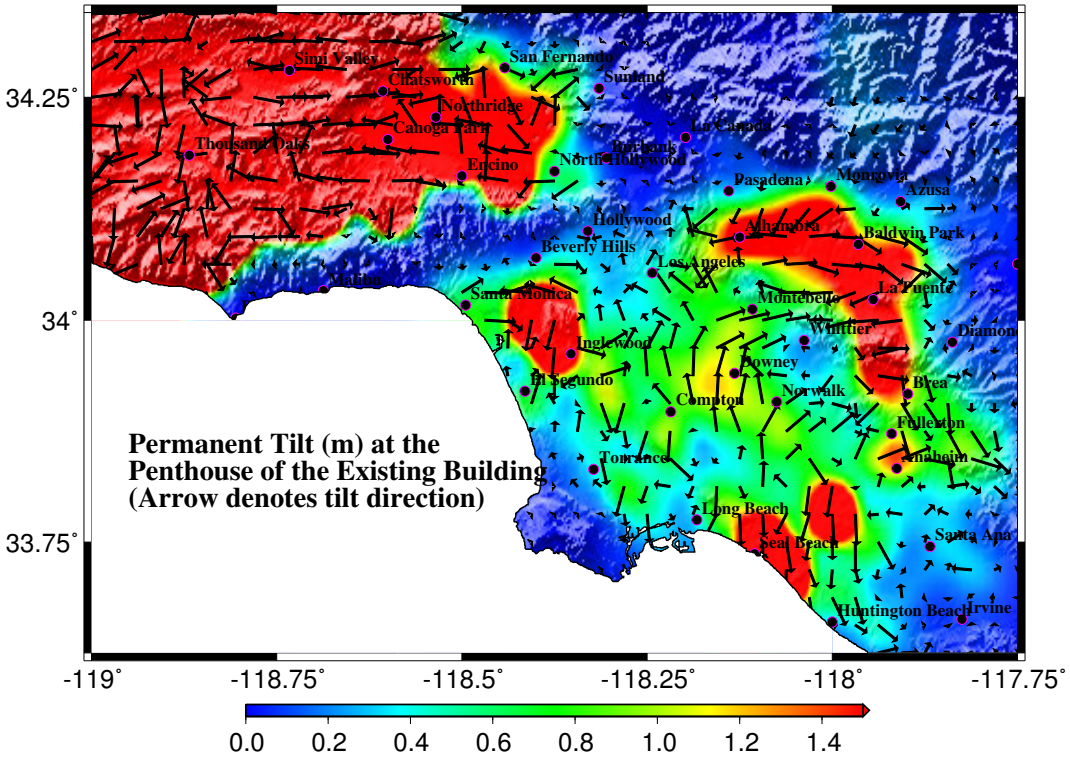

Figure 9.11: M_w7.9 earthquake (north-to-south rupture) on the San Andreas fault – existing building performance: Permanent offset at the penthouse level.

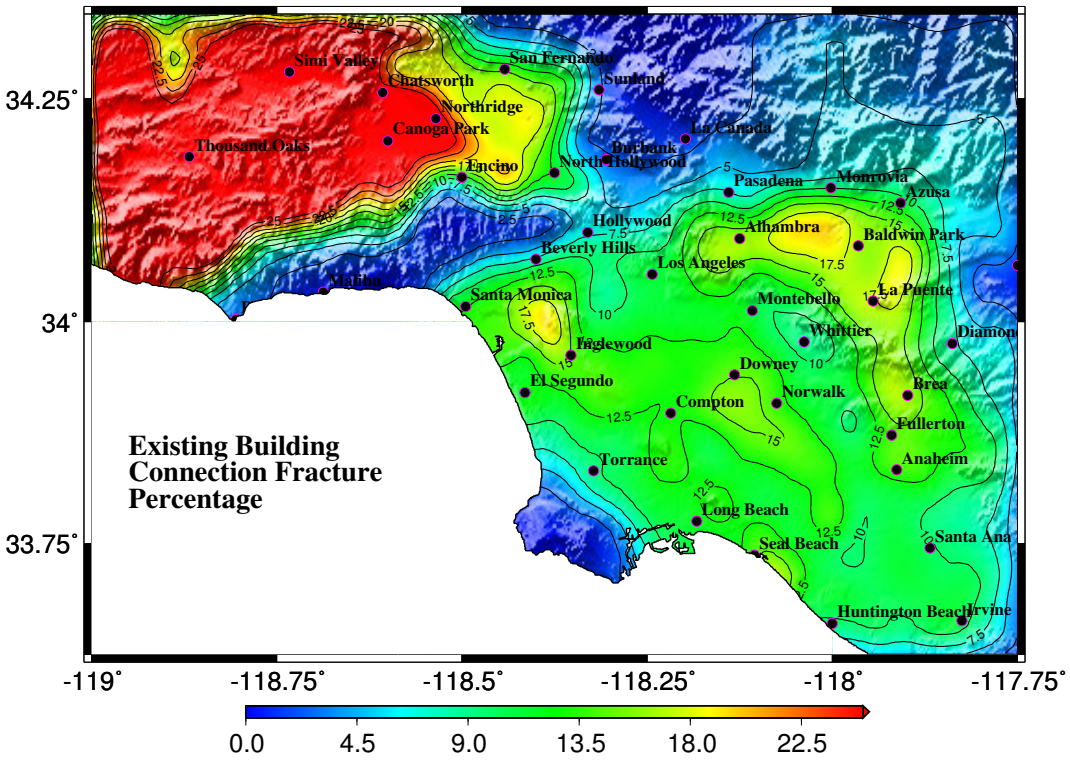

Figure 9.12: M_w7.9 earthquake (north-to-south rupture) on the San Andreas fault – existing building performance: Percentage of connections that fracture (out of a total of 710 connections with the two ends of each moment-frame beam and column defined as connections).

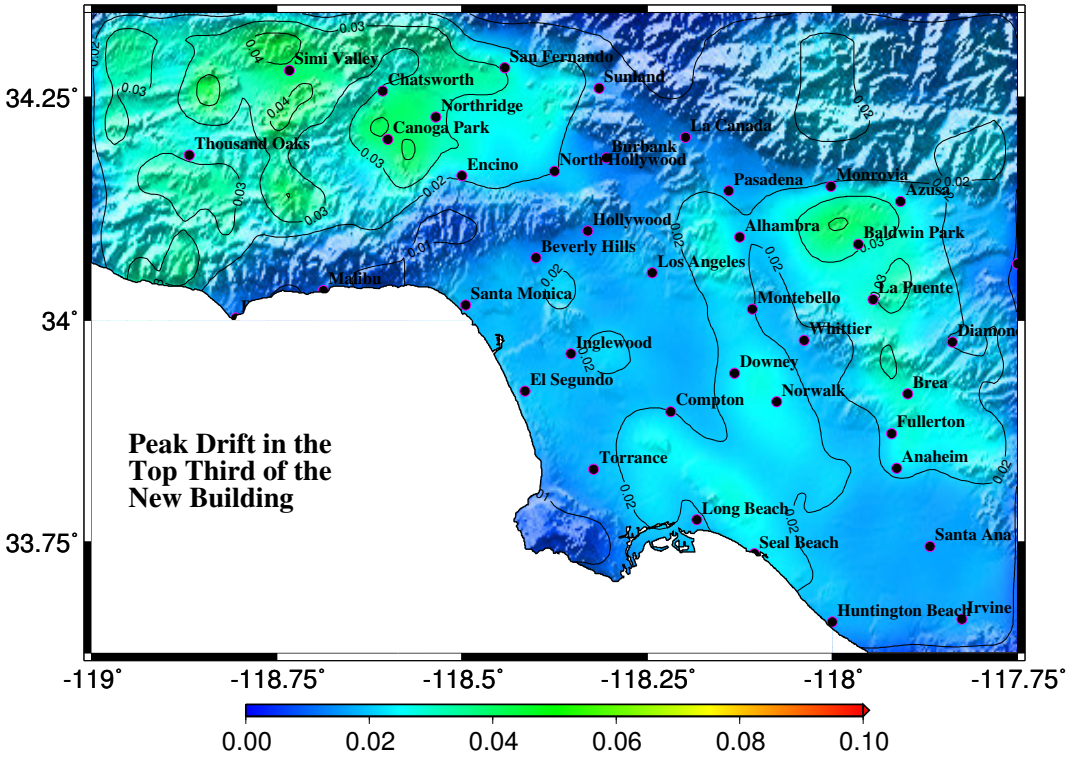

Figure 9.13: $M_w 7.9$ earthquake (north-to-south rupture) on the San Andreas fault – redesigned building performance: Peak drift ratios in the top-third of the building.

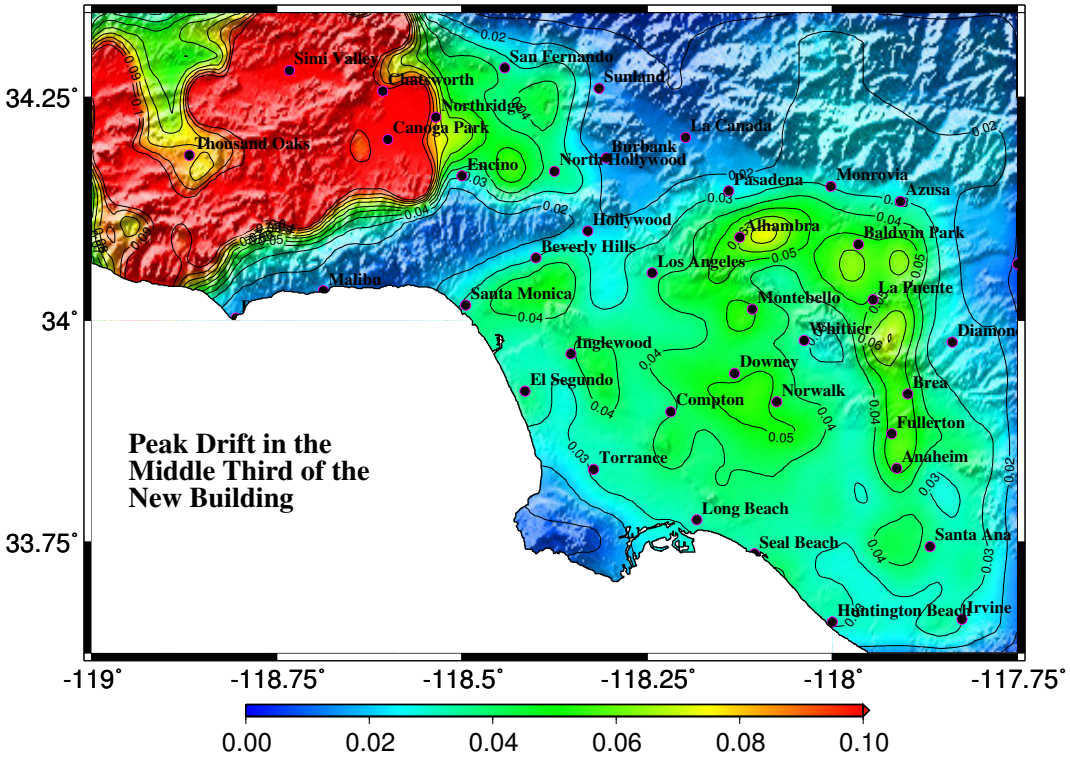

Figure 9.14: $M_w 7.9$ earthquake (north-to-south rupture) on the San Andreas fault – redesigned building performance: Peak drift ratios in the middle-third of the building.

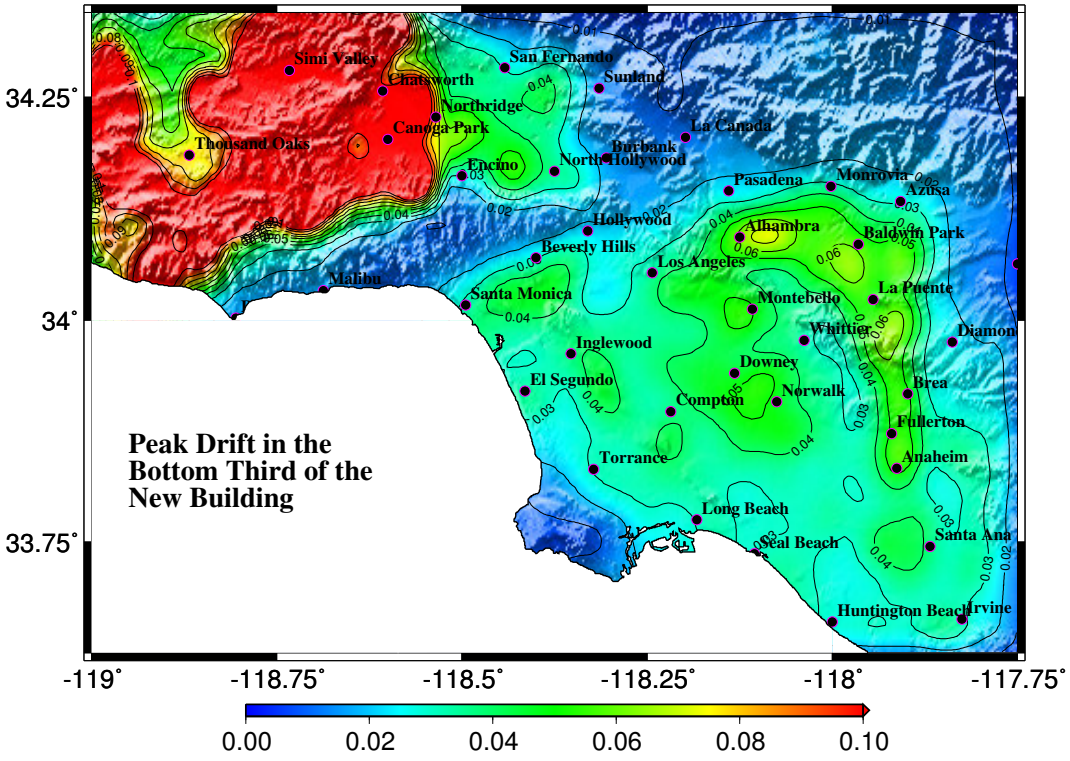

Figure 9.15: $M_w 7.9$ earthquake (north-to-south rupture) on the San Andreas fault – redesigned building performance: Peak drift ratios in the bottom-third of the building.

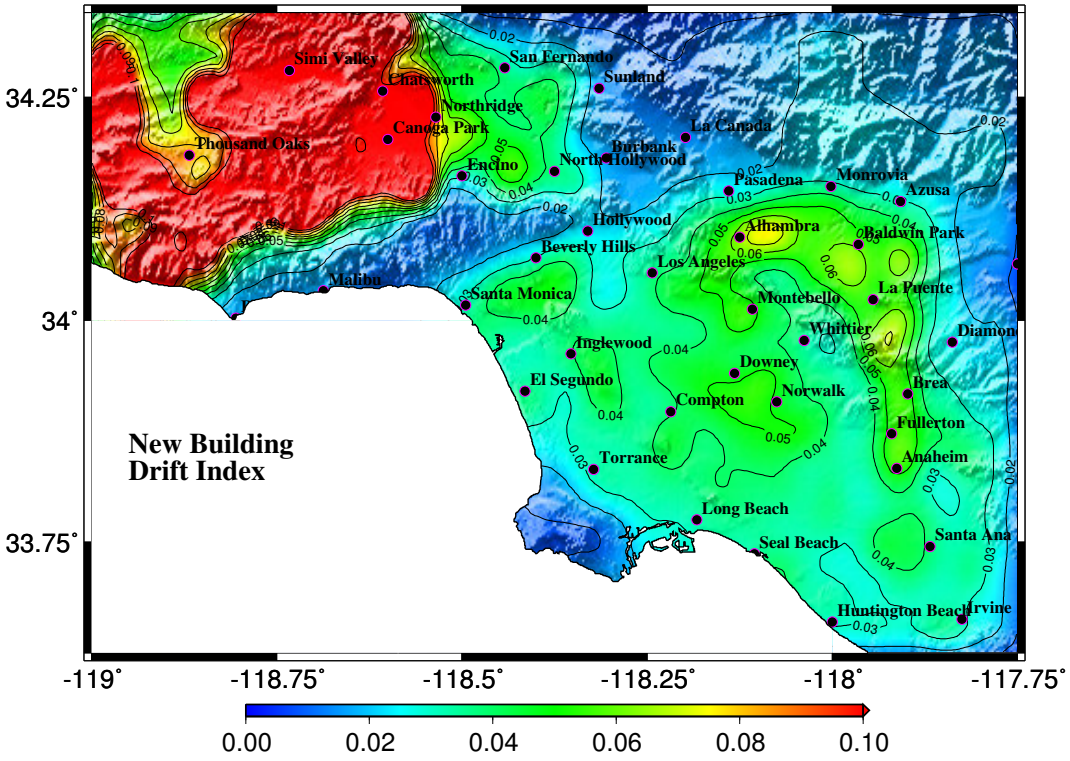

Figure 9.16: $M_w 7.9$ earthquake (north-to-south rupture) on the San Andreas fault – Redesigned Building Performance: Peak drift ratios anywhere in the building.

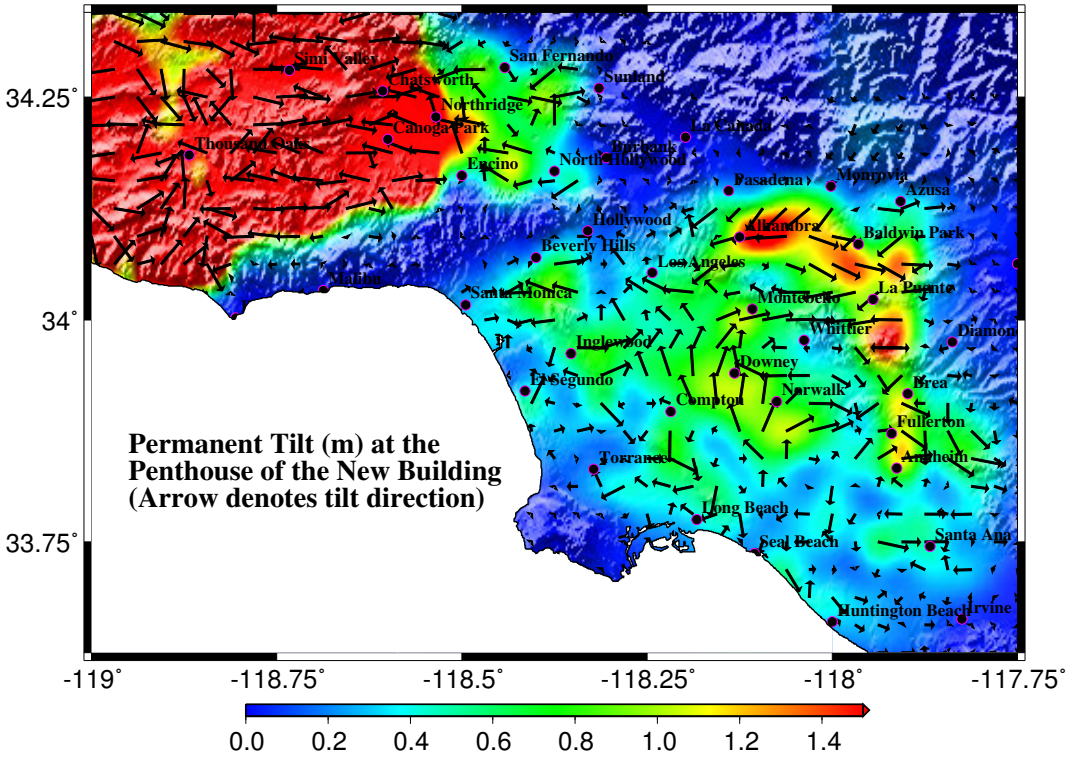

Figure 9.17: M_w7.9 earthquake (north-to-south rupture) on the San Andreas Fault – redesigned building performance: Permanent offset at the penthouse level.

Chapter 10 Scenario 2: South-to-North Rupture of the San Andreas Fault

A natural question to ask is what would happen if the rupture were to proceed from south to north instead of the other way around with the peak slip occurring close to Parkfield. The results of such a scenario (surface slip for which is shown in Figure 10.1), presented in this chapter, indicate that ground shaking would be far less severe. This demonstrates the effect of directivity and slip distribution in dictating the level of ground shaking and the associated damage in buildings.

Shown in Figures 10.2–10.4 and 10.5–10.7 are the peak velocities and displacements, respectively, of the ground motion time-histories lowpass-filtered using a Butterworth filter with a corner period at 2 s. While the San Fernando valley still experiences the most shaking, Santa Monica and, to some extent, Baldwin Park are not too far behind. The peak velocities are of the order of 0.6 m.s^{-1} in the San Fernando valley, 0.5 m.s^{-1} in Santa Monica and El Segundo, and 0.3 m.s^{-1} in the remaining parts of Los Angeles and Orange Counties. The corresponding peak displacements are in the range of 0.5-0.6 m in the San Fernando valley, 0.4-0.5 m in Santa Monica and El Segundo, and 0.3-0.4 m in the remaining parts of Los Angeles and Orange Counties.

The reduced level of shaking is reflected in the results of the building analyses (Figures 10.8–10.13 for the existing building model and Figures 10.14–10.18 for the redesigned building model). Figure 10.13 shows the percentage of connections where fracture occurs in the existing building model. Fracture occurs in 3–7% of the connections in this building when located in the San Fernando valley. About 4–5% of the connections fracture in the building model when it is located in Santa Monica or El Segundo. In most other areas, there is little or no risk associated with moment-frame connection fractures. Figures 10.8 through 10.10 show the peak interstory drift that occurs in the top-third, middle-third, and bottom-third of the existing building, respectively. Figure 10.11 collates these into a single map showing the peak drift occurring in the building. As for rupture scenario 1, the peak interstory drifts in the middle-third and bottom-third of the existing building are greater than the top-third which indicates that the damage is localized in the lower floors. Peak interstory drifts beyond 0.06 are indicative of severe damage, while drifts below 0.01 are indicative of minimal damage not requiring any repairs. Peak drifts are in the neighborhood of 0.03 in the San Fernando valley, Santa Monica, El Segundo and Baldwin Park. Peak drifts in most other areas are less than 0.02. Plotted on Figure 10.12 are the magnitude and direction of the permanent offset of the existing building model at the penthouse level following the earthquake. Once again, the length of the arrow is proportional to the magnitude. There is negligible permanent tilting of the existing building model in the entire domain of the analysis. This is dramatically different from scenario 1 results once again revealing the role of directivity and slip distribution in dictating the level of damage.

The performance of the newly designed 18-story steel building is slightly better than the existing building for the entire region. Figures 10.14 through 10.16 show the peak interstory drift that occurs in the top-third, middle-third, and bottom-third of the redesigned building, respectively. Figure 10.17 collates these into a single map showing the peak drift occurring in the building. Peak drifts are in the neighborhood of 0.02–0.03 when the building model is located in the San Fernando valley, Santa Monica, El Segundo and Baldwin Park. Building peak drifts in most other areas are in the neighborhood of 0.01. Plotted on Figure 10.18 are the magnitude and direction of the permanent offset of the redesigned building model at the penthouse level following the earthquake.

To summarize, the results for both the existing and redesigned building models indicate that there is no significant danger of collapse. However, damage would still be significant enough to warrant building closures and compromise life safety in some instances.

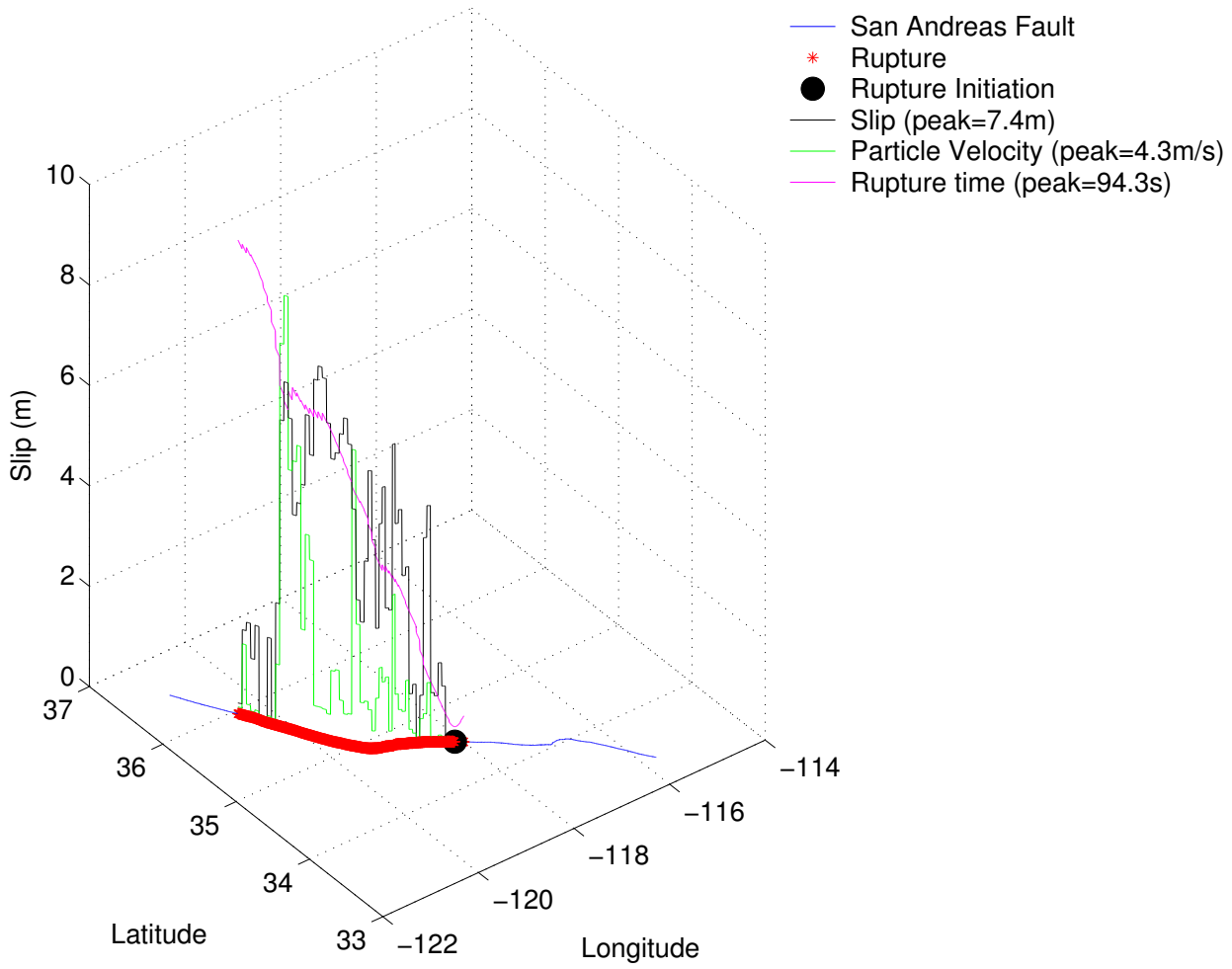

Figure 10.1: Surface slip, particle velocity, and rupture time, for the simulated magnitude 7.9 earthquake on the San Andreas fault – south-to-north rupture

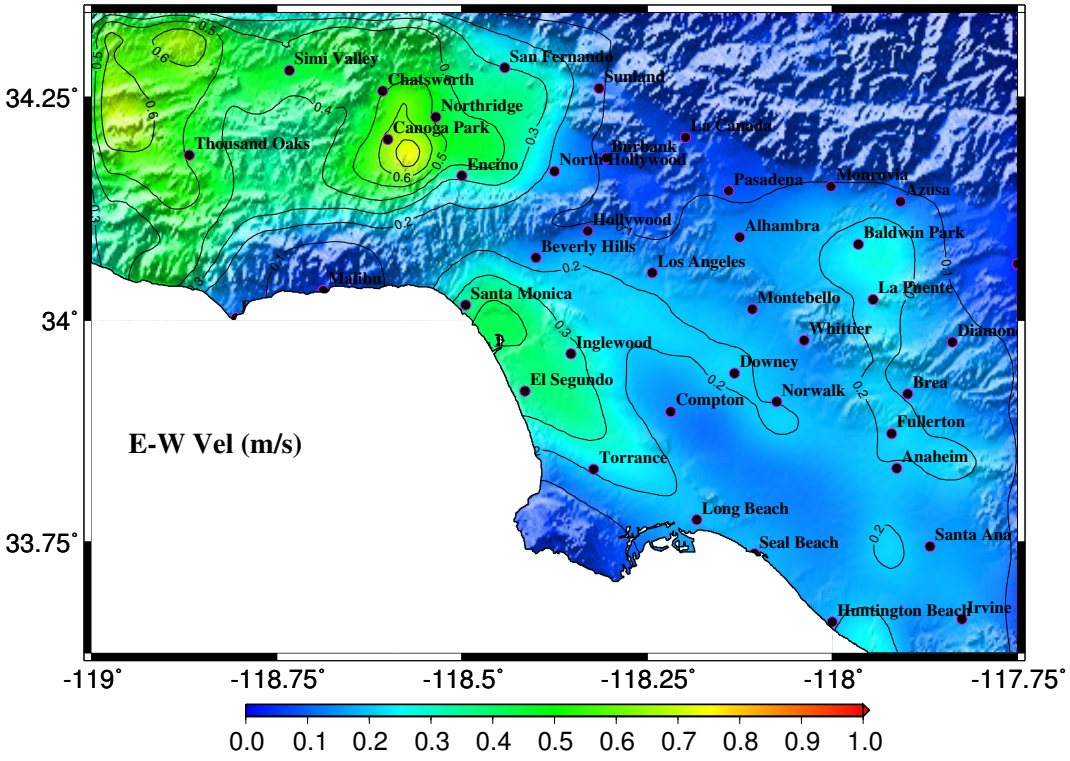

Figure 10.2: M_w7.9 earthquake (south-to-north rupture) on the San Andreas fault – ground shaking: Map of peak velocities (east component).

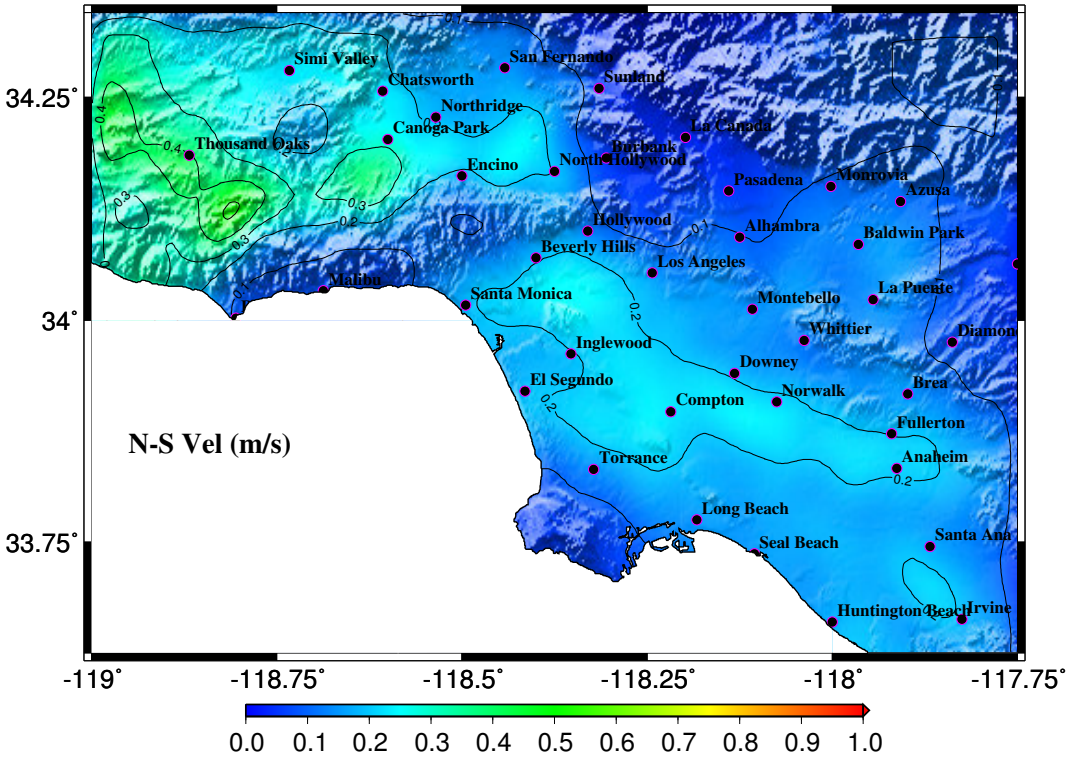

Figure 10.3: M_w7.9 earthquake (south-to-north rupture) on the San Andreas fault – ground shaking: Map of peak velocities (north component).

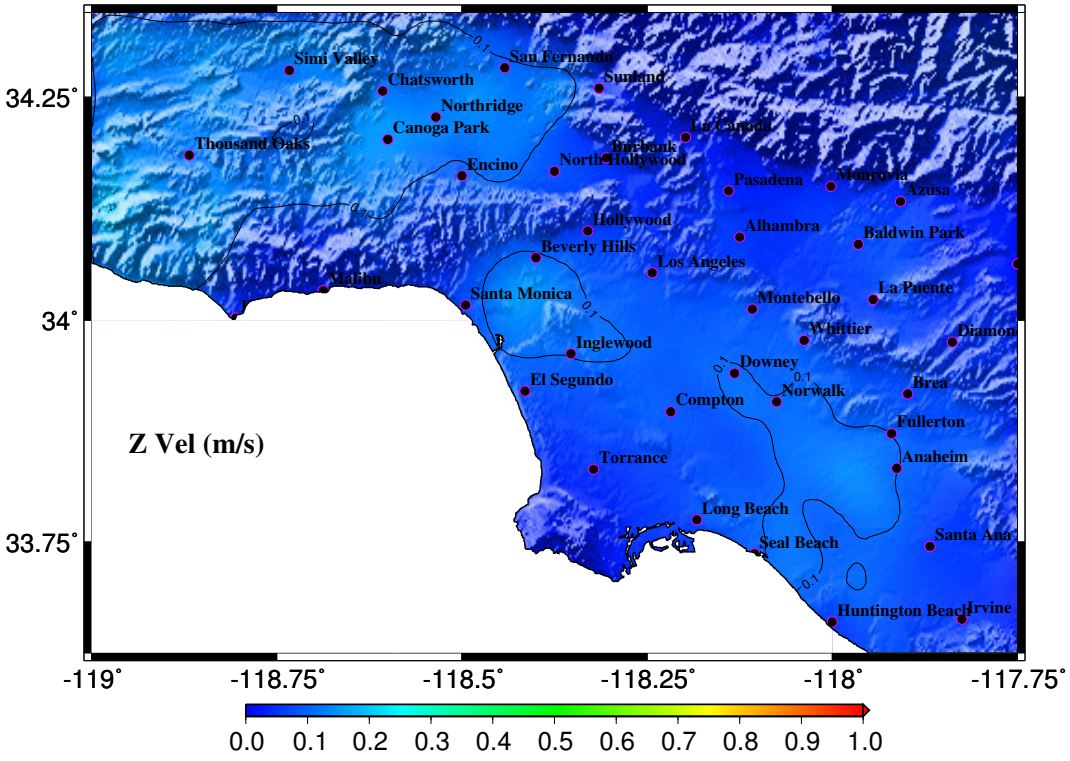

Figure 10.4: M_w7.9 earthquake (south-to-north rupture) on the San Andreas fault – ground shaking: Map of peak velocities (vertical component).

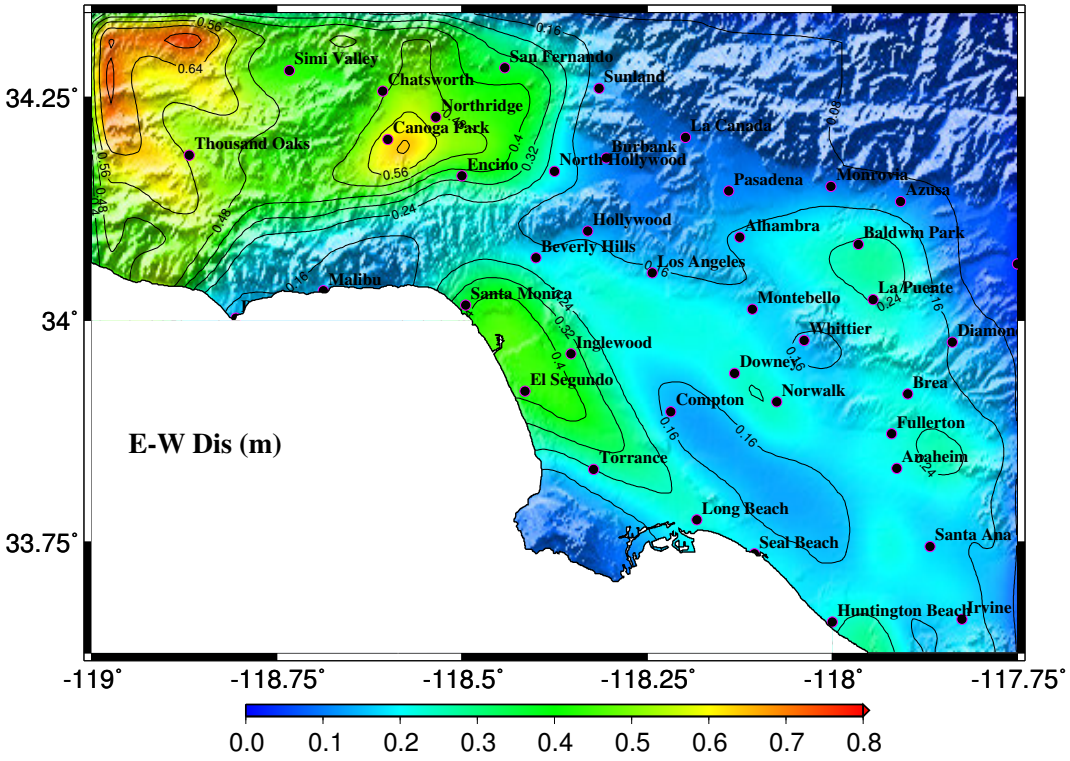

Figure 10.5: M_w7.9 earthquake (south-to-north rupture) on the San Andreas fault – ground shaking: Map of peak displacements (east component).

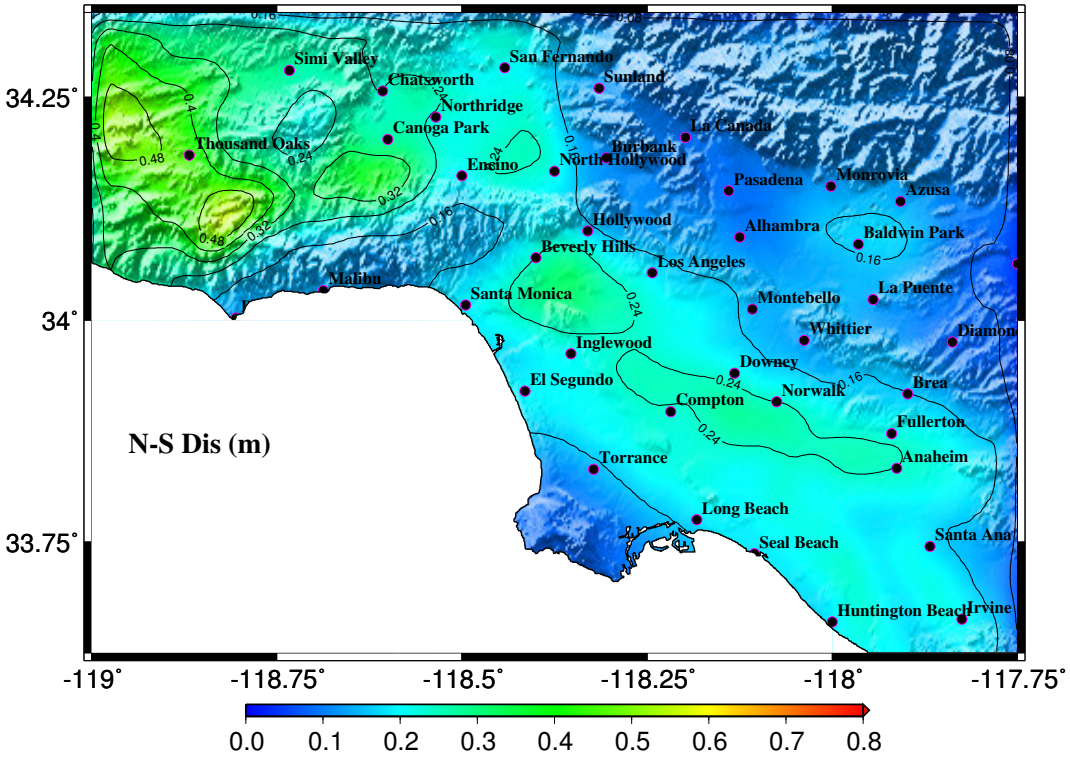

Figure 10.6: M_w7.9 earthquake (south-to-north rupture) on the San Andreas fault – ground shaking: Map of peak displacements (north component).

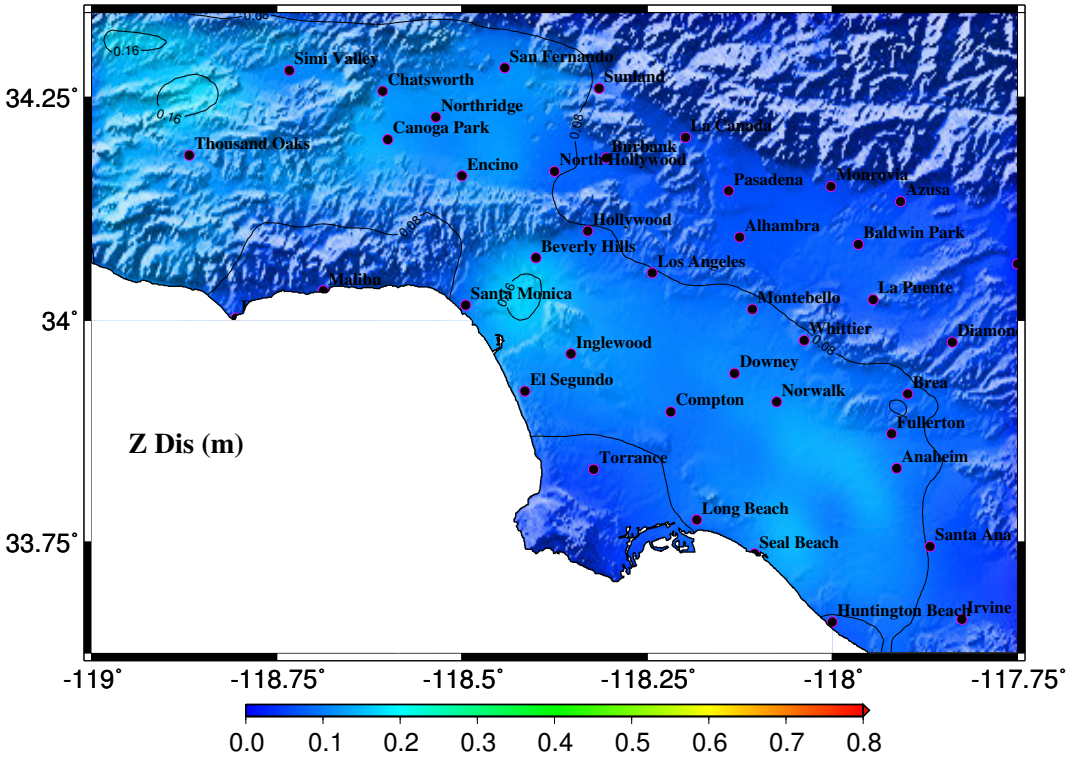

Figure 10.7: M_w7.9 earthquake (south-to-north rupture) on the San Andreas fault – ground shaking: Map of peak displacements (vertical component).

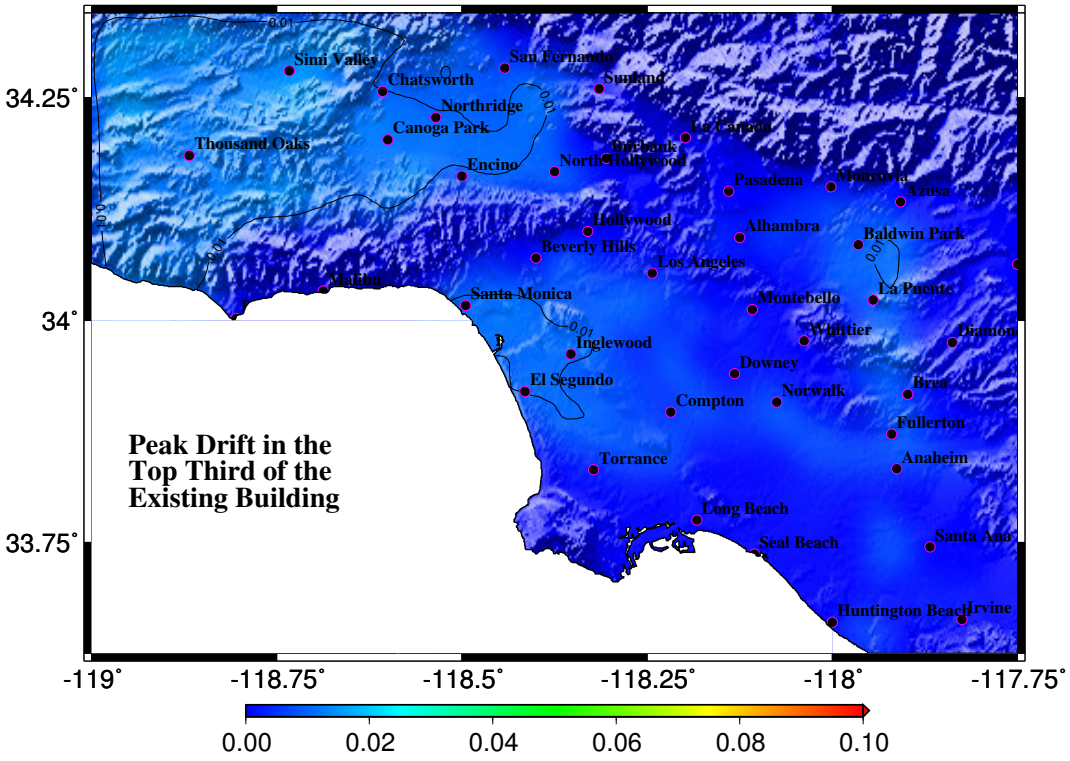

Figure 10.8: $M_w 7.9$ earthquake (south-to-north rupture) on the San Andreas fault – existing building performance: Peak drift ratios in the top-third of the building.

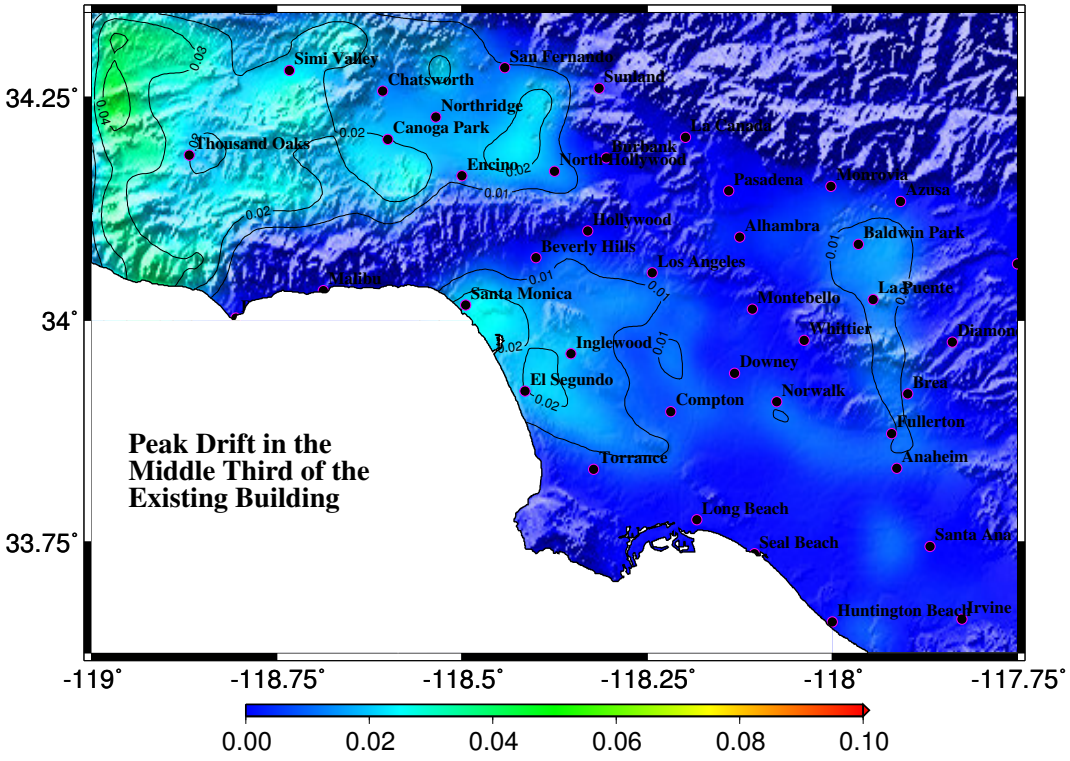

Figure 10.9: $M_w 7.9$ earthquake (south-to-north rupture) on the San Andreas fault – existing building performance: Peak drift ratios in the middle-third of the building.

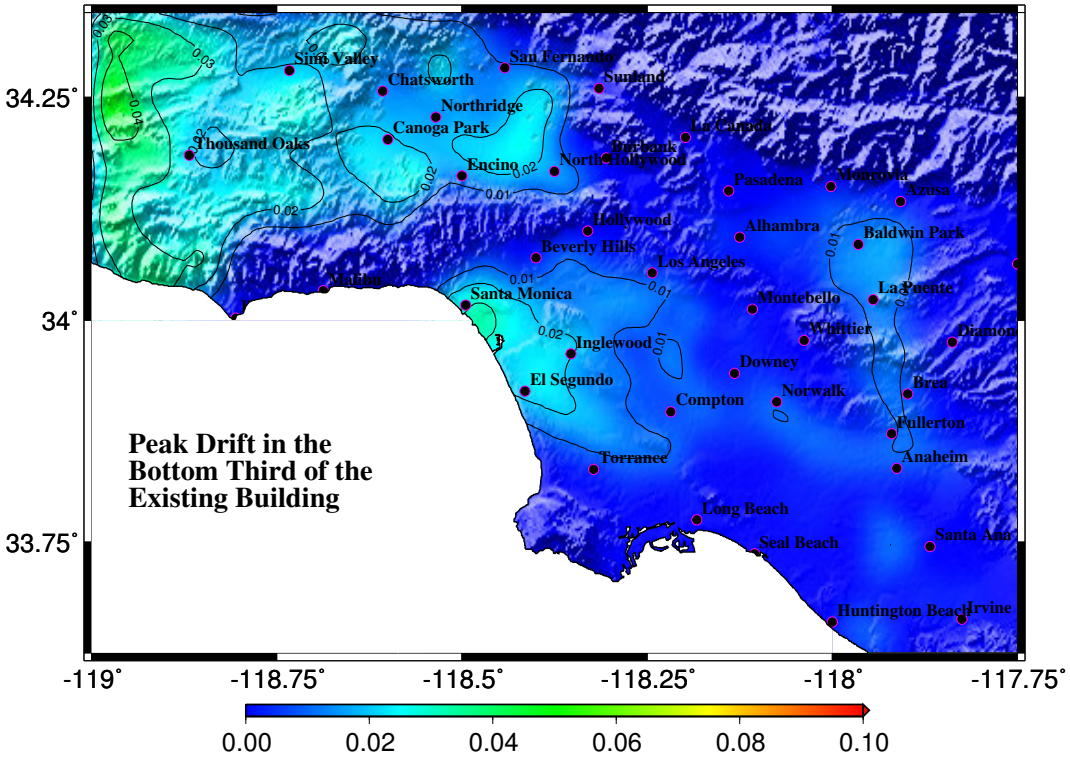

Figure 10.10: $M_w 7.9$ earthquake (south-to-north rupture) on the San Andreas fault – existing building performance: Peak drift ratios in the bottom-third of the building.

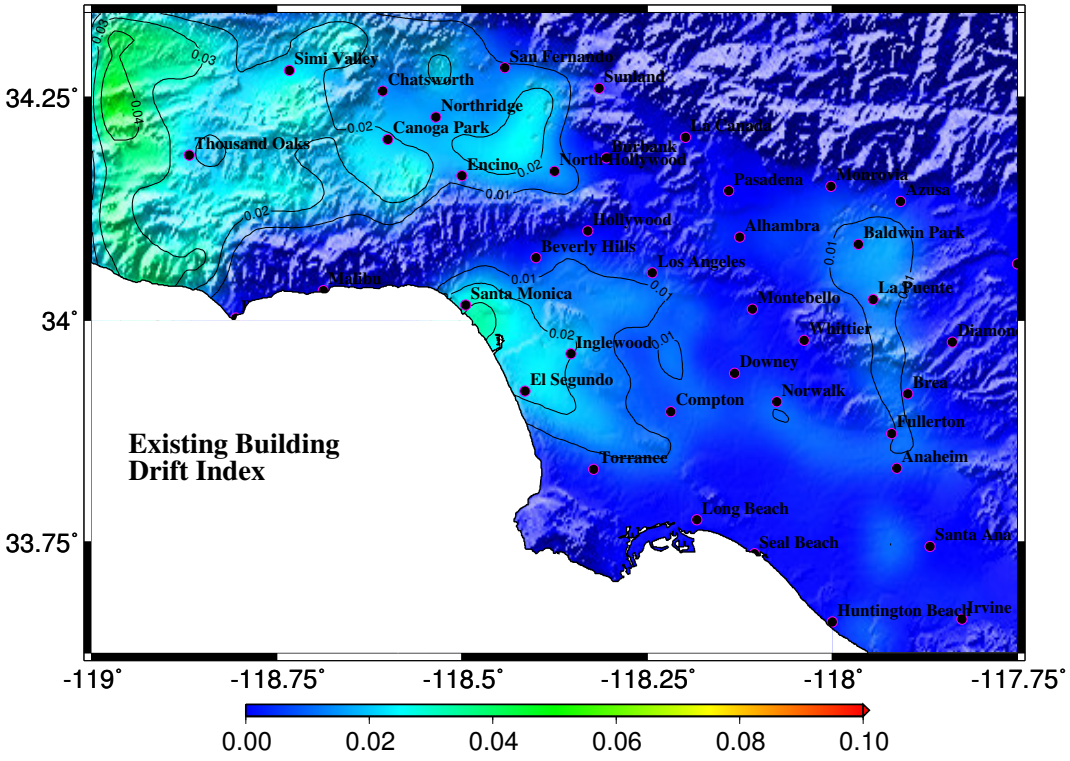

Figure 10.11: $M_w 7.9$ earthquake (south-to-north rupture) on the San Andreas fault – existing building performance: Peak drift ratios anywhere in the building.

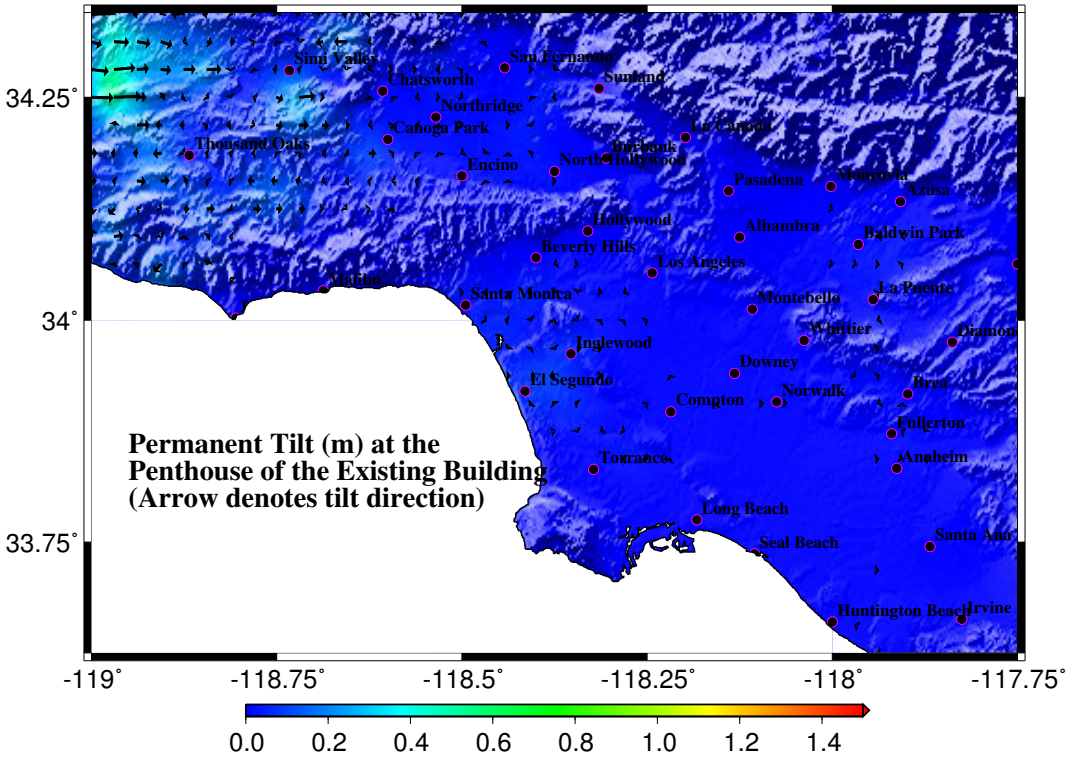

Figure 10.12: $M_w 7.9$ earthquake (south-to-north rupture) on the San Andreas fault – existing building performance: Permanent offset at the penthouse level.

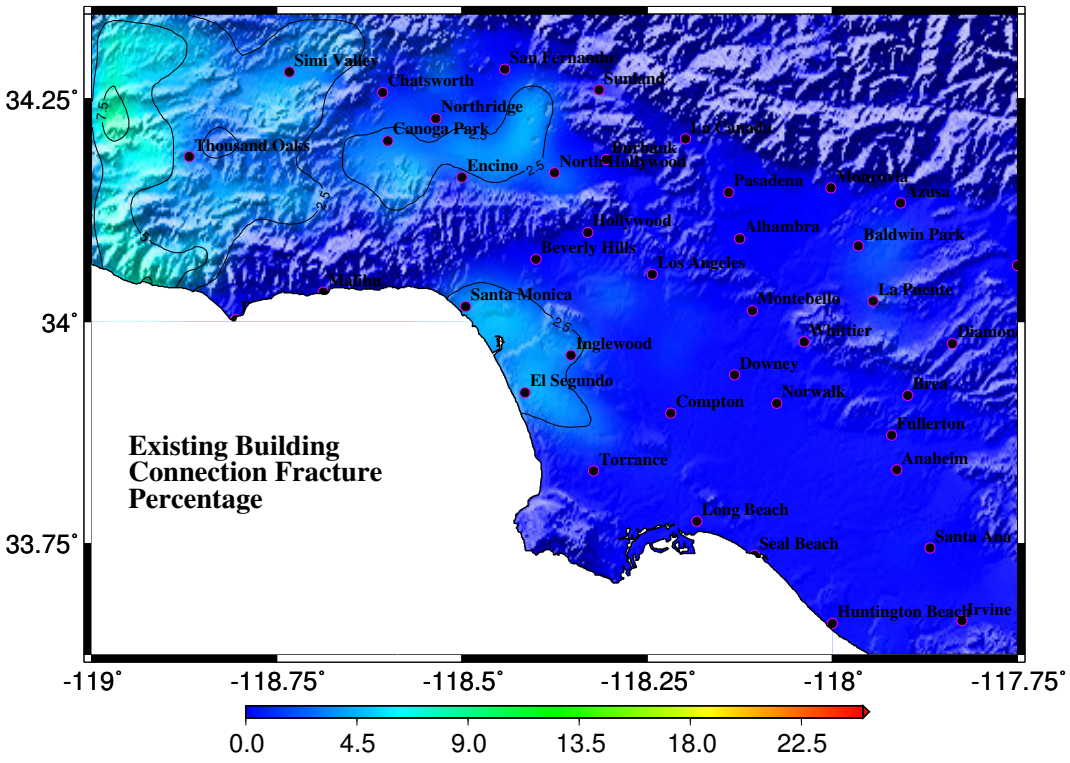

Figure 10.13: $M_w 7.9$ earthquake (south-to-north rupture) on the San Andreas fault – existing building performance: Percentage of connections that fracture (out of a total of 710 connections with the two ends of each moment-frame beam and column defined as connections).

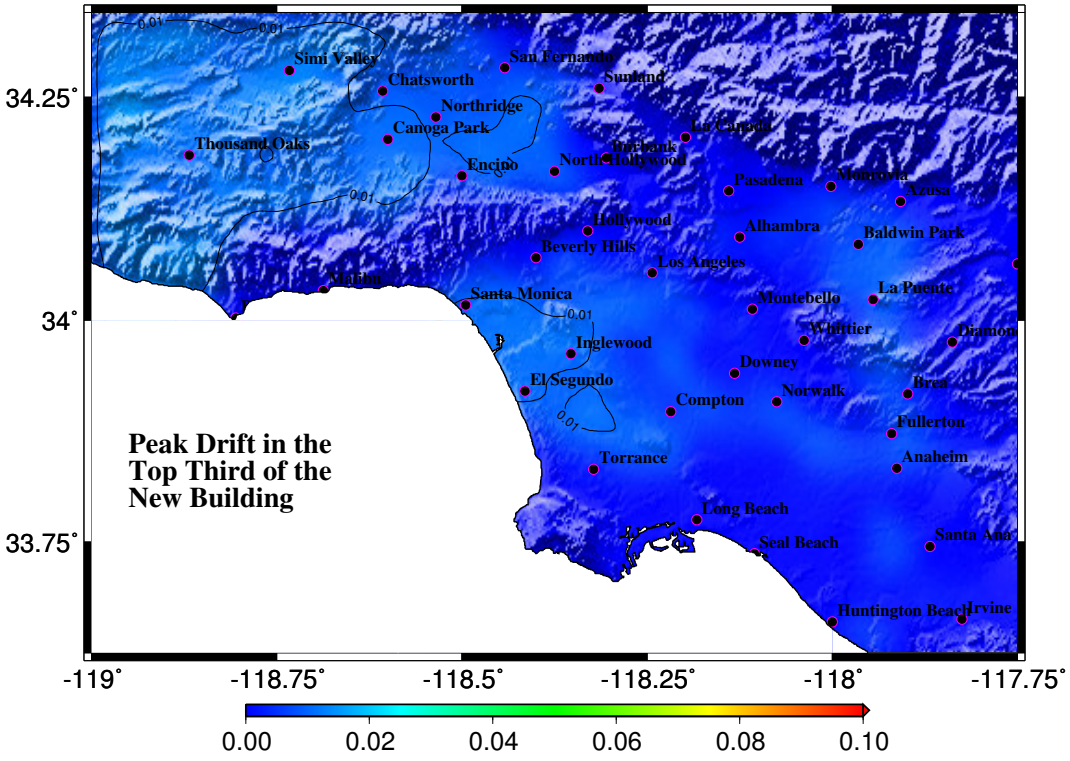

Figure 10.14: $M_w 7.9$ earthquake (south-to-north rupture) on the San Andreas fault – redesigned building performance: Peak drift ratios in the top-third of the building.

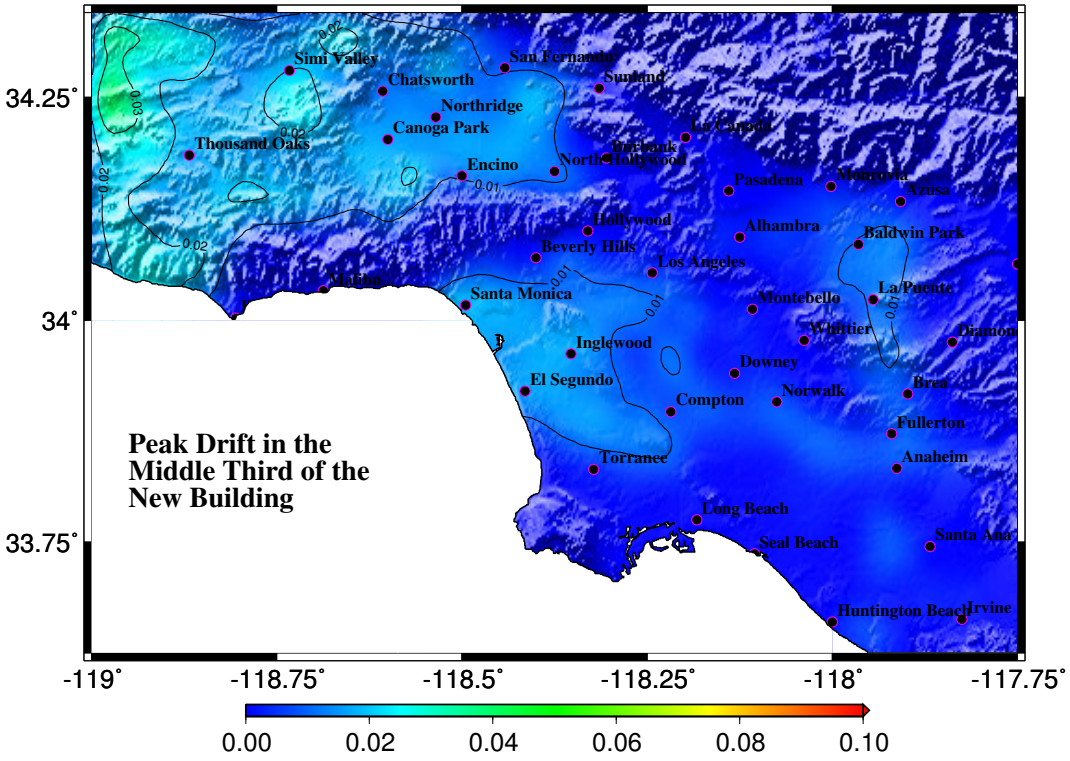

Figure 10.15: $M_w 7.9$ earthquake (south-to-north rupture) on the San Andreas fault – redesigned building performance: Peak drift ratios in the middle-third of the building.

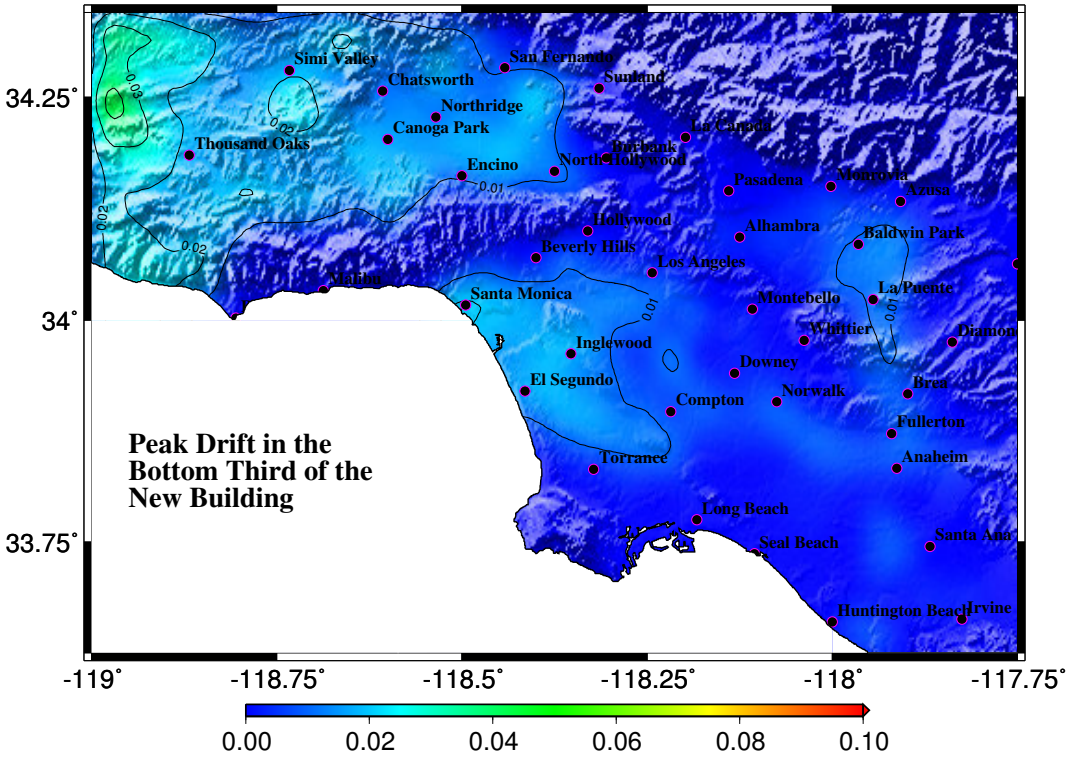

Figure 10.16: $M_w 7.9$ earthquake (south-to-north rupture) on the San Andreas fault – redesigned building performance: Peak drift ratios in the bottom-third of the building.

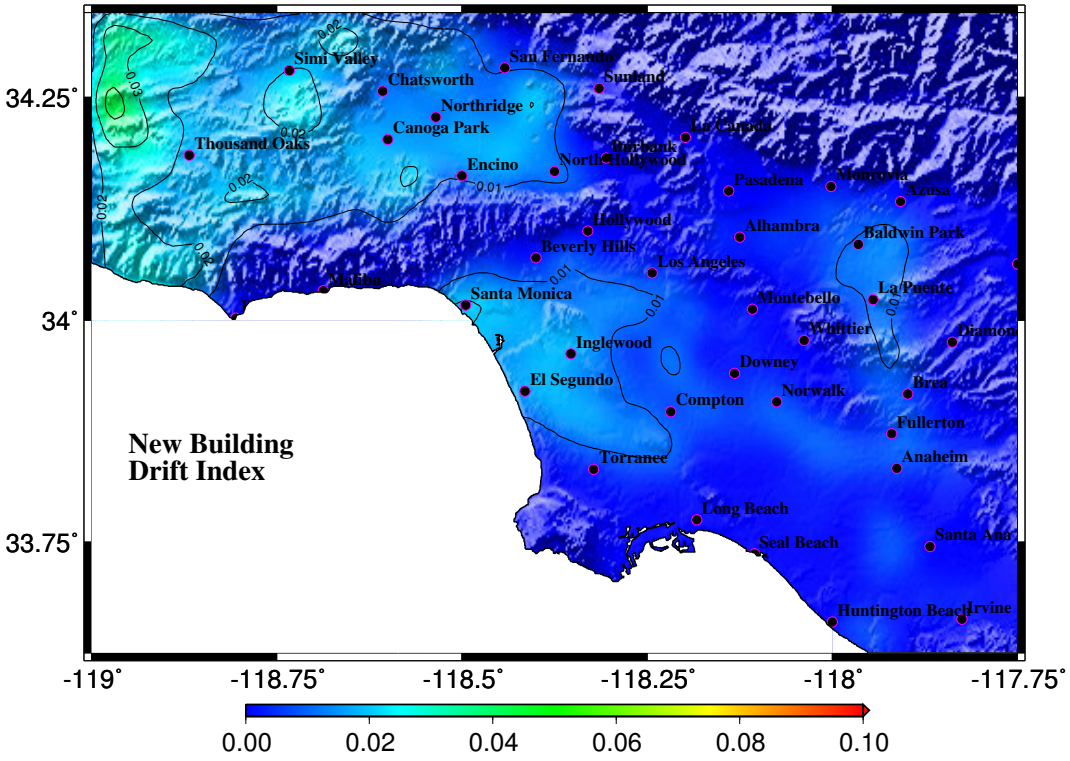

Figure 10.17: $M_w 7.9$ earthquake (south-to-north rupture) on the San Andreas fault – redesigned building performance: Peak drift ratios anywhere in the building.

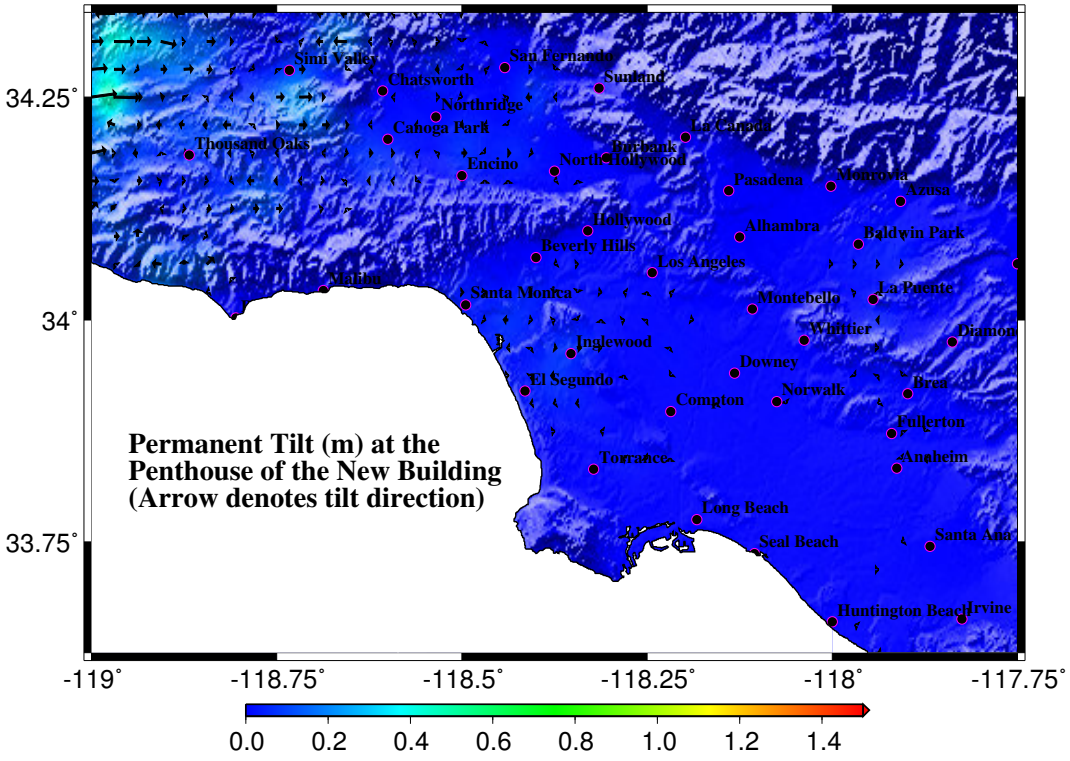

Figure 10.18: $M_w 7.9$ earthquake (south-to-north rupture) on the San Andreas fault – redesigned building performance: Permanent offset at the penthouse level.

Chapter 11 Conclusions

Comprehensive end-to-end simulations of two magnitude 7.9 earthquakes on the San Andreas fault and the resulting damage on models of an existing and a redesigned 18-story steel moment-frame building have been performed. The 2002 Denali earthquake finite-source model has been mapped to the San Andreas fault and ground motions in the southern California region are computed at 636 chosen sites for two rupture scenarios – (a) north to south with rupture initiating at Parkfield; and (b) south to north with rupture terminating at Parkfield. 3-D computer models of an existing building in Woodland Hills that got damaged during the 1994 Northridge earthquake and the same building redesigned according to the 1997 Uniform Building Code are analyzed for the three-component ground motion (lowpass-filtered using a Butterworth filter with a corner period of 2 s) at each of the 636 considered sites. Performance of the building models has been classified primarily based on the peak interstory drift ratio.

The following are the conclusions of this study:

1. For the north-to-south rupture scenario, the peak ground velocity is of the order of 2 m.s^{-1} in the San Fernando Valley and 1 m.s^{-1} in the Los Angeles basin, while the corresponding numbers for the south-to-north rupture scenario are 0.6 m.s^{-1} and 0.4 m.s^{-1}, respectively.

2. For the north-to-south rupture scenario, the peak ground displacement is of the order of 2 m in the San Fernando Valley and 1 m in the Los Angeles basin, while the corresponding numbers for the south-to-north rupture scenario are 0.6 m and 0.4 m respectively. The stark contrast between the ground motions in the two cases is an illustration of the effects of directivity and slip distribution in dictating the intensity of ground motion.

3. Under the ground motion from the north-to-south rupture, peak drifts in the existing building model far exceed 0.10 in the San Fernando Valley, Santa Monica and West Los Angeles, Baldwin Park and neighboring cities, Compton and neighboring cities, and Seal Beach and neighboring cities. Peak drifts are in the 0.06–0.08 range in Huntington Beach, Santa Ana, Anaheim and neighboring cities, while the numbers are in the 0.04–0.06 range for the remaining areas including downtown Los Angeles. Peak drifts exceeding 0.10 are indicative of probable collapse, while drifts exceeding 0.06 are indicative of severe damage. Peak drifts in excess of 0.025 could compromise life-safety.

4. The results for the redesigned building are better than the existing building. However, the peak drifts in many areas in the San Fernando valley still exceed 0.10, and they are in the range of 0.04–0.06 for most cities in the Los Angeles basin. While this may not conclusively be indicative of collapse, it certainly points to significant damage and may result in building closures.

5. Under the ground motion from the south-to-north rupture, the peak drifts in existing and redesigned building models are in the range of 0.02–0.04, indicating that there is no significant danger of collapse. However, this is indicative of damage significant enough to warrant building closures and compromise life safety in some instances.

Finally, these conclusions are particular to the two 18-story steel moment-frame buildings considered in the study. Other buildings with varied configuration, constructed with other materials, and having distinct frequency content could have damage patterns quite different from the results presented here. Having said this, the fact remains that the potential for a big earthquake with a large amount of slip on the San Andreas fault exists, and with the current state

of knowledge of the southern Californian Earth structure, this study indicates that serious damage occurs in these two 18-story steel moment-frame buildings in at least one of the plausible scenarios.

Chapter 12 Future Research

The field of end-to-end simulations is still nascent in its development and is the wave of the future. The advent of parallel computing as a seismological tool in the last decade has revolutionized the field. As more data becomes available, simulations can be validated and improved tremendously. In the coming decade, it is inevitable that this field will take center-stage in the assessment of infrastructure in the United States and elsewhere.

Future work in this area could involve one or many of the following aspects:

1. Improving the source models: This requires data gathering for earthquakes of various magnitudes on the faults of interest in a given region. It is crucial to not only have a greater number of data sets, but also have a variety of data types. Combinations of GPS, strong motion and teleseismic data sets yield the best results in terms of characterizing the source.

2. This work needs to be extended to other faults in southern California so that a broad picture of risk associated with regional earthquakes emerges. Some important faults in the region which require immediate attention are the Newport-Inglewood and Santa Monica-Hollywood-Raymond fault systems in addition to blind-thrust faults such as the Puente Hills fault under downtown Los Angeles.

3. The Earth velocity model needs to be improved to enable reliable simulation of broad-band ground motion. This is especially critical for the assessment of short structures (including wood-frame structures). This requires the procurement of large amounts of data from future earthquakes.

4. Validation of the numerical procedures, both seismological and structural, require ground-motion and building-motion and building-damage data from future earthquakes. Items 1 through 4 call for increased seismic instrumentation in the region including extensive instrumentation of building and other civil structures.

5. This work needs to be extended to other types of buildings. These should be classified based on type of lateral system, material (reinforced concrete, steel, wood etc.), geometry (height, plan), and function (residential, commercial, etc.).

6. Improving structural component and assembly modeling . This involves eliminating some of the limitations of this study described in Chapter 4 including, but not limited to, soil-structure interaction, column splices, column local flange buckling, composite action of beams, stiffness from partitions and elevator/stair enclosures, etc.

7. Including the top-soil layer in the ground motion simulation.

8. Performing similar analyses in other regions in the world. To start with, this involves instrumenting the region, recording data from regional and distant earthquakes, and creating and validating regional Earth models. Once the computational infrastructure is ready, the procedures described in this study can be adopted to perform end-to-end simulations.

Appendix A Section Database

The sizes of box-sections used for beams and columns in the redesigned building (see Appendix C for beam and column sizes) are provided in this appendix. The sizes of wide-flange sections shown in Appendices B and C are taken from the AISC LRFD manual of steel construction [54].

Section Designation	H (m)	B (m)	T_f (m)	T_w (m)
B14x14x171	0.350	0.350	0.025	0.025
B16x16x227	0.400	0.400	0.029	0.029
B18x18x282	0.450	0.450	0.032	0.032
B20x20x352	0.500	0.500	0.036	0.036
B22x22x430	0.550	0.550	0.040	0.040
B30x24x668	0.750	0.600	0.045	0.055

Appendix B Existing Building Frame Elevations and Beam and Column Sizes

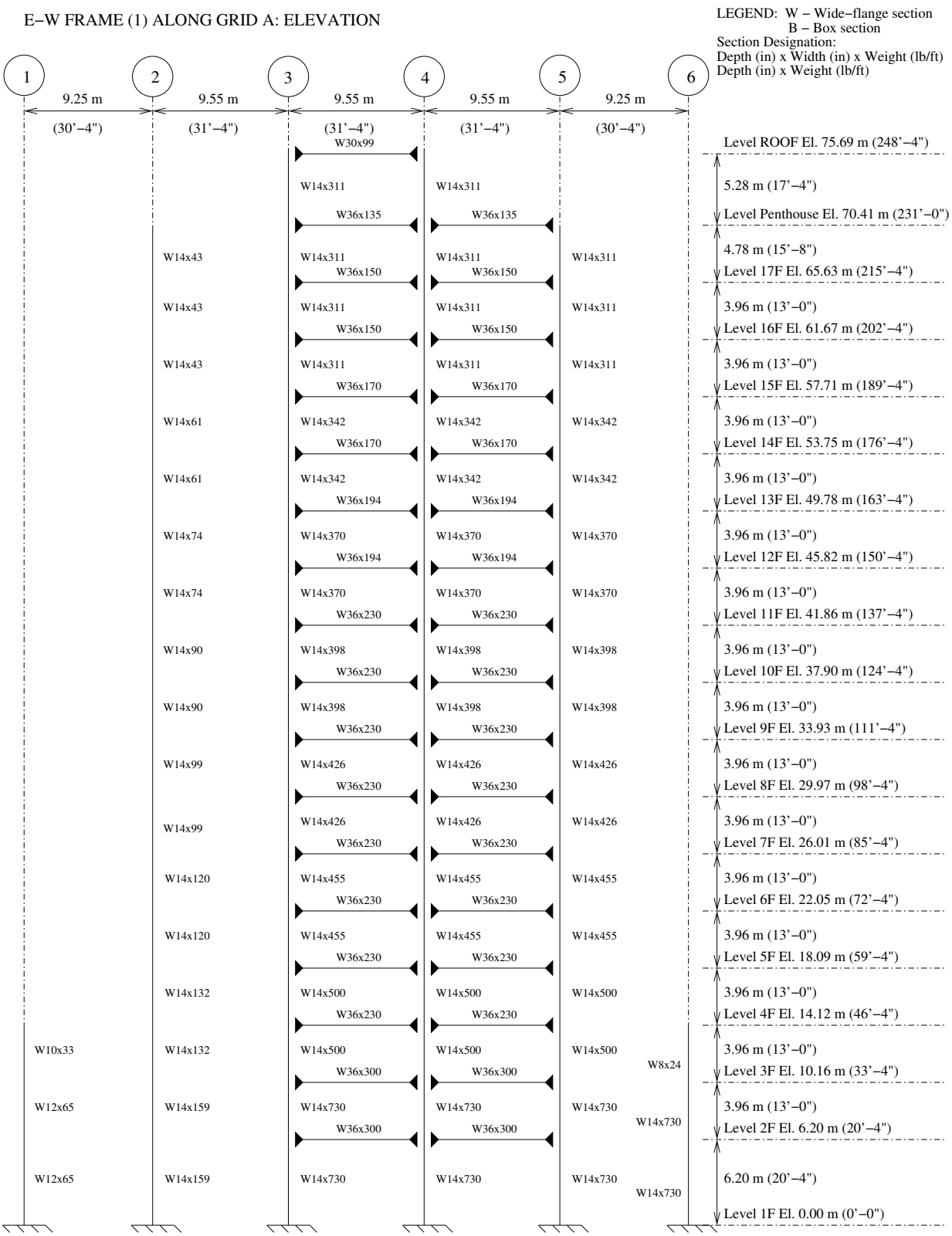

Figure B.1: Frame 1 elevation: Existing building

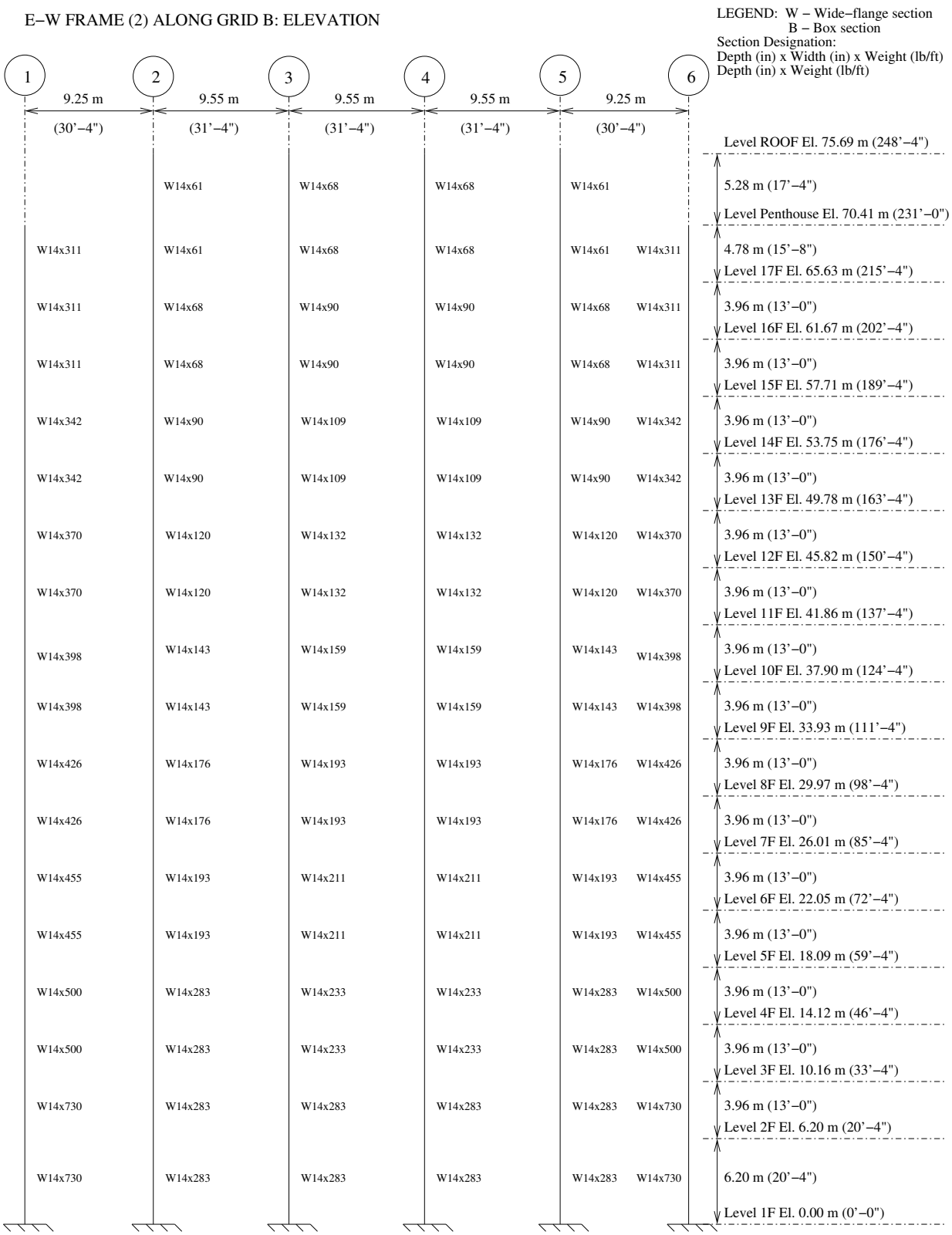

Figure B.2: Frame 2 elevation: Existing building

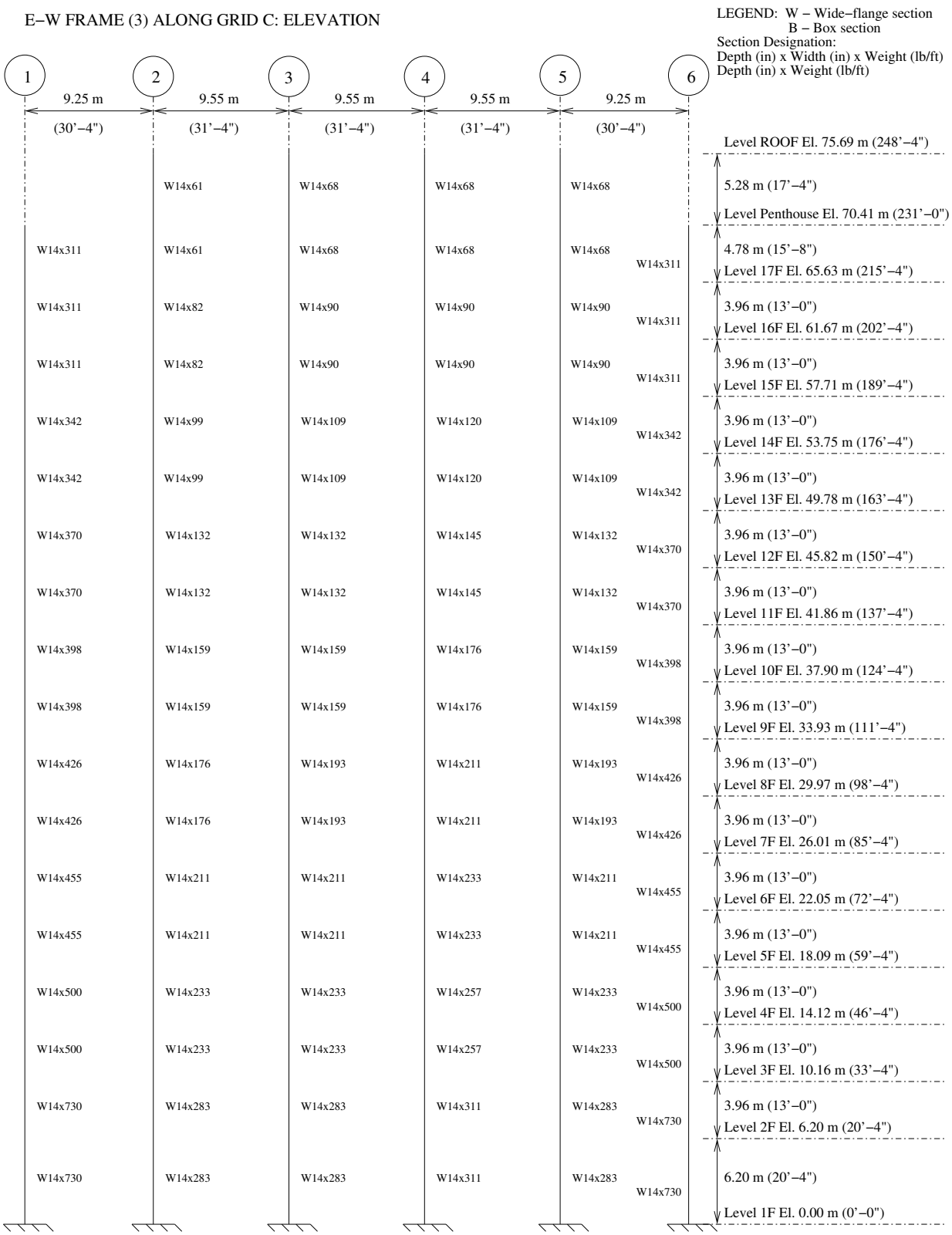

Figure B.3: Frame 3 elevation: Existing building

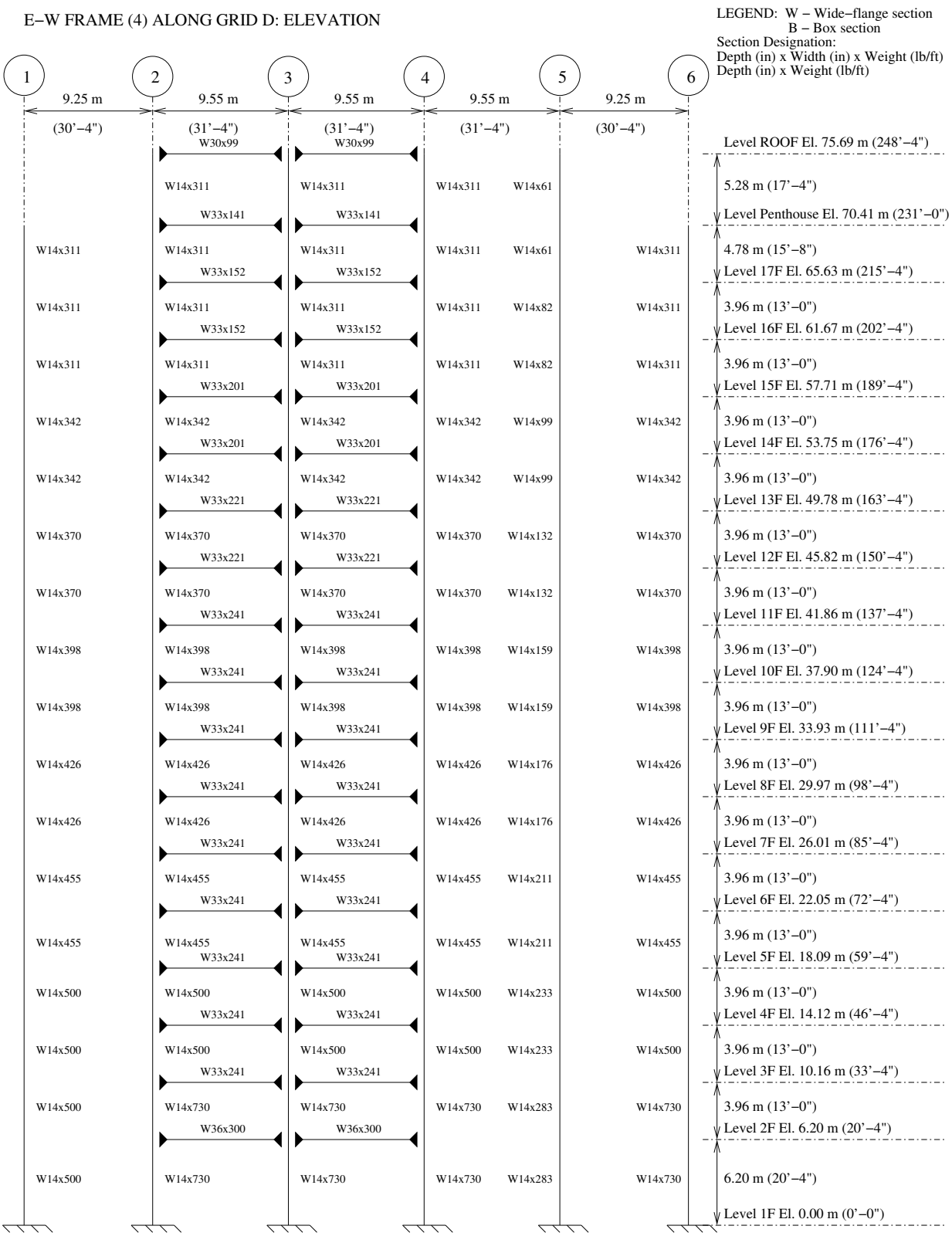

Figure B.4: Frame 4 elevation: Existing building

Figure B.5: Frame 5 elevation: Existing building

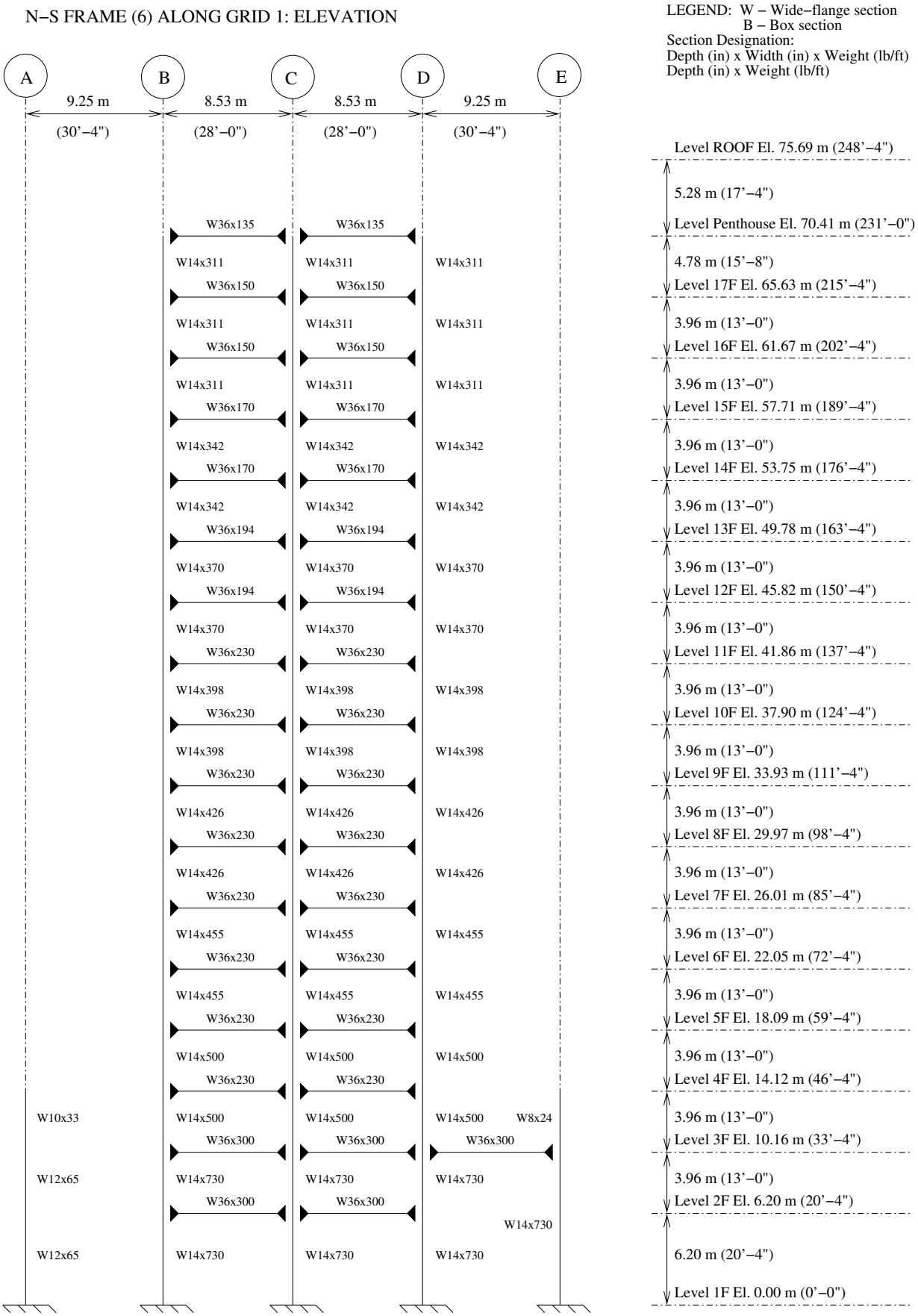

Figure B.6: Frame 6 elevation: Existing building

Appendix C Redesigned Building Frame Elevations and Beam and Column Sizes

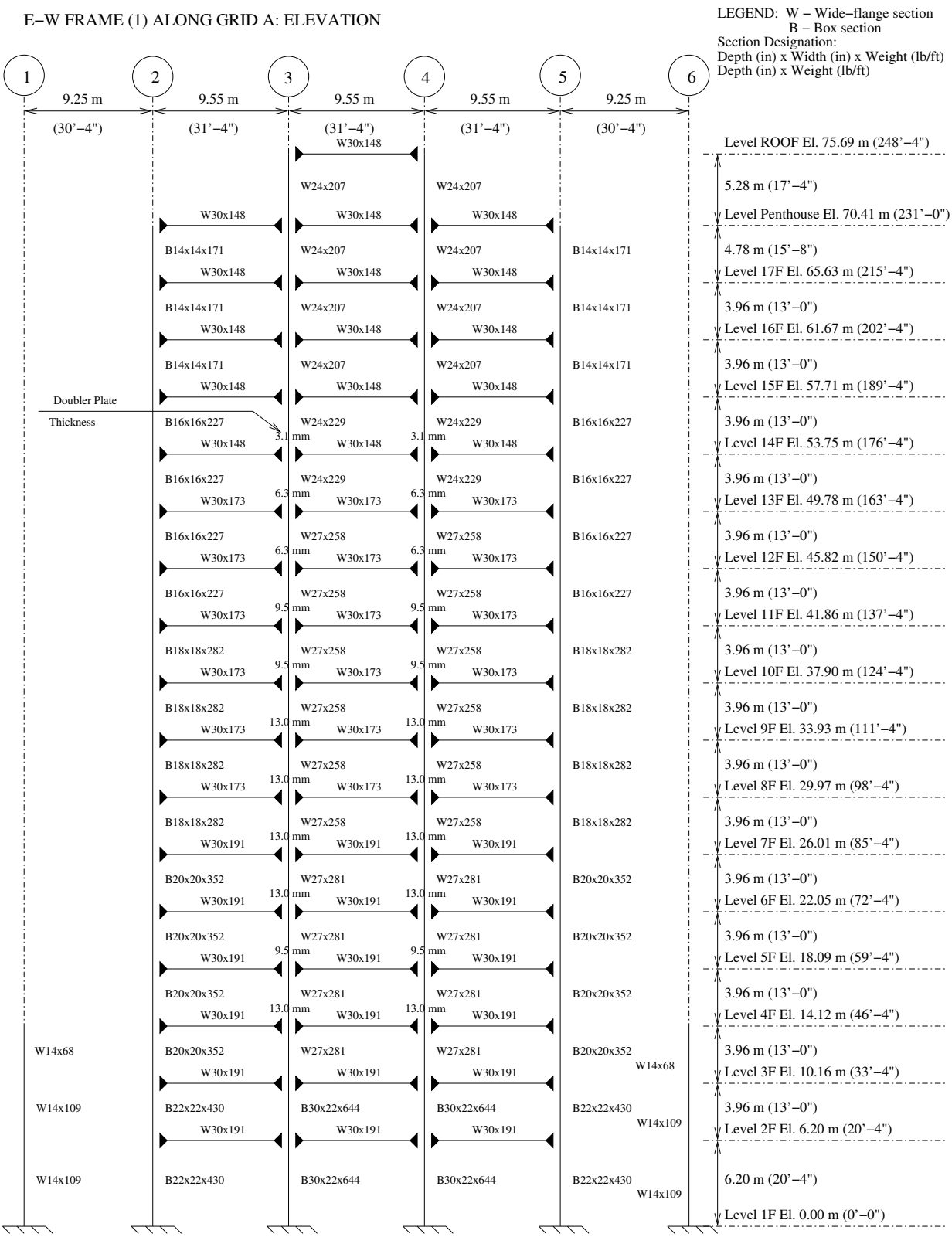

Figure C.1: Frame 1 elevation: Redesigned building

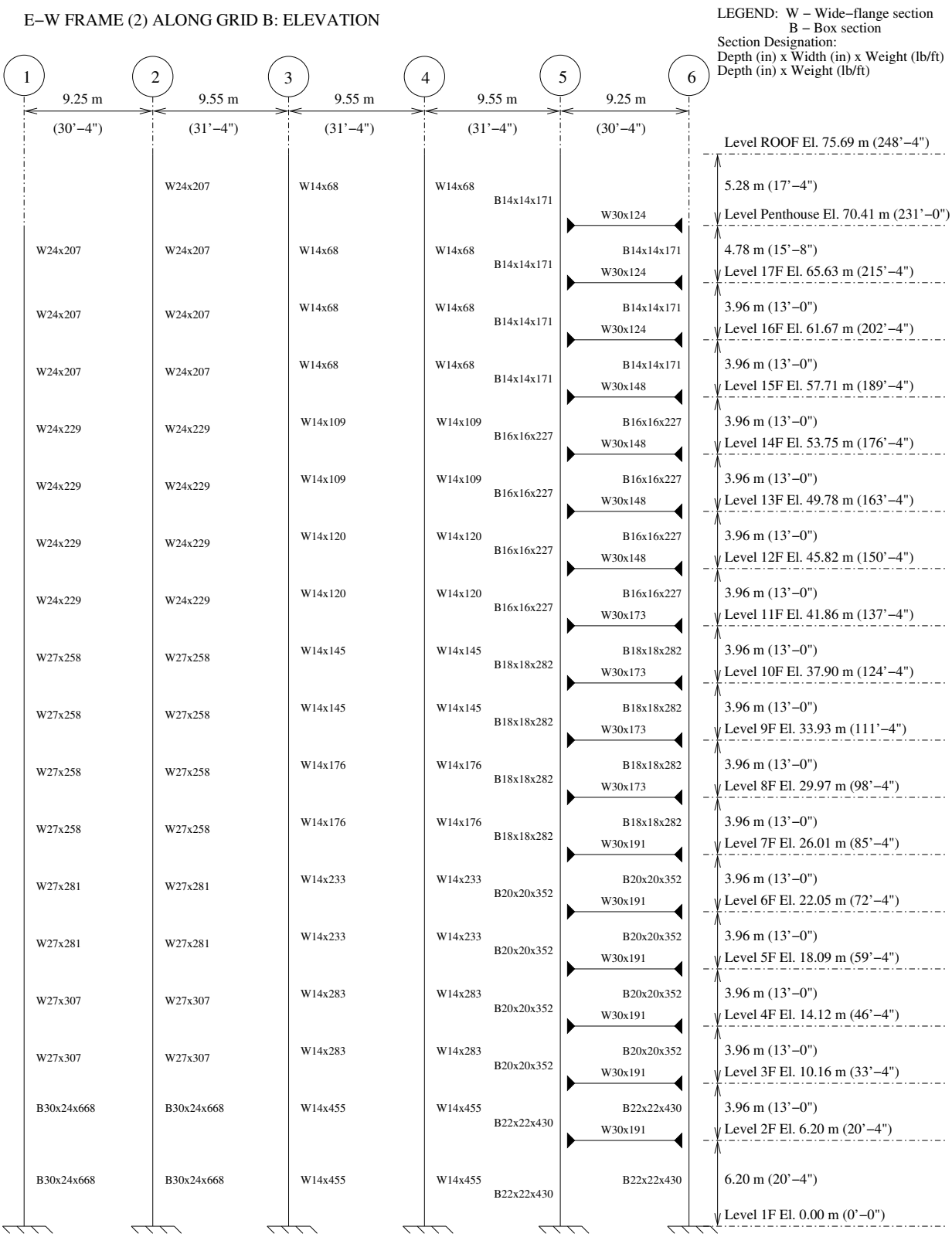

Figure C.2: Frame 2 elevation: Redesigned building

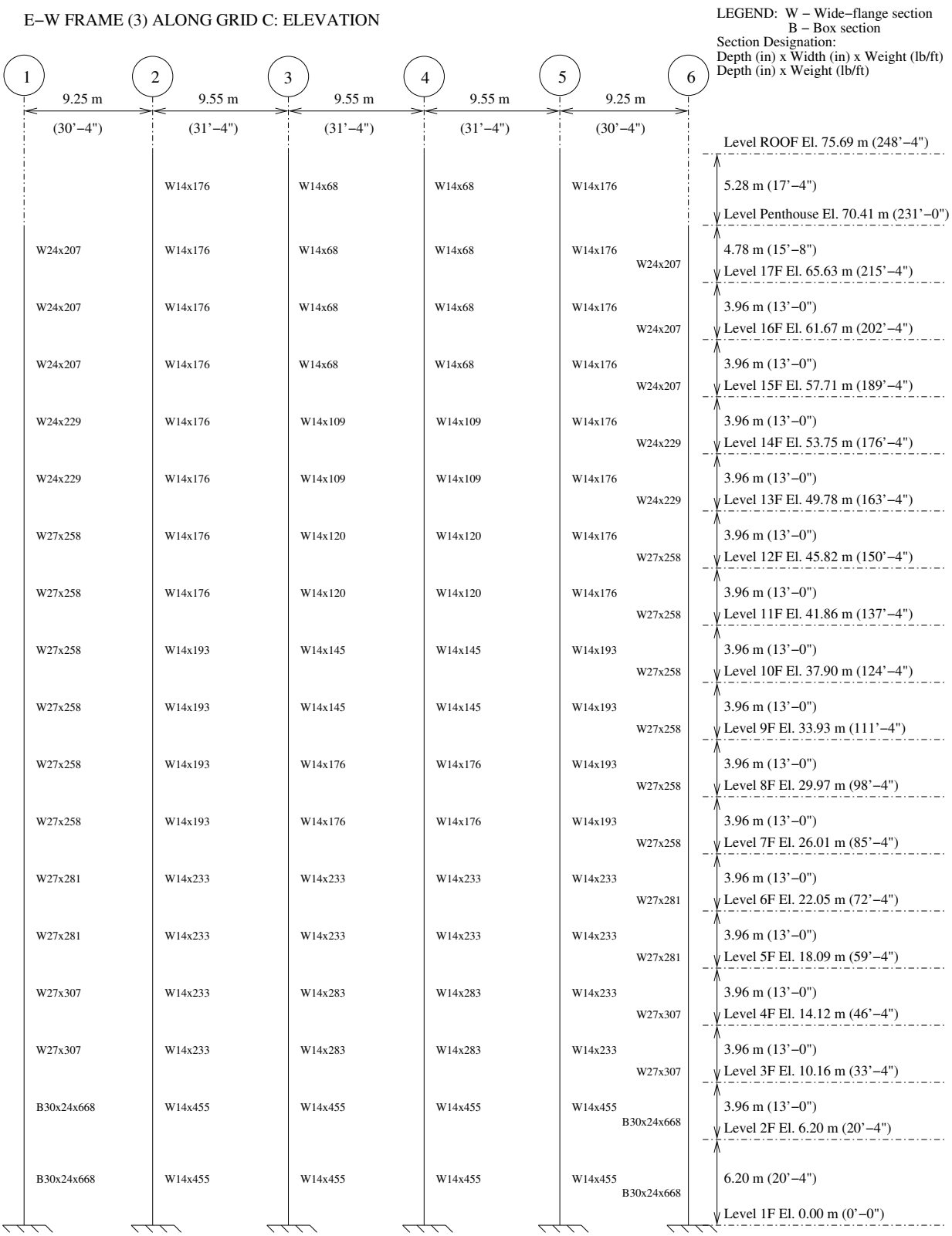

Figure C.3: Frame 3 elevation: Redesigned building

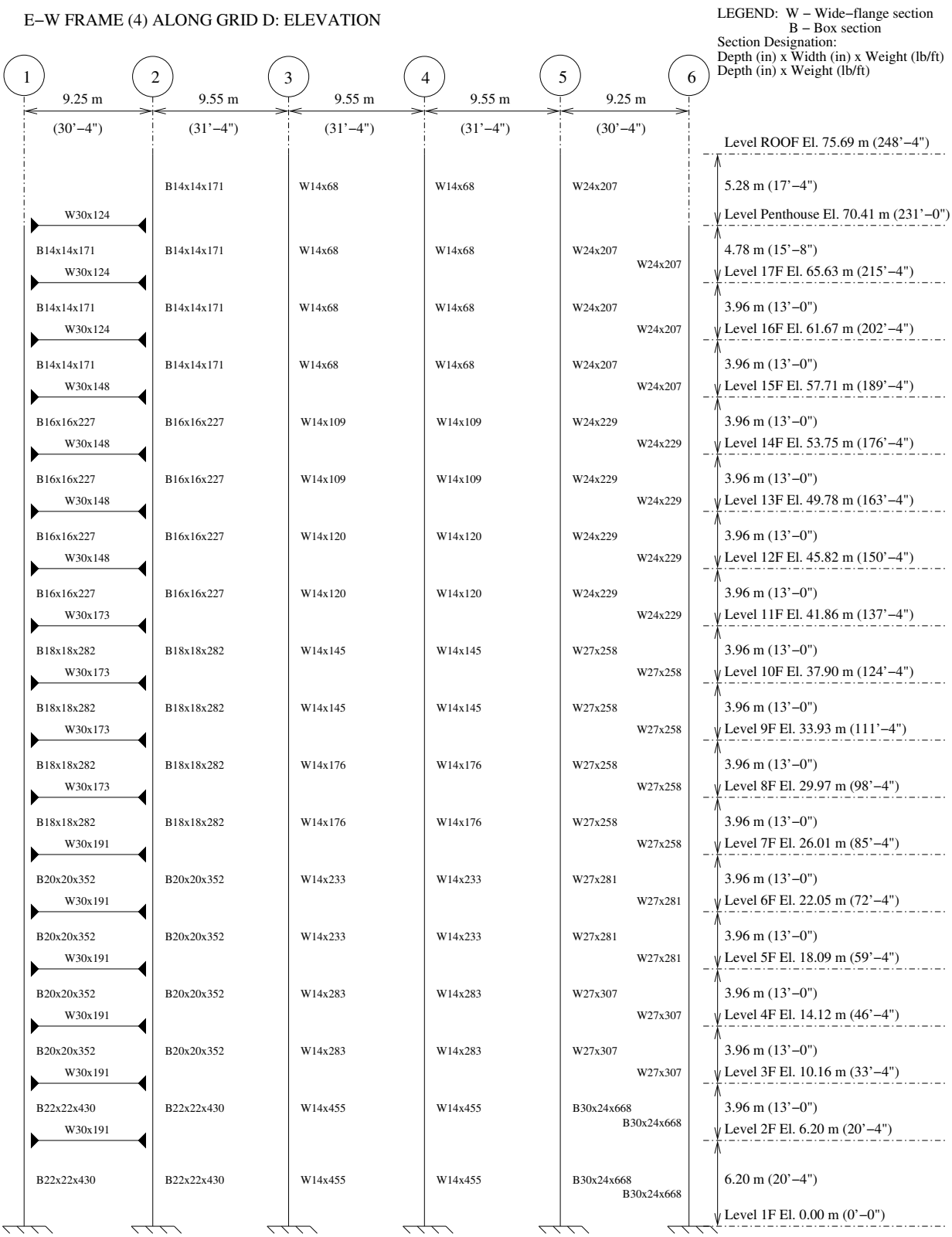

Figure C.4: Frame 4 elevation: Redesigned building

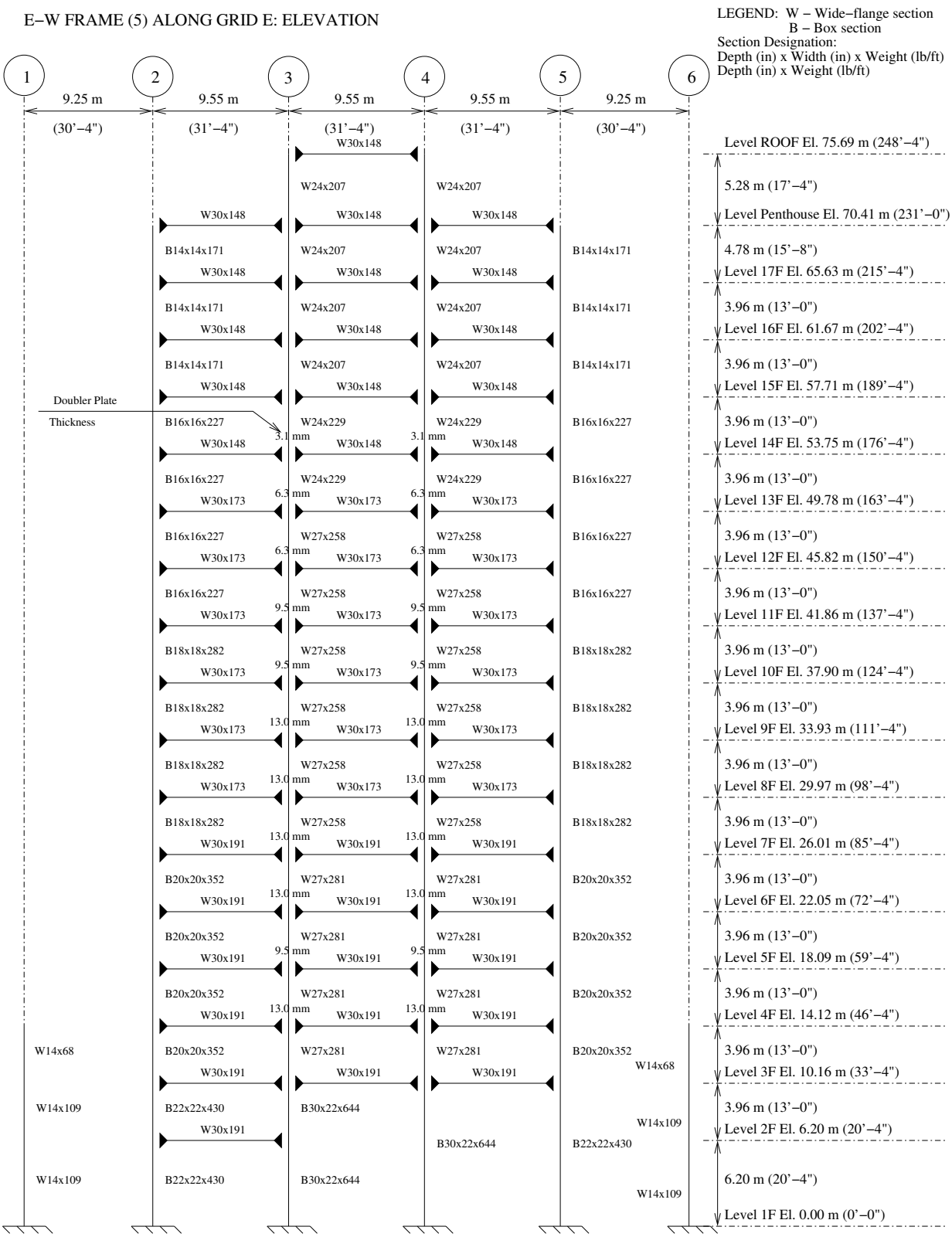

Figure C.5: Frame 5 elevation: Redesigned building

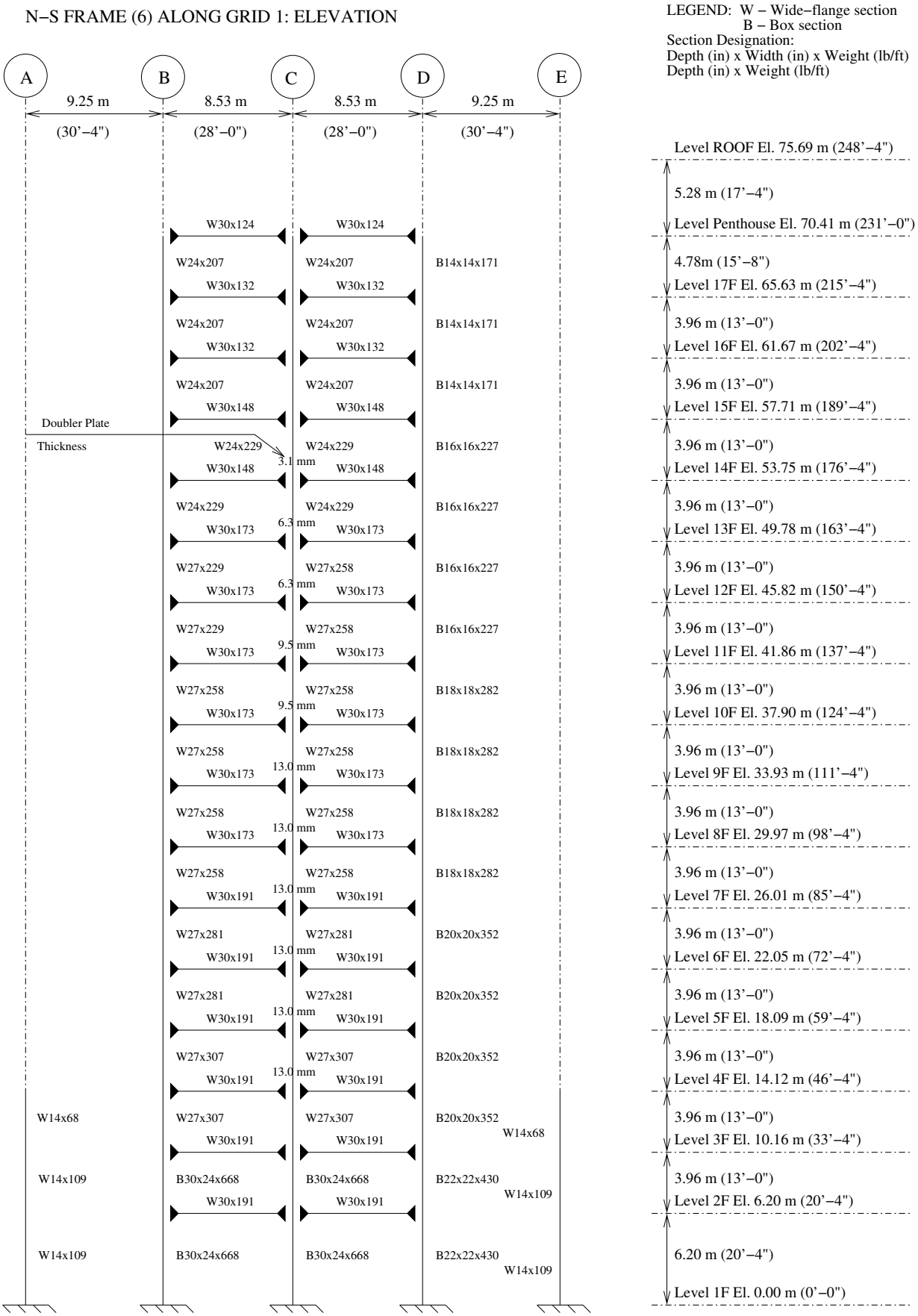

Figure C.6: Frame 6 elevation: Redesigned building

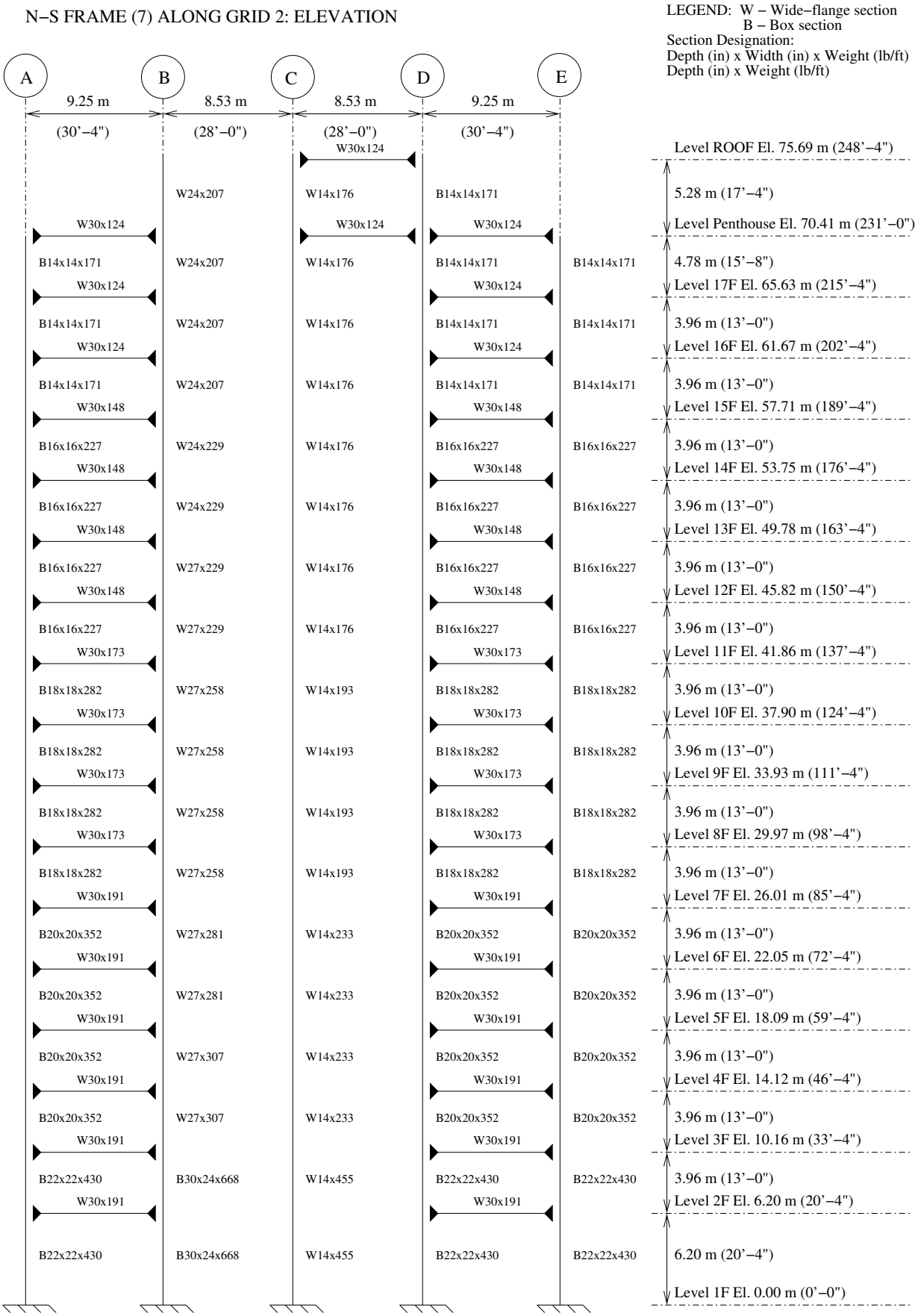

Figure C.7: Frame 7 elevation: Redesigned building

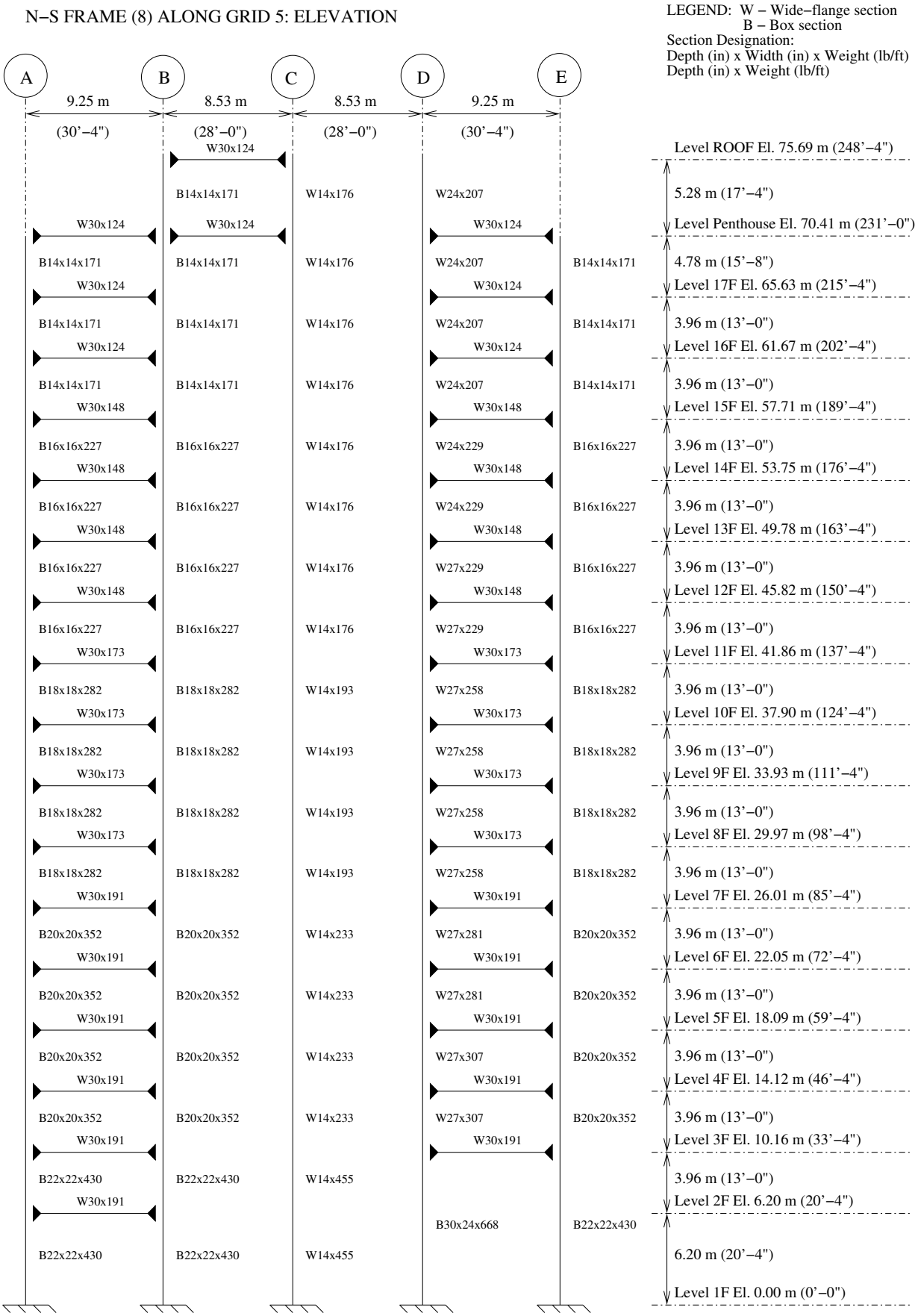

Figure C.8: Frame 8 elevation: Redesigned building

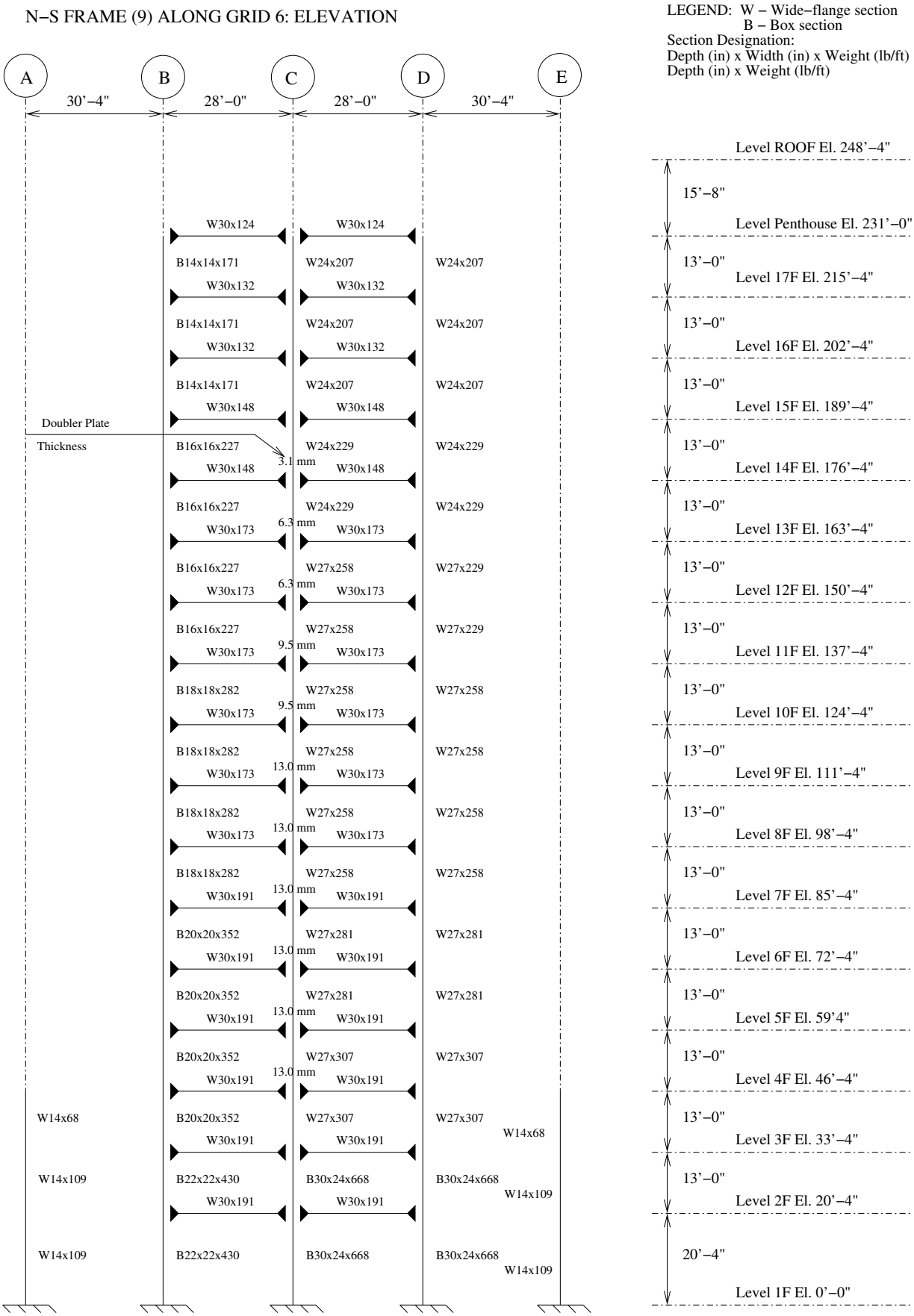

Figure C.9: Frame 9 elevation: Redesigned building

Appendix D Scenario 1 (North-to-South Rupture): Performance of Existing and Redesigned Building Models Based on Plastic Rotations in Beams and Panel Zones

Plotted in Figures D.1 through D.3 are the percentage of connections [1] in the existing building where plastic rotations exceed the IO, LS, and CP performance levels, respectively, when subjected to ground motion from scenario 1 (north-to-south rupture) earthquake on the San Andreas fault. Corresponding results for the redesigned building are shown in Figures D.4 through D.6.

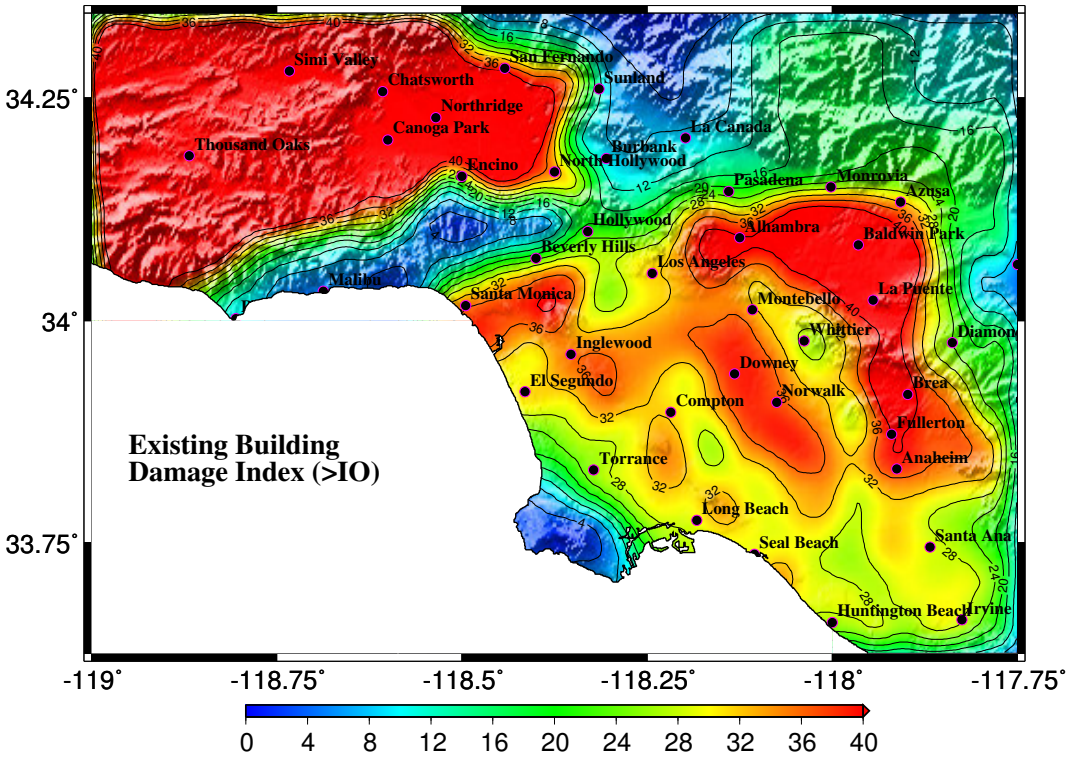

Figure D.1: $M_w 7.9$ earthquake (north-to-south rupture) on the San Andreas fault – existing building performance: Percentage of connections with plastic rotation exceeding the FEMA356 Immediate Occupancy (IO) level.

[1] Connections as defined here include the two ends each beam, and the one or two panel zones in each joint. Column ends are excluded as the FEMA356 criteria for assessing column performance make a distinction between force-controlled and deformation-controlled columns and are not amicable to presentation in a simple manner as can be done for beams and panel zones. The criteria for deformation-controlled columns (which are defined as those carrying limited axial load) are based on the plastic rotations similar to beams and panel zones. However, in the case of force-controlled columns yielding is not permissible, hence, there cannot be any performance levels associated with these columns.

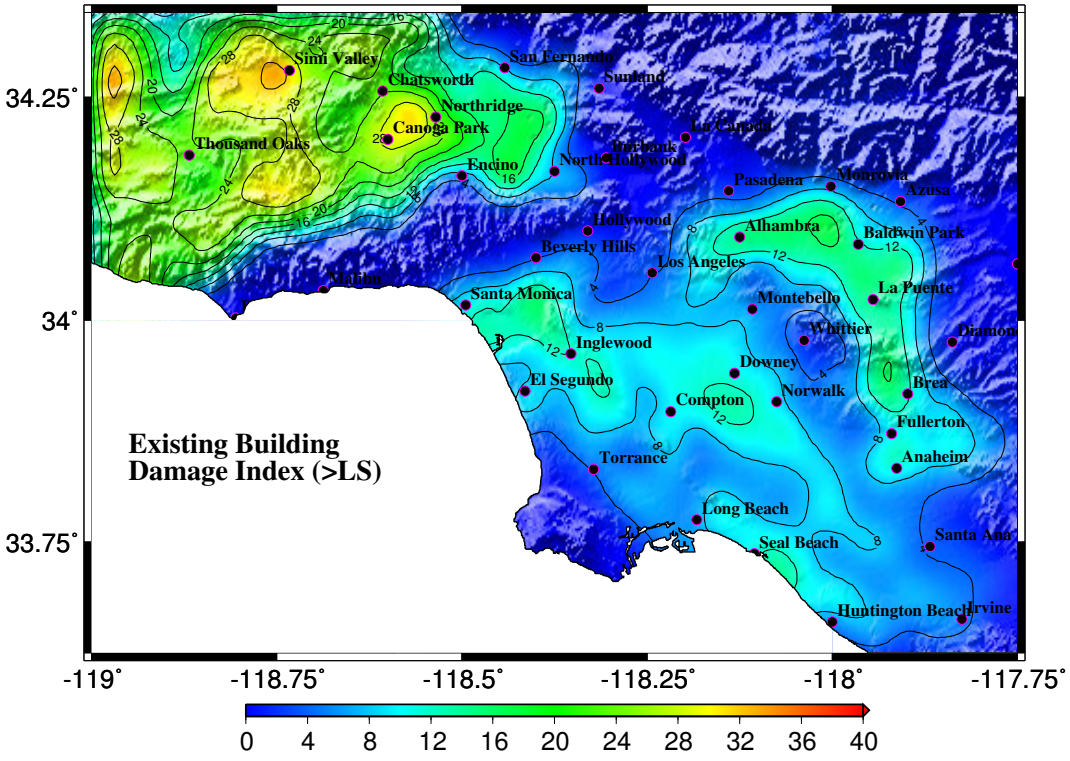

Figure D.2: $M_w 7.9$ earthquake (north-to-south rupture) on the San Andreas fault – existing building performance: Percentage of connections with plastic rotation exceeding the FEMA356 Life Safety (LS) level.

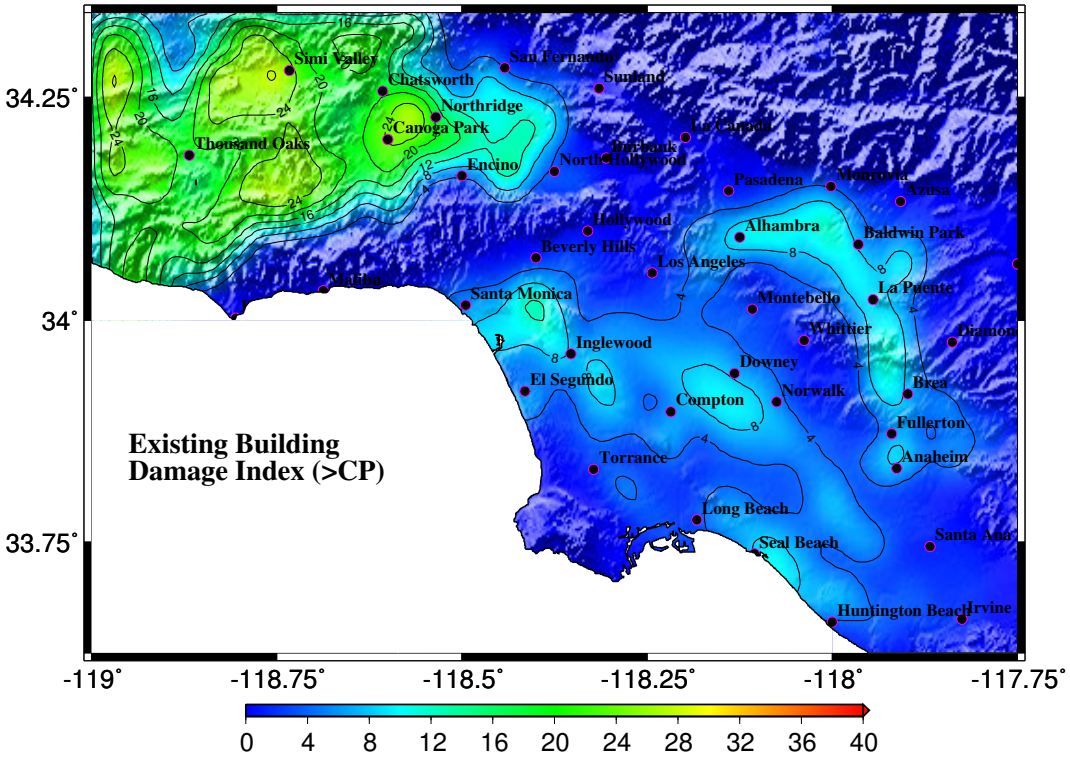

Figure D.3: $M_w 7.9$ earthquake (north-to-south rupture) on the San Andreas fault – existing building performance: Percentage of connections with plastic rotation exceeding the FEMA356 Collapse Prevention (CP) level.

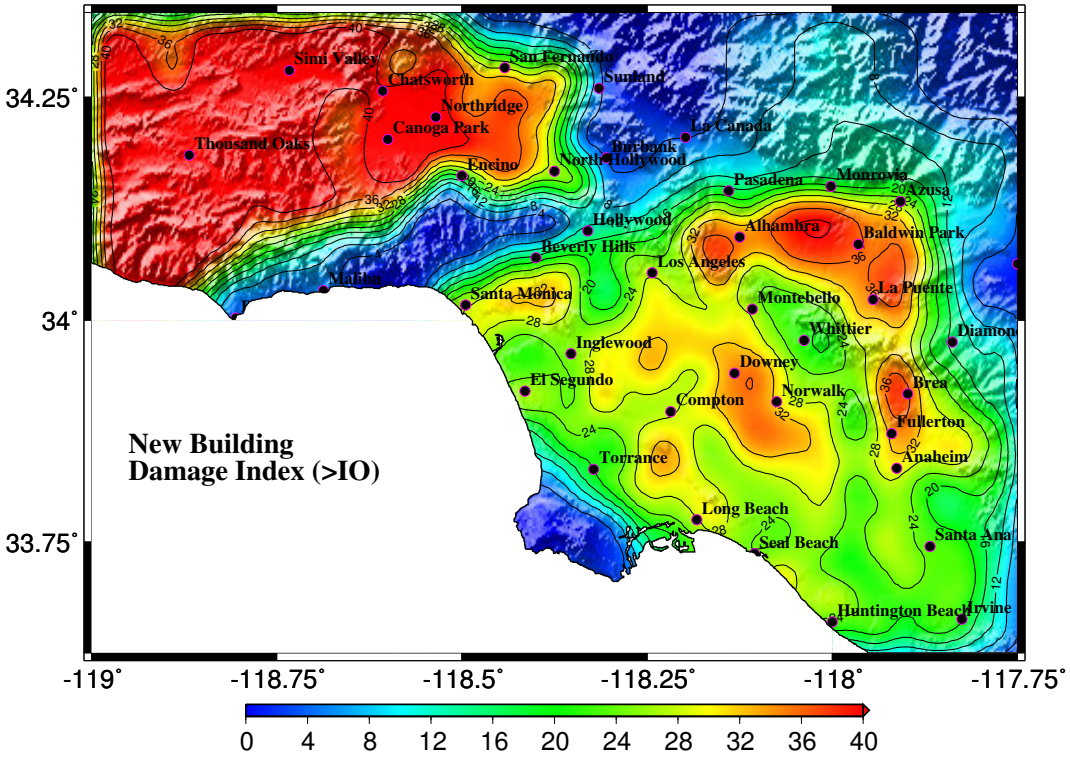

Figure D.4: M_w7.9 earthquake (north-to-south rupture) on the San Andreas fault – redesigned building performance: Percentage of connections with plastic rotation exceeding the FEMA356 Immediate Occupancy (IO) level.

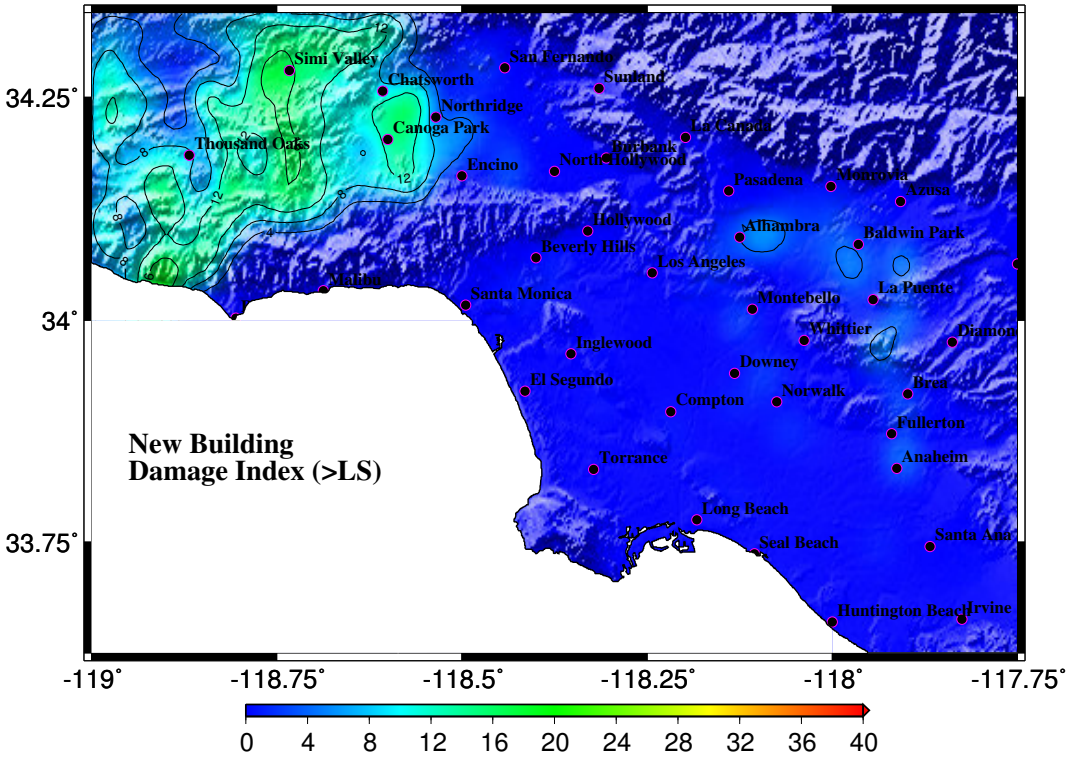

Figure D.5: M_w7.9 earthquake (north-to-south rupture) on the San Andreas fault – redesigned building performance: Percentage of connections with plastic rotation exceeding the FEMA356 Life Safety (LS) level.

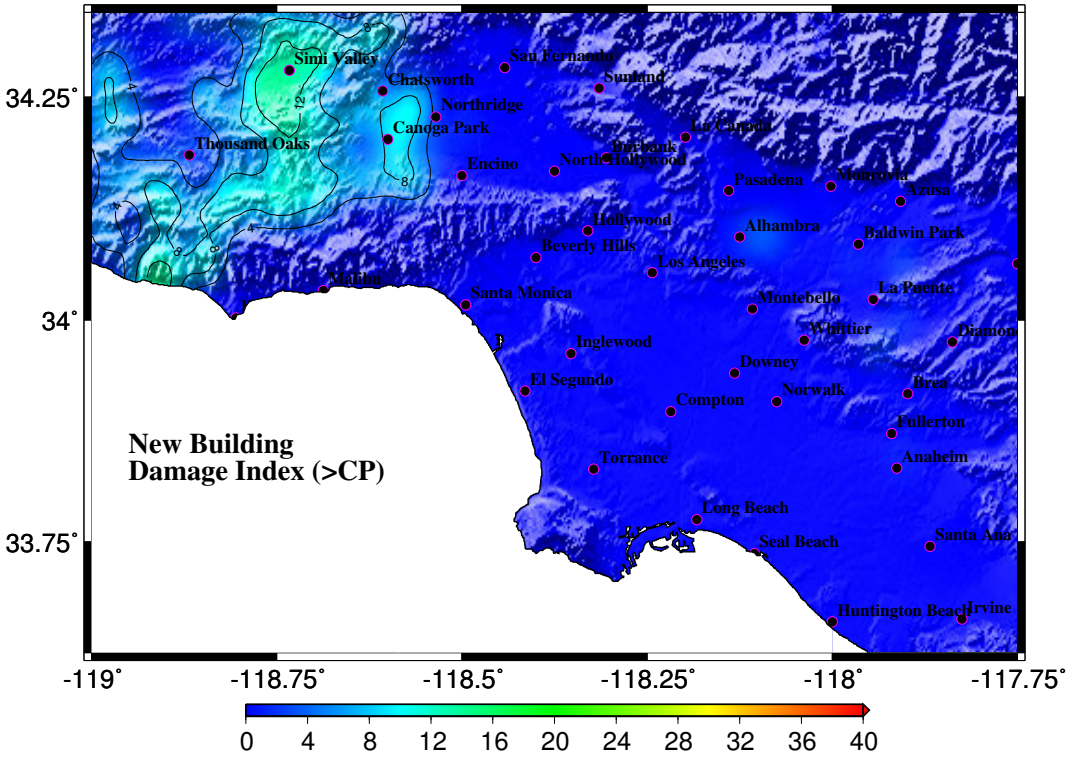

Figure D.6: $M_w 7.9$ earthquake (north-to-south rupture) on the San Andreas fault – redesigned building performance: Percentage of connections with plastic rotation exceeding the FEMA356 Collapse Prevention (CP) level.

Appendix E Scenario 2 (South-to-North Rupture): Performance of Existing and Redesigned Building Models Based on Plastic Rotations in Beams and Panel Zones

Plotted in Figures E.1 through E.3 are the percentage of connections [1] in the existing building where plastic rotations exceed the IO, LS, and CP performance levels, respectively, when subjected to ground motion from scenario 2 (south-to-north rupture) earthquake on the San Andreas fault. Corresponding results for the redesigned building are shown in Figures E.4 through E.6.

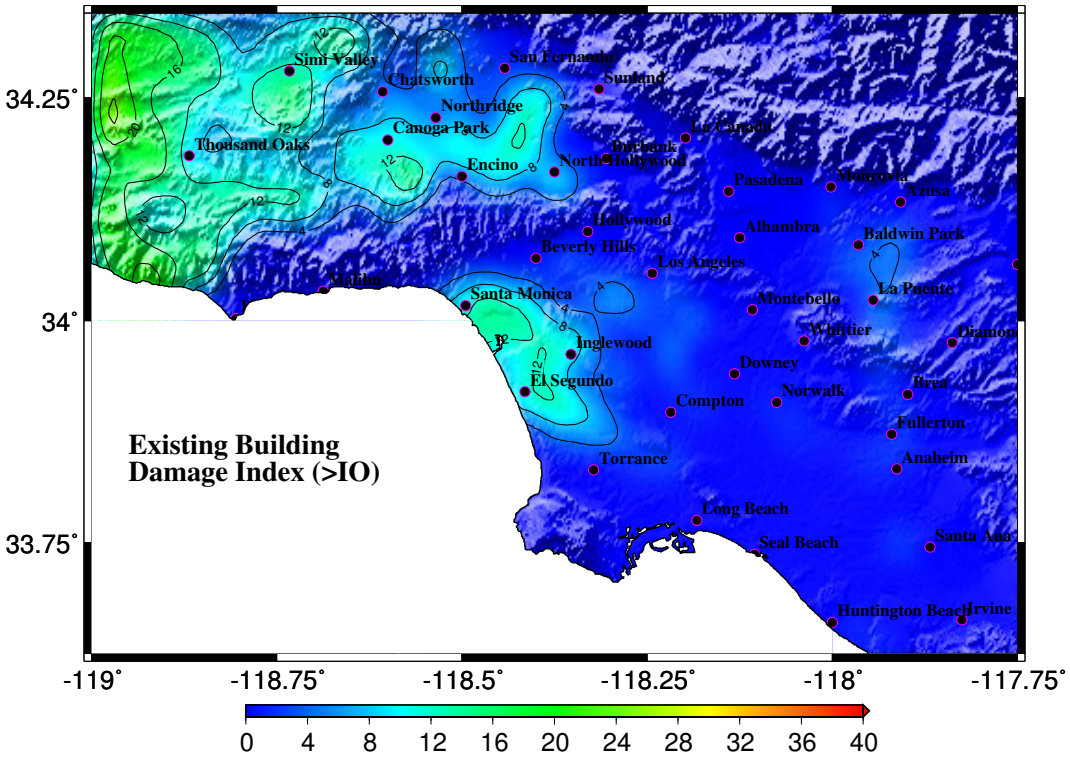

Figure E.1: $M_w 7.9$ earthquake (south-to-north rupture) on the San Andreas fault – existing building performance: Percentage of connections with plastic rotation exceeding the FEMA356 Immediate Occupancy (IO) level.

[1] Connections as defined here include the two ends each beam, and the one or two panel zones in each joint. Column ends are excluded as the FEMA356 criteria for assessing column performance make a distinction between force-controlled and deformation-controlled columns and are not amicable to presentation in a simple manner as can be done for beams and panel zones. The criteria for deformation-controlled columns (which are defined as those carrying limited axial load) are based on the plastic rotations similar to beams and panel zones. However, in the case of force-controlled columns yielding is not permissible, hence, there cannot be any performance levels associated with these columns.

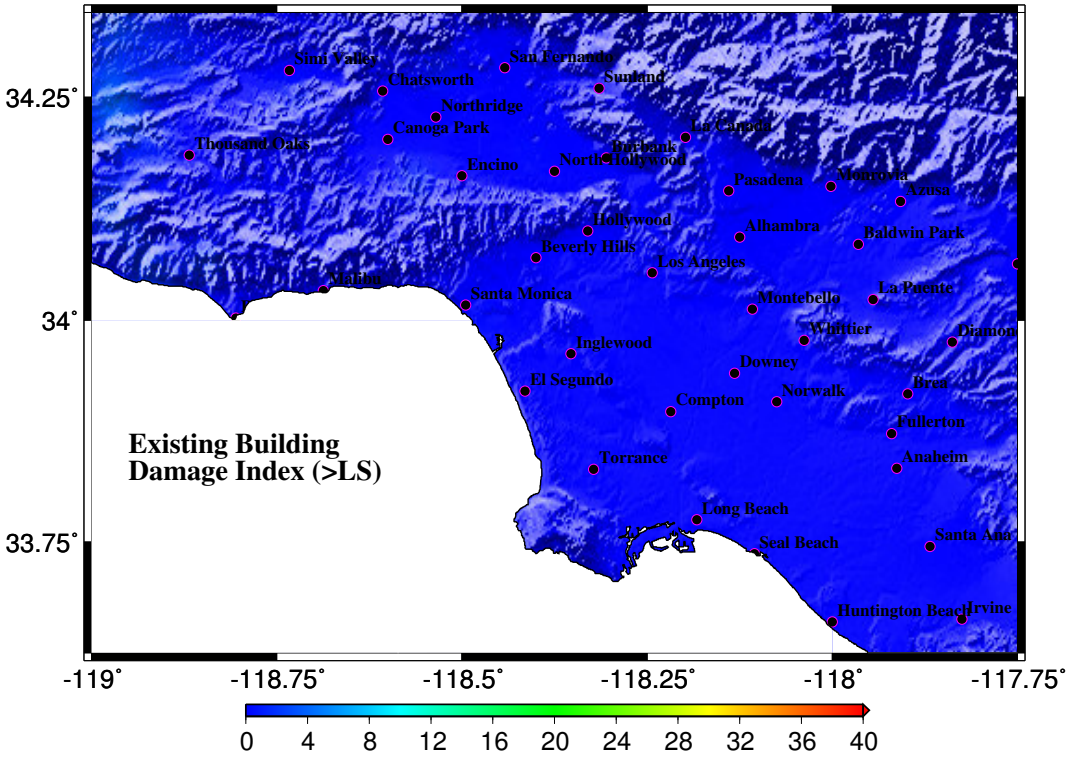

Figure E.2: M_w7.9 earthquake (south-to-north rupture) on the San Andreas fault – existing building performance: Percentage of connections with plastic rotation exceeding the FEMA356 Life Safety (LS) level.

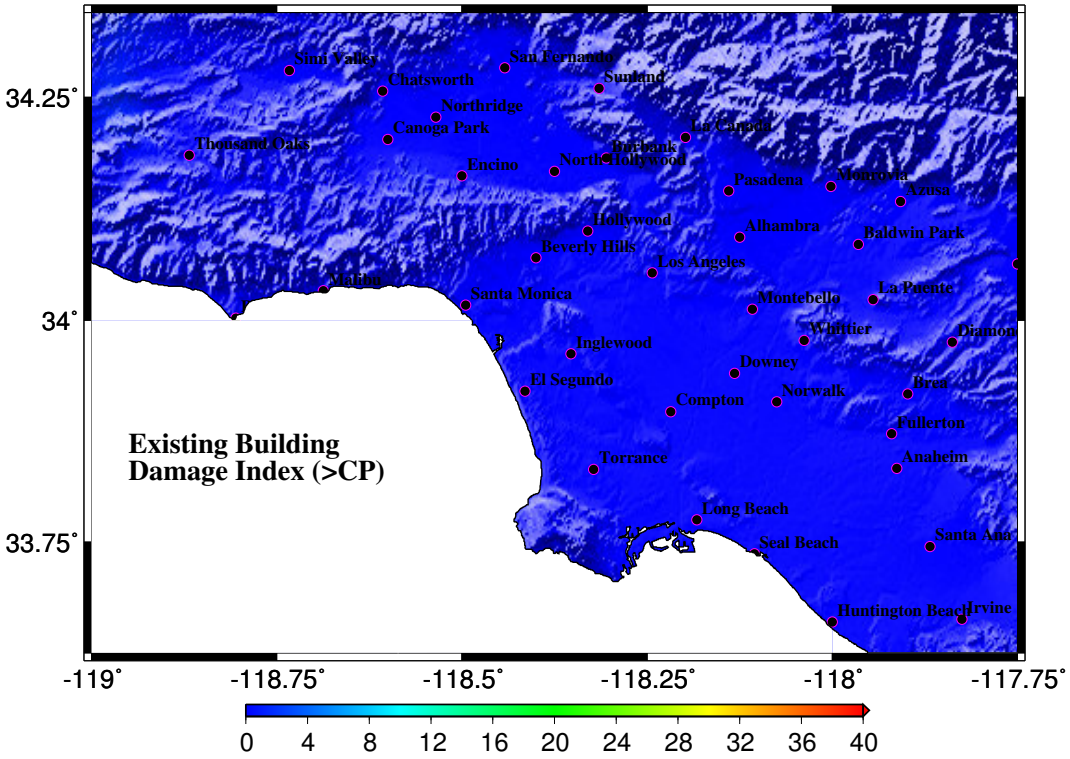

Figure E.3: M_w7.9 earthquake (south-to-north rupture) on the San Andreas fault – existing building performance: Percentage of connections with plastic rotation exceeding the FEMA356 Collapse Prevention (CP) level.

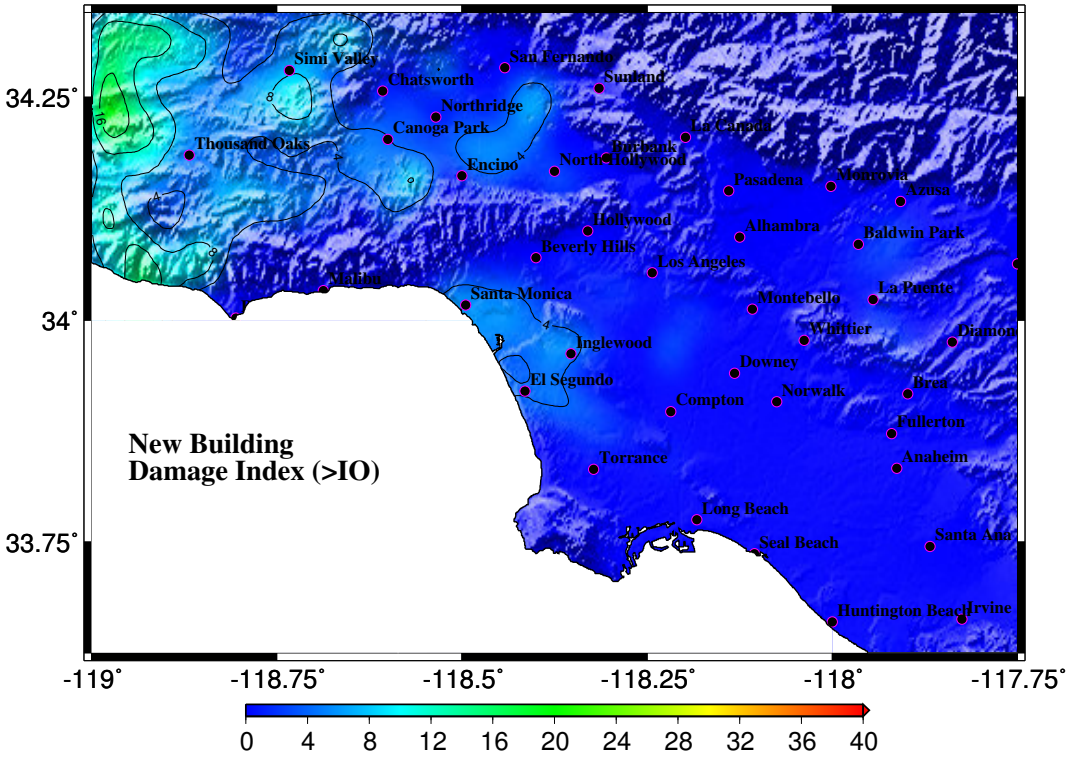

Figure E.4: $M_w 7.9$ earthquake (south-to-north rupture) on the San Andreas fault – redesigned building performance: Percentage of connections with plastic rotation exceeding the FEMA356 Immediate Occupancy (IO) level.

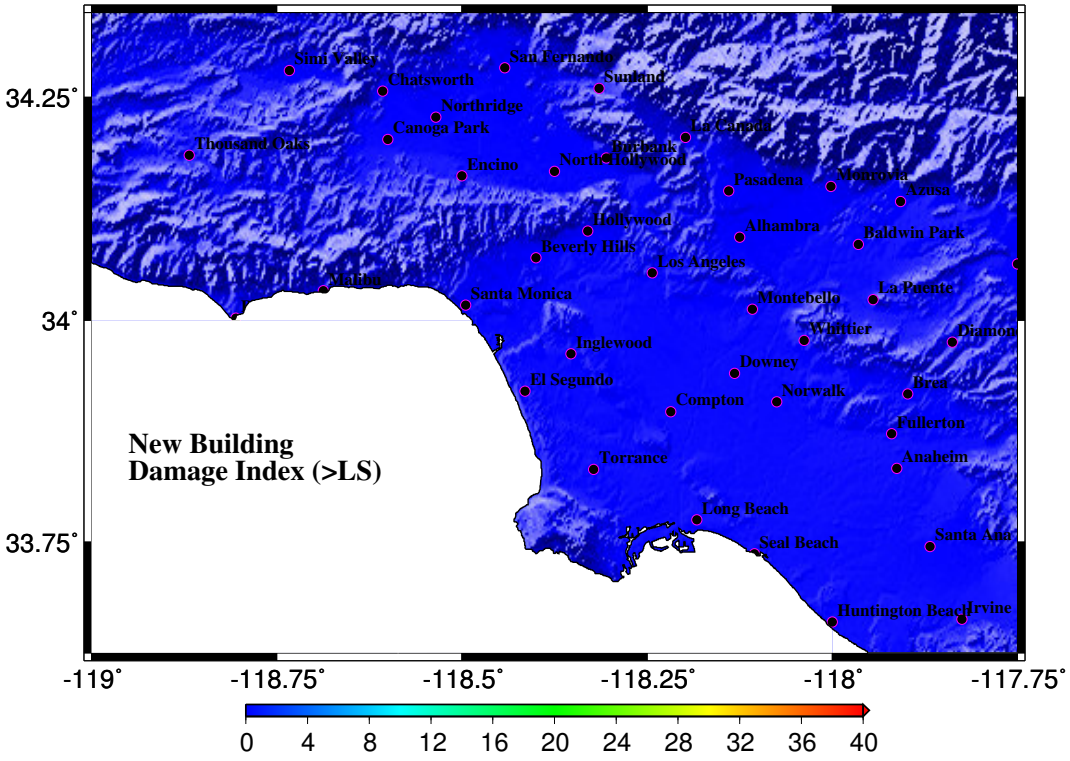

Figure E.5: $M_w 7.9$ earthquake (south-to-north rupture) on the San Andreas fault – redesigned building performance: Percentage of connections with plastic rotation exceeding the FEMA356 Life Safety (LS) level.

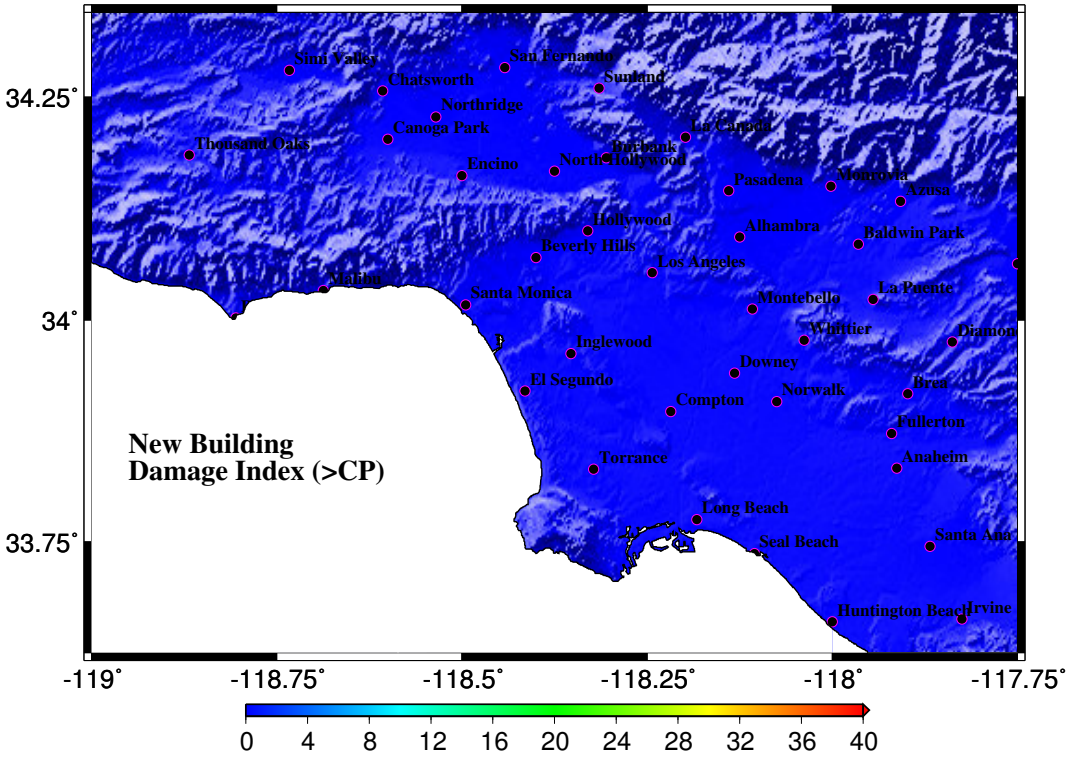

Figure E.6: $M_w 7.9$ earthquake (south-to-north rupture) on the San Andreas fault – redesigned building performance: Percentage of connections with plastic rotation exceeding the FEMA356 Collapse Prevention (CP) level.

Appendix F Details of the Performance of Existing and Redesigned Building Models in 8 Southern Californian Cities

F.1 Site: Thousand Oaks (Latitude 34.18750, Longitude 118.87500)

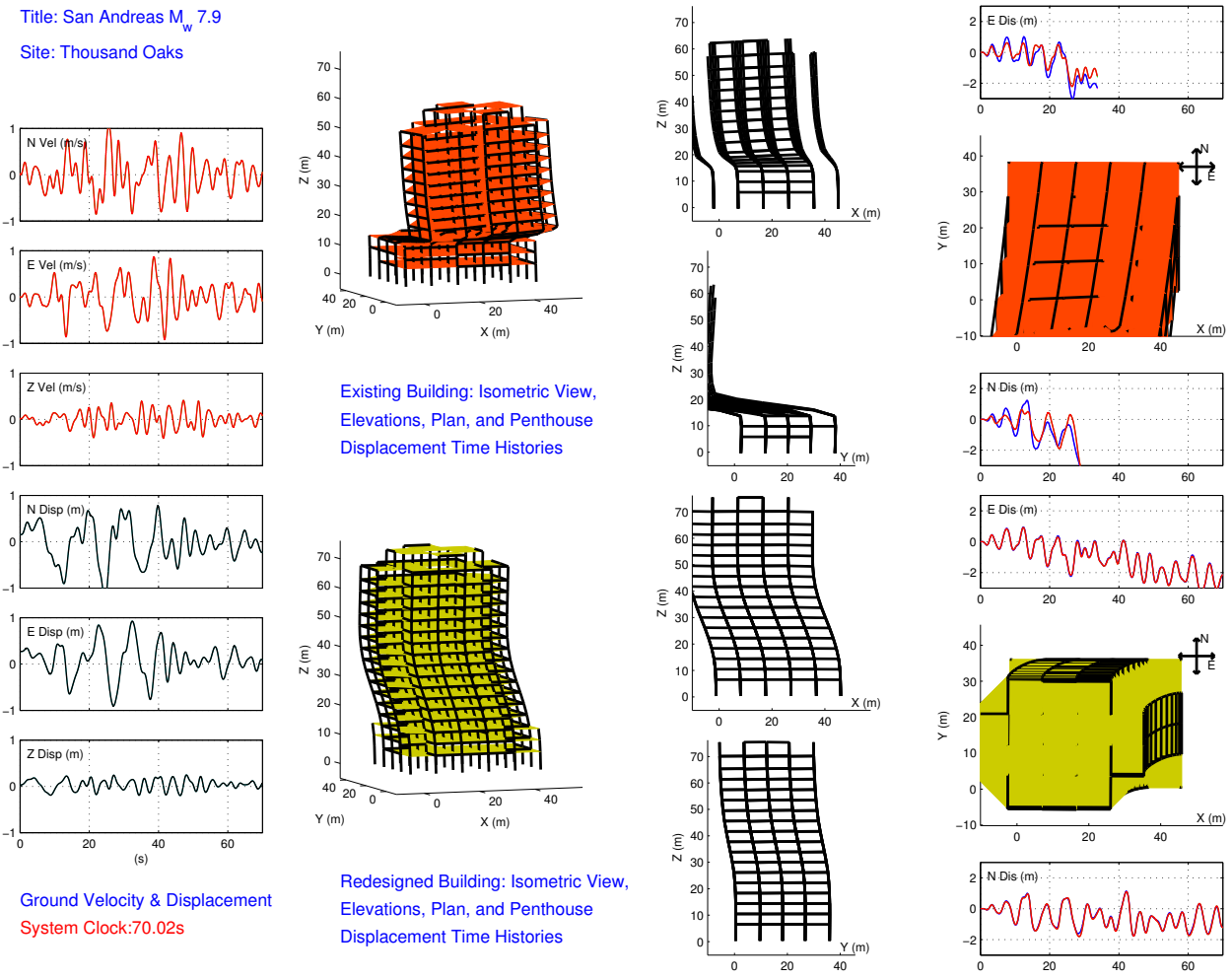

Figure F.1: $M_w 7.9$ earthquake (south-to north rupture) on the San Andreas fault – snapshot of building deformation immediately following the earthquake (scaled up by a factor of 5): Thousand Oaks. Also shown are the time-histories of the three components of the ground velocity and displacement (bandpass-filtered between 2 s and 1000 s), and the east and north components of the penthouse displacement of the existing and redesigned building models.

F.1.1 Existing Building Performance

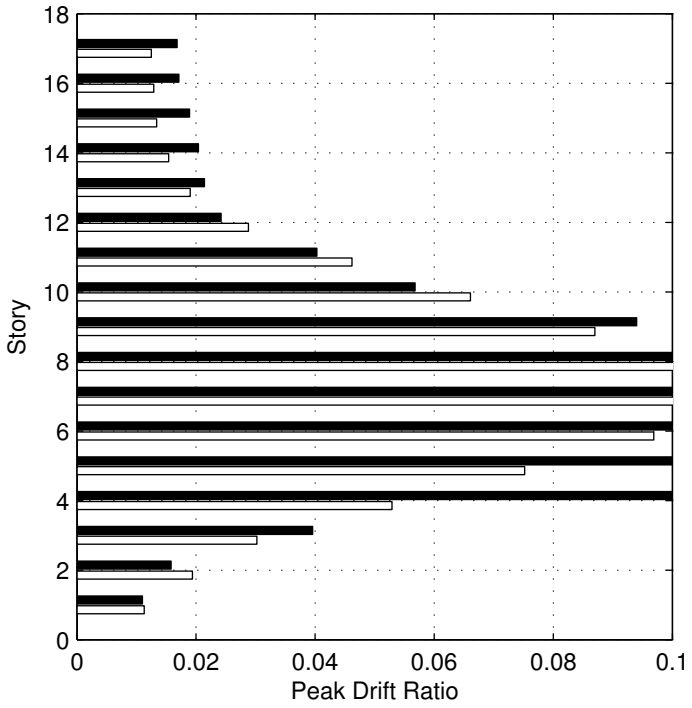

Figure F.2: Peak east-west/X (white bars) and north-south/Y (black bars) drifts in each story of the existing building model: Thousand Oaks (the drift scale is saturated at 0.10).

Component	Components within each perf. category				Perf. Level	Force-controlled components	
	IO	LS	CP	CO (> CP)		Not Yielded	Yielded
Panel Zone	130	52	8	22	CO	–	–
Beam Major Axis	140	60	12	72	CO	–	–
Beam Minor Axis	183	73	13	15	CO	–	–
Column Major Axis	764	71	9	80	CO	11	5
Column Minor Axis	712	75	12	125	CO	11	5

Table F.1: Classification of existing building model performance based on plastic rotation in panel zones, and at the ends of beams and columns, using FEMA356 acceptance criteria: Thousand Oaks.

Component	Components in the following plastic rotation ranges							
	$\leq$ 0.1%	(0.1-1.0]%	(1.0-2.0]%	(2.0-3.0]%	(3.0-4.0]%	(4.0-5.0]%	(5.0-6.0]%	> 6.0%
Panel Zone	101	70	12	11	5	4	5	4
Beam Major Axis	115	40	27	15	12	5	9	61
Beam Minor Axis	119	48	19	16	7	14	4	57
Column Major Axis	769	73	25	10	15	11	6	31
Column Minor Axis	698	83	31	28	9	2	4	85

Table F.2: Plastic rotation in panel zones, and at the ends of beams and columns of the existing building model: Thousand Oaks.

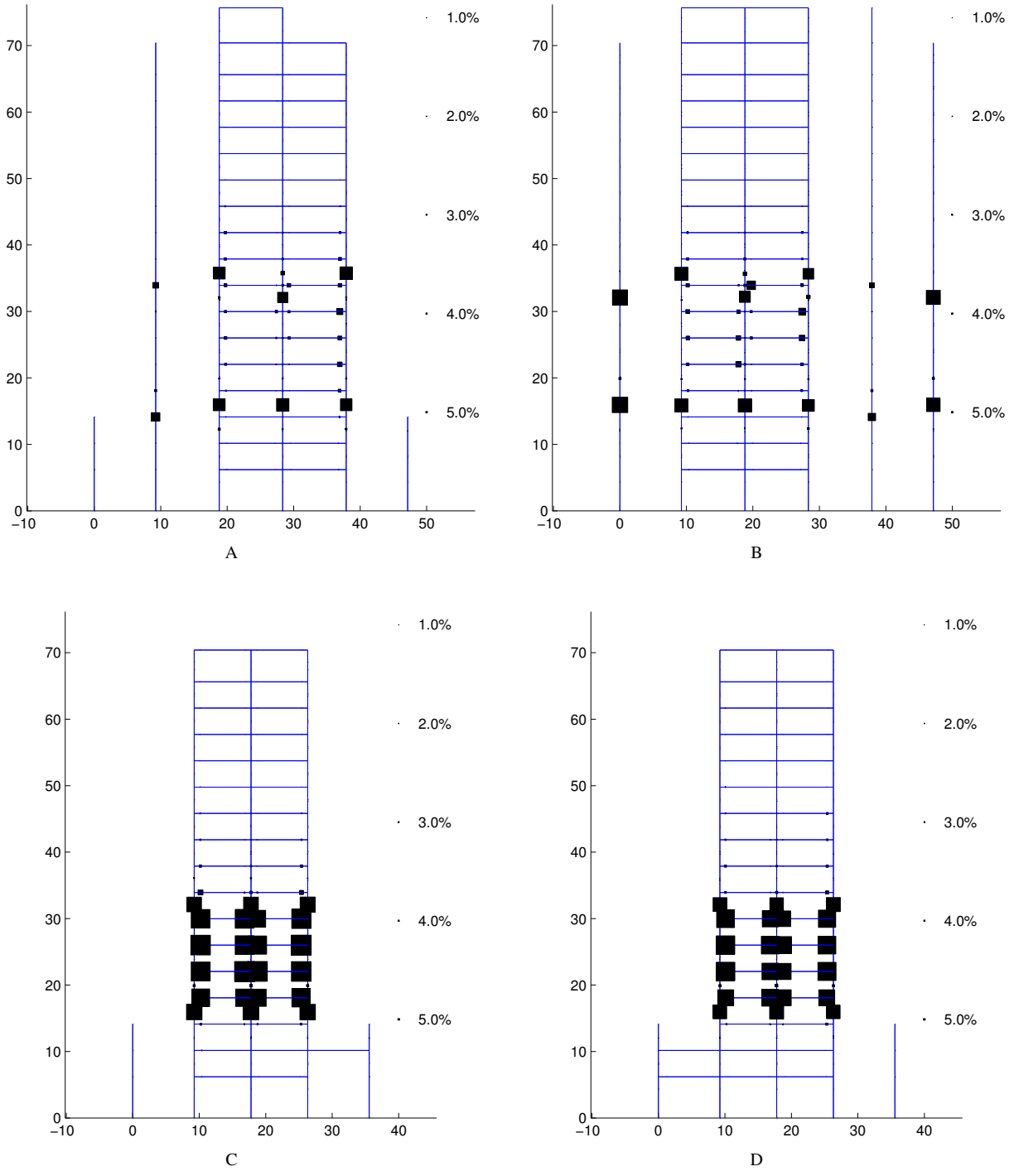

Figure F.3: Plastic rotation in percent of a radian in the moment-frames of the existing building model: Thousand Oaks – (A) Moment-frame along grid A (east-west direction); (B) Moment-frame along grid D (east-west direction); (C) Moment-frame along grid 1 (north-south direction); (D) Moment-frame along grid 6 (north-south direction). See Figure 2.2 for moment-frame configuration.

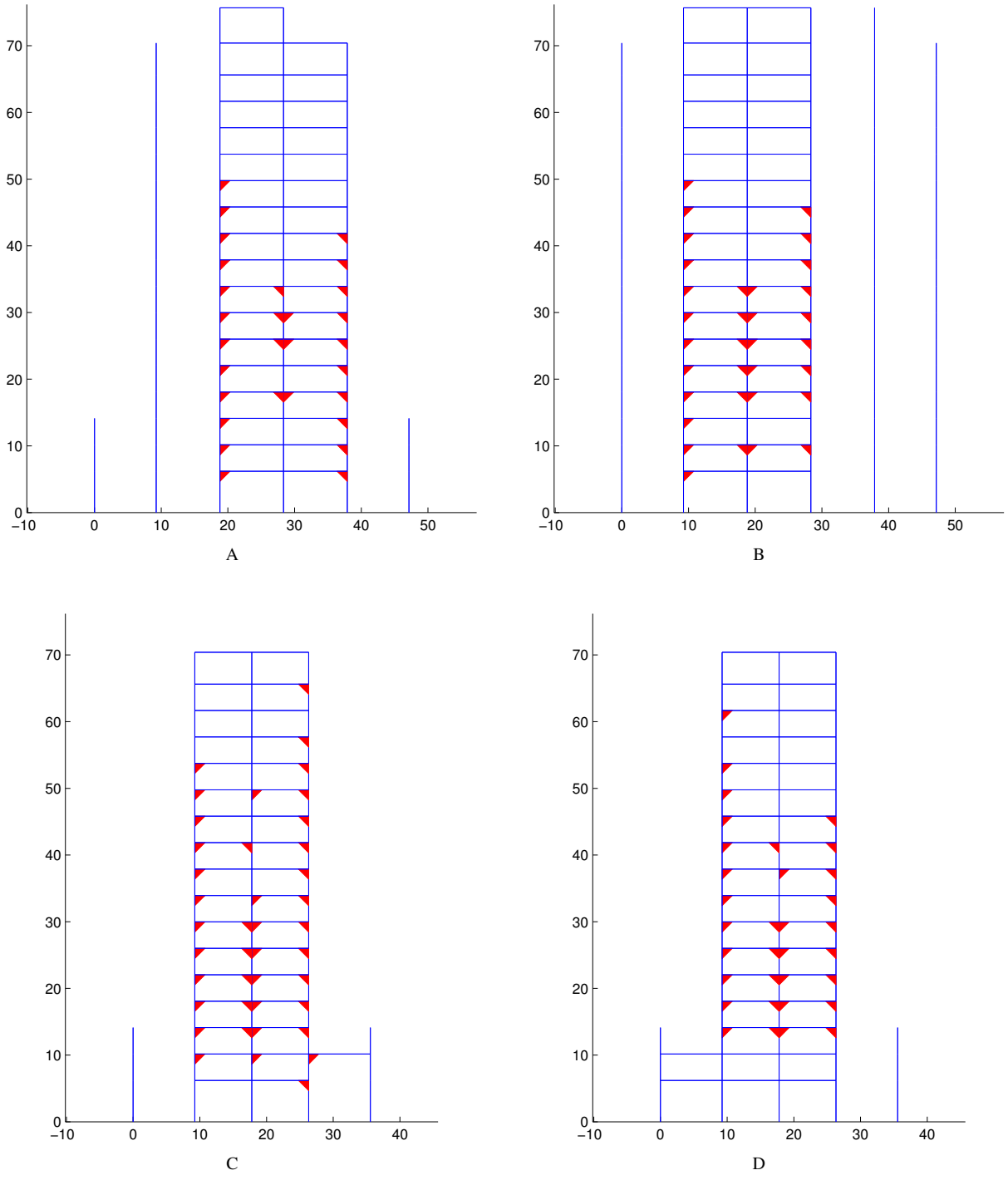

Figure F.4: Beam bottom-flange weld fracture locations in the moment-frames of the existing building model: Thousand Oaks – (A) Moment-frame along grid A (east-west direction); (B) Moment-frame along grid D (east-west direction); (C) Moment-frame along grid 1 (north-south direction); (D) Moment-frame along grid 6 (north-south direction). See Figure 2.2 for moment-frame configuration.

F.1.2 Redesigned Building Performance

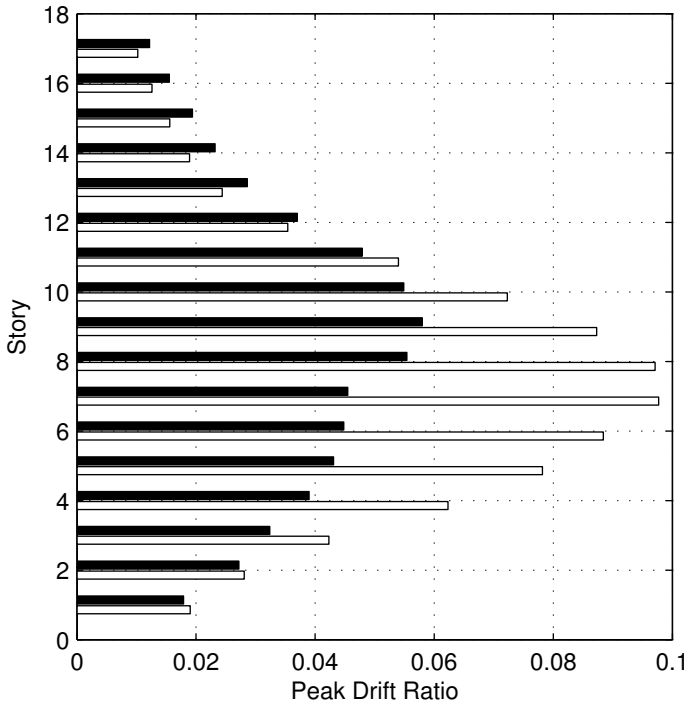

Figure F.5: Peak east-west/X (white bars) and north-south/Y (black bars) drifts in each story of the redesigned building model: Thousand Oaks.

Component	Components within each perf. category				Perf. Level	Force-controlled components	
	IO	LS	CP	CO (> CP)		Not Yielded	Yielded
Panel Zone	199	80	31	3	CO	–	–
Beam Major Axis	275	205	26	44	CO	–	–
Beam Minor Axis	530	20	0	0	LS	–	–
Column Major Axis	543	121	12	12	CO	112	140
Column Minor Axis	584	101	1	2	CO	112	140

Table F.3: Classification of redesigned building model performance based on plastic rotation in panel zones, and at the ends of beams and columns, using FEMA356 acceptance criteria: Thousand Oaks.

Component	Components in the following plastic rotation ranges							
	$\leq$ 0.1%	(0.1-1.0]%	(1.0-2.0]%	(2.0-3.0]%	(3.0-4.0]%	(4.0-5.0]%	(5.0-6.0]%	$>$ 6.0%
Panel Zone	189	61	29	34	0	0	0	0
Beam Major Axis	249	41	77	70	32	25	12	44
Beam Minor Axis	255	194	82	19	0	0	0	0
Column Major Axis	710	207	23	0	0	0	0	0
Column Minor Axis	772	168	0	0	0	0	0	0

Table F.4: Plastic rotation in panel zones, and at the ends of beams and columns of the redesigned building model: Thousand Oaks.

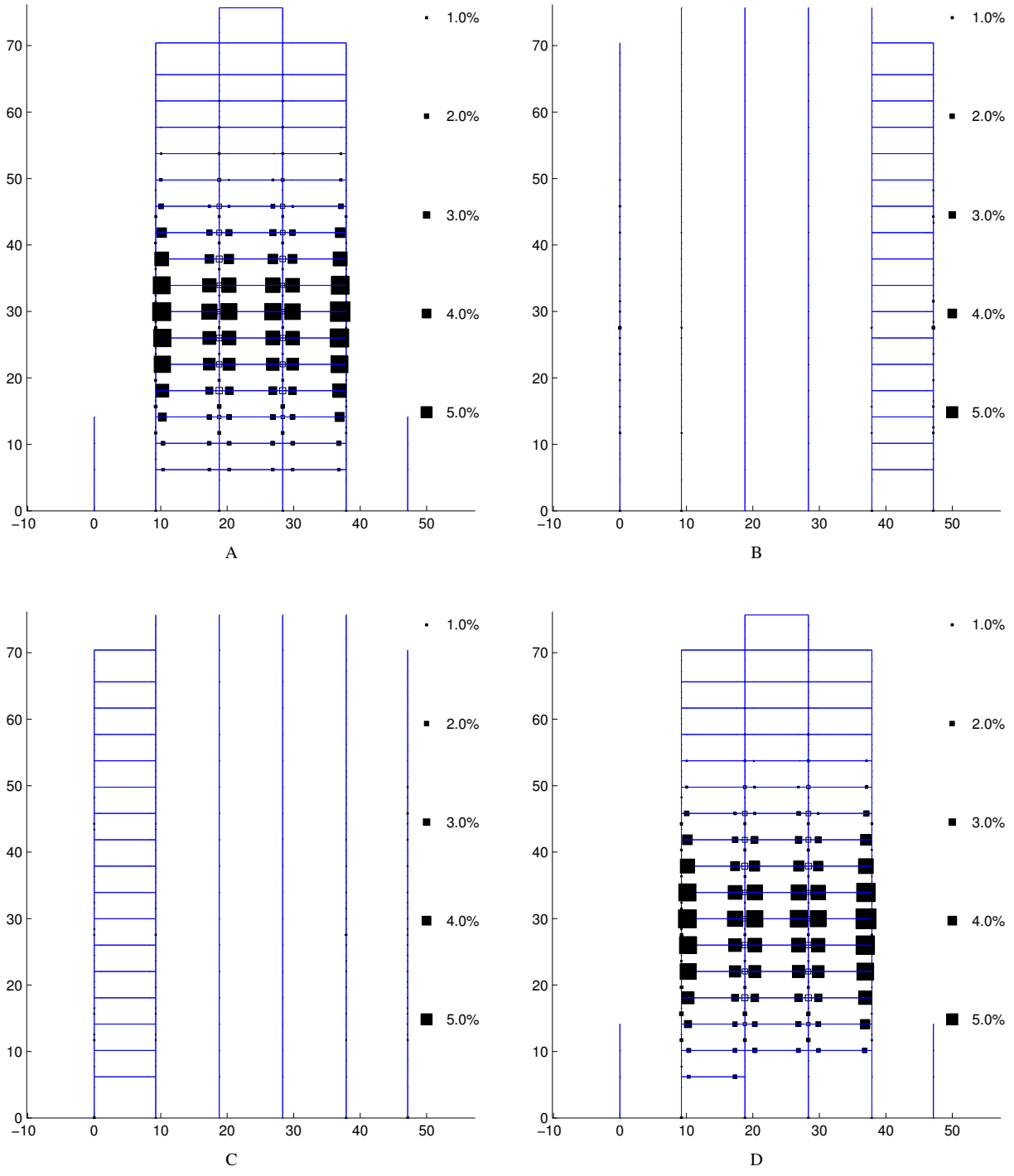

Figure F.6: Plastic rotation in percent of a radian in the moment-frames of the redesigned building model: Thousand Oaks – (A) Moment-frame along grid A (east-west direction); (B) Moment-frame along grid B (east-west direction); (C) Moment-frame along grid D (east-west direction); (D) Moment-frame along grid E (east-west direction). See Figure 2.3 for moment-frame configuration.

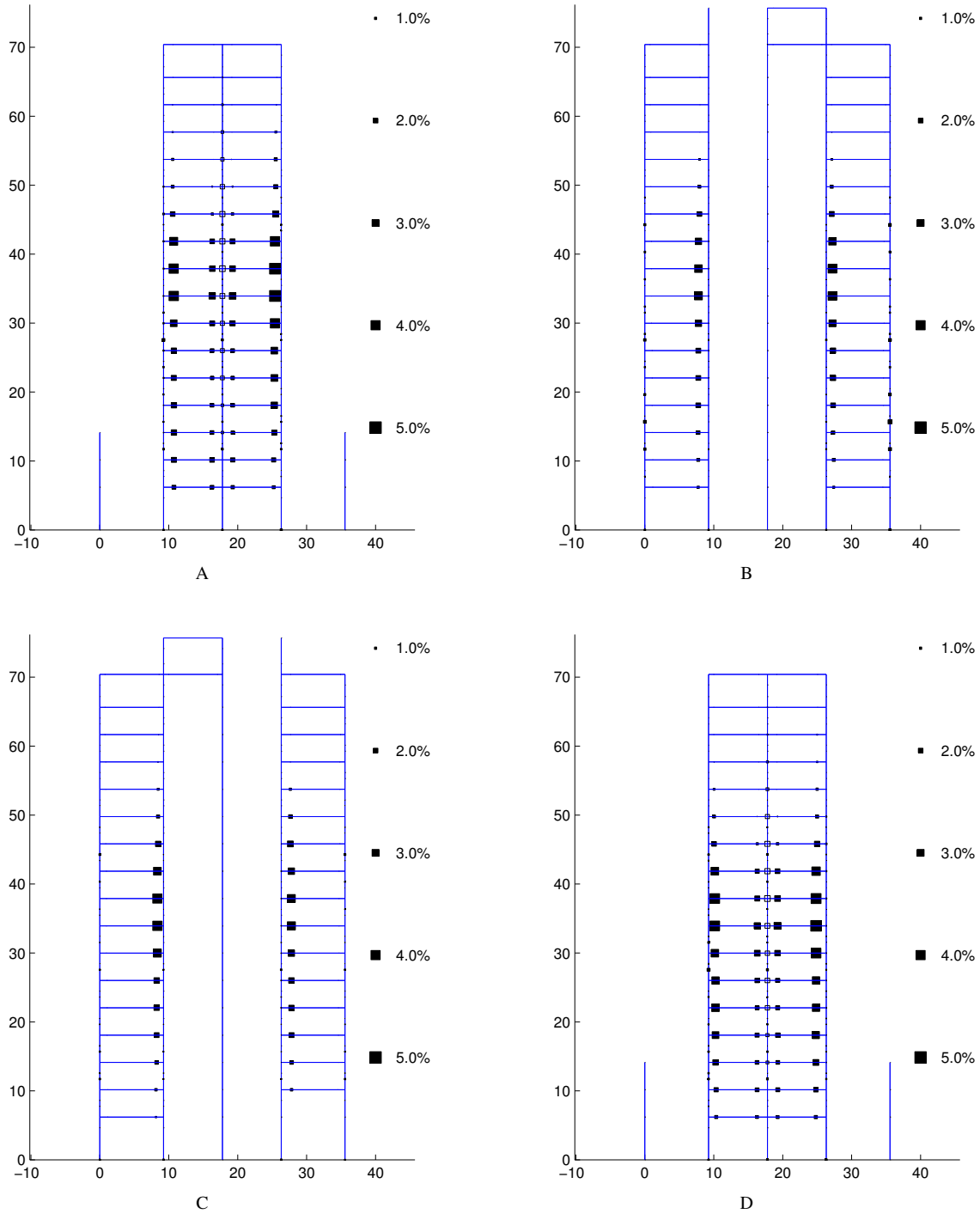

Figure F.7: Plastic rotation in percent of a radian in the moment-frames of the redesigned building model: Thousand Oaks – (A) Moment-frame along grid 1 (north-south direction); (B) Moment-frame along grid 2 (north-south direction); (C) Moment-frame along grid 5 (north-south direction); (D) Moment-frame along grid 6 (north-south direction). See Figure 2.3 for moment-frame configuration.

F.2 Site: Northridge (Latitude 34.21875, Longitude 118.53125)

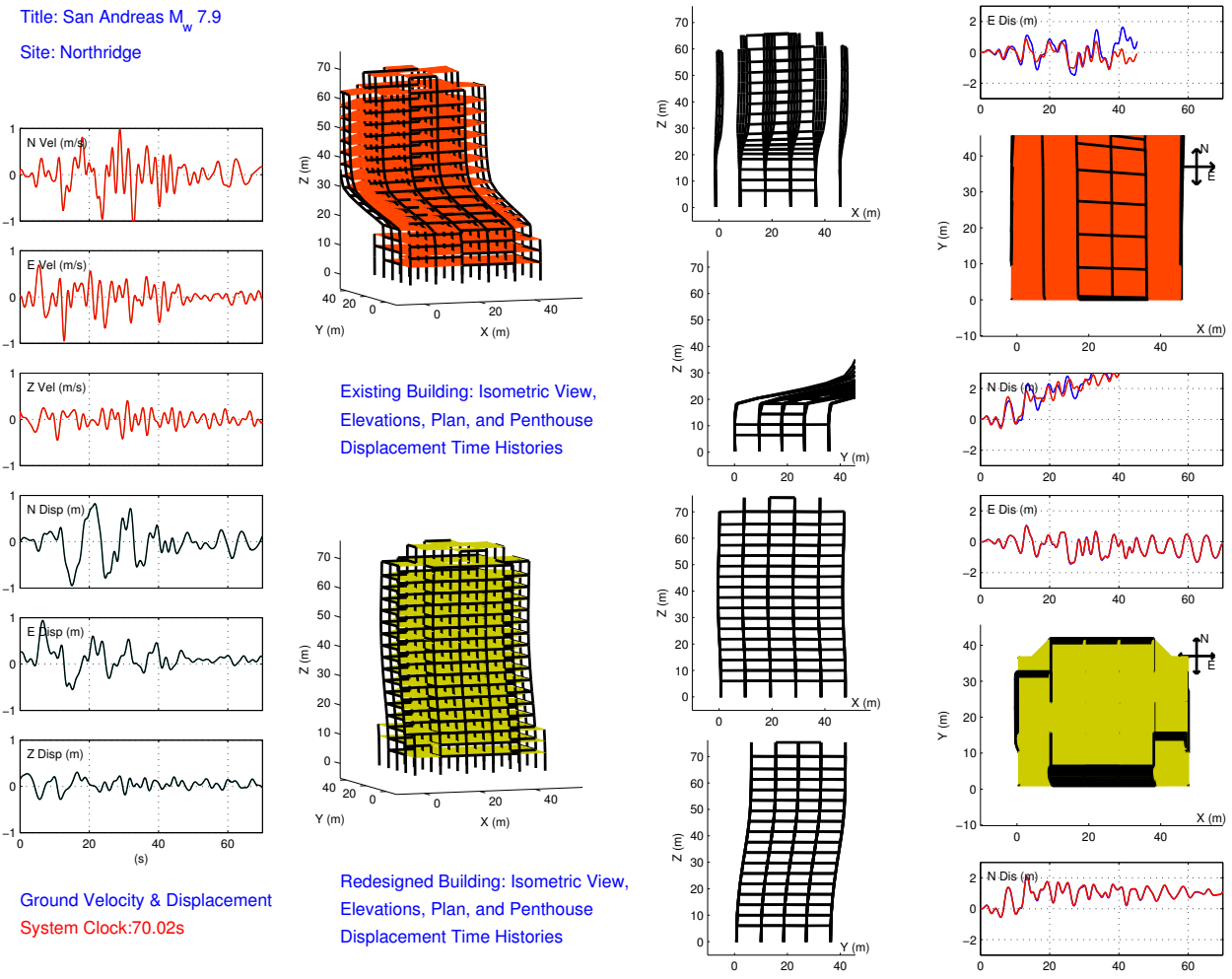

Figure F.8: $M_w 7.9$ earthquake (south-to-north rupture) on the San Andreas fault – snapshot of building deformation immediately following the earthquake (scaled up by a factor of 5): Northridge. Also shown are the time-histories of the three components of the ground velocity and displacement (bandpass-filtered between 2 s and 1000 s), and the east and north components of the penthouse displacement of the existing and redesigned building models.

F.2.1 Existing Building Performance

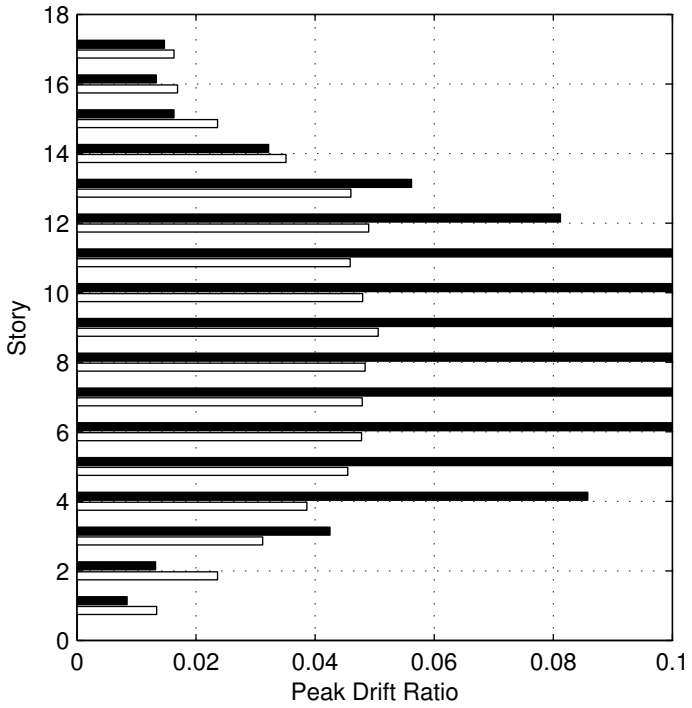

Figure F.9: Peak east-west/X (white bars) and north-south/Y (black bars) drifts in each story of the existing building model: Northridge (the drift scale is saturated at 0.10).

Component	Components within each perf. category				Perf. Level	Force-controlled components	
	IO	LS	CP	CO (> CP)		Not Yielded	Yielded
Panel Zone	114	60	11	27	CO	–	–
Beam Major Axis	112	94	16	62	CO	–	–
Beam Minor Axis	183	63	13	25	CO	–	–
Column Major Axis	811	77	4	28	CO	16	4
Column Minor Axis	694	107	19	100	CO	13	7

Table F.5: Classification of existing building model performance based on plastic rotation in panel zones, and at the ends of beams and columns, using FEMA356 acceptance criteria: Northridge.

Component	Components in the following plastic rotation ranges							
	$\leq$ 0.1%	(0.1-1.0]%	(1.0-2.0]%	(2.0-3.0]%	(3.0-4.0]%	(4.0-5.0]%	(5.0-6.0]%	> 6.0%
Panel Zone	85	78	15	13	7	7	2	5
Beam Major Axis	71	61	29	31	21	12	2	57
Beam Minor Axis	85	73	25	20	12	12	5	52
Column Major Axis	810	80	24	9	1	1	3	12
Column Minor Axis	665	120	45	25	5	4	3	73

Table F.6: Plastic rotation in panel zones, and at the ends of beams and columns of the existing building model: Northridge.

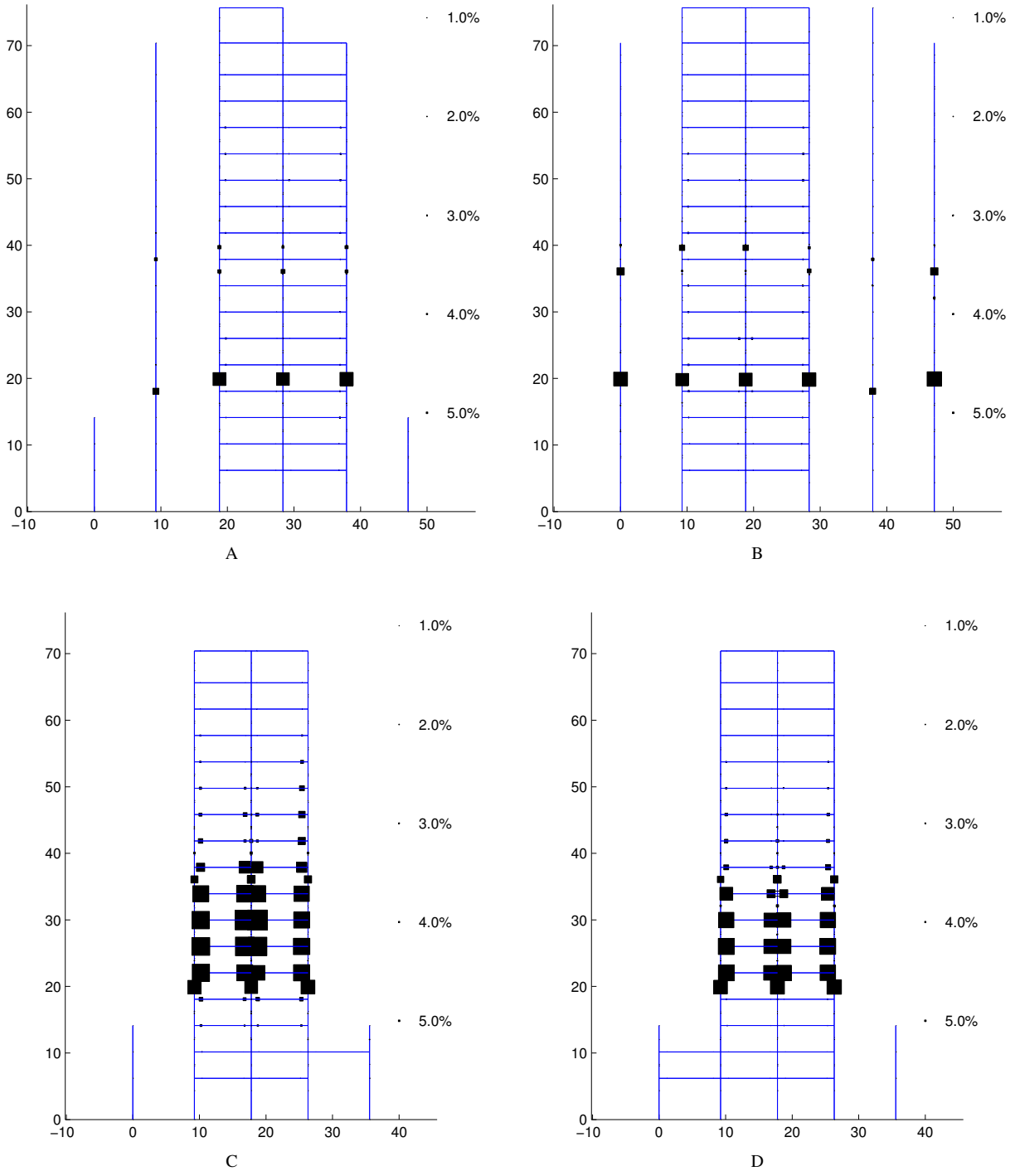

Figure F.10: Plastic rotation in percent of a radian in the moment-frames of the existing building model: Northridge – (A) Moment-frame along grid A (east-west direction); (B) Moment-frame along grid D (east-west direction); (C) Moment-frame along grid 1 (north-south direction); (D) Moment-frame along grid 6 (north-south direction). See Figure 2.2 for moment-frame configuration.

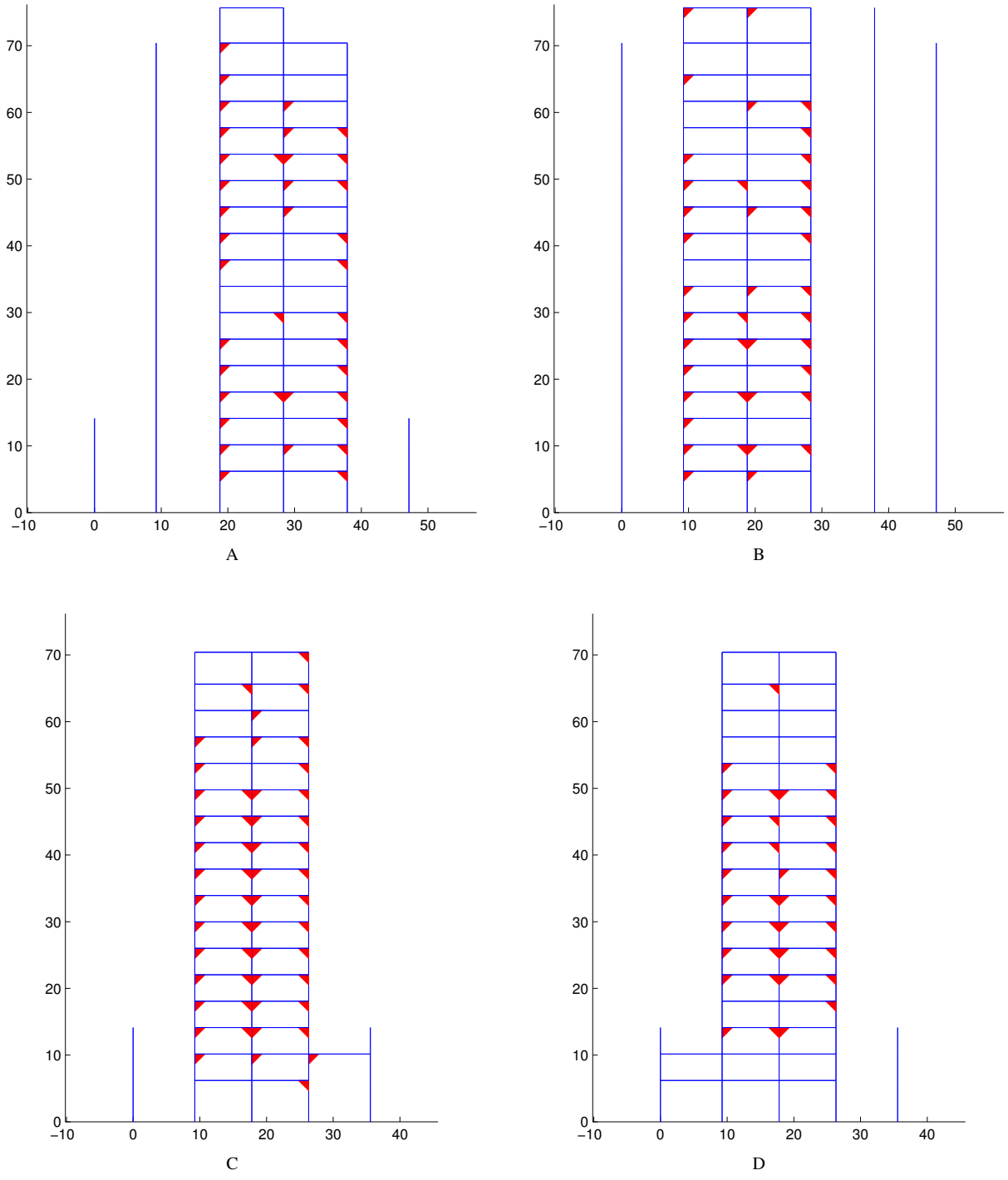

Figure F.11: Beam bottom-flange weld fracture locations in the moment-frames of the existing building model: Northridge – (A) Moment-frame along grid A (east-west direction); (B) Moment-frame along grid D (east-west direction); (C) Moment-frame along grid 1 (north-south direction); (D) Moment-frame along grid 6 (north-south direction). See Figure 2.2 for moment-frame configuration.

F.2.2 Redesigned Building Performance

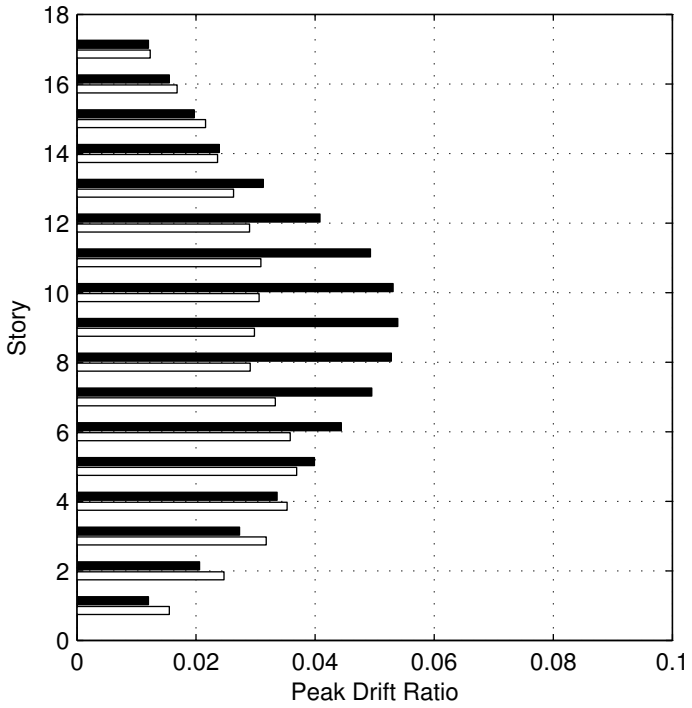

Figure F.12: Peak east-west/X (white bars) and north-south/Y (black bars) drifts in each story of the redesigned building model: Northridge.

Component	Components within each perf. category				Perf. Level	Force-controlled components	
	IO	LS	CP	CO (> CP)		Not Yielded	Yielded
Panel Zone	200	105	8	0	CP	–	–
Beam Major Axis	270	275	5	0	CP	–	–
Beam Minor Axis	550	0	0	0	IO	–	–
Column Major Axis	640	66	0	0	LS	110	124
Column Minor Axis	686	20	0	0	LS	110	124

Table F.7: Classification of redesigned building model performance based on plastic rotation in panel zones, and at the ends of beams and columns, using FEMA356 acceptance criteria: Northridge.

Component	Components in the following plastic rotation ranges							
	$\leq$ 0.1%	(0.1-1.0]%	(1.0-2.0]%	(2.0-3.0]%	(3.0-4.0]%	(4.0-5.0]%	(5.0-6.0]%	$>$ 6.0%
Panel Zone	186	60	59	8	0	0	0	0
Beam Major Axis	232	90	138	60	26	4	0	0
Beam Minor Axis	282	251	17	0	0	0	0	0
Column Major Axis	828	112	0	0	0	0	0	0
Column Minor Axis	890	50	0	0	0	0	0	0

Table F.8: Plastic rotation in panel zones, and at the ends of beams and columns of the redesigned building model: Northridge.

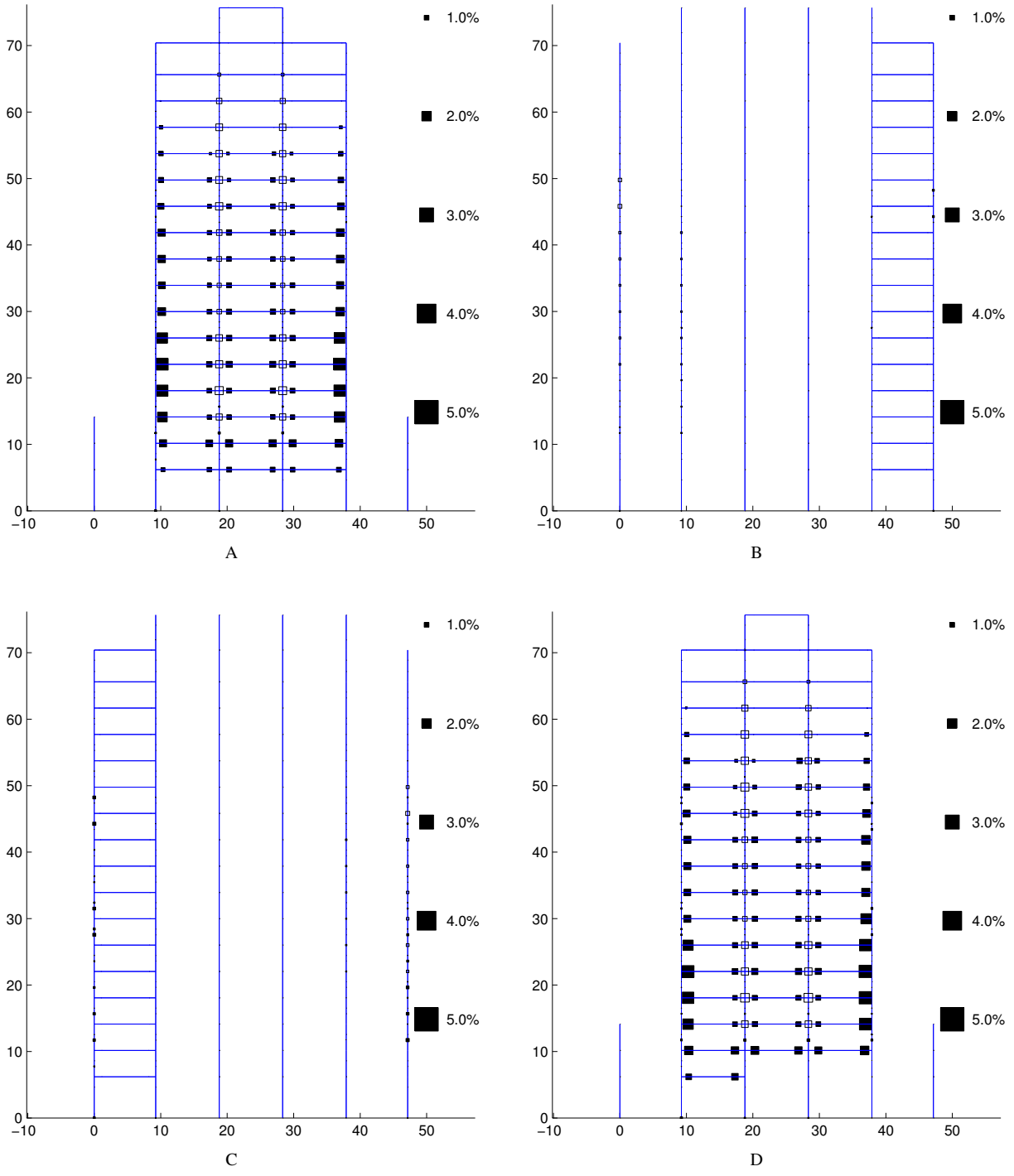

Figure F.13: Plastic rotation in percent of a radian in the moment-frames of the redesigned building model: Northridge – (A) Moment-frame along grid A (east-west direction); (B) Moment-frame along grid B (east-west direction); (C) Moment-frame along grid D (east-west direction); (D) Moment-frame along grid E (east-west direction). See Figure 2.3 for moment-frame configuration.

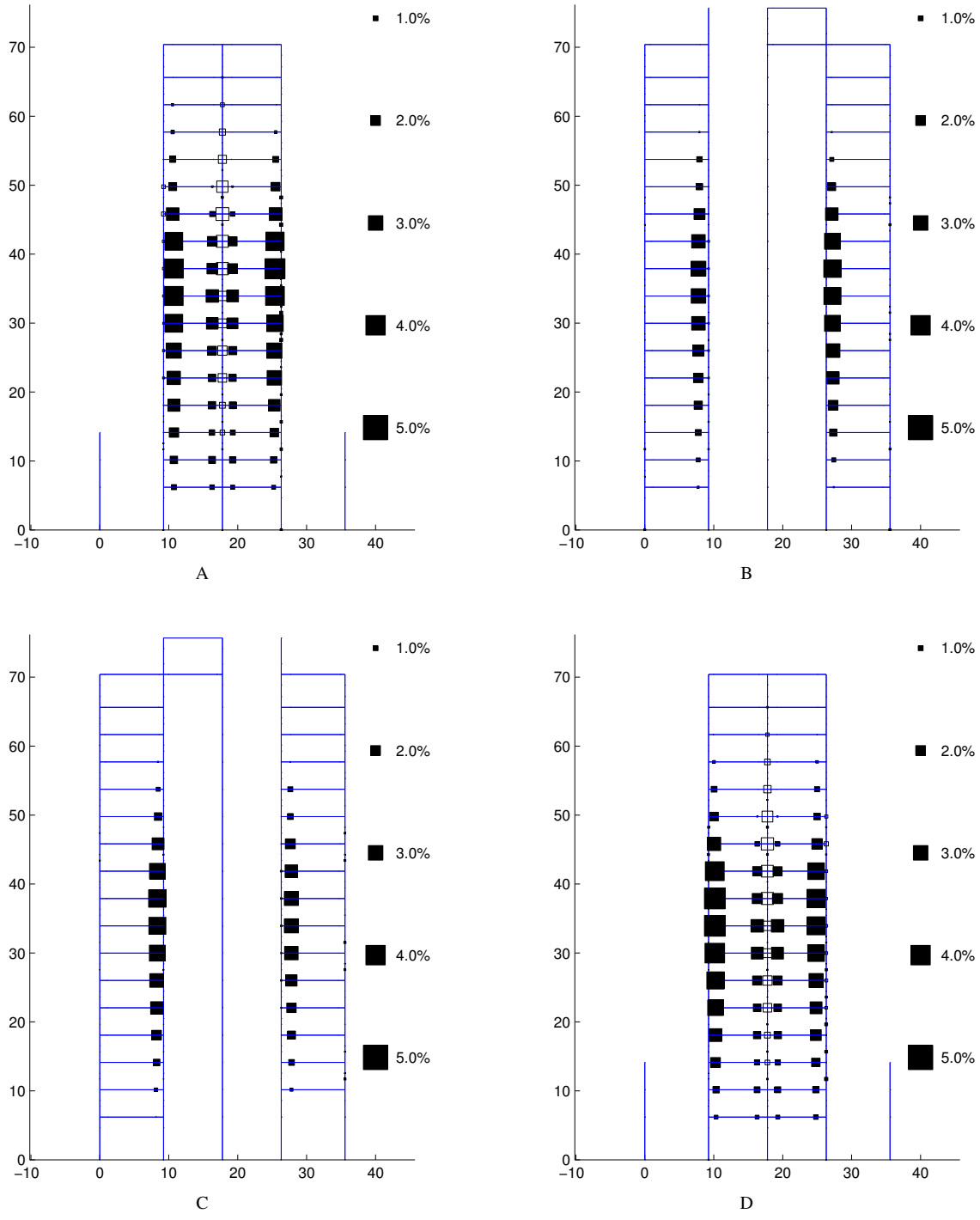

Figure F.14: Plastic rotation in percent of a radian in the moment-frames of the redesigned building model: Northridge – (A) Moment-frame along grid 1 (north-south direction); (B) Moment-frame along grid 2 (north-south direction); (C) Moment-frame along grid 5 (north-south direction); (D) Moment-frame along grid 6 (north-south direction). See Figure 2.3 for moment-frame configuration.

F.3 Site: West Los Angeles (Latitude 34.03125, Longitude 118.40625)

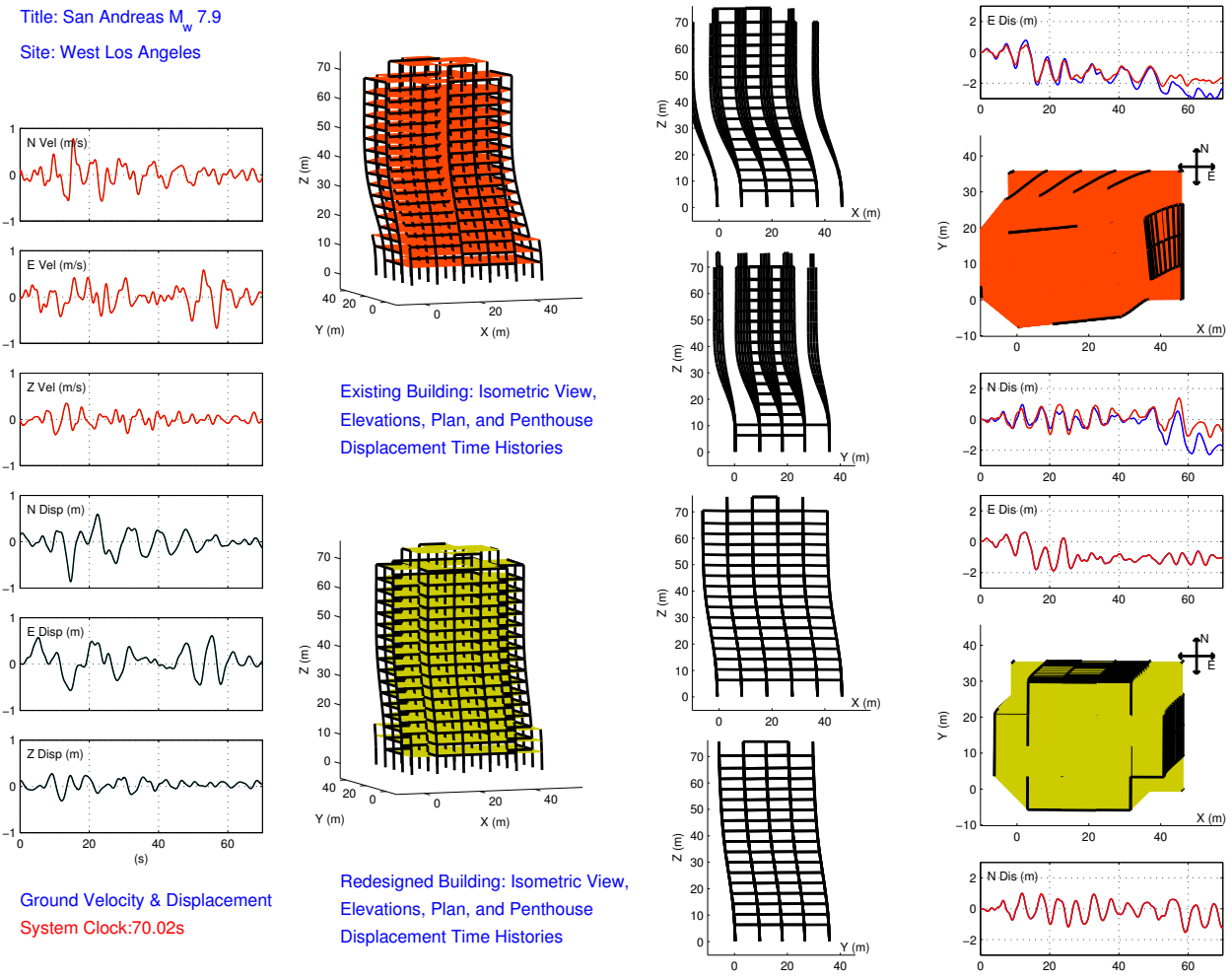

Figure F.15: $M_w 7.9$ earthquake (south-to-north rupture) on the San Andreas fault – snapshot of building deformation immediately following the earthquake (scaled up by a factor of 5): West Los Angeles. Also shown are the time-histories of the three components of the ground velocity and displacement (bandpass-filtered between 2 s and 1000 s), and the east and north components of the penthouse displacement of the existing and redesigned building models.

F.3.1 Existing Building Performance

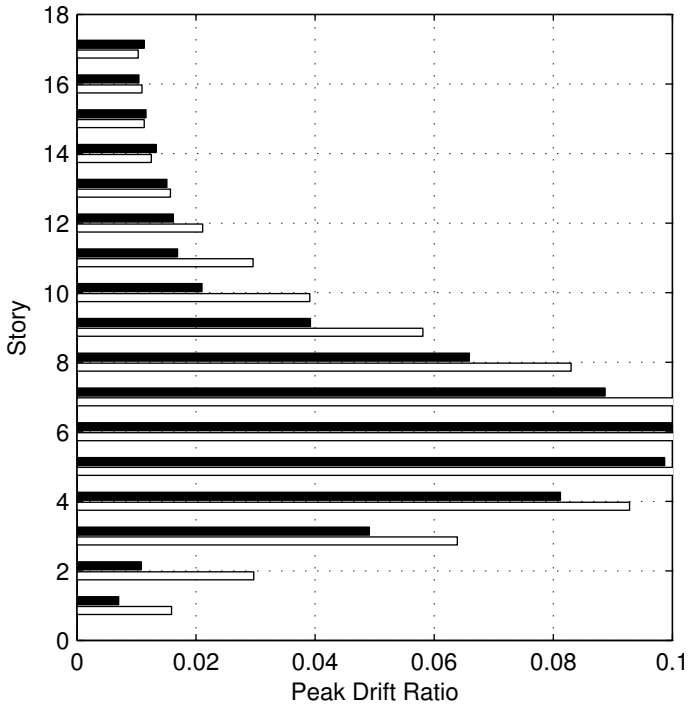

Figure F.16: Peak east-west/X (white bars) and north-south/Y (black bars) drifts in each story of the existing building model: West Los Angeles (the drift scale is saturated at 0.10).

Component	Components within each perf. category				Perf. Level	Force-controlled components	
	IO	LS	CP	CO (> CP)		Not Yielded	Yielded
Panel Zone	135	53	5	19	CO	–	–
Beam Major Axis	160	57	10	57	CO	–	–
Beam Minor Axis	222	61	1	0	CP	–	–
Column Major Axis	888	40	4	6	CO	2	0
Column Minor Axis	893	38	3	4	CO	2	0

Table F.9: Classification of existing building model performance based on plastic rotation in panel zones, and at the ends of beams and columns, using FEMA356 acceptance criteria: West Los Angeles.

Component	Components in the following plastic rotation ranges							
	$\leq$ 0.1%	(0.1-1.0]%	(1.0-2.0]%	(2.0-3.0]%	(3.0-4.0]%	(4.0-5.0]%	(5.0-6.0]%	> 6.0%
Panel Zone	107	70	13	9	4	6	3	0
Beam Major Axis	140	29	10	29	14	9	14	39
Beam Minor Axis	147	61	18	17	10	7	5	19
Column Major Axis	875	51	10	2	2	0	0	0
Column Minor Axis	878	51	8	2	1	0	0	0

Table F.10: Plastic rotation in panel zones, and at the ends of beams and columns of the existing building model: West Los Angeles.

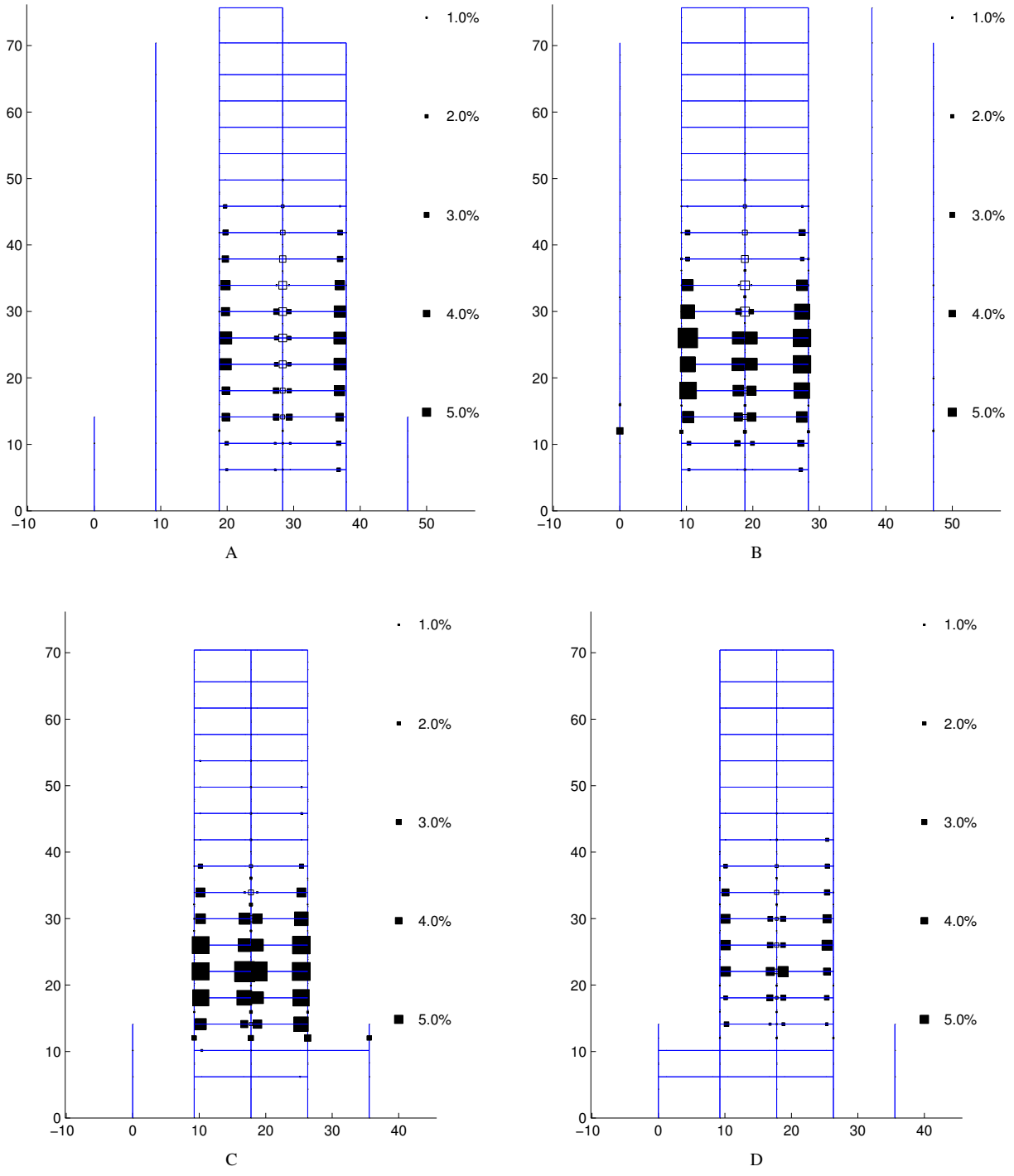

Figure F.17: Plastic rotation in percent of a radian in the moment-frames of the existing building model: West Los Angeles – (A) Moment-frame along grid A (east-west direction); (B) Moment-frame along grid D (east-west direction); (C) Moment-frame along grid 1 (north-south direction); (D) Moment-frame along grid 6 (north-south direction). See Figure 2.2 for moment-frame configuration.

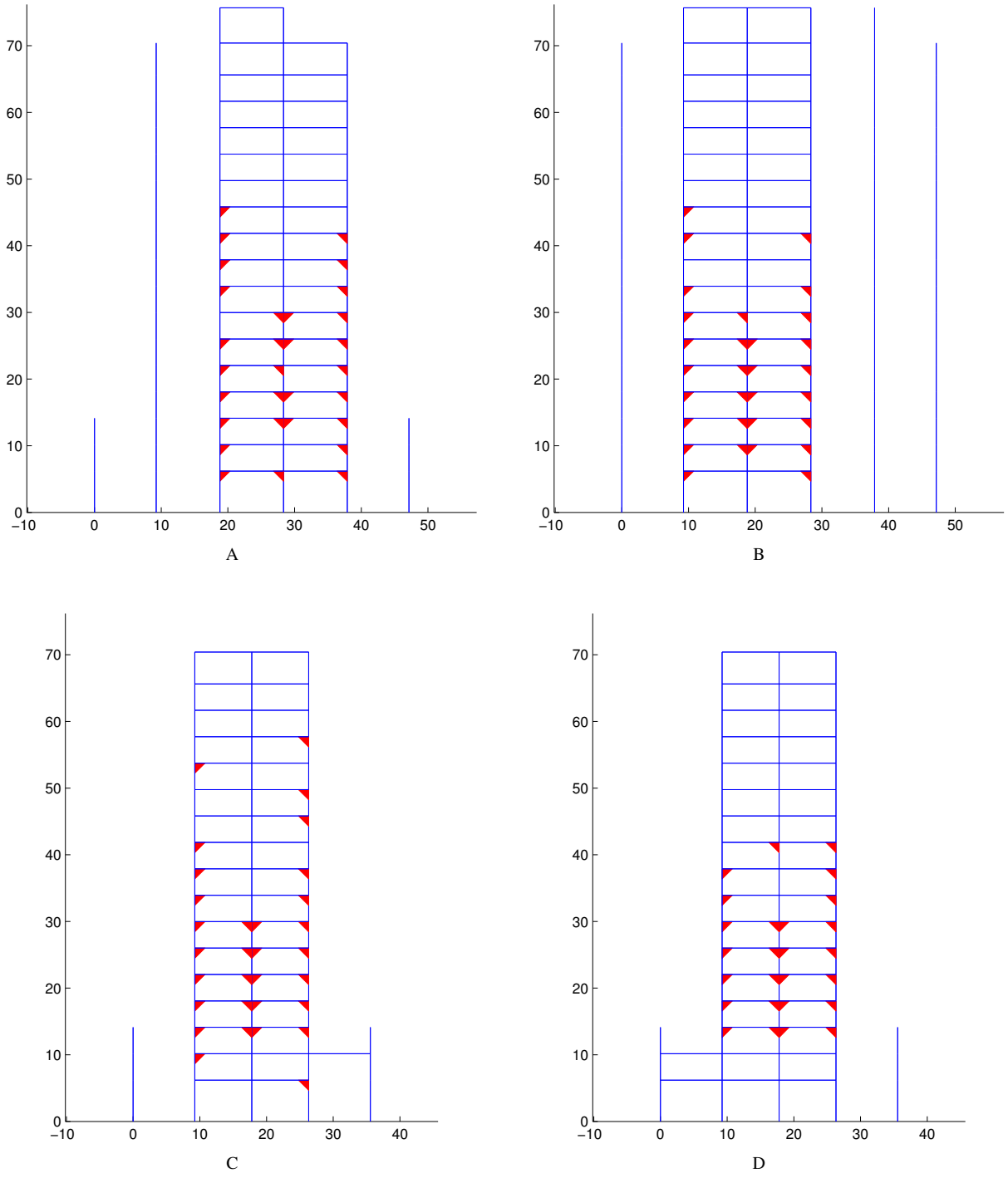

Figure F.18: Beam bottom-flange weld fracture locations in the moment-frames of the existing building model: West Los Angeles – (A) Moment-frame along grid A (east-west direction); (B) Moment-frame along grid D (east-west direction); (C) Moment-frame along grid 1 (north-south direction); (D) Moment-frame along grid 6 (north-south direction). See Figure 2.2 for moment-frame configuration.

F.3.2 Redesigned Building Performance

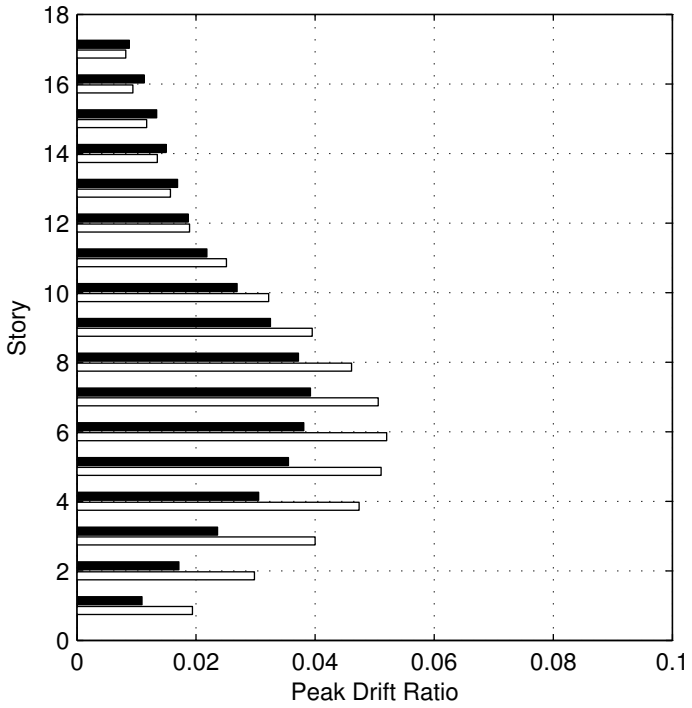

Figure F.19: Peak east-west/X (white bars) and north-south/Y (black bars) drifts in each story of the redesigned building model: West Los Angeles.

Component	Components within each perf. category				Perf. Level	Force-controlled components	
	IO	LS	CP	CO (> CP)		Not Yielded	Yielded
Panel Zone	227	74	12	0	CP	–	–
Beam Major Axis	344	206	0	0	LS	–	–
Beam Minor Axis	550	0	0	0	IO	–	–
Column Major Axis	660	64	1	1	CO	96	118
Column Minor Axis	714	12	0	0	LS	96	118

Table F.11: Classification of redesigned building model performance based on plastic rotation in panel zones, and at the ends of beams and columns, using FEMA356 acceptance criteria: West Los Angeles.

Component	Components in the following plastic rotation ranges							
	$\leq$ 0.1%	(0.1-1.0]%	(1.0-2.0]%	(2.0-3.0]%	(3.0-4.0]%	(4.0-5.0]%	(5.0-6.0]%	$>$ 6.0%
Panel Zone	204	69	28	12	0	0	0	0
Beam Major Axis	298	77	93	59	16	7	0	0
Beam Minor Axis	337	190	23	0	0	0	0	0
Column Major Axis	839	101	0	0	0	0	0	0
Column Minor Axis	904	36	0	0	0	0	0	0

Table F.12: Plastic rotation in panel zones, and at the ends of beams and columns of the redesigned building model: West Los Angeles.

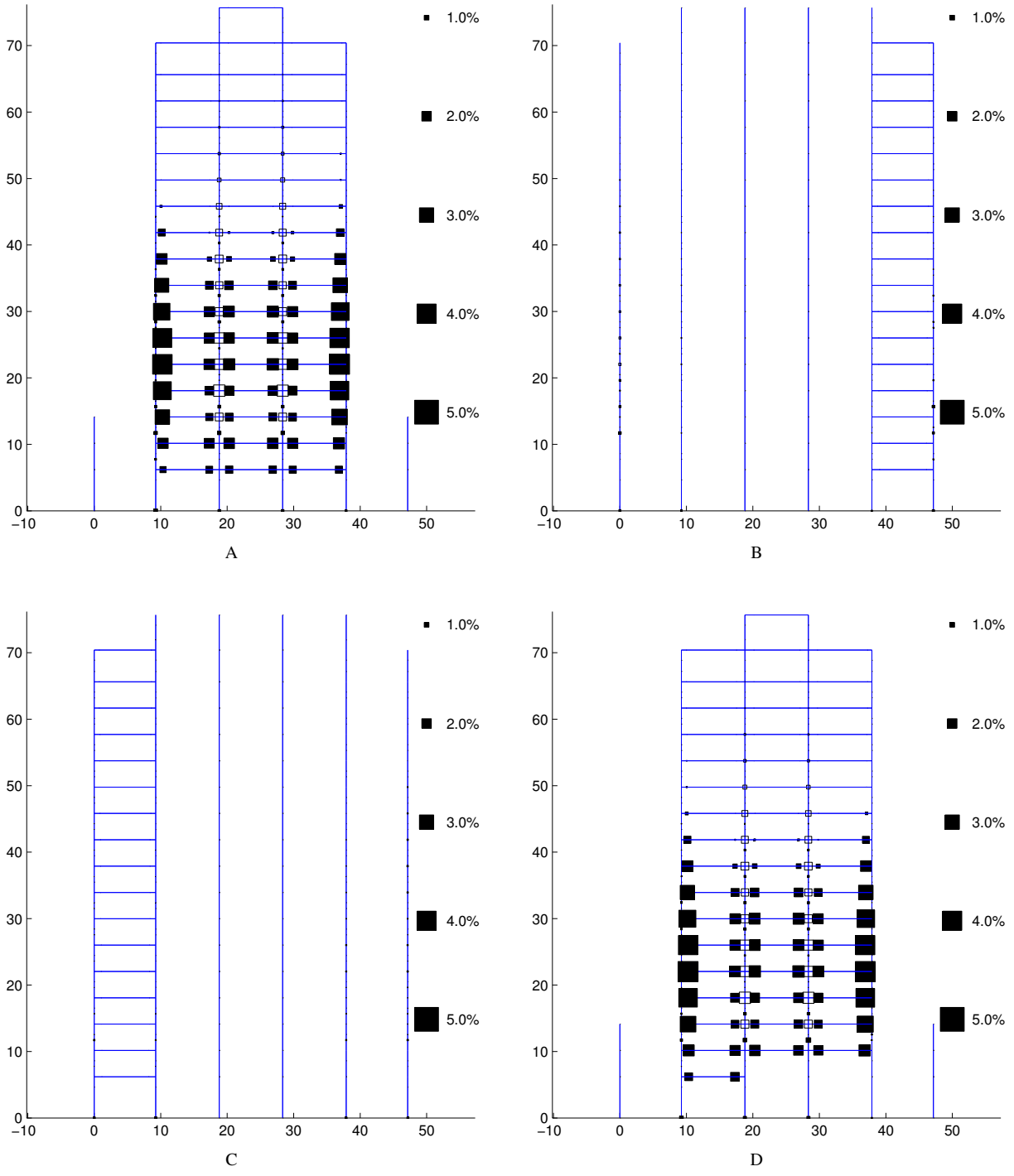

Figure F.20: Plastic rotation in percent of a radian in the moment-frames of the redesigned building model: West Los Angeles – (A) Moment-frame along grid A (east-west direction); (B) Moment-frame along grid B (east-west direction); (C) Moment-frame along grid D (east-west direction); (D) Moment-frame along grid E (east-west direction). See Figure 2.3 for moment-frame configuration.

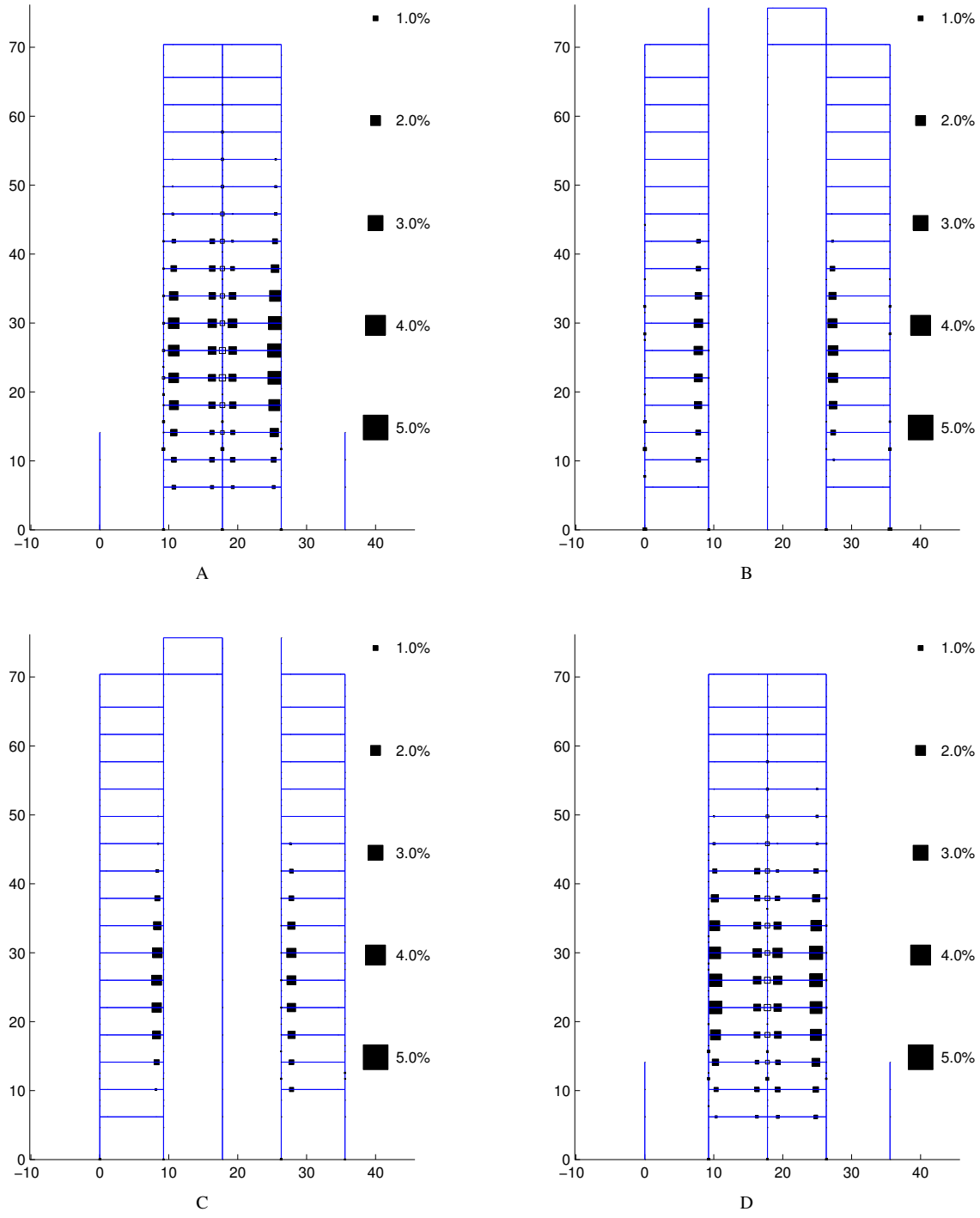

Figure F.21: Plastic rotation in percent of a radian in the moment-frames of the redesigned building model: West Los Angeles – (A) Moment-frame along grid 1 (north-south direction); (B) Moment-frame along grid 2 (north-south direction); (C) Moment-frame along grid 5 (north-south direction); (D) Moment-frame along grid 6 (north-south direction). See Figure 2.3 for moment-frame configuration.

F.4 Site: Downtown Los Angeles (Latitude 34.06250, Longitude 118.25000)

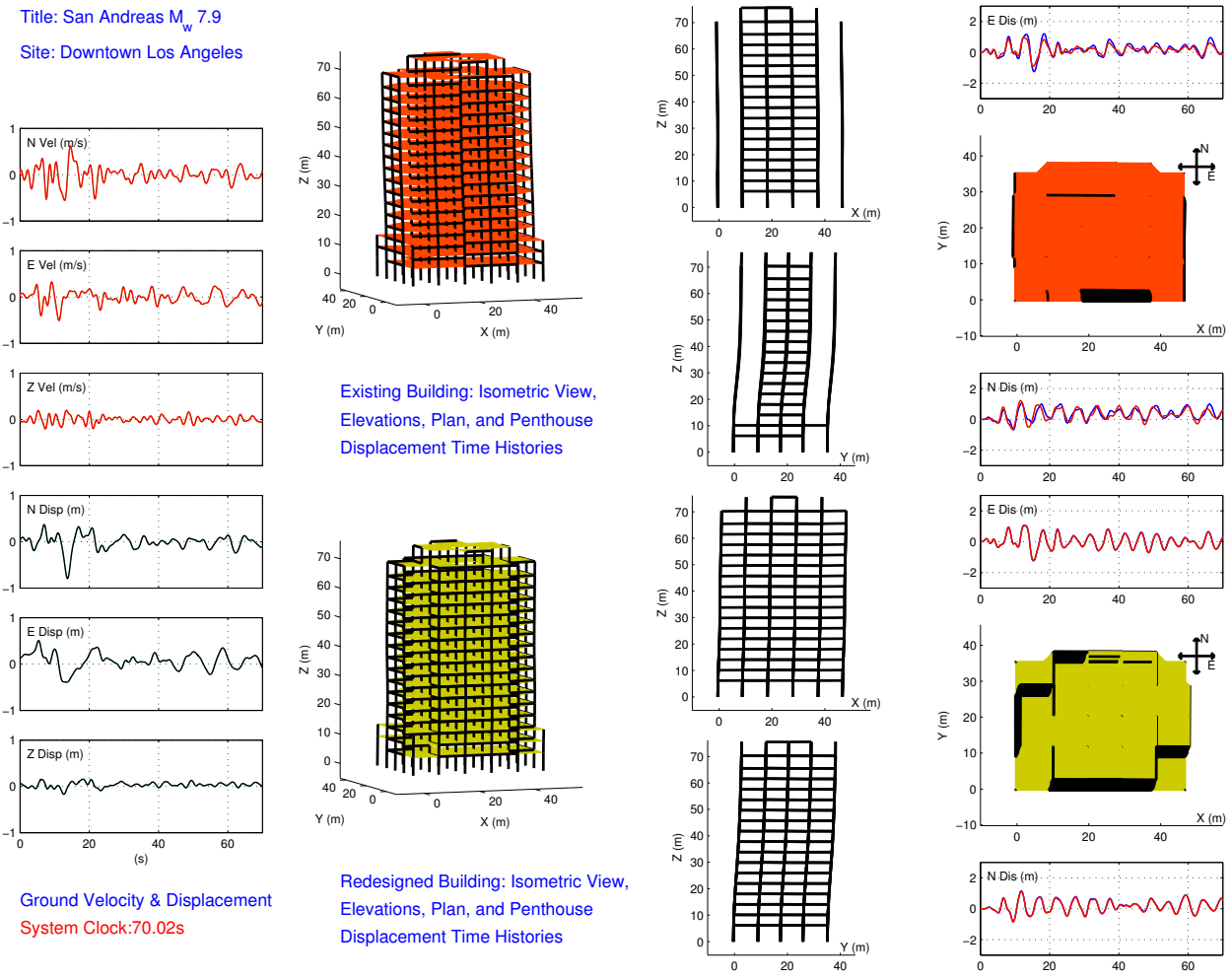

Figure F.22: M_w7.9 earthquake (south-to-north rupture) on the San Andreas fault – snapshot of building deformation immediately following the earthquake (scaled up by a factor of 5): Downtown Los Angeles. Also shown are the time-histories of the three components of the ground velocity and displacement (bandpass-filtered between 2 s and 1000 s), and the east and north components of the penthouse displacement of the existing and redesigned building models.

F.4.1 Existing Building Performance

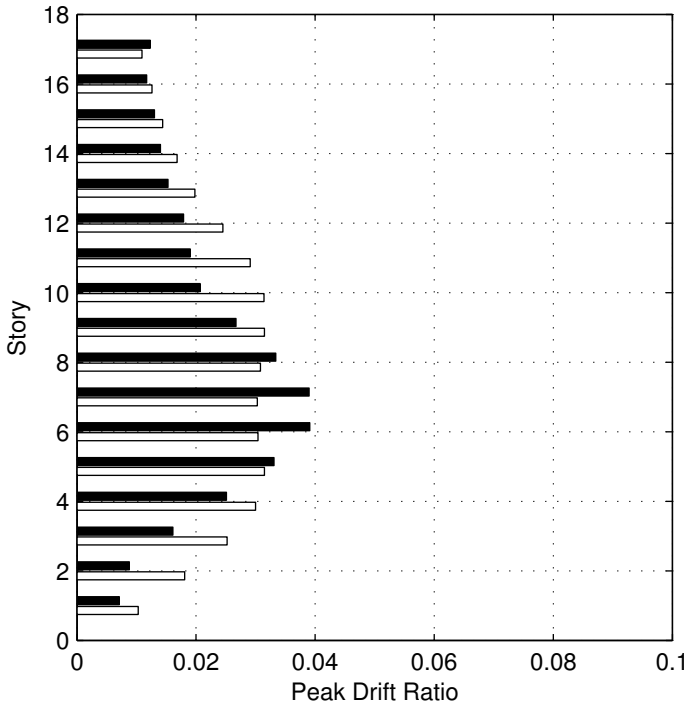

Figure F.23: Peak east-west/X (white bars) and north-south/Y (black bars) drifts in each story of the existing building model: Downtown Los Angeles.

Component	Components within each perf. category				Perf. Level	Force-controlled components	
	IO	LS	CP	CO (> CP)		Not Yielded	Yielded
Panel Zone	130	65	11	6	CO	–	–
Beam Major Axis	196	84	4	0	CP	–	–
Beam Minor Axis	277	7	0	0	LS	–	–
Column Major Axis	932	2	0	0	LS	2	4
Column Minor Axis	934	0	0	0	IO	2	4

Table F.13: Classification of existing building model performance based on plastic rotation in panel zones, and at the ends of beams and columns, using FEMA356 acceptance criteria: Downtown Los Angeles.

Component	Components in the following plastic rotation ranges							
	$\leq$ 0.1%	(0.1-1.0]%	(1.0-2.0]%	(2.0-3.0]%	(3.0-4.0]%	(4.0-5.0]%	(5.0-6.0]%	> 6.0%
Panel Zone	107	70	21	13	1	0	0	0
Beam Major Axis	167	51	39	22	5	0	0	0
Beam Minor Axis	190	84	4	5	1	0	0	0
Column Major Axis	937	3	0	0	0	0	0	0
Column Minor Axis	938	2	0	0	0	0	0	0

Table F.14: Plastic rotation in panel zones, and at the ends of beams and columns of the existing building model: Downtown Los Angeles.

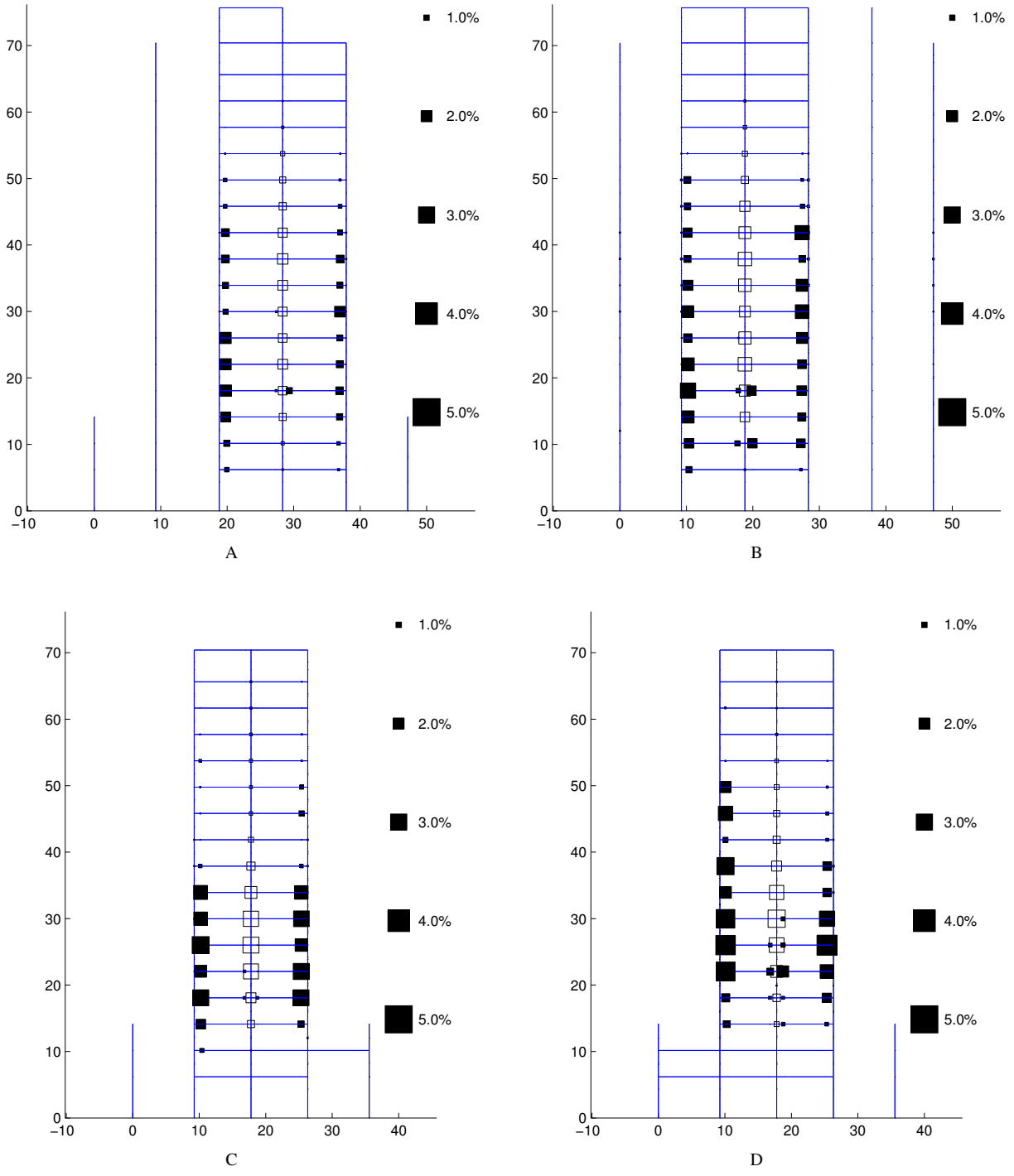

Figure F.24: Plastic rotation in percent of a radian in the moment-frames of the existing building model: Downtown Los Angeles – (A) Moment-frame along grid A (east-west direction); (B) Moment-frame along grid D (east-west direction); (C) Moment-frame along grid 1 (north-south direction); (D) Moment-frame along grid 6 (north-south direction). See Figure 2.2 for moment-frame configuration.

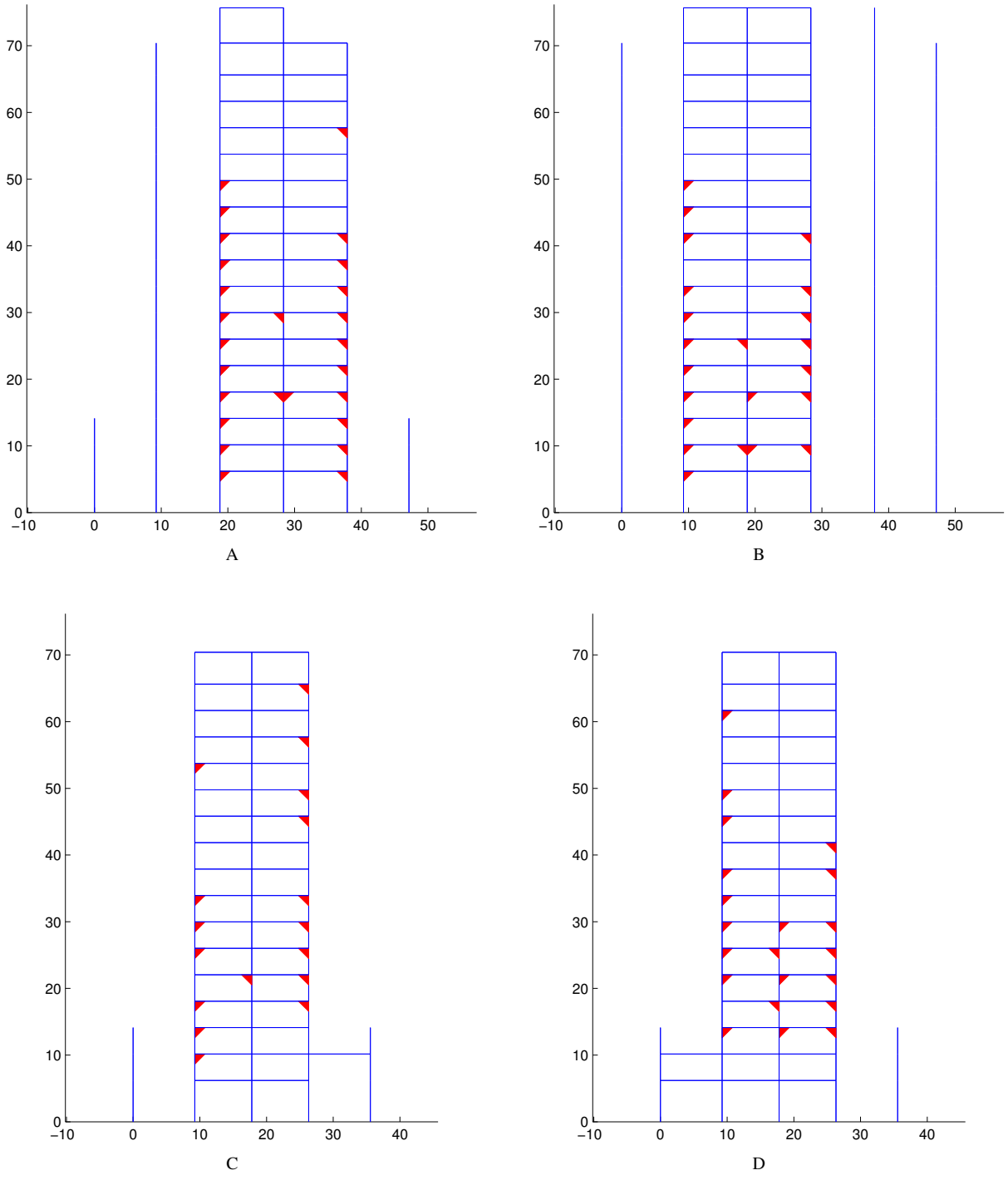

Figure F.25: Beam bottom-flange weld fracture locations in the moment-frames of the existing building model: Downtown Los Angeles – (A) Moment-frame along grid A (east-west direction); (B) Moment-frame along grid D (east-west direction); (C) Moment-frame along grid 1 (north-south direction); (D) Moment-frame along grid 6 (north-south direction). See Figure 2.2 for moment-frame configuration.

F.4.2 Redesigned Building Performance

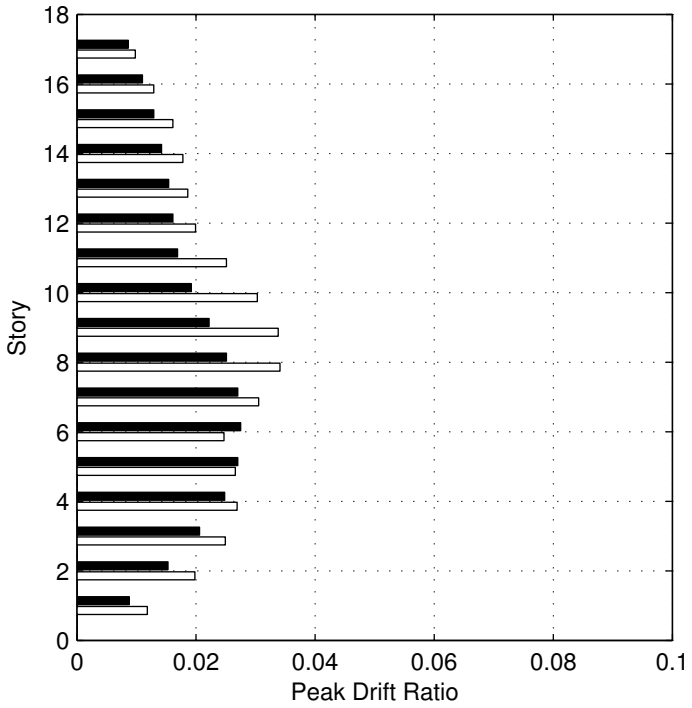

Figure F.26: Peak east-west/X (white bars) and north-south/Y (black bars) drifts in each story of the redesigned building model: Downtown Los Angeles.

Component	Components within each perf. category				Perf. Level	Force-controlled components	
	IO	LS	CP	CO (> CP)		Not Yielded	Yielded
Panel Zone	232	81	0	0	LS	–	–
Beam Major Axis	394	156	0	0	LS	–	–
Beam Minor Axis	550	0	0	0	IO	–	–
Column Major Axis	702	20	0	0	LS	100	118
Column Minor Axis	719	3	0	0	LS	100	118

Table F.15: Classification of redesigned building model performance based on plastic rotation in panel zones, and at the ends of beams and columns, using FEMA356 acceptance criteria: Downtown Los Angeles.

Component	Components in the following plastic rotation ranges							
	$\leq$ 0.1%	(0.1-1.0]%	(1.0-2.0]%	(2.0-3.0]%	(3.0-4.0]%	(4.0-5.0]%	(5.0-6.0]%	$>$ 6.0%
Panel Zone	208	82	23	0	0	0	0	0
Beam Major Axis	309	143	92	6	0	0	0	0
Beam Minor Axis	383	167	0	0	0	0	0	0
Column Major Axis	912	28	0	0	0	0	0	0
Column Minor Axis	936	4	0	0	0	0	0	0

Table F.16: Plastic rotation in panel zones, and at the ends of beams and columns of the redesigned building model: Downtown Los Angeles.

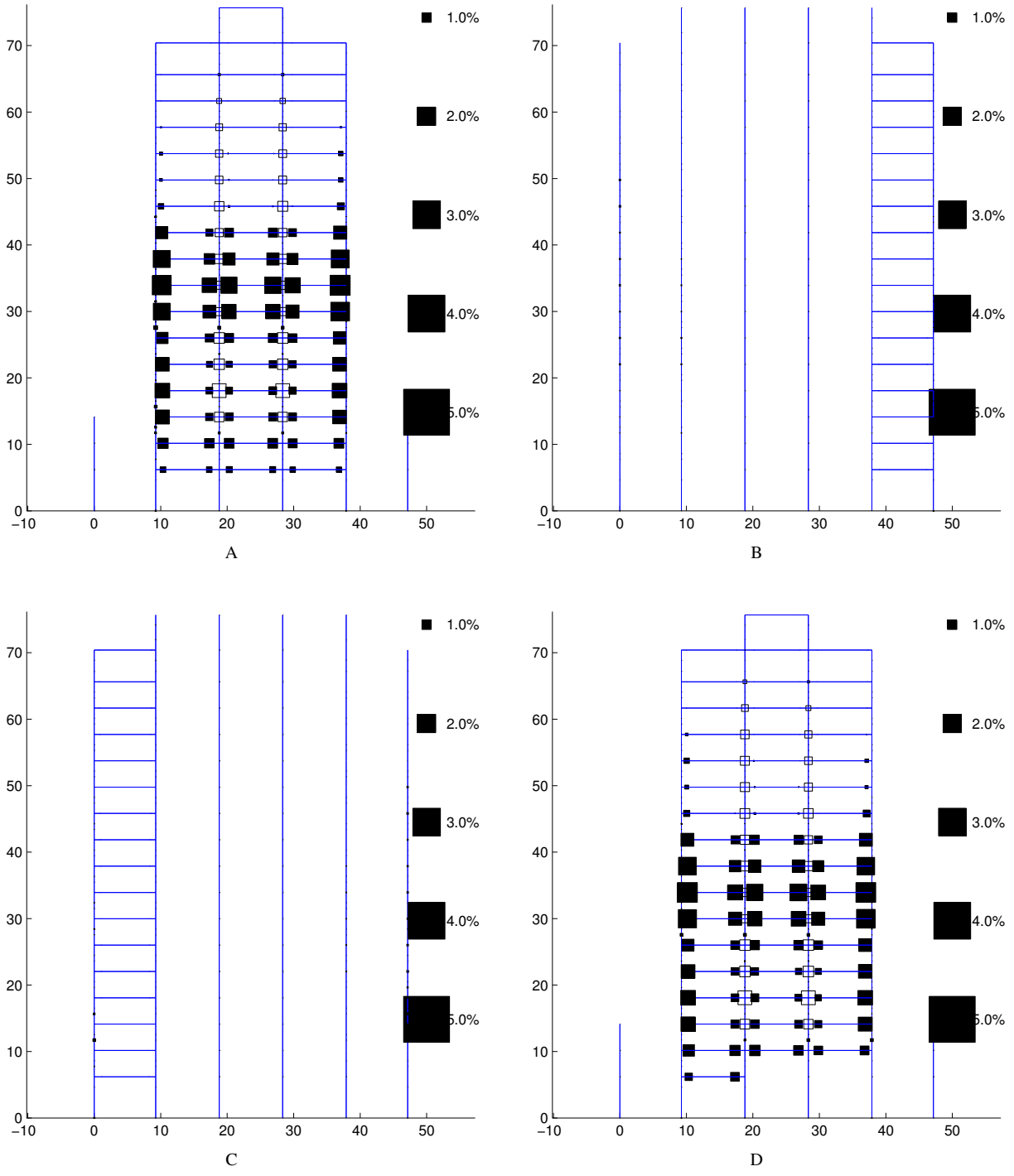

Figure F.27: Plastic rotation in percent of a radian in the moment-frames of the redesigned building model: Downtown Los Angeles – (A) Moment-frame along grid A (east-west direction); (B) Moment-frame along grid B (east-west direction); (C) Moment-frame along grid D (east-west direction); (D) Moment-frame along grid E (east-west direction). See Figure 2.3 for moment-frame configuration.

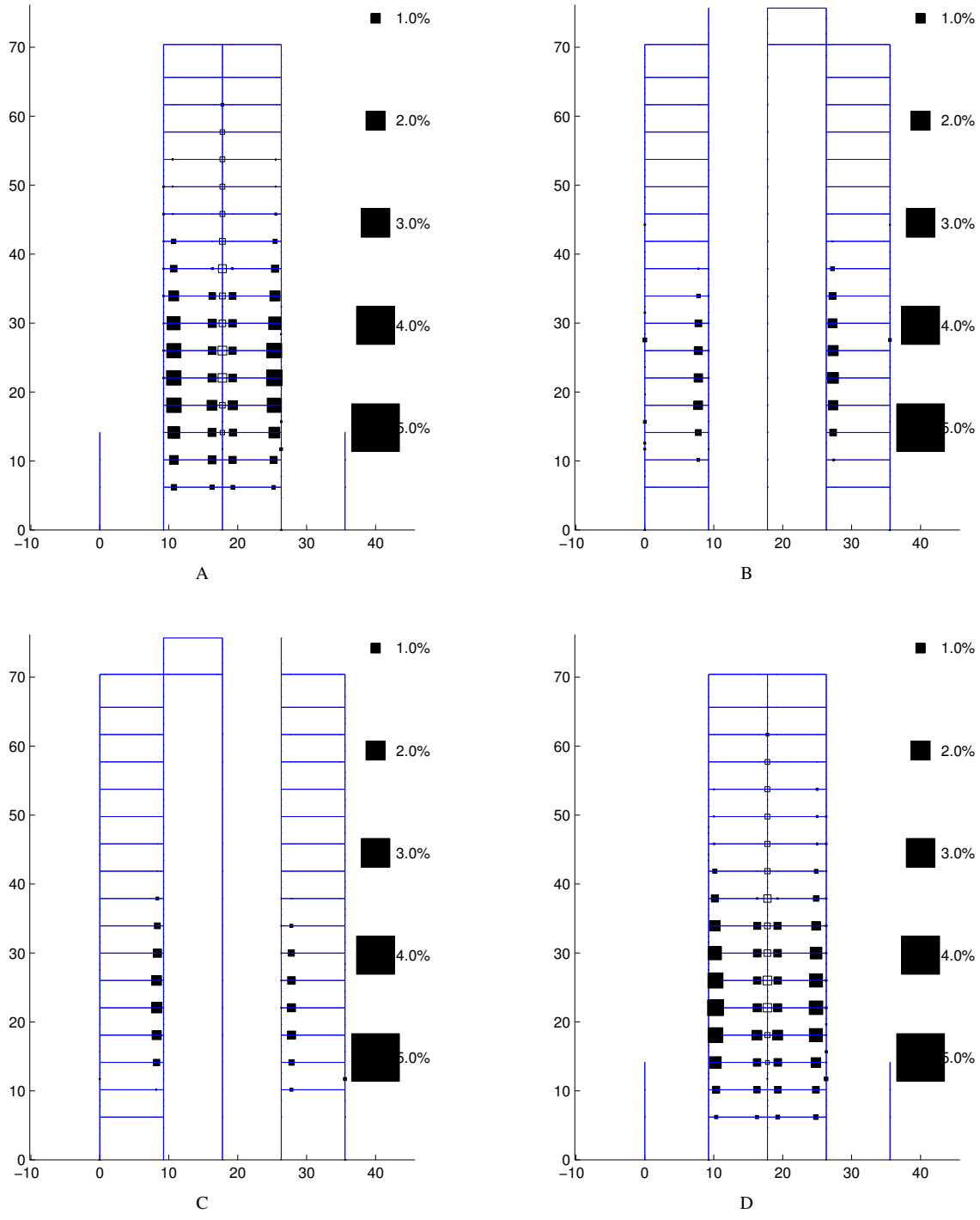

Figure F.28: Plastic rotation in percent of a radian in the moment-frames of the redesigned building model: Downtown Los Angeles – (A) Moment-frame along grid 1 (north-south direction); (B) Moment-frame along grid 2 (north-south direction); (C) Moment-frame along grid 5 (north-south direction); (D) Moment-frame along grid 6 (north-south direction). See Figure 2.3 for moment-frame configuration.

F.5 Site: Baldwin Park (Latitude 34.09375, Longitude 118.00000)

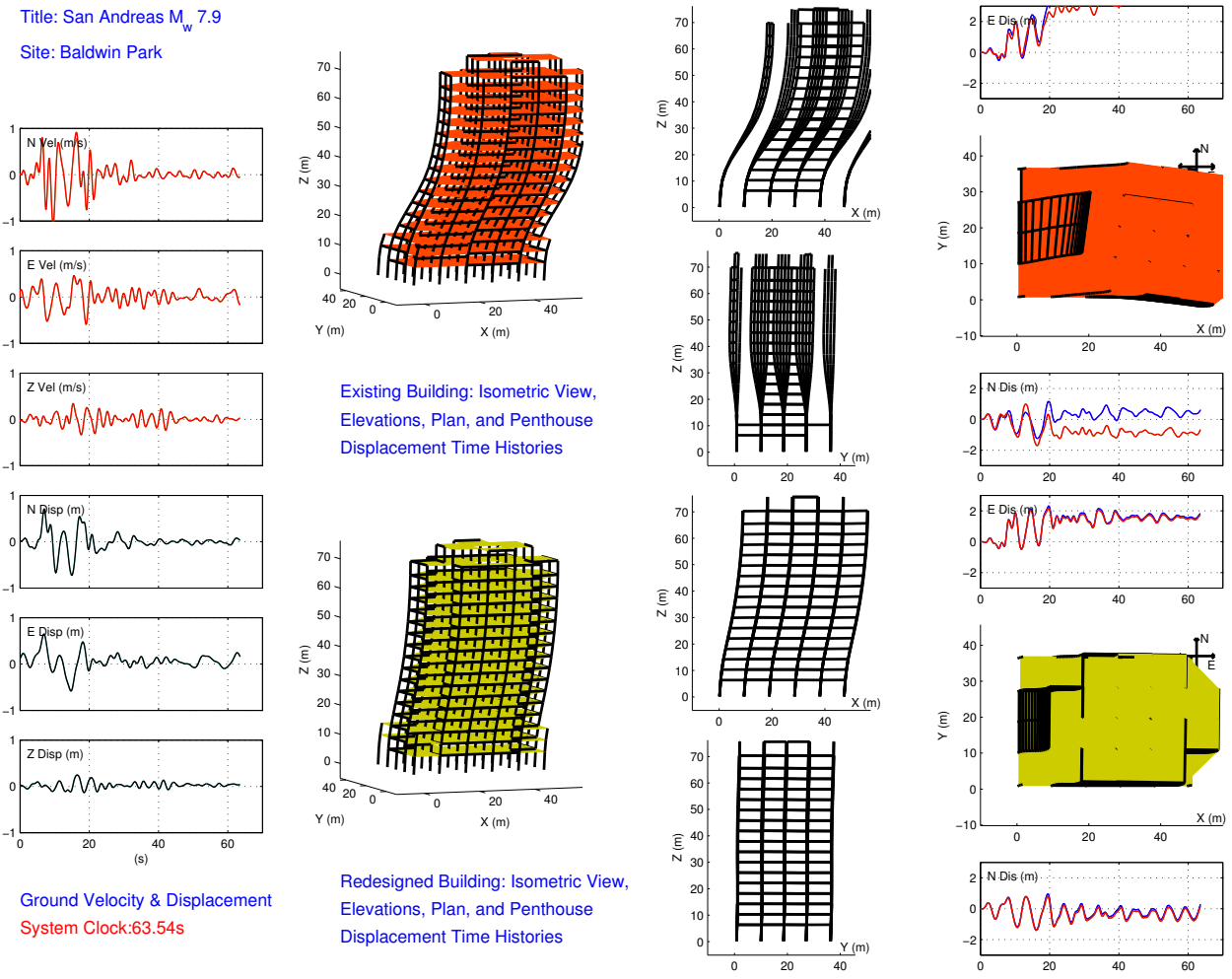

Figure F.29: M_w7.9 earthquake (south-to-north rupture) on the San Andreas fault – snapshot of building deformation immediately following the earthquake (scaled up by a factor of 5): Baldwin Park. Also shown are the time-histories of the three components of the ground velocity and displacement (bandpass-filtered between 2 s and 1000 s), and the east and north components of the penthouse displacement of the existing and redesigned building models.

F.5.1 Existing Building Performance

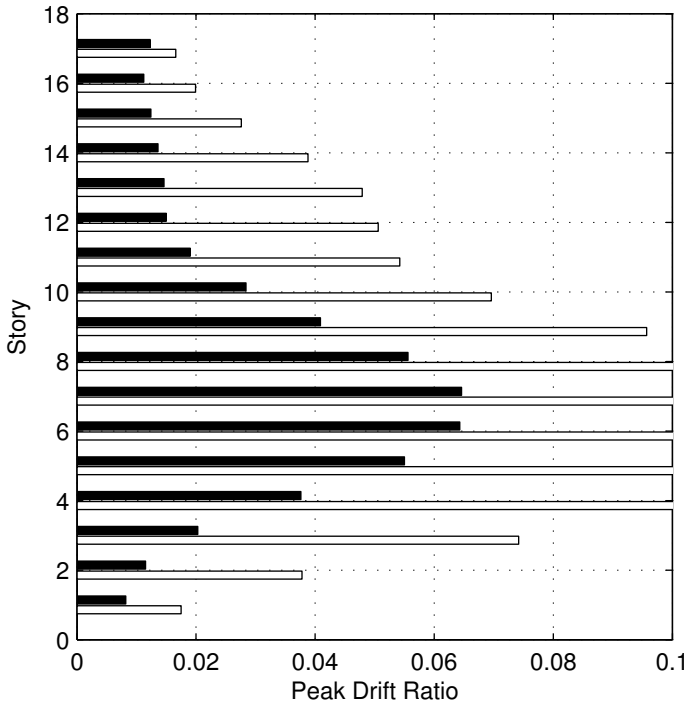

Figure F.30: Peak east-west/X (white bars) and north-south/Y (black bars) drifts in each story of the existing building model: Baldwin Park (the drift scale is saturated at 0.10).

Component	Components within each perf. category				Perf. Level	Force-controlled components	
	IO	LS	CP	CO (> CP)		Not Yielded	Yielded
Panel Zone	120	60	6	26	CO	–	–
Beam Major Axis	130	79	23	52	CO	–	–
Beam Minor Axis	218	61	5	0	CP	–	–
Column Major Axis	877	35	3	5	CO	10	10
Column Minor Axis	890	27	0	3	CO	14	6

Table F.17: Classification of existing building model performance based on plastic rotation in panel zones, and at the ends of beams and columns, using FEMA356 acceptance criteria: Baldwin Park.

Component	Components in the following plastic rotation ranges							
	$\leq$ 0.1%	(0.1-1.0]%	(1.0-2.0]%	(2.0-3.0]%	(3.0-4.0]%	(4.0-5.0]%	(5.0-6.0]%	> 6.0%
Panel Zone	96	68	17	9	7	6	5	4
Beam Major Axis	104	44	24	26	20	17	7	42
Beam Minor Axis	113	74	37	23	11	9	5	12
Column Major Axis	873	54	8	5	0	0	0	0
Column Minor Axis	885	49	6	0	0	0	0	0

Table F.18: Plastic rotation in panel zones, and at the ends of beams and columns of the existing building model: Baldwin Park.

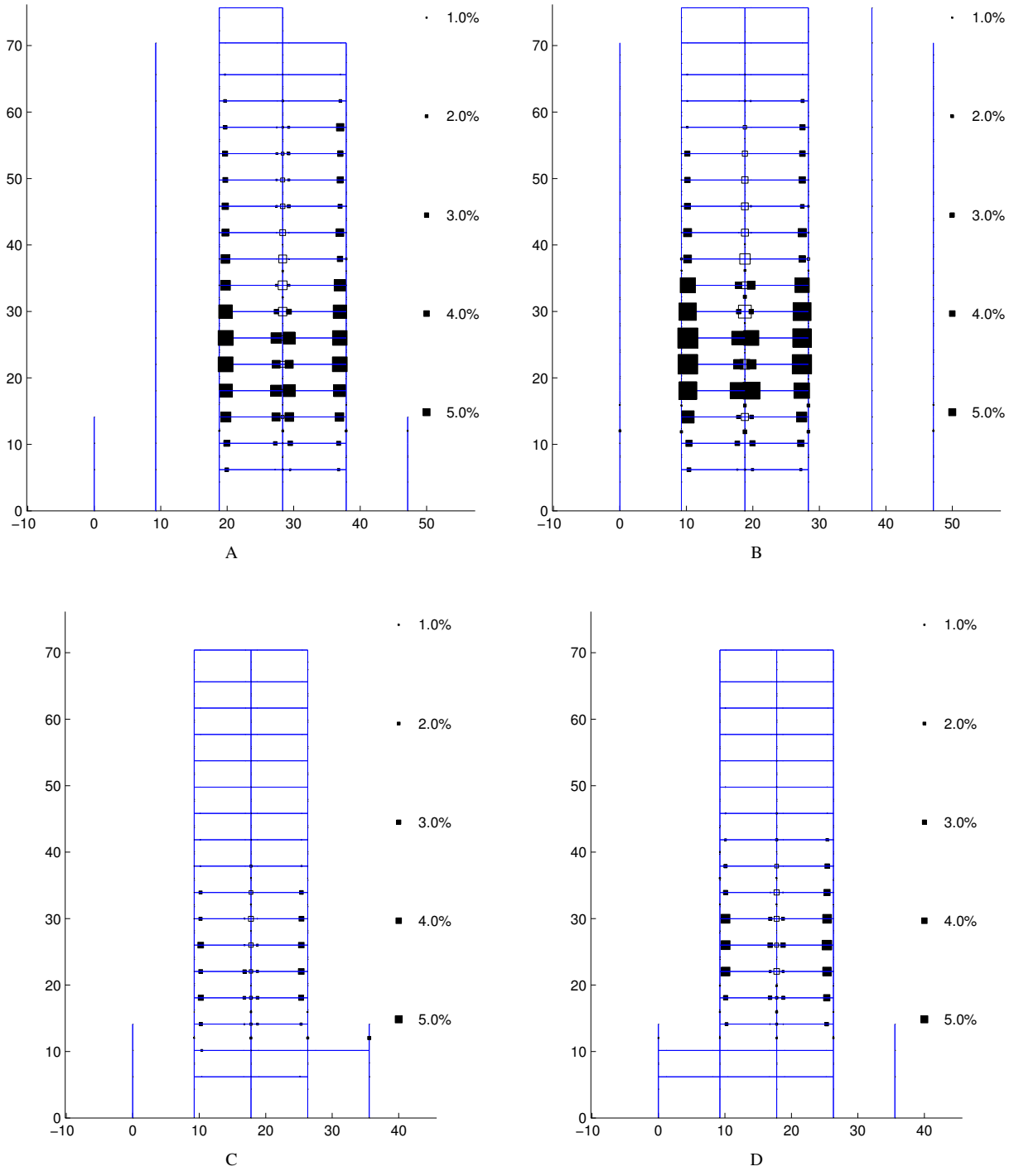

Figure F.31: Plastic rotation in percent of a radian in the moment-frames of the existing building model: Baldwin Park – (A) Moment-frame along grid A (east-west direction); (B) Moment-frame along grid D (east-west direction); (C) Moment-frame along grid 1 (north-south direction); (D) Moment-frame along grid 6 (north-south direction). See Figure 2.2 for moment-frame configuration.

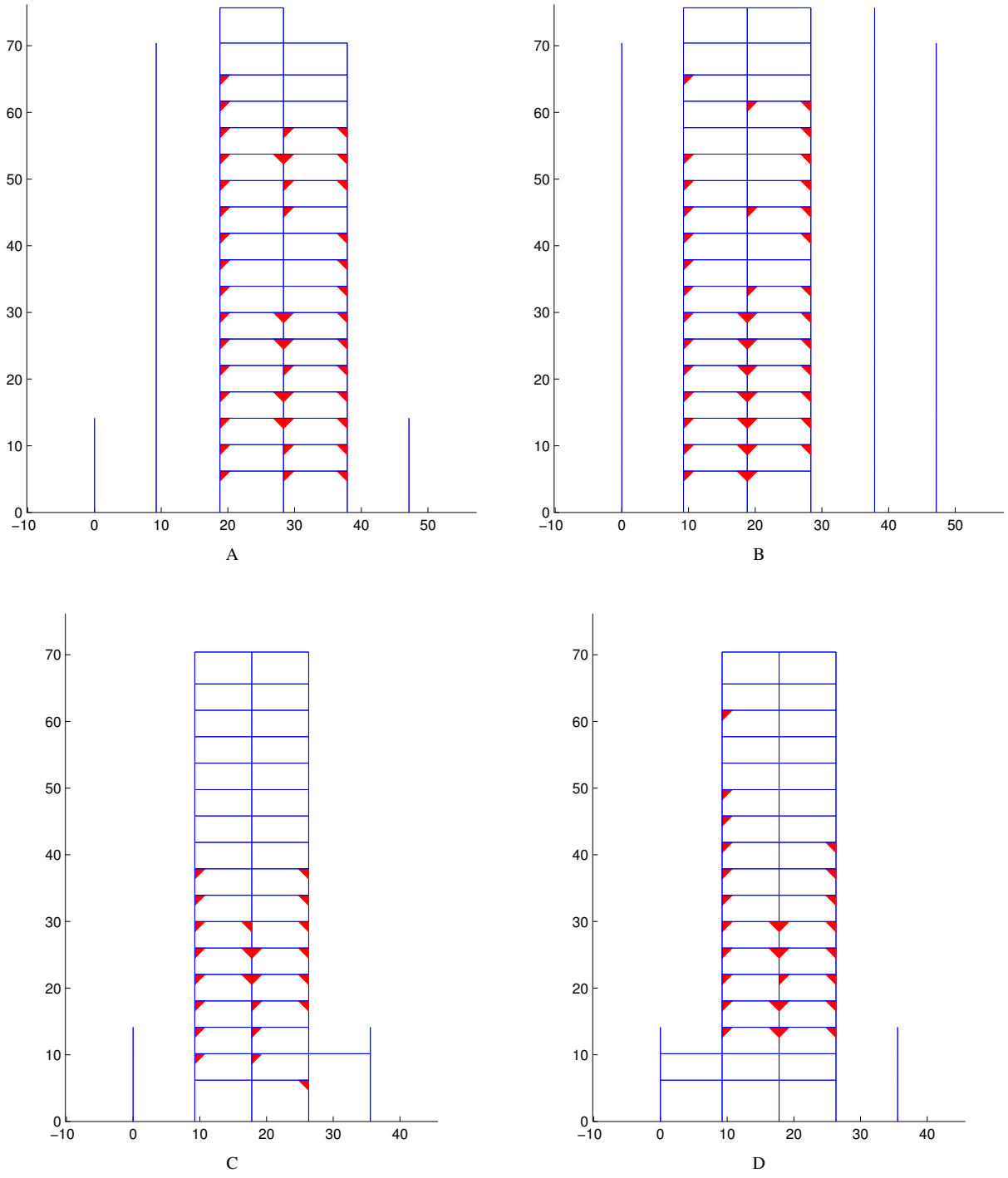

Figure F.32: Beam bottom-flange weld fracture locations in the moment-frames of the existing building model: Baldwin Park – (A) Moment-frame along grid A (east-west direction); (B) Moment-frame along grid D (east-west direction); (C) Moment-frame along grid 1 (north-south direction); (D) Moment-frame along grid 6 (north-south direction). See Figure 2.2 for moment-frame configuration.

F.5.2 Redesigned Building Performance

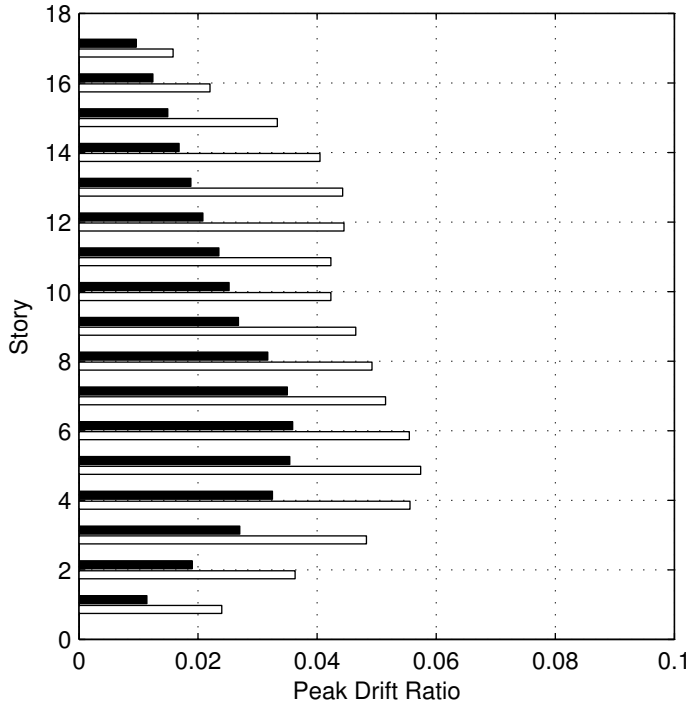

Figure F.33: Peak east-west/X (white bars) and north-south/Y (black bars) drifts in each story of the redesigned building model: Baldwin Park.

Component	Components within each perf. category				Perf. Level	Force-controlled components	
	IO	LS	CP	CO (> CP)		Not Yielded	Yielded
Panel Zone	219	62	29	3	CO	–	–
Beam Major Axis	295	251	4	0	CP	–	–
Beam Minor Axis	550	0	0	0	IO	–	–
Column Major Axis	613	81	5	1	CO	108	132
Column Minor Axis	670	30	0	0	LS	108	132

Table F.19: Classification of redesigned building model performance based on plastic rotation in panel zones, and at the ends of beams and columns, using FEMA356 acceptance criteria: Baldwin Park.

Component	Components in the following plastic rotation ranges							
	$\leq$ 0.1%	(0.1-1.0]%	(1.0-2.0]%	(2.0-3.0]%	(3.0-4.0]%	(4.0-5.0]%	(5.0-6.0]%	> 6.0%
Panel Zone	193	52	36	32	0	0	0	0
Beam Major Axis	249	66	111	92	19	13	0	0
Beam Minor Axis	261	286	3	0	0	0	0	0
Column Major Axis	798	137	5	0	0	0	0	0
Column Minor Axis	879	60	1	0	0	0	0	0

Table F.20: Plastic rotation in panel zones, and at the ends of beams and columns of the redesigned building model: Baldwin Park.

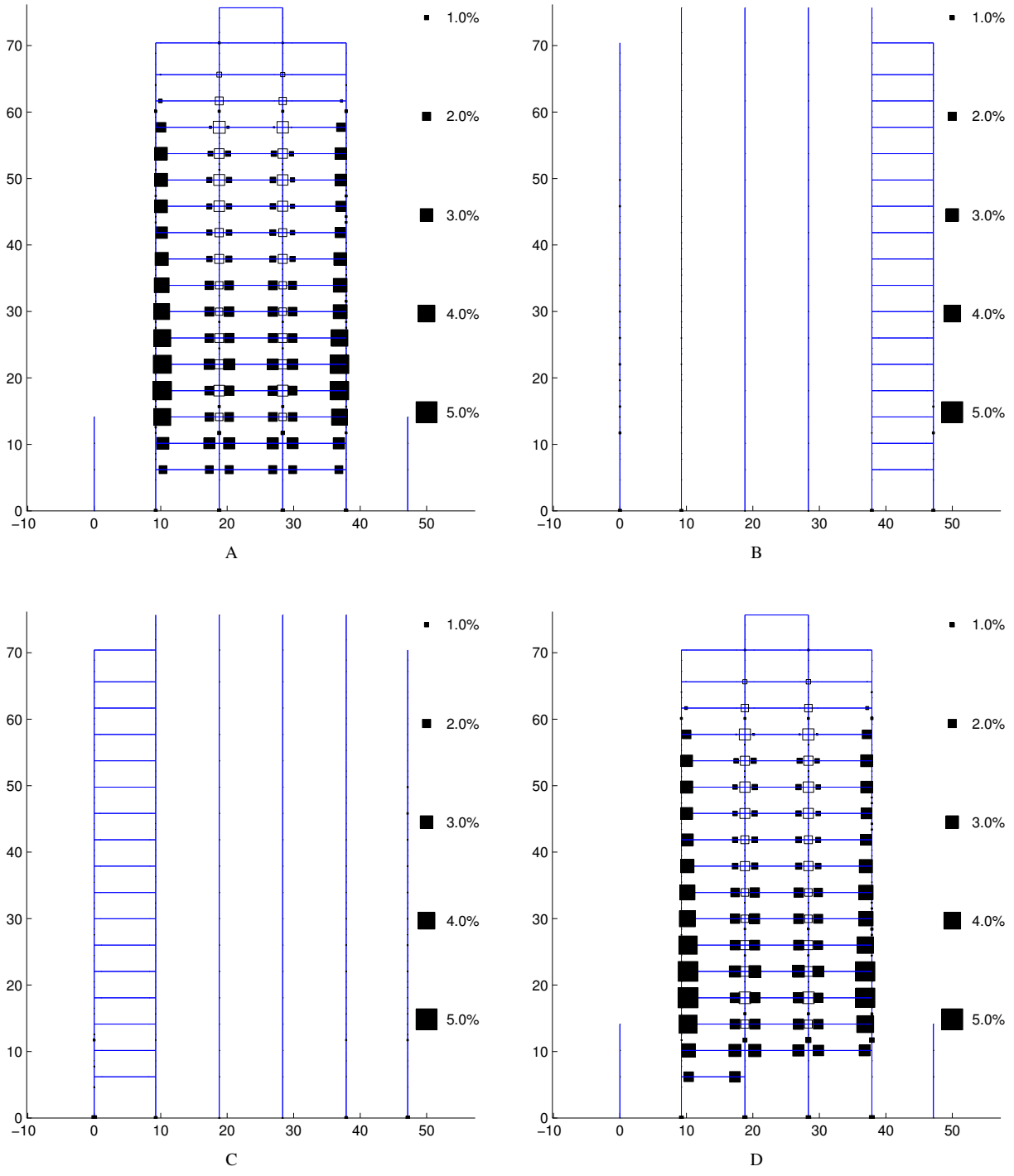

Figure F.34: Plastic rotation in percent of a radian in the moment-frames of the redesigned building model: Baldwin Park – (A) Moment-frame along grid A (east-west direction); (B) Moment-frame along grid B (east-west direction); (C) Moment-frame along grid D (east-west direction); (D) Moment-frame along grid E (east-west direction). See Figure 2.3 for moment-frame configuration.

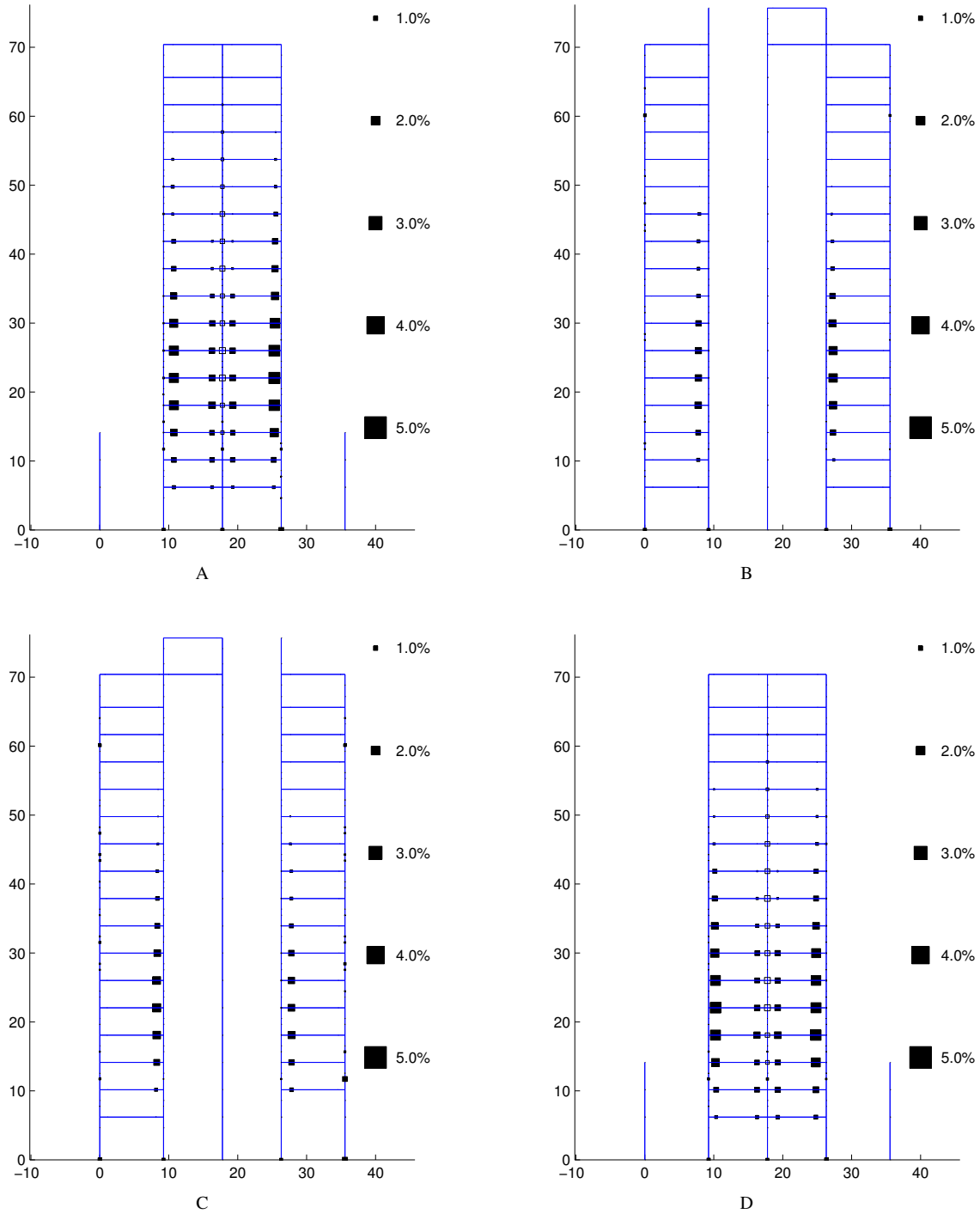

Figure F.35: Plastic rotation in percent of a radian in the moment-frames of the redesigned building model: Baldwin Park – (A) Moment-frame along grid 1 (north-south direction); (B) Moment-frame along grid 2 (north-south direction); (C) Moment-frame along grid 5 (north-south direction); (D) Moment-frame along grid 6 (north-south direction). See Figure 2.3 for moment-frame configuration.

F.6 Site: Anaheim (Latitude 33.84375, Longitude 117.90625)

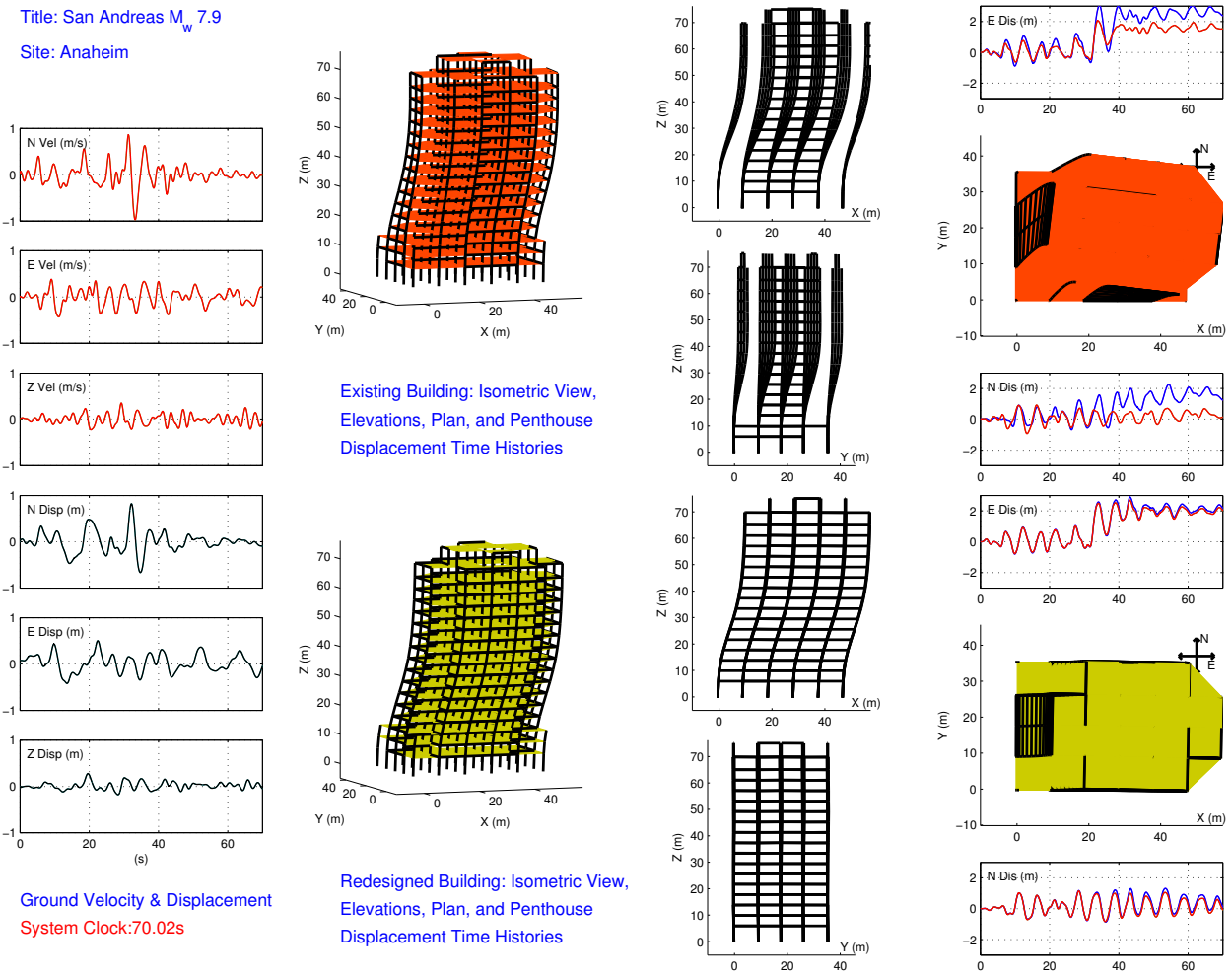

Figure F.36: $M_w 7.9$ earthquake south-to-north rupture) on the San Andreas fault – snapshot of building deformation immediately following the earthquake (scaled up by a factor of 5): Anaheim. Also shown are the time-histories of the three components of the ground velocity and displacement (bandpass-filtered between 2 s and 1000 s), and the east and north components of the penthouse displacement of the existing and redesigned building models.

F.6.1 Existing Building Performance

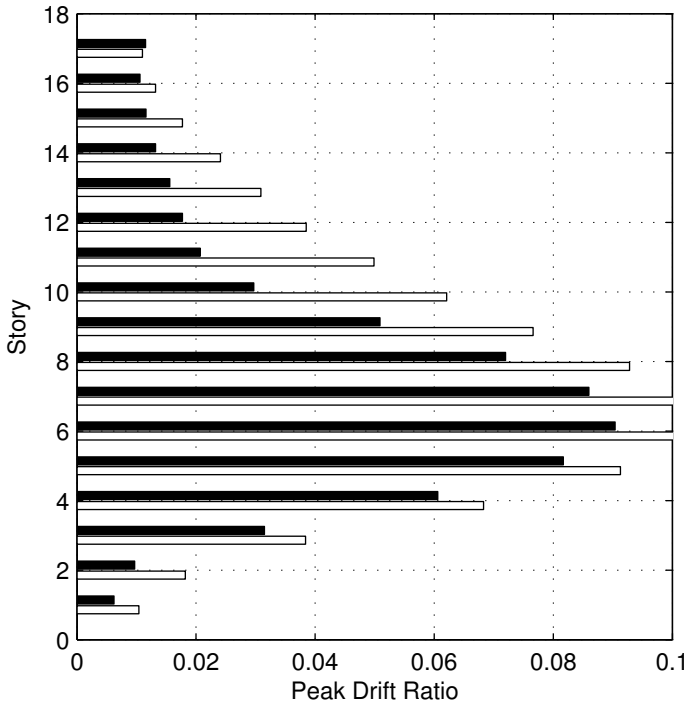

Figure F.37: Peak east-west/X (white bars) and north-south/Y (black bars) drifts in each story of the existing building model: Anaheim (the drift scale is saturated at 0.10).

Component	Components within each perf. category				Perf. Level	Force-controlled components	
	IO	LS	CP	CO (> CP)		Not Yielded	Yielded
Panel Zone	124	64	4	20	CO	–	–
Beam Major Axis	161	69	11	43	CO	–	–
Beam Minor Axis	232	48	4	0	CP	–	–
Column Major Axis	898	30	0	2	CO	2	8
Column Minor Axis	909	19	1	1	CO	2	8

Table F.21: Classification of existing building model performance based on plastic rotation in panel zones, and at the ends of beams and columns, using FEMA356 acceptance criteria: Anaheim.

Component	Components in the following plastic rotation ranges							
	$\leq$ 0.1%	(0.1-1.0]%	(1.0-2.0]%	(2.0-3.0]%	(3.0-4.0]%	(4.0-5.0]%	(5.0-6.0]%	> 6.0%
Panel Zone	120	72	15	5	5	4	6	3
Beam Major Axis	134	45	25	23	8	8	15	26
Beam Minor Axis	132	79	19	16	11	9	3	15
Column Major Axis	900	33	6	1	0	0	0	0
Column Minor Axis	907	29	4	0	0	0	0	0

Table F.22: Plastic rotation in panel zones, and at the ends of beams and columns of the existing building model: Anaheim.

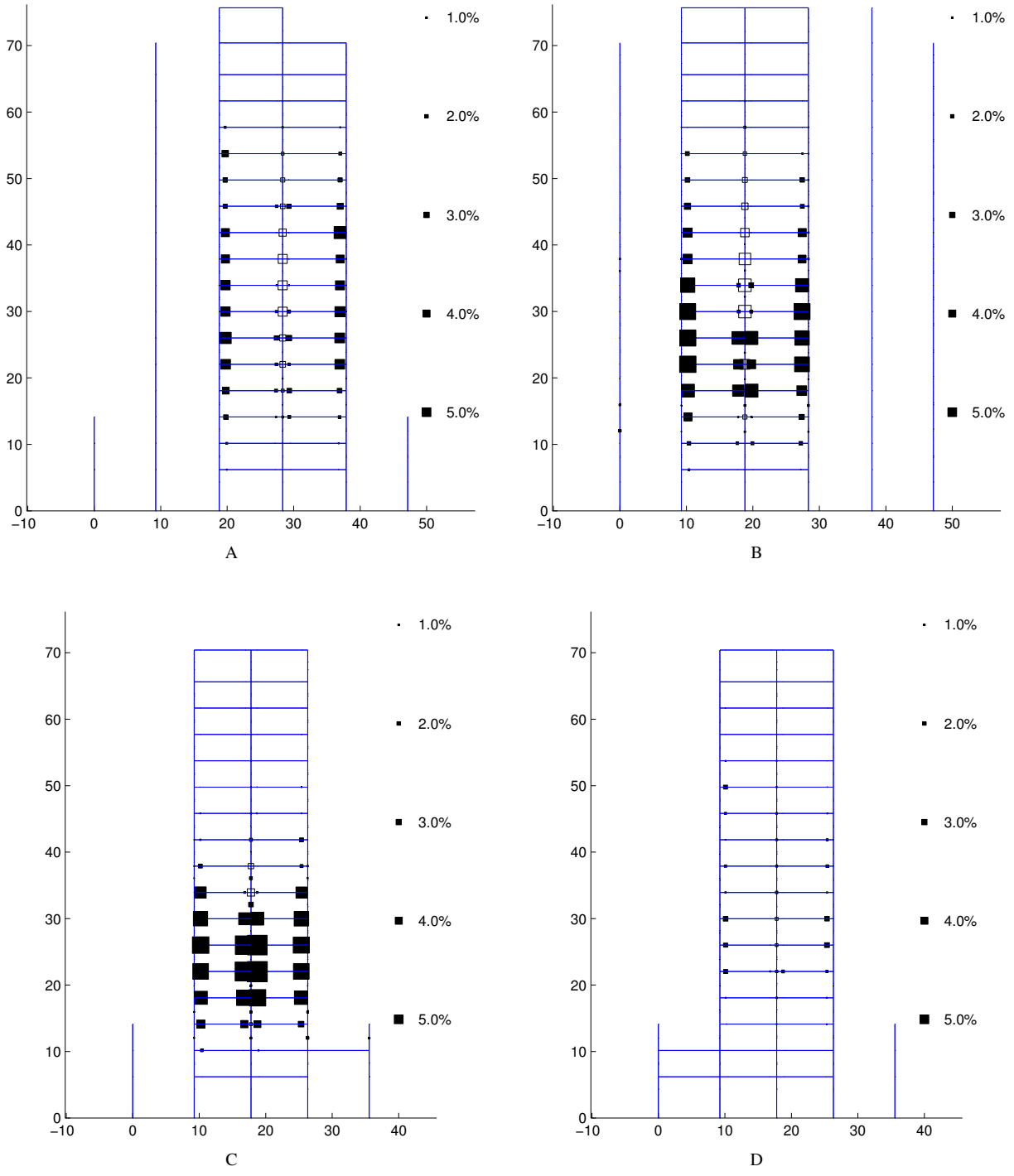

Figure F.38: Plastic rotation in percent of a radian in the moment-frames of the existing building model: Anaheim – (A) Moment-frame along grid A (east-west direction); (B) Moment-frame along grid D (east-west direction); (C) Moment-frame along grid 1 (north-south direction); (D) Moment-frame along grid 6 (north-south direction). See Figure 2.2 for moment-frame configuration.

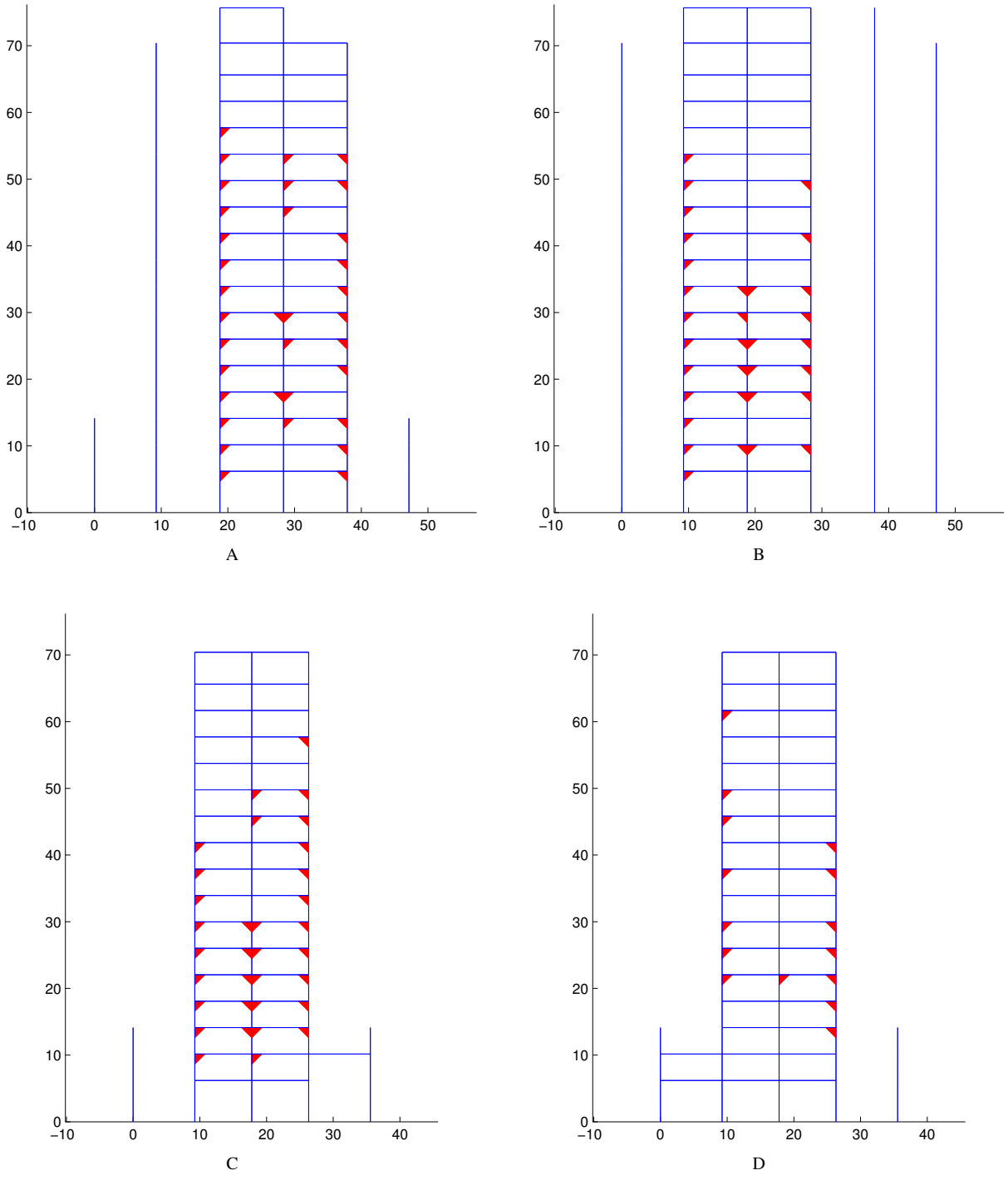

Figure F.39: Beam bottom-flange weld fracture locations in the moment-frames of the existing building model: Anaheim – (A) Moment-frame along grid A (east-west direction); (B) Moment-frame along grid D (east-west direction); (C) Moment-frame along grid 1 (north-south direction); (D) Moment-frame along grid 6 (north-south direction). See Figure 2.2 for moment-frame configuration.

F.6.2 Redesigned Building Performance

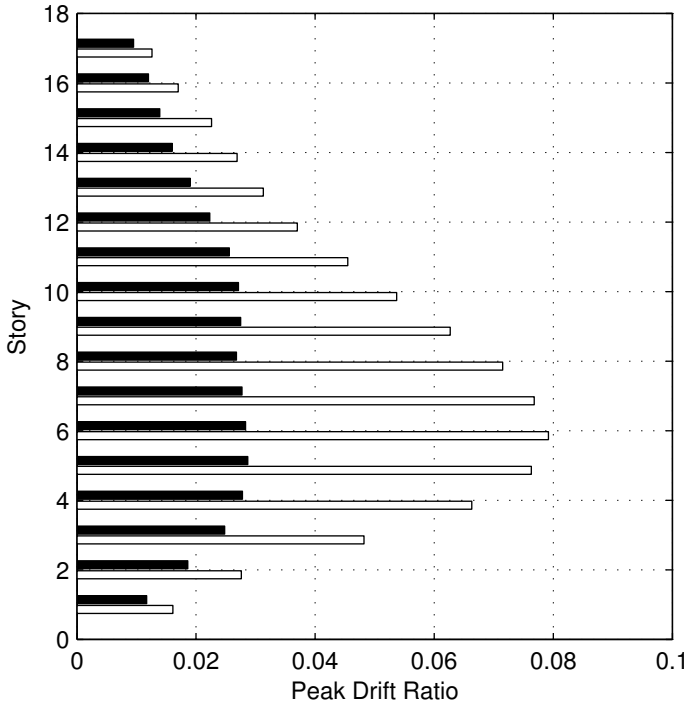

Figure F.40: Peak east-west/X (white bars) and north-south/Y (black bars) drifts in each story of the redesigned building model: Anaheim.

Component	Components within each perf. category				Perf. Level	Force-controlled components	
	IO	LS	CP	CO (> CP)		Not Yielded	Yielded
Panel Zone	226	56	27	4	CO	–	–
Beam Major Axis	350	162	26	12	CO	–	–
Beam Minor Axis	547	3	0	0	LS	–	–
Column Major Axis	650	55	3	8	CO	102	122
Column Minor Axis	689	25	0	2	CO	102	122

Table F.23: Classification of redesigned building model performance based on plastic rotation in panel zones, and at the ends of beams and columns, using FEMA356 acceptance criteria: Anaheim.

Component	Components in the following plastic rotation ranges							
	$\leq$ 0.1%	(0.1-1.0]%	(1.0-2.0]%	(2.0-3.0]%	(3.0-4.0]%	(4.0-5.0]%	(5.0-6.0]%	> 6.0%
Panel Zone	199	52	33	27	2	0	0	0
Beam Major Axis	266	117	71	26	20	32	6	12
Beam Minor Axis	288	202	58	2	0	0	0	0
Column Major Axis	822	107	9	2	0	0	0	0
Column Minor Axis	871	66	3	0	0	0	0	0

Table F.24: Plastic rotation in panel zones, and at the ends of beams and columns of the redesigned building model: Anaheim.

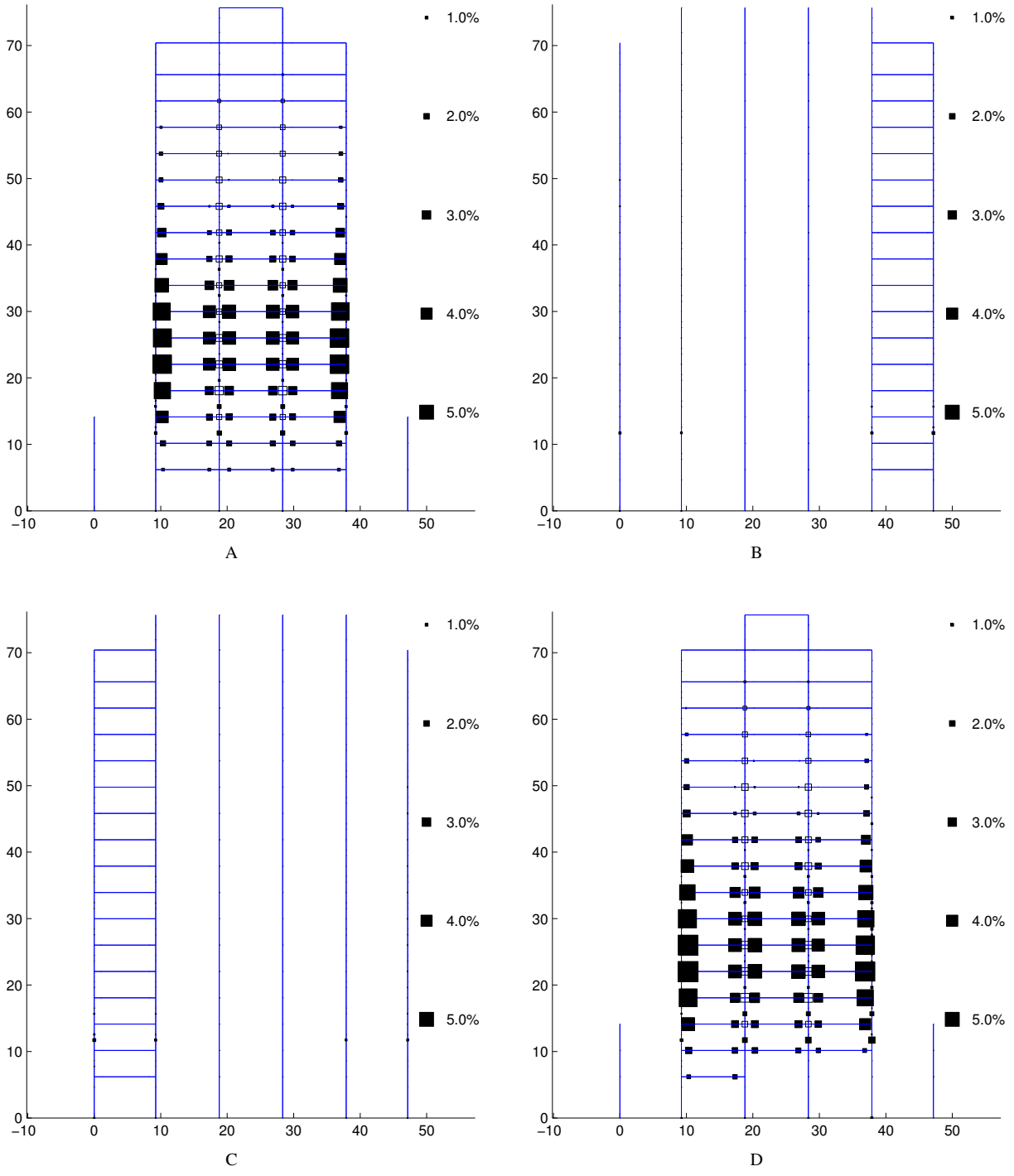

Figure F.41: Plastic rotation in percent of a radian in the moment-frames of the redesigned building model: Anaheim – (A) Moment-frame along grid A (east-west direction); (B) Moment-frame along grid B (east-west direction); (C) Moment-frame along grid D (east-west direction); (D) Moment-frame along grid E (east-west direction). See Figure 2.3 for moment-frame configuration.

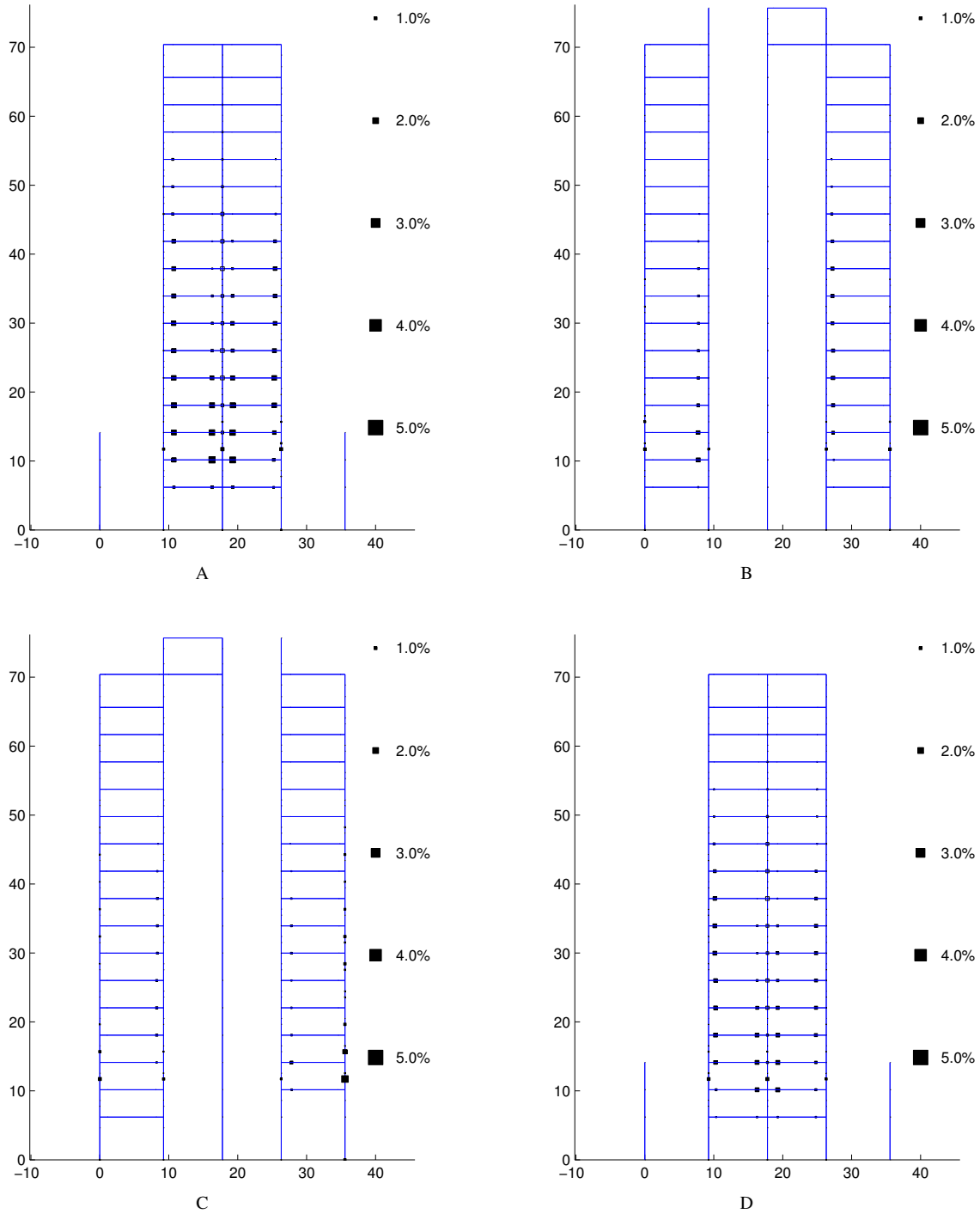

Figure F.42: Plastic rotation in percent of a radian in the moment-frames of the redesigned building model: Anaheim – (A) Moment-frame along grid 1 (north-south direction); (B) Moment-frame along grid 2 (north-south direction); (C) Moment-frame along grid 5 (north-south direction); (D) Moment-frame along grid 6 (north-south direction). See Figure 2.3 for moment-frame configuration.

F.7 Site: Long Beach (Latitude 33.78125, Longitude 118.18750)

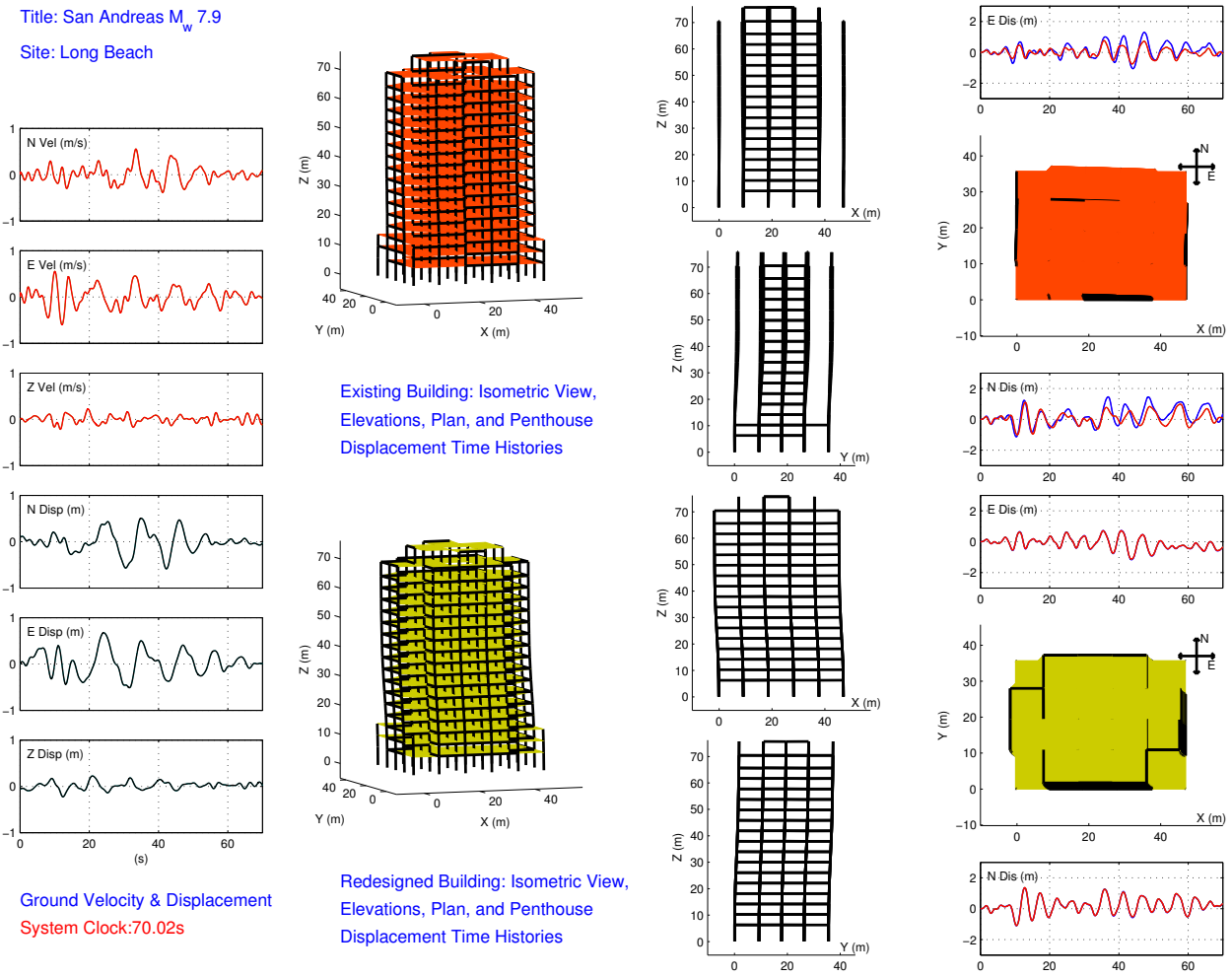

Figure F.43: M_w7.9 earthquake (south-to-north rupture) on the San Andreas fault – snapshot of building deformation immediately following the earthquake (scaled up by a factor of 5): Long Beach. Also shown are the time-histories of the three components of the ground velocity and displacement (bandpass-filtered between 2 s and 1000 s), and the east and north components of the penthouse displacement of the existing and redesigned building models.

F.7.1 Existing Building Performance

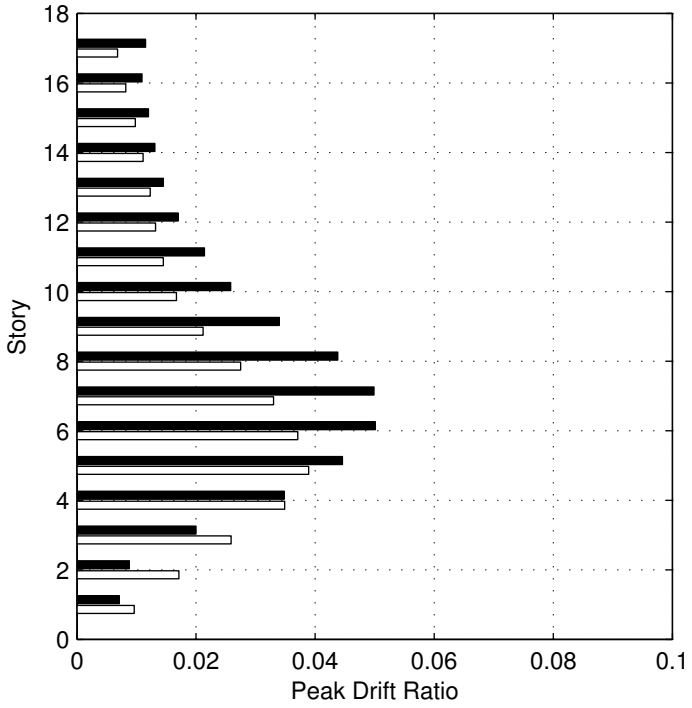

Figure F.44: Peak east-west/X (white bars) and north-south/Y (black bars) drifts in each story of the existing building model: Long Beach.

Component	Components within each perf. category				Perf. Level	Force-controlled components	
	IO	LS	CP	CO (> CP)		Not Yielded	Yielded
Panel Zone	156	45	9	2	CO	–	–
Beam Major Axis	201	67	8	8	CO	–	–
Beam Minor Axis	272	12	0	0	LS	–	–
Column Major Axis	934	2	0	0	LS	2	2
Column Minor Axis	934	2	0	0	LS	2	2

Table F.25: Classification of existing building model performance based on plastic rotation in panel zones, and at the ends of beams and columns, using FEMA356 acceptance criteria: Long Beach.

Component	Components in the following plastic rotation ranges							
	$\leq$ 0.1%	(0.1-1.0]%	(1.0-2.0]%	(2.0-3.0]%	(3.0-4.0]%	(4.0-5.0]%	(5.0-6.0]%	> 6.0%
Panel Zone	128	58	15	10	1	0	0	0
Beam Major Axis	177	42	27	19	9	8	2	0
Beam Minor Axis	188	74	14	4	3	0	0	1
Column Major Axis	933	7	0	0	0	0	0	0
Column Minor Axis	931	9	0	0	0	0	0	0

Table F.26: Plastic rotation in panel zones, and at the ends of beams and columns of the existing building model: Long Beach.

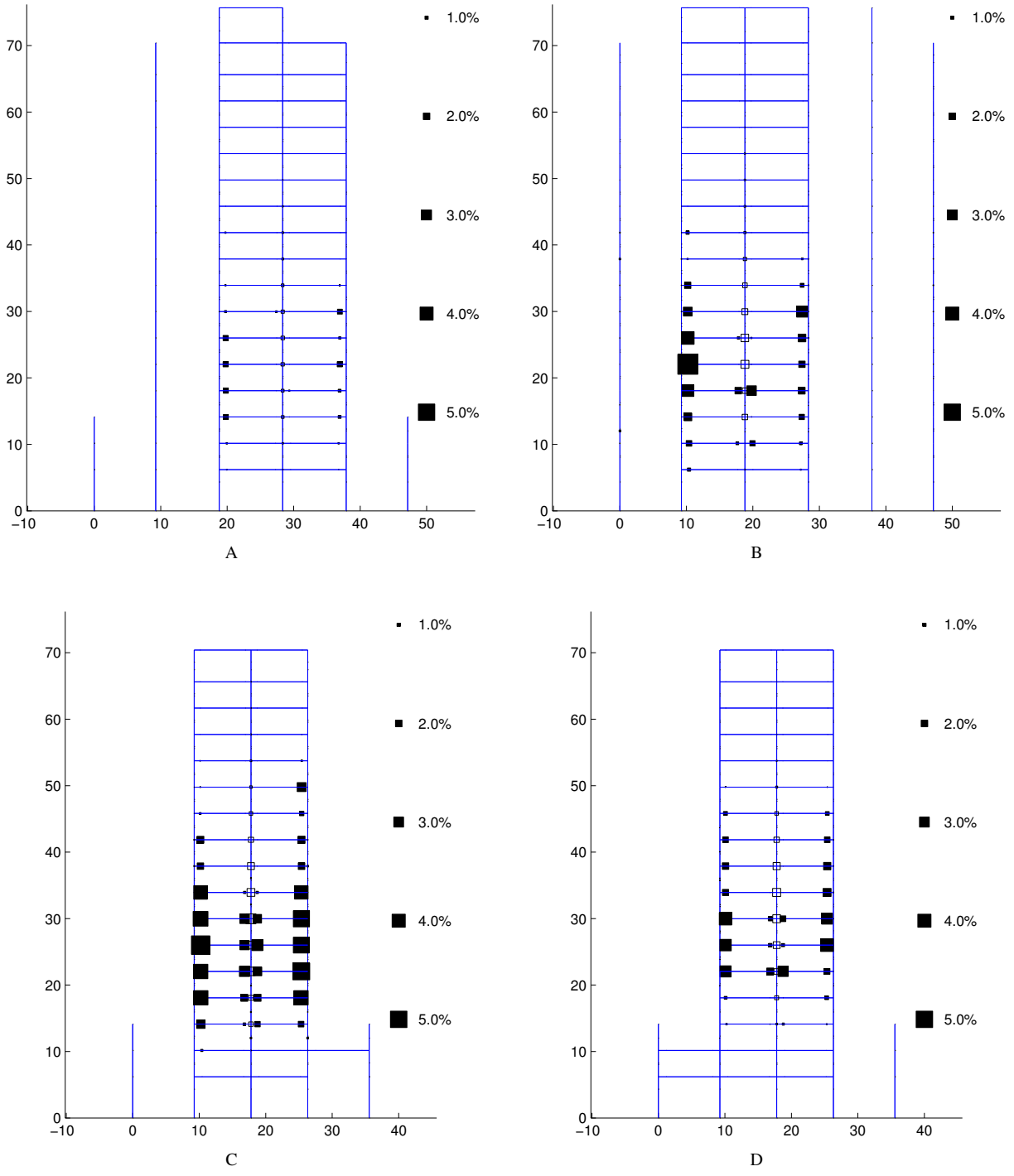

Figure F.45: Plastic rotation in percent of a radian in the moment-frames of the existing building model: Long Beach – (A) Moment-frame along grid A (east-west direction); (B) Moment-frame along grid D (east-west direction); (C) Moment-frame along grid 1 (north-south direction); (D) Moment-frame along grid 6 (north-south direction). See Figure 2.2 for moment-frame configuration.

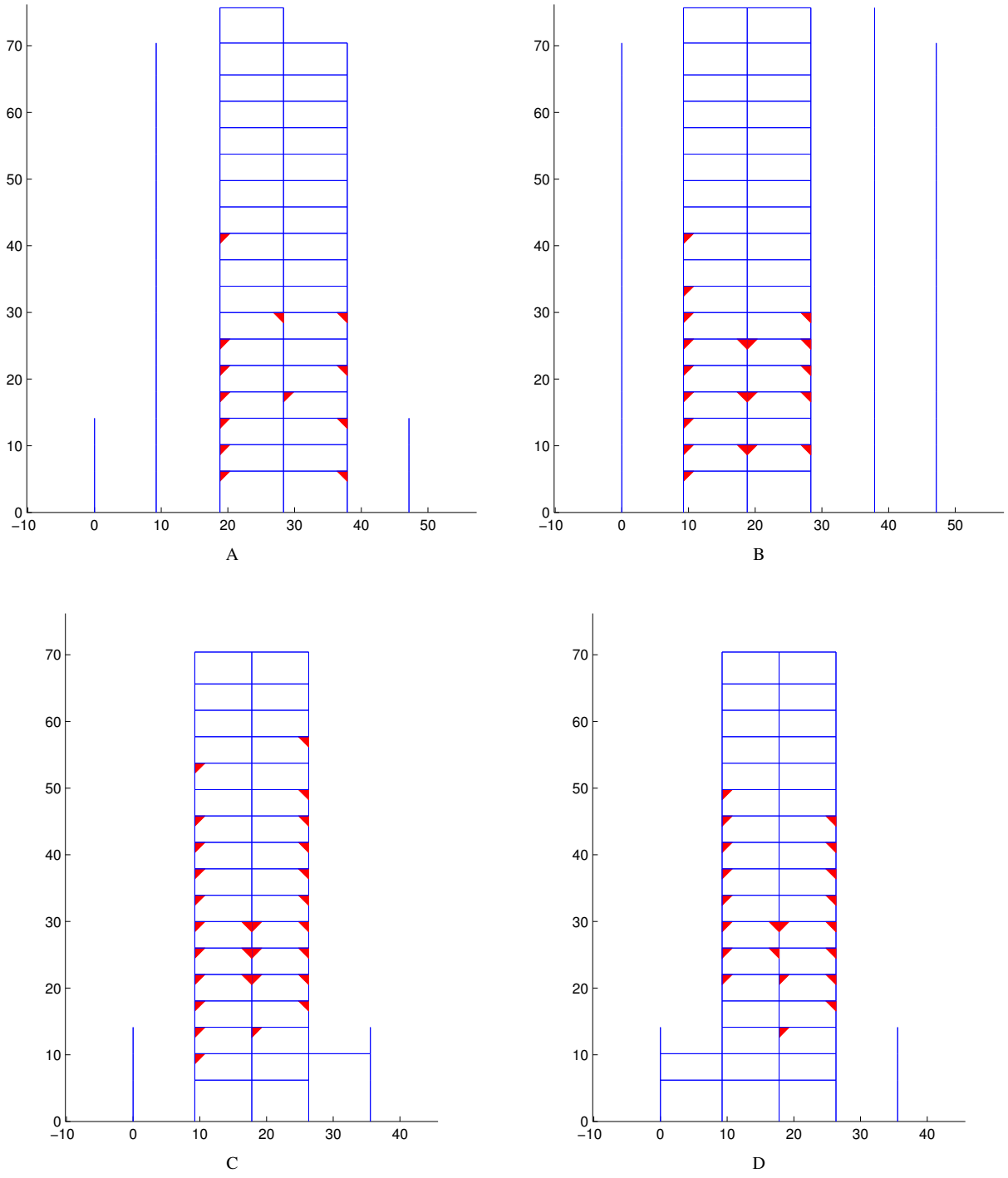

Figure F.46: Beam bottom-flange weld fracture locations in the moment-frames of the existing building model: Long Beach – (A) Moment-frame along grid A (east-west direction); (B) Moment-frame along grid D (east-west direction); (C) Moment-frame along grid 1 (north-south direction); (D) Moment-frame along grid 6 (north-south direction). See Figure 2.2 for moment-frame configuration.

F.7.2 Redesigned Building Performance

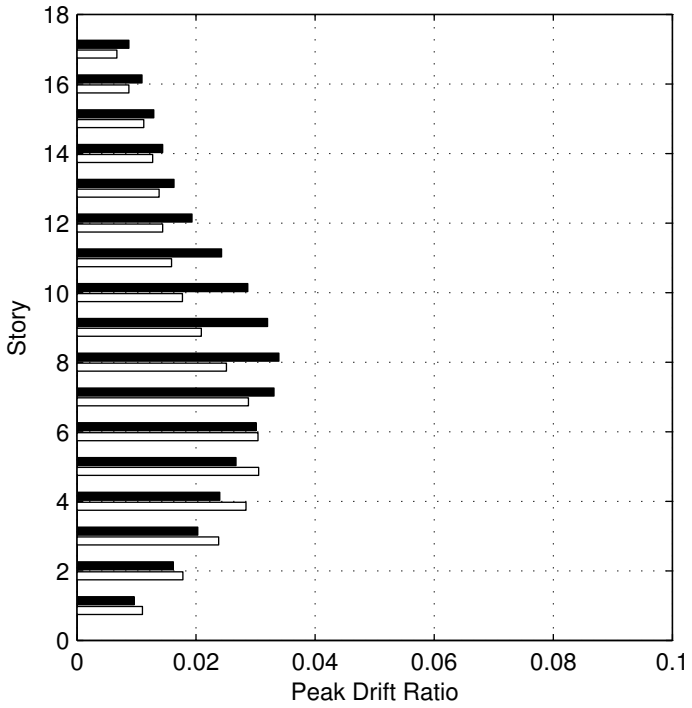

Figure F.47: Peak east-west/X (white bars) and north-south/Y (black bars) drifts in each story of the redesigned building model: Long Beach.

Component	Components within each perf. category				Perf. Level	Force-controlled components	
	IO	LS	CP	CO (> CP)		Not Yielded	Yielded
Panel Zone	233	80	0	0	LS	–	–
Beam Major Axis	377	173	0	0	LS	–	–
Beam Minor Axis	550	0	0	0	IO	–	–
Column Major Axis	716	14	0	0	LS	90	120
Column Minor Axis	729	1	0	0	LS	90	120

Table F.27: Classification of redesigned building model performance based on plastic rotation in panel zones, and at the ends of beams and columns, using FEMA356 acceptance criteria: Long Beach.

Component	Components in the following plastic rotation ranges							
	$\leq$ 0.1%	(0.1-1.0]%	(1.0-2.0]%	(2.0-3.0]%	(3.0-4.0]%	(4.0-5.0]%	(5.0-6.0]%	$>$ 6.0%
Panel Zone	205	98	10	0	0	0	0	0
Beam Major Axis	323	120	104	3	0	0	0	0
Beam Minor Axis	388	161	1	0	0	0	0	0
Column Major Axis	904	36	0	0	0	0	0	0
Column Minor Axis	937	3	0	0	0	0	0	0

Table F.28: Plastic rotation in panel zones, and at the ends of beams and columns of the redesigned building model: Long Beach.

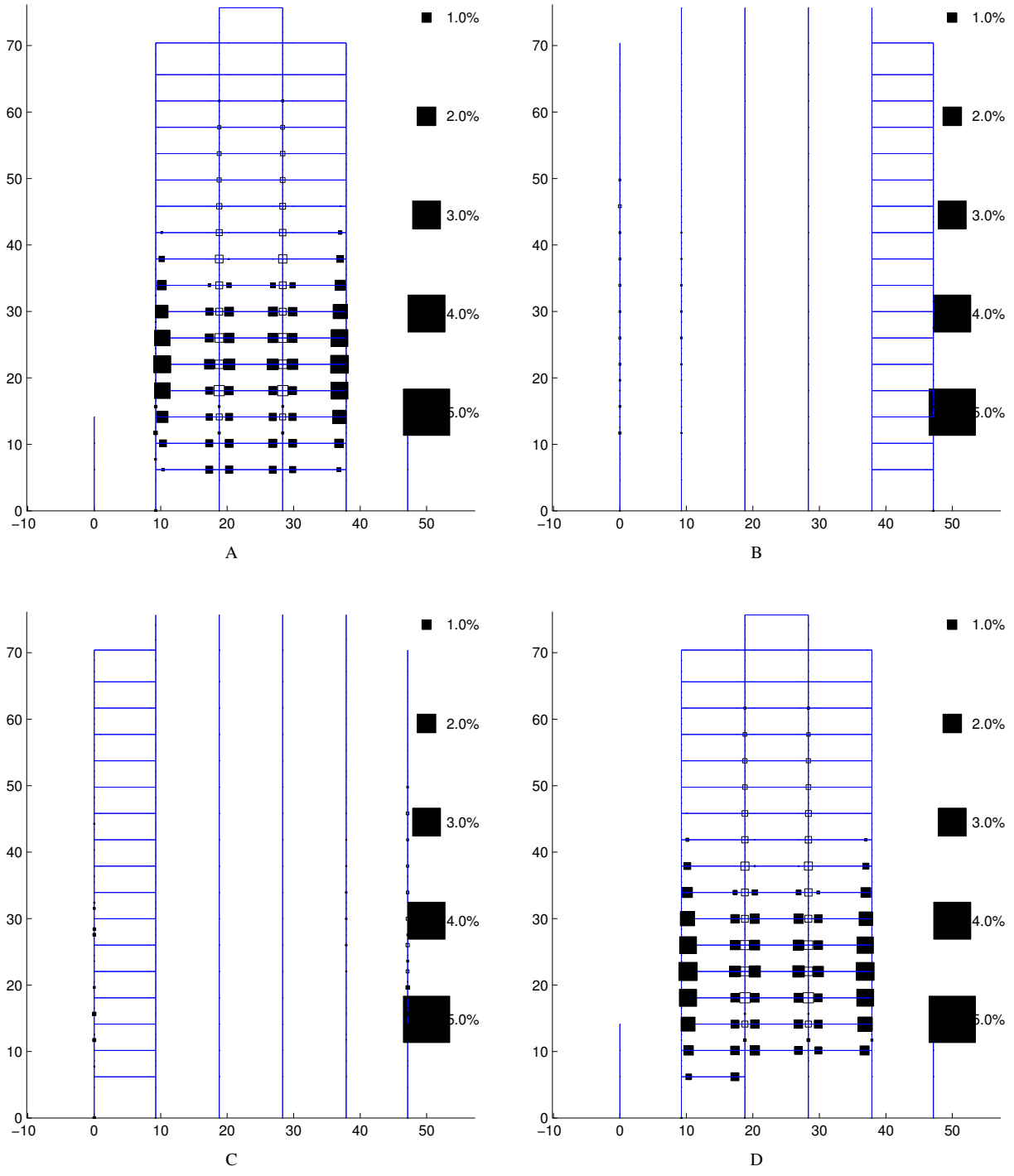

Figure F.48: Plastic rotation in percent of a radian in the moment-frames of the redesigned building model: Long Beach – (A) Moment-frame along grid A (east-west direction); (B) Moment-frame along grid B (east-west direction); (C) Moment-frame along grid D (east-west direction); (D) Moment-frame along grid E (east-west direction). See Figure 2.3 for moment-frame configuration.

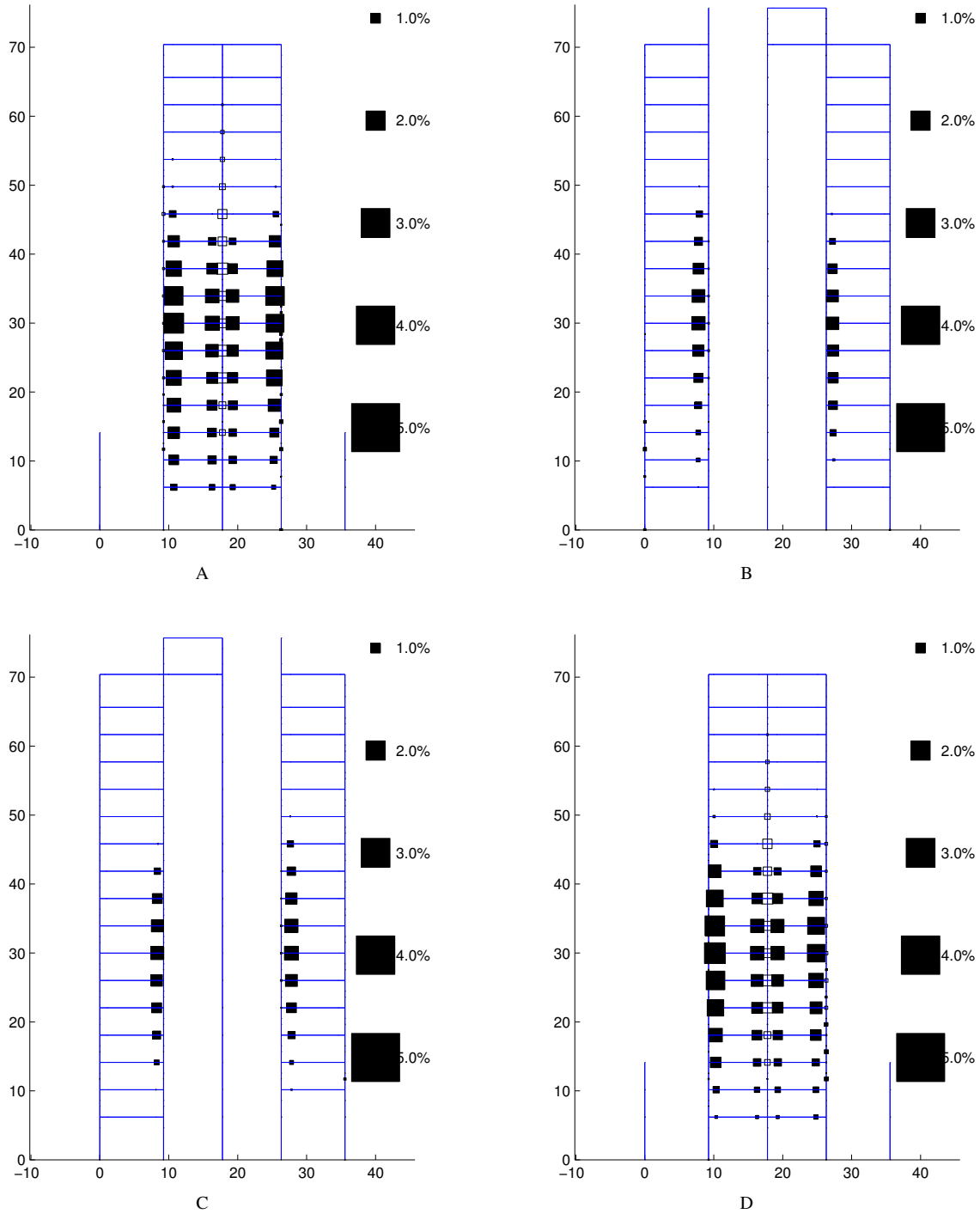

Figure F.49: Plastic rotation in percent of a radian in the moment-frames of the redesigned building model: Long Beach – (A) Moment-frame along grid 1 (north-south direction); (B) Moment-frame along grid 2 (north-south direction); (C) Moment-frame along grid 5 (north-south direction); (D) Moment-frame along grid 6 (north-south direction). See Figure 2.3 for moment-frame configuration.

F.8 Site: Santa Ana (Latitude 33.75000, Longitude 117.87500)

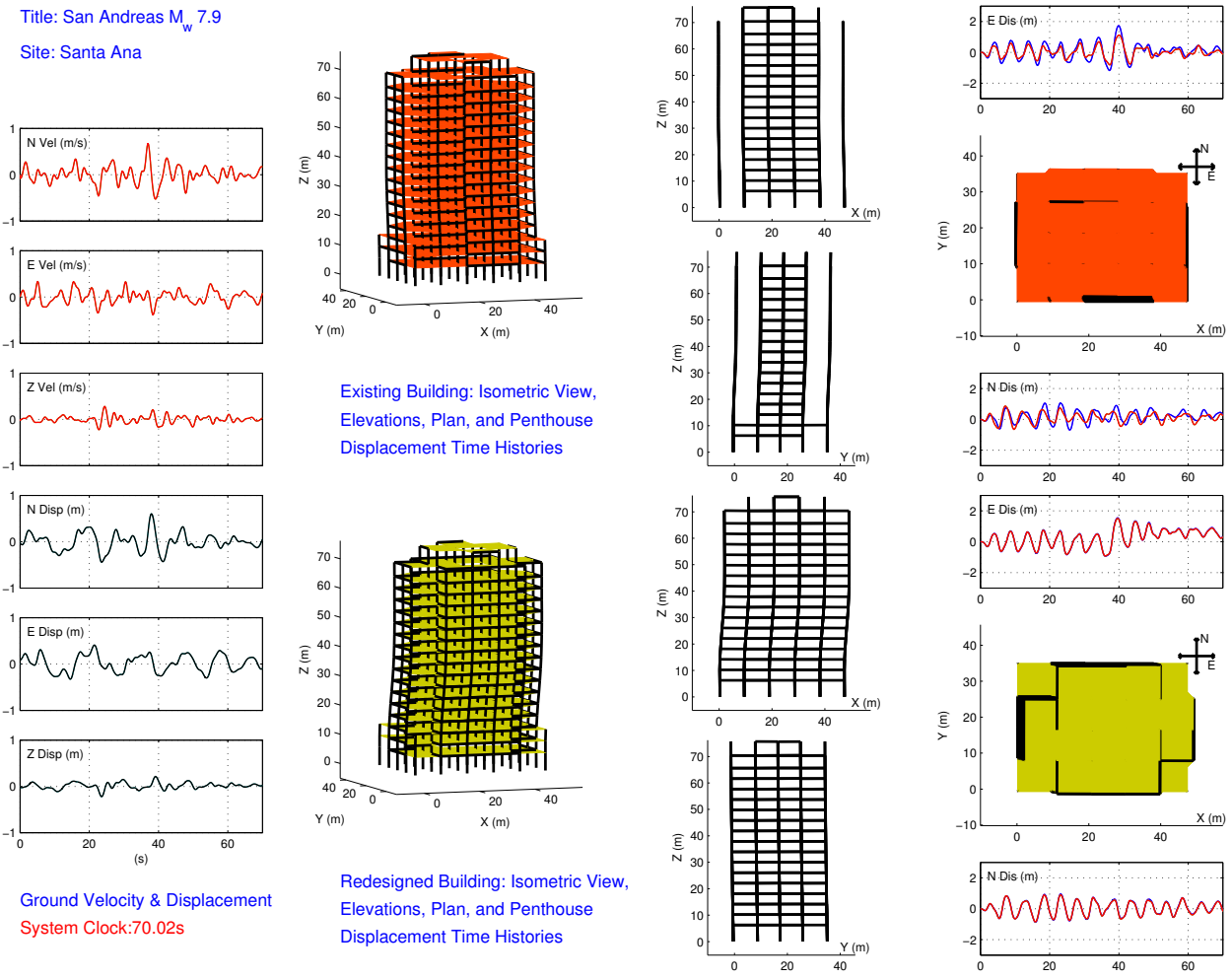

Figure F.50: $M_w 7.9$ earthquake (south-to-north rupture) on the San Andreas fault – snapshot of building deformation immediately following the earthquake (scaled up by a factor of 5): Santa Ana. Also shown are the time-histories of the three components of the ground velocity and displacement (bandpass-filtered between 2 s and 1000 s), and the east and north components of the penthouse displacement of the existing and redesigned building models.

F.8.1 Existing Building Performance

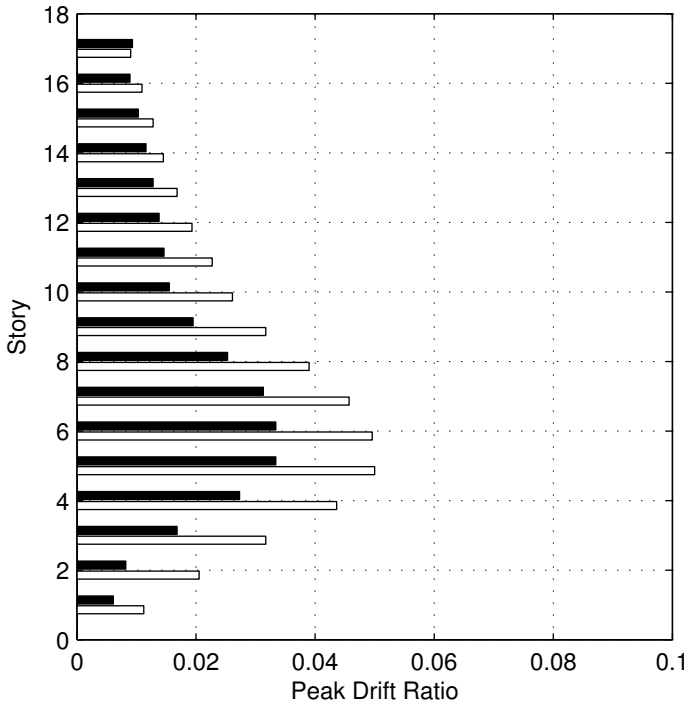

Figure F.51: Peak east-west/X (white bars) and north-south/Y (black bars) drifts in each story of the existing building model: Santa Ana.

Component	Components within each perf. category				Perf. Level	Force-controlled components	
	IO	LS	CP	CO (> CP)		Not Yielded	Yielded
Panel Zone	151	51	5	5	CO	–	–
Beam Major Axis	200	78	6	0	CP	–	–
Beam Minor Axis	264	20	0	0	LS	–	–
Column Major Axis	933	3	0	0	LS	2	2
Column Minor Axis	936	0	0	0	IO	2	2

Table F.29: Classification of existing building model performance based on plastic rotation in panel zones, and at the ends of beams and columns, using FEMA356 acceptance criteria: Santa Ana.

Component	Components in the following plastic rotation ranges							
	$\leq$ 0.1%	(0.1-1.0]%	(1.0-2.0]%	(2.0-3.0]%	(3.0-4.0]%	(4.0-5.0]%	(5.0-6.0]%	> 6.0%
Panel Zone	117	67	19	7	2	0	0	0
Beam Major Axis	172	51	30	18	11	2	0	0
Beam Minor Axis	187	65	12	11	4	3	2	0
Column Major Axis	935	5	0	0	0	0	0	0
Column Minor Axis	939	1	0	0	0	0	0	0

Table F.30: Plastic rotation in panel zones, and at the ends of beams and columns of the existing building model: Santa Ana.

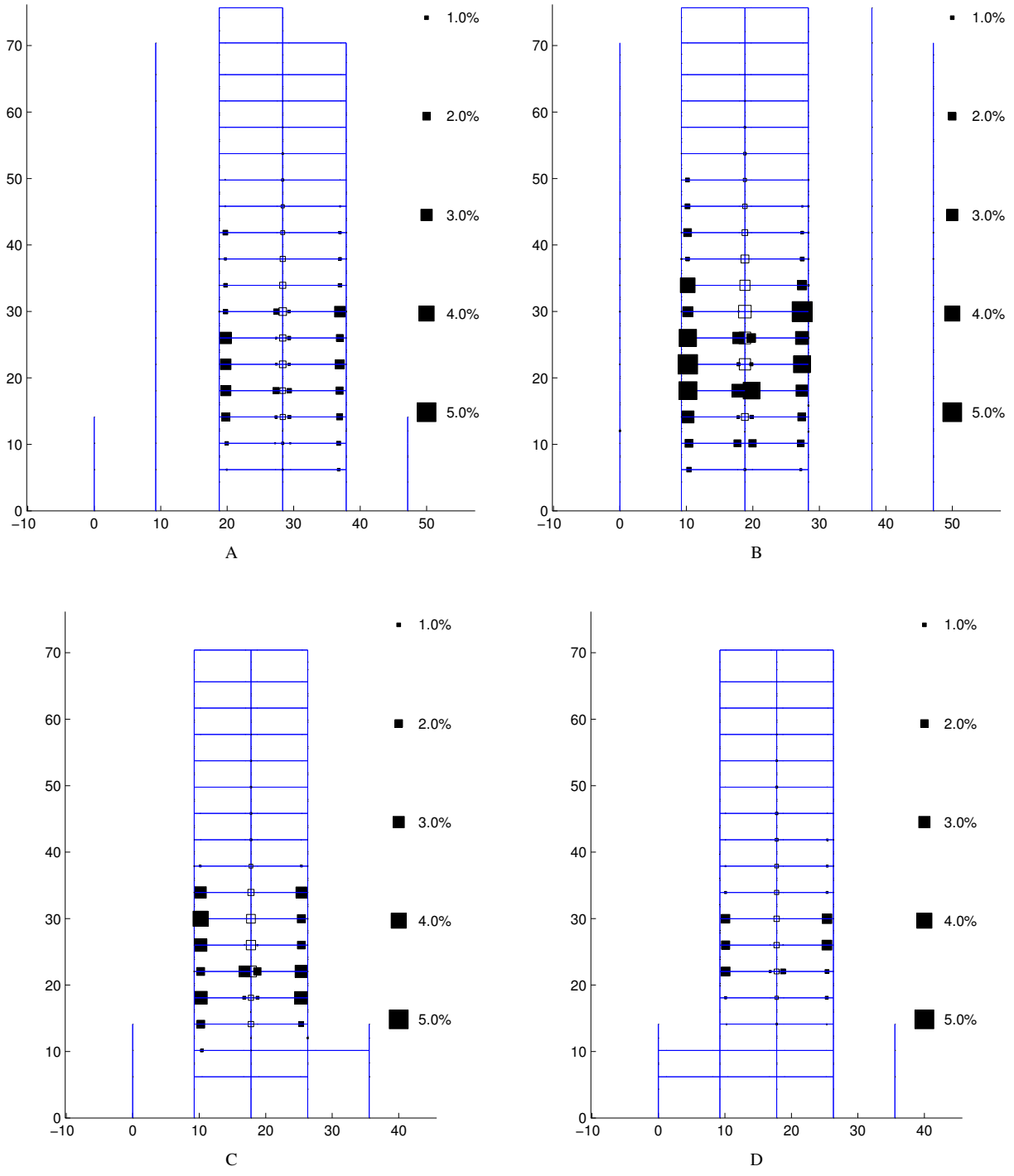

Figure F.52: Plastic rotation in percent of a radian in the moment-frames of the existing building model: Santa Ana – (A) Moment-frame along grid A (east-west direction); (B) Moment-frame along grid D (east-west direction); (C) Moment-frame along grid 1 (north-south direction); (D) Moment-frame along grid 6 (north-south direction). See Figure 2.2 for moment-frame configuration.

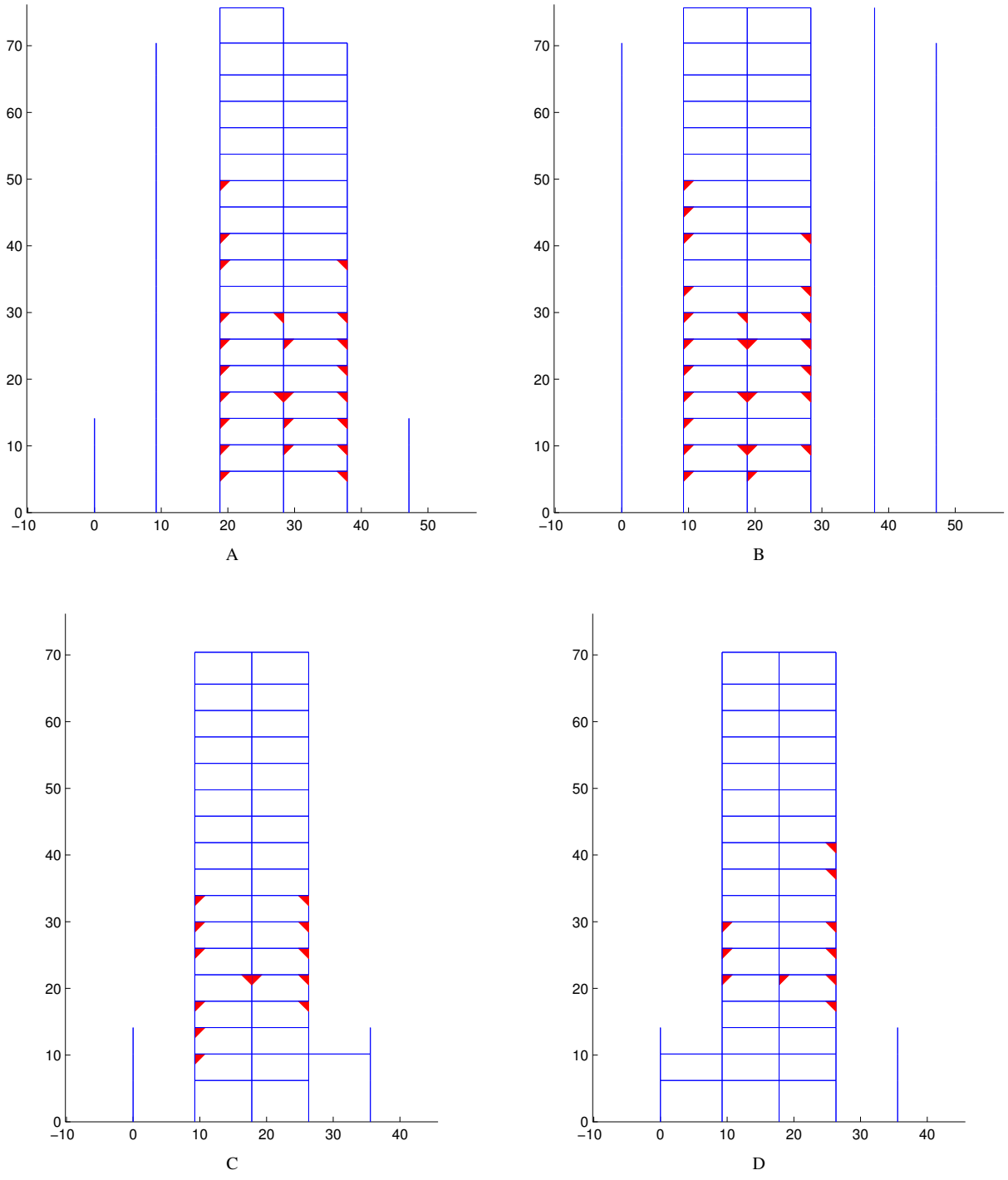

Figure F.53: Beam bottom-flange weld fracture locations in the moment-frames of the existing building model: Santa Ana – (A) Moment-frame along grid A (east-west direction); (B) Moment-frame along grid D (east-west direction); (C) Moment-frame along grid 1 (north-south direction); (D) Moment-frame along grid 6 (north-south direction). See Figure 2.2 for moment-frame configuration.

F.8.2 Redesigned Building Performance

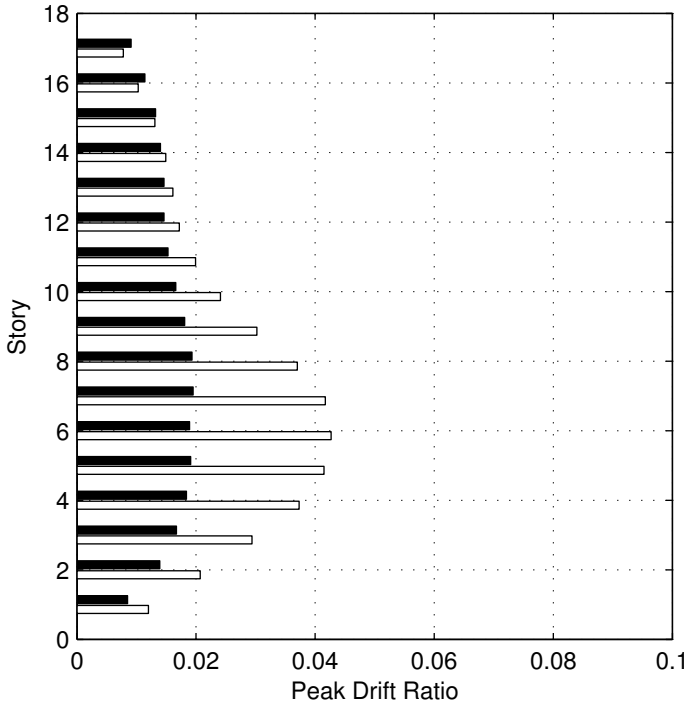

Figure F.54: Peak east-west/X (white bars) and north-south/Y (black bars) drifts in each story of the redesigned building model: Santa Ana.

Component	Components within each perf. category				Perf. Level	Force-controlled components	
	IO	LS	CP	CO (> CP)		Not Yielded	Yielded
Panel Zone	235	78	0	0	LS	–	–
Beam Major Axis	439	111	0	0	LS	–	–
Beam Minor Axis	550	0	0	0	IO	–	–
Column Major Axis	715	25	0	0	LS	96	104
Column Minor Axis	740	0	0	0	IO	96	104

Table F.31: Classification of redesigned building model performance based on plastic rotation in panel zones, and at the ends of beams and columns, using FEMA356 acceptance criteria: Santa Ana.

Component	Components in the following plastic rotation ranges							
	$\leq$ 0.1%	(0.1-1.0]%	(1.0-2.0]%	(2.0-3.0]%	(3.0-4.0]%	(4.0-5.0]%	(5.0-6.0]%	> 6.0%
Panel Zone	217	72	24	0	0	0	0	0
Beam Major Axis	347	115	60	20	8	0	0	0
Beam Minor Axis	412	138	0	0	0	0	0	0
Column Major Axis	905	35	0	0	0	0	0	0
Column Minor Axis	938	2	0	0	0	0	0	0

Table F.32: Plastic rotation in panel zones, and at the ends of beams and columns of the redesigned building model: Santa Ana.

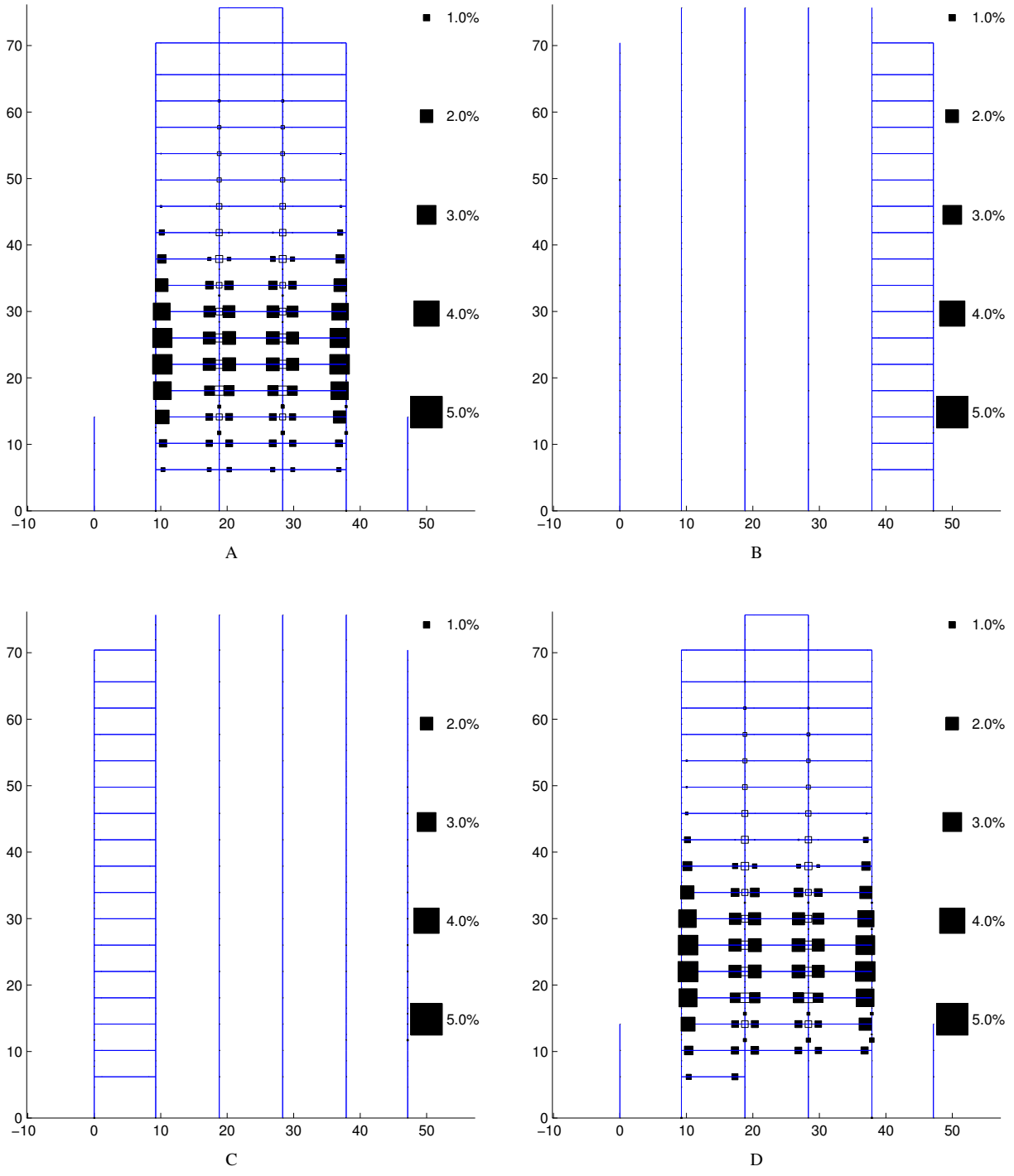

Figure F.55: Plastic rotation in percent of a radian in the moment-frames of the redesigned building model: Santa Ana – (A) Moment-frame along grid A (east-west direction); (B) Moment-frame along grid B (east-west direction); (C) Moment-frame along grid D (east-west direction); (D) Moment-frame along grid E (east-west direction). See Figure 2.3 for moment-frame configuration.

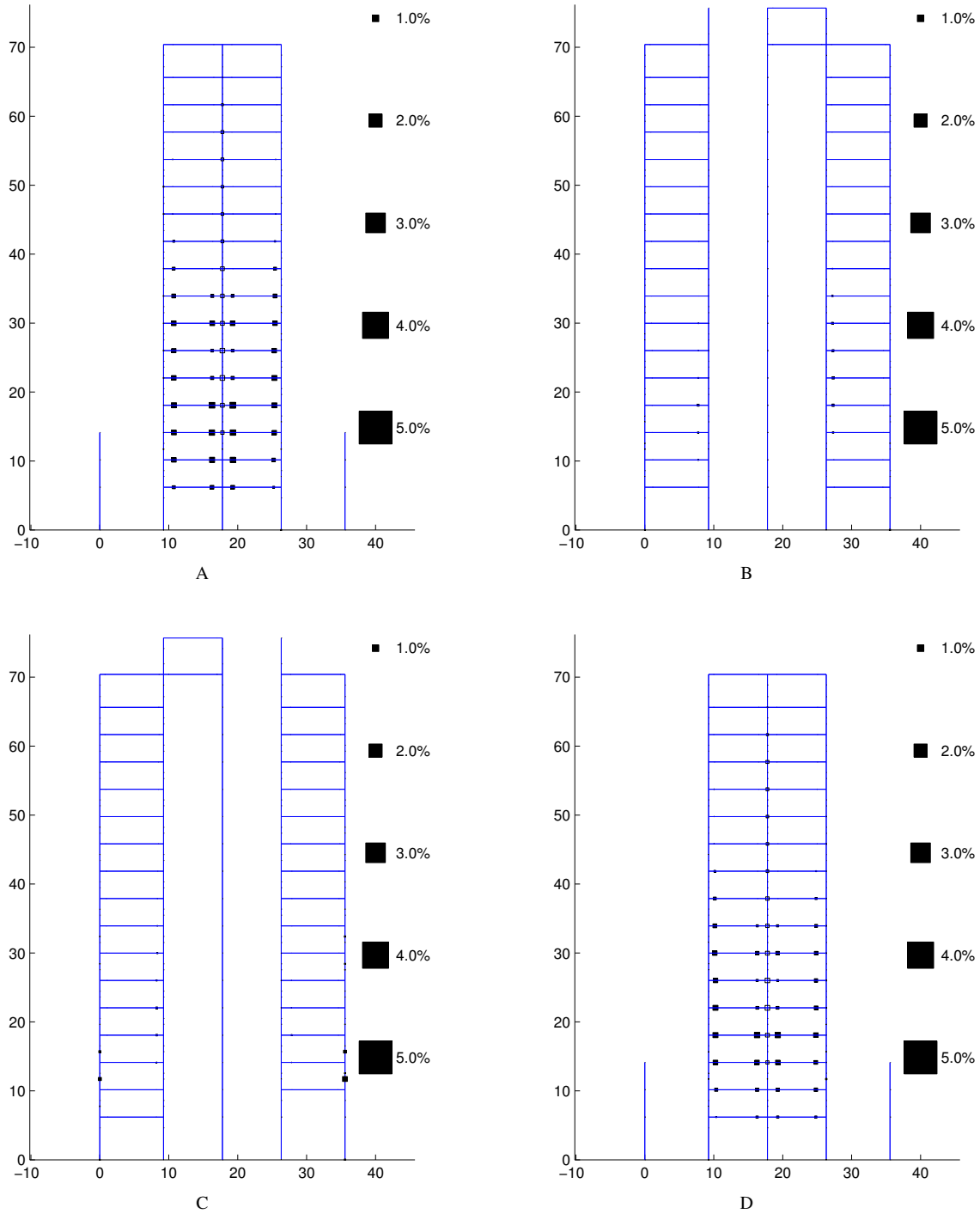

Figure F.56: Plastic rotation in percent of a radian in the moment-frames of the redesigned building model: Santa Ana – (A) Moment-frame along grid 1 (north-south direction); (B) Moment-frame along grid 2 (north-south direction); (C) Moment-frame along grid 5 (north-south direction); (D) Moment-frame along grid 6 (north-south direction). See Figure 2.3 for moment-frame configuration.

References

[1] Kerry E. Sieh. Slip along the San Andreas fault associated with the great 1857 earthquake. *Bulletin of the Seismological Society of America*, 68(5):1421–1448, 1978.

[2] Duncan Carr Agnew and Kerry Sieh. A documentary study of the felt effects of the great California earthquake of 1857. *Bulletin of the Seismological Society of America*, 68(6):1717–1729, 1978.

[3] Aron J. Meltzner and David J. Wald. Foreshocks and aftershocks of the great 1857 California earthquake. Technical Report USGS Open-File Report 98-465, United States Department of the Interior, USGS, Pasadena, California, USA, 1998.

[4] FEMA. *Prestandard and Commentary for the Seismic Rehabilitation of Buildings*. FEMA-356. Federal Emergency Management Agency, USA, 2000.

[5] FEMA. *Recommended Seismic Design Criteria for New Steel Moment-Frame Buildings*. FEMA-350. Federal Emergency Management Agency, USA, 2000.

[6] ICBO. *1997 Uniform Building Code*. Volume 2. International Conference of Building Officials, Whittier, California, USA, 1997.

[7] Kerry E. Sieh. Pre-historic large earthquakes produced by slip on the San Andreas fault at Pallett creek, California. *Journal of Geophysical Research*, 83:3907–3939, 1978.

[8] Kerry E. Sieh. A study of late Holocene displacement history along the South-Central reach of the San Andreas fault. Technical Report Ph.D. Dissertation, Stanford University, California, USA, 1977.

[9] J. H. Shaw and J. Suppe. Earthquake hazards of active blind-thrust faults under the central Los Angeles basin. *Journal of Geophysical Research*, 101(B4):8623–8642, 1996.

[10] Ronald T. Eguchi, James D. Goltz, Craig E. Taylor, Stephanie E. Chang, Paul J. Flores, Laurie A. Johnson, Hope A. Seligson, and Neil C. Blais. Direct economic losses in the Northridge earthquake: A three-year post-event perspective. *Earthquake Spectra*, 14(2):245–264, 1998.

[11] William J. Petak and Shirin Elahi. The Northridge earthquake, USA, and its economic and social impact. In *EuroConference on Global Change and Catastrophe Risk Management, Earthquake Risks in Europe, IIASA, Laxenburg, Austria*, 2000.

[12] SAC. Analytical and field investigations of buildings affected by the Northridge earthquake of January 17, 1994 – Part 1. Technical Report SAC 95-04, Part 1, Structural Engineers Association of California, Applied Technology Council, and California Universities for Research in Earthquake Engineering, USA, 1995.

[13] SAC. Analytical and field investigations of buildings affected by the Northridge earthquake of January 17, 1994 – Part 2. Technical Report SAC 95-04, Part 2, Structural Engineers Association of California, Applied Technology Council, and California Universities for Research in Earthquake Engineering, USA, 1995.

[14] SAC. Surveys and assessments of damage to buildings affected by the Northridge earthquake of January 17, 1994. Technical Report SAC 95-06, Structural Engineers Association of California, Applied Technology Council, and California Universities for Research in Earthquake Engineering, USA, 1995.

[15] EQE. The Northridge earthquake of January 17, 1994: Report of data collection and analysis, Part A: Damage and inventory data. Technical Report EQE Project No. 36386.02, EQE International Inc. and The Geographic Information Systems Group of the Governor's Office of Emergency Services, California, USA, 1995.

[16] T. Heaton, J. Hall, D. Wald, and M. Halling. Response of high-rise and base-isolated buildings to a hypothetical M_w 7.0 blind thrust earthquake. *Science*, 267:206–211, 1995.

[17] J. Hall, T. Heaton, M. Halling, and D. Wald. Near-source ground motion and its effects on flexible buildings. *Earthquake Spectra*, 11(4):569–605, 1995.

[18] John F. Hall. Seismic response of steel frame buildings to near-source ground motions. *Earthquake Engineering and Structural Dynamics*, 27:1445–1464, 1998.

[19] K. B. Olsen, R. J. Archuleta, and J. R. Matarese. Three dimensional simulation of a magnitude 7.75 earthquake on the San Andreas fault. *Science*, 270:1628–1632, 1995.

[20] Robert W. Graves. Three-dimensional finite-difference modeling of the San Andreas fault: Source parameterization and ground-motion levels. *Bulletin of the Seismological Society of America*, 88(4):881–897, 1998.

[21] Chen Ji, David J. Wald, and Don V. Helmberger. Source description of the 1999 Hector Mine, California, earthquake – Part I: Wavelet domain inversion theory and resolution analysis. *Bulletin of the Seismological Society of America*, 92(4):1192–1207, 2002.

[22] Chen Ji, Y. Tan, Don Helmberger, and Jeroen Tromp. Modeling teleseismic P and SH static offsets for great strike-slip earthquakes. In *Proceedings of the American Geophysical Union Fall Meeting, USA*, 2003.

[23] Dimitri Komatitsch, Qinya Liu, Jeroen Tromp, Peter Suss, Christiane Stidham, and John H. Shaw. Simulations of ground motion in the Los Angeles basin based upon the spectral element method. *Bulletin of the Seismological Society of America*, 94:187–206, 2004.

[24] Qinya Liu, Jascha Polet, Dimitri Komatitsch, and Jeroen Tromp. Spectral-element moment tensor inversions for earthquakes in Southern California. *Bulletin of the Seismological Society of America*, 94(5):1748–1761, 2004.

[25] Dimitri Komatitsch and Jeroen Tromp. Introduction to the spectral element method for three-dimensional seismic wave propagation. *Geophys. J. Int.*, 139:806–822, 1999.

[26] Swaminathan Krishnan. Three-dimensional nonlinear analysis of tall irregular steel buildings subject to strong ground motion. Technical Report EERL 2003-01, Earthquake Engineering Research Laboratory, California Institute of Technology, Pasadena, California, USA, 2003.

[27] Anders Carlson. Three-dimensional nonlinear inelastic analysis of steel moment-frame buildings damaged by earthquake excitations. Technical Report EERL 99-02, Earthquake Engineering Research Laboratory, California Institute of Technology, Pasadena, California, USA, 1999.

[28] ICBO. *1982 Uniform Building Code*. Volume 2. International Conference of Building Officials, Whittier, California, USA, 1982.

[29] M. P. Suss and J. H. Shaw. P-wave seismic velocity structure derived from sonic logs and industry reflection data in the Los Angeles basin. *Journal of Geophysical Research*, 108(B3):Article no. 2170, 2003.

[30] Swaminathan Krishnan. FRAME3D – A program for three-dimensional nonlinear time-history analysis of steel buildings: User guide. Technical Report EERL 2003-03, Earthquake Engineering Research Laboratory, California Institute of Technology, Pasadena, California, USA, 2003.

[31] Swaminathan Krishnan and John F. Hall. Modeling steel frame buildings in three dimensions – Part I: Panel zone and plastic hinge beam elements. *Journal of Engineering Mechanics, ASCE (Scheduled for publication in April 2006)*, 2006.

[32] Swaminathan Krishnan and John F. Hall. Modeling steel frame buildings in three dimensions – Part II: Elastofiber beam element and examples. *Journal of Engineering Mechanics, ASCE (Scheduled for publication in April 2006)*, 2006.

[33] Norman A. Haskell. Crustal reflection of plane SH waves. *Journal of Geophysical Research*, pages 4147–4150, 1996.

[34] J. G. Anderson, Y. Lee, Y. Zeng, and S. M. Day. Control of strong motion by the upper 30 meters. *Bulletin of the Seismological Society of America*, 86:1749–1759, 1996.

[35] M.D. Trifunac, M.I. Todorovska, and T.Y. Hao. Full-scale experimental studies of soil-structure interaction – a review. In *Proceedings of the Second US–Japan Workshop on Soil-Structure Interaction, Tsukuba City, Japan, 52 pages (published on CD-ROM)*, 2001.

[36] Jonathan P. Stewart, Raymond B. Seed, and Gregory L. Fenves. Empirical evaluation of inertial soil-structure interaction effects. Technical Report PEER-98/07, Pacific Earthquake Engineering Center, University of California, Berkeley, California, USA, 1998.

[37] Giorgio Serino. Dynamic soil-structure interaction in building response from earthquake records. Technical Report UCB/SEMM-1989/01, Department of Civil Engineering, University of California, Berkeley, California, USA, 1989.

[38] Gregory L. Fenves and Giorgio Serino. Soil-structure interaction in buildings from earthquake records. *Earthquake Spectra*, 6(4):641–655, 1990.

[39] M.D. Trifunac, T.Y. Hao, and M.I. Todorovska. Response of a 14-story reinforced concrete structure to nine earthquakes: 61 years of observation in the Hollywood storage building. Technical Report CE 01-02, Department of Civil Engineering, University of Southern California, Los Angeles, California, USA, 2001.

[40] S. H. Hartzell, P. Liu, and C. Mendoza. The 1994 Northridge, California, earthquake: Investigation of rupture velocity, rise time, and high-frequency radiation. *Journal of Geophysical Research*, 101(B9):20091–20108, 1996.

[41] David J. Wald, Thomas H. Heaton, and Ken W. Hudnut. A dislocation model of the 1994 Northridge, California, earthquake determined from strong-motion, GPS, and leveling-line data. *Bulletin of the Seismological Society of America*, 86:S49–S70, 1996.

[42] R. Darragh, T. Cao, V. Graizer, A. Shakal, and M. Huang. Los Angeles code-instrumented building records from the Northridge, California earthquake of January 17 1994: Processed release No. 1. Technical Report OSMS 94-17, California Strong Motion Instrumentation Program, California Department of Conservation, Division of Mines and Geology (now California Geological Survey), California, USA, 1994.

[43] FEMA. *Recommended Specifications and Quality Assurance Guidelines for Steel Moment-Frame Construction for Seismic Applications*. FEMA-353. Federal Emergency Management Agency, USA, 2000.

[44] Kerry E. Sieh, Minze Stuiver, and David Brillinger. A more precise chronology of earthquakes produced by the San Andreas fault in southern California. *Journal of Geophysical Research*, 94:603–623, 1989.

[45] Ray J. Weldon, Thomas E. Fumal, Glenn P. Biasi, and Katharine M. Scharer. Past and future earthquakes on the San Andreas fault. *Science*, 308:966–967, 2005.

[46] Donna Eberhart-Phillips, Peter J. Haeussler, Jeffrey T. Freymueller, Arthur D. Frankel, Charles M. Rubin, Patricia Craw, Natalia A. Ratchkovski, Greg Anderson, Gary A. Carver, Anthony J. Crone, Timothy E. Dawson, Hilary Fletcher, Roger Hansen, Edwin L. Harp, Ruth A. Harris, David P. Hill, Sigrun Hreinsdottir, Randall W. Jibson, Lucile M. Jones, Robert Kayen, David K. Keefer, Christopher F. Larsen, Seth C. Moran, Stephen F. Personius, George Plafker, Brian Sherrod, Kerry Sieh, Nicholas Sitar, and Wesley K. Wallace. The 2002 Denali fault earthquake, Alaska: A large magnitude, slip-partitioned event. *Science*, 300:1113–1118, 2003.

[47] Chen Ji, Don V. Helmberger, T. Song, K. F. Ma, and David J. Wald. Co-seismic slip distribution and tectonic implication of the 1999 Chi-Chi, Taiwan, earthquake. *Geophysical Research Letters*, 28(23):4379–4382, 2001.

[48] Shui-Beih Yu, Long-Chen Kuo, Ya-Ju Hsu, Hsuan-Han Su, Chi-Ching Lui, Chin-Shyong Hou, Jiin-Fa Lee, Teng-Chang Lai, Chih-Chung Liu, Cheng-Lun Liu, Teh-Fu Tseng, Chun-Shyong Tsai, and Tzay-Chyn Shin. Preseismic deformation and coseismic displacements associated with the 1999 Chi-Chi, Taiwan, earthquake. *Bulletin of the Seismological Society of America*, 91(5):995–1012, 2001.

[49] H. Magistrale, K. McLaughlin, and S. Day. A geology based 3-D velocity model of the Los Angeles basin sediments. *Bulletin of the Seismological Society of America*, 86:1161–1166, 1996.

[50] H. Magistrale, S. Day, R. Clayton, and R. Graves. The SCEC southern California reference three-dimensional seismic velocity model version 2. *Bulletin of the Seismological Society of America*, 90(6B):S65–S76, 2000.

[51] M. Kohler, H. Magistrale, and R. Clayton. Mantle heterogeneities and the SCEC three-dimensional seismic velocity model version 3. *Bulletin of the Seismological Society of America*, 93:757–774, 2003.

[52] Robert W. Graves and Arben Pitarka. Simulation of broadband time-histories combining deterministic and stochastic methodologies. In *Proceedings of the American Geophysical Union Fall Meeting, USA*, 2003.

[53] Robert W. Graves. Broadband simulation for a mw 6.7 earthquake on the puente hills fault. *Seismological Research Letters*, 76:242, 2005.

[54] AISC. *Manual of Steel Construction, Load and Resistance Factor Design (Second Edition)*. American Institute of Steel Construction, Inc., USA, 1994.